UNIVERSITAT POLITÈCNICA
DE CATALUNYA
BARCELONATECH

Understanding and mitigating the post-injection seismicity induced by fluid injection in Enhanced Geothermal Systems

Auregan Boyet

Ph.D. thesis
Civil Engineering Program, UPC

Understanding and mitigating the post-injection seismicity induced by fluid injection in Enhanced Geothermal Systems

by Auregan Boyet

Hydrogeology Group (GHS)
Department of Civil and Environmental Engineering, Universitat Politècnica de Catalunya (UPC)
Instituto Mediterráneo de Estudios Avanzados (IMEDEA, CSIC)

Thesis supervisors: Dr. Víctor Vilarrasa Riaño and Dr. Silvia De Simone

December 2023

UNIVERSITAT POLITÈCNICA DE CATALUNYA
BARCELONATECH

Department of Civil and Environmental Engineering

EXCELENCIA
MARÍA
DE MAEZTU
2023-2027

This thesis was funded from the European Research Council (ERC) under the European Union's Horizon 2020 Research and Innovation Program through the Starting Grant GEoREST (www.georest.eu) under Grant agreement No. 801809.

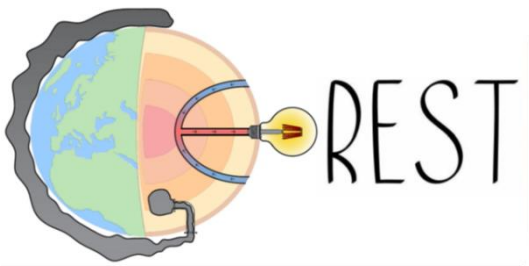

Summary

Induced seismicity due to hydraulic stimulation and circulation is a hurdle for the development of Enhanced Geothermal Systems (EGS). The monitored seismicity has occasionally reached magnitudes large enough to be felt by local populations, and in several EGS cases the largest magnitude earthquakes occur few hours to several months after the cessation of the injection operations. This thesis aims to i) deepen the understanding of the processes that trigger such induced seismicity, ii) improve forecasting methodologies and iii) explore strategies to mitigate its occurrence. The focus is especially placed on post-injection seismicity. The well-documented case of Basel EGS, Switzerland, is adopted as verification example.

Firstly, the identification of the triggering mechanisms at Basel is performed making use of a coupled hydro-mechanical model with increasing level of complexity. A simple fault-crossed elastic domain is compared with a homogeneous elastic domain to highlight the importance of structural heterogeneities on the direct and indirect (poroelastic) effects of pressure diffusion as triggering mechanisms of seismicity. Additionally, another hydro-mechanical model is implemented by a discrete faulting network, based on seismic interpretations. The model simulates the plastic reactivations of faults, and the effects of pore pressure diffusion, poroelastic stressing, shear-slip stress transfer and slip weakening are distinguished. Simulation results show that the faults located in the vicinity of the injection well fail during injection, mainly triggered by pore pressure build-up. At the stop of injection, poroelastic stress relaxation leads to the immediate rupture of faults that were stabilized during the injection. Stress redistribution is also a prominent triggering mechanisms of post-injection reactivation of distant faults. Slip-induced friction weakening on certain faults amplifies the potential of these faults to reactivate multiple time during injection and after its stop.

The development of a forecasting methodology for induced seismicity is the second major achievement of this thesis. The hydro-mechanical model previously implemented is combined with a seismicity rate model, the Gutenberg-Richter law and the Epidemic Type Aftershock Sequence model to quantify the seismicity magnitude, of both mainshocks and aftershocks, associated to the stress changes due to fluid injection. The application of this hybrid methodology on the discrete-faulted hydro-mechanical model of Basel EGS gives the opportunity to explore the effects of different strategies of injection on the enhancement of fault permeability and induced seismicity rate. A constant injection protocol followed by a progressive decrease of injection rate mitigates post-injection seismicity, while enhancing the permeability of the faults in the domain. The thesis also addresses the discussion of the final cessation of injection, comparing the results of shut-in and bleed-off of the well. Results suggest that shutting-in the well can mitigate better early post-injection seismicity than bleeding-off the well, but pore pressure diffusion can destabilize critically-oriented faults in the reservoir for a longer period of time.

By providing enhanced understanding, new methodologies and practical solutions, this thesis represents a substantial step-forward in the mitigation and control of induced seismicity, and in particular of post-injection seismicity, in EGS.

Resumen

La sismicidad inducida por la estimulación hidráulica y la circulación de fluidos es un obstáculo para el desarrollo de los sistemas geotérmicos mejorados (EGS por sus siglas en inglés). La sismicidad registrada ha alcanzado ocasionalmente magnitudes lo suficientemente grandes como para ser percibida por la población local, y en varios casos de EGS los terremotos de mayor magnitud se producen entre pocas horas y varios meses después del cese de las operaciones de inyección. Esta tesis tiene como objetivos i) profundizar en el conocimiento de los procesos que desencadenan esa sismicidad inducida, ii) mejorar las metodologías de previsión y iii) explorar estrategias para mitigar su aparición. El foco se centra especialmente en la sismicidad posterior a la inyección. Como ejemplo de verificación se adopta el bien documentado caso del EGS de Basilea (Suiza).

En primer lugar, se realiza la identificación de los mecanismos desencadenantes de la sismicidad en Basilea haciendo uso de un modelo hidromecánico acoplado con un nivel de complejidad creciente. Se compara un dominio elástico atravesado por una zona de falla con un dominio elástico homogéneo para destacar la importancia de las heterogeneidades estructurales en los efectos directos e indirectos (poroelásticos) de la difusión de la presión como mecanismos desencadenantes de la sismicidad. Además, otro modelo hidromecánico se implementa incluyendo una red discreta de fallas, basada en interpretaciones sísmicas. El modelo simula las reactivaciones plásticas de las fallas, y se distinguen los efectos de la difusión de la presión de poro, la tensión poroelástica, la transferencia de tensión por cizalla y el debilitamiento por deslizamiento. sugerirlos resultados de las simulaciones muestran que las fallas situadas en las proximidades del pozo de inyección rompen durante la inyección, provocado principalmente por el aumento de la presión de poro. Al cesar la inyección, la relajación de tensiones poroelástica provoca la ruptura inmediata de las fallas que se estabilizaron durante la inyección. La redistribución de tensiones es también un importante mecanismo desencadenante de la reactivación de fallas distantes tras la inyección. El debilitamiento de la fricción inducido por deslizamiento en fallas amplifica el potencial de estas fallas para reactivarse varias veces durante la inyección y después de su cese.

El desarrollo de una metodología de previsión de la sismicidad inducida es el segundo gran logro de esta tesis. El modelo hidromecánico previamente implementado se combina con un modelo de tasa de sismicidad, la ley de Gutenberg-Richter y el modelo de secuencia de réplicas (ETAS por sus siglas en inglés) para cuantificar la magnitud de la sismicidad de los terremotos pronosticados, asociados a los cambios de tensión debidos a la inyección de fluidos. La aplicación de esta metodología híbrida al modelo hidromecánico de fallas discreta de Basilea EGS brinda la oportunidad de explorar los efectos de diferentes estrategias de inyección en el aumento de la permeabilidad de las fallas y la tasa de sismicidad inducida. Un protocolo de inyección constante, seguido de una disminución progresiva de la tasa de inyección, mitiga la sismicidad posterior a la inyección, y sigue aumentando la permeabilidad de las fallas del dominio. La tesis también aborda el debate sobre el cese final de la inyección, comparando los resultados del cierre y la purga del pozo. Los resultados sugieren que el cierre del pozo puede mitigar la sismicidad temprana posterior a la inyección mejor que la purga, pero la difusión de la presión de poros puede desestabilizar las fallas críticamente orientadas del yacimiento durante un período de tiempo más largo.
Al proporcionar una mejor comprensión, nuevas metodologías y soluciones prácticas, esta tesis representa un avance sustancial en la mitigación y el control de la sismicidad inducida, especialmente de la posterior al cese de la inyección, en EGS.

Acknowledgements

I would like to express my deepest gratitude to my supervisors, Dr Víctor Vilarrasa and Dr. Silvia De Simone. I thank Víctor for trusting me and giving me the opportunity to try the adventure of the PhD and for his guidance during these three years. I thank Silvia for her support and her encouragements during this academic journey. I am grateful for their patience, their exigence and for pushing me to do better each time, for sharing their knowledge and their passion.

I would like to thank the researchers that shared their insights during the different steps of the thesis writing, Dr. Keurfon Luu, Dr. Frédéric Cappa, Dr. Jonny Rutqvist and Dr. Shemin Ge. I thank all the members of the Georest group for their recommendations and their support. I have to thank individually IMan and Linus for their attentive ears and their wise advices, and their generosity outside of work.

Finally, I want to thank everyone else. The persons that supported me blindly during these years without understanding what I was doing, my struggles, and who celebrated with me my little victories. I thank Claudia and Aina for sharing with me their island and so many good moments, for making me feel home.

I also have to thank the ones that are with me since a long time. I thank my friends, Léa, Anna, Elise, Iris, Juliette, Margaux, Océane, Yesmine and Lilian, for always helping me to always laugh and to be bold.

Et pour finir, je remercie JC et Véro pour m'avoir toujours donné la chance d'être qui je voulais et de faire ce que je voulais. Merci tout court à Benjamin, Tanguy et Eliot. Et merci à mes grands-parents, Louise, Nicole et Paul, et François, pour leur soutien, les hachis Parmentiers et les glaces au chocolat quand je rentrais me reposer.

Contents

Summary i
Resumen ii
Acknowledgements iii
Contents iv
List of figures vii
List of tables x
Chapter 1: Introduction 1
1.1. Background and motivations 1
1.2. Objectives and methodology 4
1.3. Thesis layout 5
Chapter 2: Post-injection induced seismicity: a counterintuitive and restraining consequence of fluid injection in Enhanced Geothermal Systems 8
2.1. Introduction 8
2.2. Physical processes of injection-induced seismicity in Enhanced Geothermal Systems 12
2.2.1. Fault activation causing induced seismicity in EGS 12
2.2.2. Stress changes driving fault activation 14
2.2.3. Field and laboratory experiments 16
2.2.4. Triggering mechanisms of injection-induced seismicity in EGS 16
2.3. Identification of the potential mechanisms that triggered post-injection LME in EGS: summary of documented cases 24
2.3.1. EGS cases in which the largest magnitude earthquake occurs early in the post-injection stage 25
2.3.2. EGS cases at which the largest magnitude earthquake occurs lately in the post-injection stage 30
2.4. Recent advances in the mitigation of induced seismicity 33
2.4.1 Understanding of the post-injection induced seismicity 33
2.4.2. Real-time monitoring and mitigation of induced seismicity 34
2.4.3 Forecasting methodologies and mitigation of induced seismicity 35
2.4.4 Injection protocols to mitigate induced seismicity 36
2.5. Future perspectives 36
Chapter 3: Physics-based modelling to understand and to propose forecasting methods of induced seismicity 38
3.1. Introduction 38
3.1.1. Pore pressure build-up alone is not enough to explain induced seismicity 39
3.1.2. Including geological structures in models 39
3.2. Model settings 40

3.3. Identification of the triggering mechanisms 43
3.4. Evolution of the destabilizing effects of pore pressure and poroelastic stressing 47
3.5. Effect of geological structures on the seismicity rate 48
3.6. Discussion 51
3.6.1. Beyond pore pressure diffusion 51
3.6.2. Adding relevant geological structures into models 52
3.7. Conclusions 53
Chapter 4: Poroelastic stress relaxation, slip stress transfer and friction weakening controlled post-injection seismicity at the Basel Enhanced Geothermal System 54
4.1. Introduction 54
4.2. Methods 57
4.2.1. Fault network 57
4.2.2. Hydro-mechanical problem 57
4.3. Modelling approach 59
4.3.1. Conceptual model 59
4.3.2. Numerical Model setup 61
4.4. Results 63
4.4.1. Comparison of modelled slip with Basel microseismicity 63
4.4.2. Pore pressure diffusion 65
4.4.3. Stress variations 67
4.5. Discussion and conclusions 70
Chapter 5: Forecasting fluid-injection induced seismicity to choose the best injection strategy for safety and efficiency 76
5.1. Introduction 76
5.2. Hybrid method to forecast induced seismicity 79
5.2.1. Hydro-mechanical model 79
5.2.2. Seismicity rate model 81
5.2.3. Magnitude attribution with Gutenberg-Richter law 82
5.2.4. The Epidemic Type Aftershock Sequence model 83
5.3. Calibration and application of the hybrid method to the case of the Basel EGS 83
5.4. Effects of different injection protocols on the stability of discrete faults 85
5.4.1. Permeability enhancement 86
5.4.2. Forecasted seismicity 88
5.5. Spatially forecasting the seismicity 89
5.6. Discussion 91
5.7. Conclusions 93
Chapter 6: To bleed-off or not to bleed-off? 94
6.1. Introduction 94

6.2. Methodology to forecasting seismicity rate 94
6.3. Bleed-off or shut-in? 98
6.4. The importance of progressive decrease of pressure rate at the stop of injection 99
6.5. Conclusions 100
Chapter 7: Conclusions 103
Appendices 105
A. Supplementary information for Chapter 3 105
A.1. Hydro-mechanical problem 105
A.2. Calculation of the static stress transfer 106
A.3. Seismicity rate model 107
B. Supplementary information for Chapter 4 109
C. Supplementary information for Chapter 6 114
D. Publications and conference presentations 117
Publications in scientific journals 117
Presentations in Congresses 117
References 118

List of figures

Figure 1.1: Worldwide distribution of injection-induced seismicity cases in the applications of gas storage, hydraulic fracturing, research studies, geothermal systems and waste fluid disposal (Kivi et al., 2023) 2

Figure 1.2: Profile of wellhead pressure (black line) and injection flow rate (red line) of hydraulic stimulation at Basel. (b) Time history of moment magnitude (Ml) of induced seismicity recorded by microseismic monitoring network (blue: co-injection, orange: post-injection). (c) Microseismic hypocentre distribution, before and after shut-in, in EW and NS cross sections of reservoir. The larger events with Mw > 2.0 are plotted with circles, with their size scaled to magnitude. The grey dots indicate the hypocentres of events that occurred after 20 days (Mukuhira et al., 2017). 3

Figure 2.1: The Mohr circle represents the stress tensor, with every point corresponding to a different orientation. The grey circle illustrates the initial stress state. The red dot indicates the fault plane orientations that fail corresponding to the points where the Mohr circle touches the failure envelope. (a) Pressure-driven mechanisms modify the stress tensor: the blue circle corresponds to the shift of the grey circle in response to an increase of pore pressure Δp, while the green circle corresponds to the combination of pressure increase with variation of total stress due to poroelasticity. (b) Thermoelasticity induces the shift of the initial circle to the left or to the right, and it can also induce variation of the circle size. (c) Geochemical interactions alter fault strength, i.e., cohesion and friction, which can facilitate reaching failure conditions. d. Static stress transfer from adjacent faults lead to decrease or increase of the circle, which can stabilize or destabilize the faults. 15

Figure 2.2: Asymmetric static stress transfer due to dextral fault reactivation. Left-lateral static stress transfer is shown in blue and right-lateral stress transfer in red. The magnitude of stress redistribution depends on the surface of the fault, the amount of slip, the initial stress state and on mechanical properties of the rock. Dextral faults affected by right-lateral static stress transfer could be reactivated. 20

Figure 2.3: Fluid injection induces an aseismic creep propagation ahead of the pressurized front. (a) The stress perturbation due to creep can induce seismic activation on faults far from the injection well during the injection. (b) At the stop of injection, the aseismic creep is self-propagating without any further fluid pressure increase.....21

Figure 2.4: Conceptual illustration explaining (a) co-injection and (b) post-injection triggering mechanisms of fluid-injection induced seismicity. Fluid is injected along a well and circulated through fractures. (1) The increase of pore pressure opens fractures and enhances their permeability and consequently the circulation. (2). The deformation due to the pore pressure build-up in the vicinity of the well affects a wider area and produces poroelastic stress that can induce slip along distant faults. (3) Thermoelastic stressing affects the stability of fault from the start of injection. (4) Chemical interactions affect the frictional properties of faults. (5) The seismic, or aseismic, fault slips redistribute the stresses around the faults and can nucleate more seismicity and fault slips. (6) Aseismic creep diffuses from the injection well to the outside of the reservoir, even after the stop of injection. (7) Earthquake rupture induces others earthquakes on the same fault. (8) Stress accumulation on large faults due to distant and/or previous injections can induce high-magnitude seismic events. 22

Figure 2.5: Temporal evolution of the largest magnitude earthquake (LME) monitored after the stop of injection (full circle), compared to the LME monitored during the fluid injection (empty circle). The grey vertical line separates cases with seismic delay shorter or longer than two days. SsF: Soultz-sous-Forêts. 25

Figure 2.6: (a) Catalog of the clustered main events occurring during injection and after it stops at Basel, as reported by Deichmann et al. (2014). (b) Mohr circles for the fault build from the Cluster 88 in the hydro-mechanical model of a fault network (Boyet et al., 2023b). Dashed circle correspond to the co-injection stress tensor and solid circles for the post-injection stage. The blue circle corresponds to the effects of pore pressure build-up, the green to the poroelasticity and the orange to the static stress transfer. During injection, the fault is stabilized by poroelastic effects but the shut-in induces stress changes and the reactivation of the fault.....28

Figure 3.1: Schematic of the model setting. Injection pressure, plotted in the inset in the lower right part of the domain, is imposed at the centre of the domain (black dot). Initial stress conditions are aligned with the orthogonal axes. The fault zone is represented with the grey band. Fixed pressure and zero normal displacement conditions are applied to the boundaries. 42

Figure 3.2: Difference between pore pressure due to fluid injection and critical pressure, $p - pc$, at each Basel EGS seismic event location and time of occurrence in (a, b) the homogeneous domain [74 events out of 185 with positive values] and (c, d) the domain crossed by a fault zone (represented by the grey band in (d)) [111 events out of 185 with positive values]. In (a, c) results are plotted as a function of the distance from the injection well and time, while in (b, d) they are projected on a horizontal plane at the depth of the injection well. The magnitude of the largest events is indicated in (a) and (b). The orientation of the focal mechanisms is represented in (b) and (d). 44

Figure 3.3: CFS and ΔCFS due to the effects, combined and individually, of pore pressure diffusion ($\Delta CFSpp$), poroelastic stressing ($\Delta CFSpe$) and static-stress transfer ($\Delta CFStr$) at the time and location of occurrence of seismic events at Basel EGS in (a) homogeneous and (b) fault-crossed domains. Results are plotted as a function of distance from the injection well and time in the top row, while their spatial distribution is shown in the bottom row, where they are projected on a horizontal plane at the depth of the injection well. Positive values (red) indicate mechanical destabilization, while negative values (blue) indicate mechanical stabilization. The number of events for which we estimate a CFS>0 is reported for each mechanism. (c) The difference between the CFS estimated for the fault-crossed and homogeneous models highlights that the fault-crossed model is more capable to simulate the observed seismicity as it reproduces a larger destabilization than the homogeneous domain (green tones, positive values), which is also equivalent to the difference of DCFS of the two models..... 46

Figure 3.4: CFS variation at the stop of injection (day 6) and 2 days after (day 8) caused by the individual effects of pore pressure variation, $\Delta CFSpp$, and poroelastic stressing, $\Delta CFSpe$, and caused by their combined effects, $CFSpp + pe$, in (a) the homogeneous and (b) the fault-crossed models for the most critical orientation. The contour line corresponds to the value 0. Areas with positive CFS are in failure conditions. (c) Temporal evolution, in the homogeneous (solid lines) and in the fault-crossed domains (dashed lines), of the surface area (in m²) with positive CFS (orange lines), with $CFS > 5\ MPa$ (red lines) and $CFS > 10\ MPa$ (dark red lines). 48

Figure 3.5: Evolution of the probable induced seismicity rate PSR during injection (day 4), at the stop of injection (day 6) and 1 day after (day 7) in (a) the homogeneous and (b) the fault-crossed models. (c) Temporal evolution of the cumulative PSR (PSR) in the homogeneous (dark orange) and fault-crossed (light orange) domains, and (d) temporal evolution of the absolute seismicity rate SR at four points of the fault-cross domain for both dominant strikes of the fracture network (colors corresponding to the colored markers shown on the day-7 plots). The vertical dashed lines in (c) and (d) indicate the stop of injection. 50

Figure 4.1: Geometry and conditions of the model. a) Plan view of the location of seismic events at Basel, sorted by clusters according to Deichmann et al. (2014). Colours correspond to different clusters as indicated by the numbers. b) Model setup showing geometry, fault network and boundary conditions. The central black dot represents the injection well and the grey area the damaged zone. Initial values of principal stresses and pore pressure are indicated, along with the boundary conditions of constant pressure prescribed at the outer boundaries (represented by the crossed circle) and no displacement perpendicular to the boundaries (represented by the triangles). Note the (b) represents the central region of the model containing the faults, but that boundaries are actually at 950 m away from the well. The direction of shear slip is also indicated for each fault. c) Pressure evolution in time at the well location, according to Häring et al. (2008) 62

Figure 4.2: Temporal evolution of modelled plastic strain, εp (solid lines), at different locations on each fault (represented by different colors as indicated in the top-left plot), and of the cumulative seismic moment Mo (grey solid lines) of the observed seismic events as reported by Deichmann et al. (2014). At fault C, εp for the case without friction coefficient weakening is represented by the dashed lines. The vertical grey line represents the stop of injection at day 6. Note that the scale of the plastic strain is different for each fault. 64

Figure 4.3: Pore pressure evolution in the domain. a) Contour plot of pressure at the end of injection (day 6), b) contour plot of pressure in the post-injection stage (day 7), c) spatial distribution of pressure at different days from day 2 to day 10 along a cross-section extending from the injection well to the bottom-left corner of the domain, which crosses faults A and C, as represented by the dashed white line in (a). The damaged zone is represented by the grey band in Figure 4.3c. 66

Figure 4.4: Temporal evolution of effective normal and shear stresses changes (blue and yellow lines, respectively), Coulomb Failure Stress changes (green lines) and pore pressure (red line) under elastic (solid lines) and visco-plastic (dashed lines) behaviour at the central location of the selected faults. The critical

pressure for failure is represented by the horizontal dark red line. The grey shadowed regions correspond to times with increasing εp for each fault according to Figure 4.2. Note that the scale of stress variation is different in each plot. The behaviour of the rest of the faults is shown in Figure SI B.5. 67

Figure 4.5: Shear stress variation $\Delta\tau xy$ in the elastic scenario before and after the stop of injection. Observe the spatial distribution of the poroelastic stressing due to the injection-driven volume expansion during injection (a) and volume contraction during bleed-off (b and c), evolving as four antisymmetric lobes with respect to the injection well (black dot). Positive shear stress indicates left-lateral movement. 69

Figure 4.6: Shear stress variation $\Delta\tau xy$ in the visco-plastic scenario at different times. a) At day 5.8, fault B is affected by the injection. b) At day 6.4, the rupture of fault B induces stress transfer, and amplifies the stress redistribution caused by poroelastic contraction due to bleed-off. (c) At day 6.7, fault F yields due to the combination of the shear-slip stress transfer and poroelastic mechanisms. Observe the evolution of the positive small lobe from poroelastic stressing after the bleed-off at day 6 that affects fault B. Note that the figure shows a close-up of the domain focusing on the area of interaction between faults B and F. 69

Figure 4.7: Temporal evolution of the portion of each fault reactivated by the different combinations of triggering mechanisms. Faults G is not reactivated by any mechanisms.....73

Figure 4.8: Schematic illustration of the triggering mechanisms of induced seismicity. (a)-(c) Evolution of pore pressure, poroelastic stress and shear-slip stress transfer, respectively, before, during and after injection in a simplified generic fault network. The black dot in the centre represents the injection well. (d)-(f) Mohr circles illustrating the stress state of the faults at each stage. (a) At initial conditions, faults F1 and F2 undergo right-lateral slip while fault F3 undergoes left-lateral slip (dashed arrows), in accordance with the maximum (σH) and minimum (σh) horizontal stresses. (b) During injection, pore pressure diffuses in the vicinity of the well. Poroelastic stressing extends farther and faster, and it exerts an inversed stress than the initial shear stress on F2 and F3, which are thus stabilized during injection. Combined with pore pressure, poroelastic stressing triggers the reactivation of F1, with the decrease of normal stress and the increase of the shear stress (e). Subsequently, F1 is stabilized by the shear stress drop (c and f). After the stop of injection, the pore pressure front continues to diffuse, while poroelastic stress relaxes (c). This change of direction leads to the increase of shear stress at the previously stabilized F2 and F3, which reach the failure envelope (f). The shear-slip stress transfer due to the reactivation of F2 affects F3, emphasizing the poroelastic effects until reaching failure.....74

Figure 5.1: Hybrid methodology: The CFS outputted from the hydro-mechanical (HM) model is the main input of the seismicity rate model. The Gutenberg-Richter law and the ETAS model estimate the magnitude and the aftershock-sequence of the mainshocks. (a) Hydro-mechanical model with the fault network. Note that the x- and y-axes are not aligned with the north but with the principal stresses. The injection well is represented by the black dot in the centre. Colours refer to the probability of hosting a fracture, which is equal to 1 on faults A to G. (b) Temporal evolution of cumulative number of observed mainshocks from the catalogue of Deichmann et al. (2014) (blue line) and of simulated mainshocks in the injection scenario used for calibration, which reproduces the operations at Basel (injection during 6 days followed by 5-hour shut-in and a bleed-off until the end) (red line). (c) Time evolution of number of mainshocks (red) and aftershocks (grey); and time evolution of the magnitude of seismic events in the domain during the calibration injection case. 79

Figure 5.2: (a) Simulated wellhead pressure for the different injection protocols in the hydro-mechanical model. (b), (c) and (d) show, on top, the forecasted seismicity rate in the domain $SRfault$ through time, and on the bottom, the estimated magnitude Mw of the forecasted earthquakes for the progressive, cyclic and constant injection protocols, respectively. The mainshock seismicity rate and earthquakes follow the same colour code that in figure (a), while the aftershocks are in grey. Vertical lines correspond to the stop of the injections. 86

Figure 5.3: (a) Evolution of the permeability of the faults outputted from the hydro-mechanical model. The permeability varies when the fault fails is shear mode. (b) Seismicity rate of each fault, $SRfault$, through time for each of the injection strategies. Although some faults reach failure conditions in the hydro-mechanical model, their CFS is too low to forecast the reactivation of the faults as seismic according to the calibrated seismicity rate model. Vertical lines correspond to the stop of the injections. 87

Figure 5.4: Pressure at the stop of injection for each strategy (day 6 for progressive injection, day 7.5 for cyclic injection (peak of injection of the last long-term cycle) and day 4.5 for constant injection) in the domain, outputted from the hydro-mechanical model.....87

Figure 5.5: (a) Cumulative seismic moment $Mo = 101.5Mw + 6.07$ (Kanamori & Brodsky, 2004) of the forecasted earthquakes (lines) and maximum magnitude Mmax for both co-injection (circle) and post-

injection (square) stages. Vertical lines correspond to the stop of injections. (b) Maximum earthquake magnitude as a function on the normalized injected volume for each timestep. The grey band corresponds to the time after the stop of injection. 89

Figure 5.6: Time evolution of forecasted seismicity rate of the whole domain $SRdom$ and corresponding magnitude for the (a) progressive, (c) cyclic and (e) constant injections. Colours represent the mainshock seismicity rate and magnitude while grey represents the aftershocks. (b), (d) and (f) the 2D spatial distribution of the co- and the post-injection seismicity plotted for the three protocols. The colour scale represents the magnitude of the estimated earthquakes. For plotting purpose, the location of the earthquakes within the faults and in the matrix are adjusted to avoid overlapping. 91

Figure 6.1: (a) Pressure applied at the injection well, similar to the monitored wellhead pressure at Basel. The stop of injection is represented in blue for the bleed-off scenario and in orange for the shut-in scenario. (b) Pressure at the two different points, plotted in the subplot (c) during the simulation of both scenarios. (c) Pressure simulated by the hydro-mechanical model at day 8, 2 days after the stops of injection, and at day 25 for the two stop scenarios. 99

Figure 6.2: Seismicity rate of each fault, $SRfault$, through time, for each fault under the two scenarios of bleed-off (blue lines) and shut-in (orange lines). Vertical dotted lines correspond to the stop of injection. 99

Figure 6.3: Plastic strain rate evolution of each fault, $\frac{d\varepsilon_p}{dt}$, for each fault under the two scenarios of bleed-off (blue lines) and shut-in (orange lines). Vertical dotted lines correspond to the stop of injection. 100

Figure 6.4: (a) Pressure applied at the injection well for the scenarios with progressive (greens) and stepping (pinks) stop of injection; the standard shut-in scenario is represented in orange. (b) Total seismicity rate (sum of the seismicity rate of the Faults A to G) through time. (c) Cumulative number of mainshocks (solid lines and left axis) and cumulative number of aftershocks (dashed lines and right axis) through time for each scenario. (d) Maximum forecasted magnitude of mainshocks (filled squares) and aftershocks (empty squares) in the post-injection stage. The vertical lines at day 8 and 10 mark the end of the injection reduction. 101

List of tables

Table 2.1 EGS cases for which the post-injection induced earthquakes have higher magnitude (Mw, Ml in certain cases annotated with *) than during the injection phase, sorted as a function of the delay between shut-in and the time of the maximum magnitude earthquake. Note that the largest magnitude earthquake is not always felt on surface ($Mw < 2$). SS: strike-slip; NF: normal faulting 11

Table 4.1: Characteristics and estimated parameters for each fault in the numerical model of the Basel EGS project. Mw is the seismic event magnitude of the largest event of the cluster group associated with the corresponding fault. Friction angle φ is calibrated to reproduce fault reactivation occurrence. Critical pressure Pc is calculated with Equation (4.13), using a friction coefficient of $\mu = 0.6$ (corresponding to $\varphi = 30°$), while critical pressure $Pc\varphi$ using the friction coefficient that leads to failure at the time of the onset of induced seismicity for each fault, i.e., $\mu\varphi = tan(\varphi)$. Net slip is calculated with Equation (4.1). 61

Table 4.2: Hydromechanical properties of the materials composing the numerical model. 62

Table 5.1 Parameters of the seismic models, with values for natural earthquakes and for the case of Basel EGS project. Bold values are calibrated so that the models reproduce the monitored number of mainshocks (185 earthquakes with a magnitude $Mw > 0$ (Deichmann et al., 2014)) and the total number of monitored earthquakes (11,200 events during and shortly after the stop of injection (Häring et al., 2008)). 84

Table 5.2: Material properties of matrix and fault elements of the hydro-mechanical model (Boyet et al., 2023b) 85

Chapter 1: Introduction

1.1. Background and motivations

The Paris Agreement was signed in 2015 by 196 nations during the UN Climate Change Conference (COP21). The Agreement legally binds the signing parties to take actions aimed at mitigating climate change with the goal of keeping the rise in mean global temperature below 2°C above pre-industrial levels, and preferably limit the increase to 1.5 °C. The transition towards a net-zero carbon emissions require the exploitation of green energy technologies. Geothermal energy is a key alternative to fossil combustion to reach the mid-century net-zero targets to mitigate climate change, because it allows producing electricity without intermittency and carbon emissions (IPCC, 2023). Depending on the thermal conditions and depth of rocks, geothermal energy can be used for individual house heating or for power-plant development. Electricity production requires high temperature (T > 150°C), generally found in volcanic systems and in deep crystalline rock (depth larger than 3-5 km). However, the low permeability of crystalline rock implies low fluid circulation capacity. To overcome this limitation, the engineering of the reservoir enhances the permeability to facilitate fluid circulation and heat exchange between the injection and the production wells through an optimal generation of connected high-permeability fault network (Jung, 2013; Tester et al., 2007). These systems are named Enhanced Geothermal Systems (EGS) and are developed since the 1990s.

Induced seismicity is an expected result of fluid injection. In general, induced earthquakes are smaller than natural earthquakes and are not felt by populations due to their depth and low magnitude ($M_w < 2$) (Keranen & Weingarten, 2018; Majer et al., 2007). Fluid injection, operated at high pressure during hydraulic stimulation of the low-permeability rock or at lower pressure during circulation phases, changes the stress conditions of the subsurface and modifies the geomechanical properties of the rock and of the faults (Ge & Saar, 2022). Fluid-injection induced seismicity is mainly triggered by the increase of the pore pressure in the rock which destabilizes pre-existing faults and fractures (Ellsworth, 2013). The destabilization is mostly concentrated in the vicinity of the well, but the associated poroelastic deformation of the rock affects farther subsurface volumes and consequently induces seismicity far from the well (De Simone et al., 2017b; Goebel et al., 2017; Segall & Lu, 2015). Thermal disparities between the rock and the injected fluid also modify the stress and chemical conditions of the reservoir, as well as the chemical interactions between the injected fluid, the rock and the fluid present in the reservoir (De Simone et al., 2013; Kivi et al., 2022). Fault destabilization, in the form of a seismic or aseismic slip, redistributes stresses in the surrounding rock, further affecting the stability of the subsurface.

Although fluid-injection induced seismicity is expected in small magnitudes, the occurrence of earthquakes with magnitudes large enough to be felt by local inhabitants has increased the concern and criticism about the technology, thus limiting the deployment of new EGS projects, and geo-applications in general (Figure 1.1; Albaric et al., 2014; Buijze et al., 2019; Evans et al., 2012; Foulger et al., 2018; Gaucher et al., 2015; Ge & Saar, 2022; Kivi et al., 2023). Post-injection induced seismicity (i.e., seismicity observed after the stop of injection operations) is a recurrent process in geo-applications and it especially questions the viability of their development and the positive public perception of new projects, because it appears difficult to control. Numerous cases of EGS hosted large magnitude earthquakes after the cessation of injection, as it was the case at Pohang, M_w5.5, Korea Republic 2017 (Ellsworth et al., 2019), Vendenheim, M_l3.9, France 2021 (Lengliné et al., 2023) and Basel, M_l3.4, Switzerland 2006 (Häring et al., 2008). These occurrences are counterintuitive, as it is expected that the induced seismicity potential decays in magnitude and frequency after the cessation of injection.

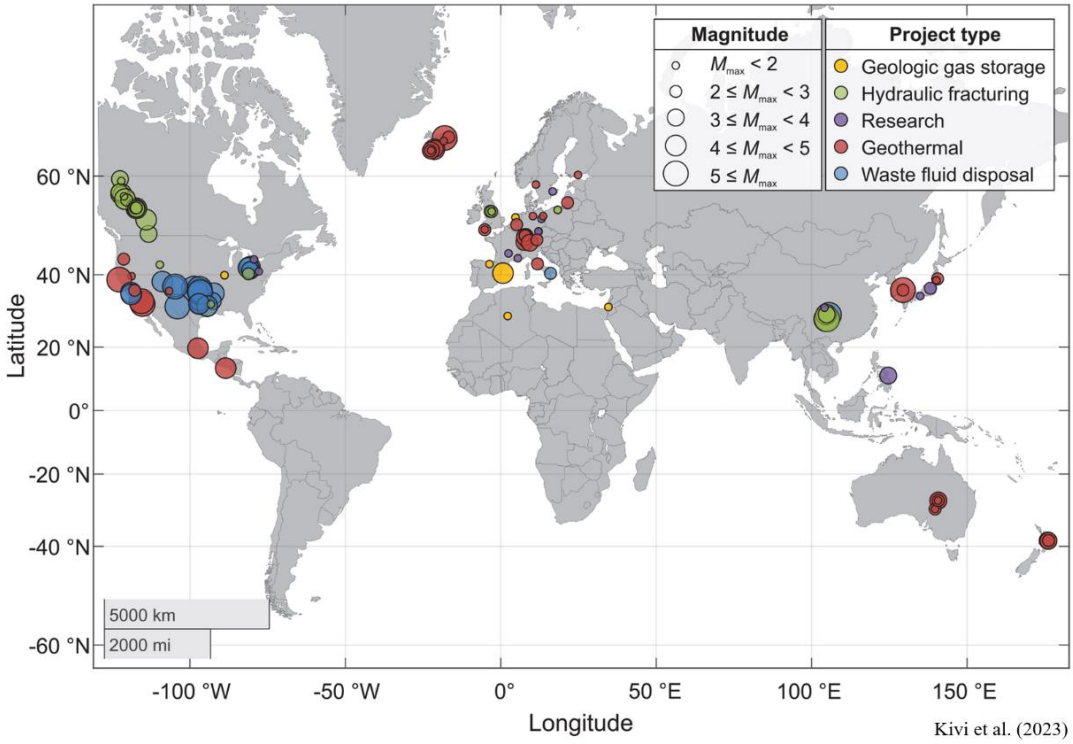

Figure 1.1: Worldwide distribution of injection-induced seismicity cases in the applications of gas storage, hydraulic fracturing, research studies, geothermal systems and waste fluid disposal (Kivi et al., 2023)

The case of the Deep Heat Mining Project at Basel (Switzerland) is particularly interesting because of the occurrence of large magnitude earthquakes right after the cessation of injection. After only 6 days of hydraulic stimulation of the granitic basement (11,570 m^3 of water injected at 4,630-m depth, Figure 1.2a) in December 2006, levels of observed seismicity higher than the traffic light system threshold ($M > 2$) led to the decision of stopping the injection (Häring et al., 2008). 5 hours later, the Largest Magnitude Earthquake (LME) ($M_l3.4 - M_w2.95$) occurred at

the edge of the pressurized area (Deichmann et al., 2014; Herrmann et al., 2019; Kraft & Deichmann, 2014; Mukuhira et al., 2017). The well was then bled-off with the aim of mitigating the nucleation of more high-magnitude events, but levels of seismicity higher than $M_w 1$ were recorded for months, including three events with magnitude close to the LME. After investigations and consequent to the strong public concern, the project was cancelled, remaining as a marked example to highlight the importance of controlling the post-injection induced seismicity.

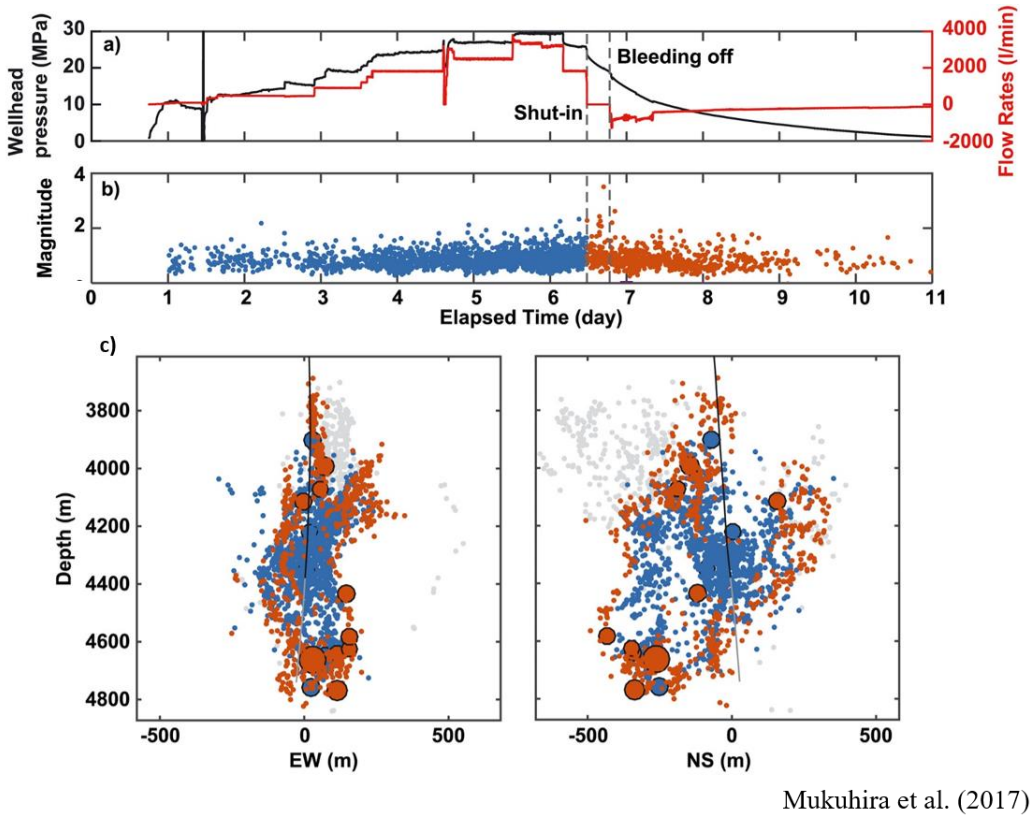

Mukuhira et al. (2017)

Figure 1.2: Profile of wellhead pressure (black line) and injection flow rate (red line) of hydraulic stimulation at Basel. (b) Time history of moment magnitude (M_l) of induced seismicity recorded by microseismic monitoring network (blue: co-injection, orange: post-injection). (c) Microseismic hypocentre distribution, before and after shut-in, in EW and NS cross sections of reservoir. The larger events with Mw > 2.0 are plotted with circles, with their size scaled to magnitude. The grey dots indicate the hypocentres of events that occurred after 20 days (Mukuhira et al., 2017).

To understand and forecast induced seismicity, different modelling tools can be adopted. On the one hand, numerical models are extensively employed to analyse how rocks respond to fluid injection based on physical laws reproducing the involved coupled processes. Empirical and deterministic physics-based models enable the replication of fault activation and induced seismicity over the injection period. Coupled thermo-hydro-mechanical-chemical (THMC) models serve as valuable tools in comprehending seismicity potentially induced by pressure-driven mechanisms, thermal interactions, geochemical reactions, and the geomechanical responses of rocks to fluid injection. On the other hand, statistical models play a crucial role in

describing and forecasting seismicity by using statistical laws. Examples are the Gutenberg-Richter law, which delineates the frequency-magnitude distribution of earthquakes (Gutenberg & Richter, 1942) and Omori's law, elucidating the decay rate of aftershocks near the rupture zone following the initiation of a mainshock (Omori, 1895; Utsu, 1961). Each type of models has its strength in the understanding and the mitigation of the induced seismicity.

Because induced seismicity is controlled by injection, novel injection strategies have been proposed in order to control the occurrence of induced seismicity above an undesired magnitude while still favouring permeability enhancement. For instance, a cyclic soft injection was suggested as a method to control the co-injection induced seismicity and keep it below a magnitude threshold (Jia et al., 2022; Zang et al., 2019). This injection strategy consists in cycles of high-rate/low-rate injection of specific duration, typically in the order of minutes, in order to weaken the rock resistance by inducing microcracks that anticipate large failures (Hofmann et al., 2019; Zang et al., 2019). While the cyclic injection has been successful to limit the magnitude of the induced seismicity, but without enough permeability enhancement, at the St1 Deep Heat Oy energy-company joint pilot project near Helsinki, Finland (Kwiatek et al., 2019), it was applied at the Pohang EGS, but did not mitigate the $M_w 5.5$ earthquake occurring two months after the cessation of the fifth circulation (Ellsworth et al., 2019). Furthermore, the protocol that defines the cessation of injection is key in the mitigation of post-injection induced seismicity. The use of shut-in and bleed-off of the injection well are standard protocols that intend to mitigate early and late post-injection induced seismicity. In the case of Basel EGS, the shut-in did not avoid the $M_l 3.4$ earthquake five hours after the injection stop (Figure 1.2; Häring et al., 2008). On the other end, the bleeding-off of the injection well at Vendenheim, did not avoid the $M_l 3.9$ earthquake two weeks after the injection stop (Lengliné et al., 2023; Schmittbuhl et al., 2022). It has been suggested that an abrupt shut-in would destabilize the faults in the reservoir more than a progressive decrease of injection rate, which mitigates the poroelastic effects (Alghannam & Juanes, 2020; McClure & Horne, 2011; Segall & Lu, 2015). Clearly, a better understanding of the underlying processes and the overall response to flow rate variations is required for the deployment of new projects and the development of mitigation tools. This passes through the development of improved forecasting models and injection protocols in order to consider future deployments of EGS projects, especially in high densely populated areas like Western Europe.

1.2. Objectives and methodology

The aim of this thesis is to better understand the processes triggering the induced seismicity in EGS and to propose a forecasting tool and operational strategies in order to mitigate the magnitude and frequency of both co- and post-injection induced seismicity.

The first objective of the thesis is to provide a literature review of the different potential triggering mechanisms of post-injection induced seismicity in EGS. These mechanisms are described in relationship with the numerous cases where post-injection induced seismicity was monitored with magnitude larger than the co-injection seismicity.

The second objective of the thesis is to develop a methodology that allows to distinguish the different triggering mechanisms, which is achieved by using a coupled hydro-mechanical model solving flow and geomechanical response. The model is calibrated on the case of the Basel EGS, which is adopted as case study. A simple elastic model is assumed and the effect of structural heterogeneity on the hydro-mechanical response is investigated by comparing results obtained for a homogeneous domain against those obtained for a fault-crossed domain.

This second objective emphasizes the importance of coupling models and introduces the third objective of the thesis: the identification of the triggering mechanisms that controlled the induced seismicity at the Basel EGS. A hydro-mechanical model with a domain including a discrete faulting network with plastic behaviour is developed, based on the interpretation and cluster characterization of the monitored seismicity in Basel as proposed by (Deichmann et al., 2014). The model reproduces the fluid injection taking into account the pressure-driven mechanisms, i.e., pore pressure diffusion and poroelasticity, the stress redistribution due to fault reactivation, the fault permeability enhancement and the slip weakening of the faults.

The fourth objective of the thesis is to develop a hybrid methodology that aims to forecast induced seismicity. The accurate discrete hydro-mechanical model of Basel EGS is the core of the forecasting methodology. In order to forecast seismicity in addition to fault reactivation, a seismicity rate model is implemented. Based on the rate-and-state friction law, the seismicity rate model is combined to the hydro-mechanical model to estimate the number of induced earthquakes (Dieterich, 1994; Segall & Lu, 2015). The forecasting methodology is used for the final specific objective of the thesis which is to propose and explore strategies to limit the magnitude of the potential induced seismicity. To this end, the impacts of different injection strategies on the co- and post-injection induced seismicity is compared. Likewise, different protocols for injection stop are investigated to mitigate the risk of post-injection seismicity.

1.3. Thesis layout

The thesis is presented in the shape of 5 chapters:

Chapter 2: In this chapter, the cases of EGS that hosted their LME in the post-injection stage are documented, along with the explanations of triggering mechanisms proposed in the literature and the methodologies used in the different studies. The chapter also provides an in-depth explanation of the coupled mechanisms responsible for triggering induced seismicity during and after the

injection stage in EGS. Recent efforts devoted to develop effective methodologies to mitigate induced seismicity, and the current research perspectives to forecast and mitigate induced seismicity are also presented. This chapter resulted in a paper by Boyet et al., which is currently under review in an international scientific journal.

Chapter 3: The third chapter introduces the importance of considering physics-based models to better understand and investigate the triggering mechanisms of fluid-injection induced seismicity. Coupled hydro-mechanical models, considering both a homogeneous and a fault-crossed domains (based on the case of Basel EGS, Switzerland), are used to propose a methodology that distinguishes the effects of pore pressure diffusion, poroelastic stressing and static stress transfer on the stability of the faults of the domains. The seismicity rate model is introduced and implemented to the two hydro-mechanical models. The importance of representing heterogeneities in physic-based hydro-mechanical models is demonstrated by the comparison of the seismicity observed in the two hydro-mechanical models. This study has been published in the scientific journal *Seismological Research Letter* by (Boyet et al, 2023a)

Chapter 4: Chapter 4 proposes an insight in the understanding of the mechanisms triggering the induced seismicity during the controversial case of the Basel EGS, Switzerland. The hydro-mechanical model developed in the previous chapter is improved by introducing a discrete faulting network, built on the basis of the monitored seismicity. The plastic responses of the faults due to different processes (pore pressure build-up, poroelastic stressing, stress transfer and slip weakening) are studied to distinguish the triggering mechanisms of each fault reactivation. After proper calibration, the coupled model is able to reproduce fault reactivations in agreement with the observed seismicity at Basel both in space and time, which allows to identify the triggering mechanisms of each fault reactivation and identify the post-injection triggering mechanisms. The chapter brings novelty in the explanation of the post-injection induced seismicity, suggesting that the triggering effects of the poroelastic stress relaxation leads to the reactivation of previously stabilized faults after the stop of injection. This chapter resulted in a paper by Boyet et al., 2023b, published in the scientific journal *Nature Communications Earth and Environment*.

Chapter 5: This chapter introduces the hybrid methodology to forecast fluid-injection induced seismicity. The discrete-faulted hydro-mechanical model of Basel EGS is combined with a seismicity rate model that forecasts mainshock earthquakes as a function of the Coulomb Failure stressing rate. The statistical Gutenberg-Richter law (Gutenberg & Richter, 1942) and the Epidemic Type Aftershocks Sequence (ETAS) model (Ogata, 1988) are implemented in the forecasting methodology in order to attribute aftershock sequences and magnitude to the forecasted seismicity. Progressive, constant and cyclic injection strategies are compared as a function of the forecasted seismic events nucleation (frequency and magnitude) during and after

the injection. This chapter resulted in a paper by Boyet et al., which is currently under review to be included in a Special Issue for the *Philosophical Transactions A* journal of the Royal Society.

Chapter 6: The last chapter of the thesis approaches the controversial discussion on the mitigation of the post-injection induced seismicity through ending the fluid injection by either a bleed-off or a simple shut-in of the injection. By using the same forecasting methodology as in Chapter 5, different protocols are compared to determine the best strategy of injection stop to mitigate the occurrence of post-injection induced seismicity in both short- and long-term stages. This chapter has resulted in a paper by Boyet et al., which is about to be submitted for review in an international scientific journal.

Chapter 7: Finally, the most relevant outcomes of the thesis are summarized.

In addition, Appendix D summarizes publications and presentations in congresses which are related with the thesis.

Chapter 2: Post-injection induced seismicity: a counterintuitive and restraining consequence of fluid injection in Enhanced Geothermal Systems

2.1. Introduction

Geothermal systems are considered a key solution to drive the energy transition towards net-zero carbon emissions because geothermal energy is a secure, clean and renewable source of energy as it can be produced without intermittency, pollution and carbon emissions (IPCC, 2023). Geothermal energy utilizes the inexhaustible heat from the planet interior. This energy is primarily harnessed in regions where the Earth's crust is relatively thin, facilitating the transfer of heat to the surface through rock and fluids. Such regions usually exceed the mean Earth geothermal gradient of 30°C/km. Depending on the thermal conditions and the reservoir depth, geothermal energy is envisioned for heating and/or for power-plant development. The latter requires high temperature (T > 150°C), which can be found in volcanic systems and in deep crystalline rock, and occasionally at depth in sedimentary rock. The main limitation of these rock types is usually their low permeability, especially in crystalline rock, implying low fluid-circulation capacity, a hurdle for effective heat production. To overcome this limitation, Enhanced Geothermal Systems (EGS) are developed by engineering the natural reservoir to enhance the permeability in order to facilitate fluid circulation and heat exchange between the injection and the production wells through an optimal generation of connected, high-permeability fracture/fault network (Tester et al., 2007). The goal of the EGS stimulation is to reach an efficient circulation aimed to generate ~20 MW_e for a period of 20 to 40 years. This engineered enhancement of permeability is achieved by means of forced injections, such as hydraulic or acid stimulations. The first EGS projects were initiated in the 1990s at Fenton Hill, United States, (Aki et al., 1982; Norbeck et al., 2018), at Hijiori, Japan, (Sasaki, 1998), and at Rosemanowes, United Kingdom, (Parker, 1999; Richards et al., 1994). Since then, the widespread deployment of EGS projects have increased around the world (Buijze et al., 2019; Evans et al., 2012; Majer et al., 2007; Zang et al., 2014).

Fluid injection, operated at high pressure (i.e., several megapascals) during hydraulic stimulation of the low-permeability rock or at lower pressure during circulation phases, causes not only permeability enhancement, but also mechanical stress changes, which may lead to the triggering of earthquakes along pre-existing faults in the upper crust (Ellsworth, 2013; Elsworth et al., 2016). Seismic activities have been documented in a number of geothermal projects worldwide (Ellsworth, 2013; Keranen & Weingarten, 2018). Based on the location of the seismicity towards the pressurized rock volume and on the amount of stress perturbation that leads to a seismic event,

as compared to the initial in-situ conditions, and the associated energy change, this human-induced seismicity is classified as '*triggered'* or '*induced'* (Dahm et al., 2015; Ellsworth et al., 2019; see also the discussion in Grigoli et al., 2017; McGarr et al., 2002). However, for simplicity in this paper, the term '*induced'* is used for all the earthquakes with anthropogenic origin, without distinction between '*triggered'* and '*induced'* seismicity.

Over the instrumental seismology period, induced seismicity was observed for the first time at Rangely, Colorado (United States), where several tests of water injection where performed between 1969 and 1974, showing a marked correlation of the injected flow rate with the recorded seismicity (Byrne et al., 2020; Raleigh et al., 1976). The first pioneering EGS projects induced maximum magnitude of $M_l 1.3$ (Fenton Hill), $M_l 0.6$ (Hijiori) and $M_l 2.0$ (Rosemanowes), which did not affect the public perception on the projects. Induced seismicity is a reasonably accepted consequence of hydraulic stimulations as long as its magnitude remains low, i.e., $M_w < 2$ (Bao & Eaton, 2016; Evans et al., 2012; Majer et al., 2007; Schultz et al., 2020). While the vast majority of these events consist of microearthquakes, too small to be felt on the ground surface, instances of earthquakes with magnitude M_w exceeding 3 have taken place, potentially causing perceptible ground shaking among the local population, damages, and the termination of a few projects (Ellsworth, 2013; Evans et al., 2012; Grigoli et al., 2017; Keranen & Weingarten, 2018). Examples of those cases are the 2017 $M_w 5.5$ Pohang earthquake in South Korea (Ellsworth et al., 2019), the 2006 $M_l 3.4$ Basel earthquake in Switzerland (Deichmann & Giardini, 2009), the 2021 $M_l 3.9$ Vendenheim in France (Lengliné et al., 2023; Schmittbuhl et al., 2022) or the 2003 $M_w 4.4$ Berlín earthquake in El Salvador (Bommer et al., 2006). What is striking is the frequent occurrence of the largest magnitude earthquake (LME) after the cessation of injection (Table 2.1, Kim et al., 2022), with delays from the shut-in varying between one hour, as in Paralana EGS in Australia (Albaric et al., 2014), to six months, as for the circulation at the Vendenheim EGS in France (Schmittbuhl et al., 2021). The late post-injection seismicity (later than 2 days after shut-in) is particularly counterintuitive and appears difficult to control, posing challenges to the viability and safety of EGS deployments.

To mitigate such undesirable LME, research in the last two decades has put a special effort in improving the understanding of the mechanisms that ultimately cause these induced earthquakes, and drive their migration in the fault networks. Traditionally, fluid pressure variation resulting from injection has been considered the main cause of induced seismicity. This traditional conceptualization cannot explain the occurrence of the LME after the stop of injection because pressure rapidly drops after shut-in and, thus, induced seismicity would also be expected to decay both in frequency and magnitude. In line of the traditional conceptualization of induced seismicity and considering that pressure changes are proportional to the injected fluid volume, relationships correlating the maximum seismic magnitude with the cumulative injected volume have been

suggested (McGarr, 1976, 2014). However, some observed cases significantly deviate from this scaling between earthquake magnitude and injected fluid volume, which implies that other triggering mechanisms are involved in the activation process of the induced seismicity (e.g., De Barros et al., 2019). In fact, induced seismicity is also controlled by other triggering mechanisms, such as thermal and chemical interactions between the rock and the fluids, poroelastic effects, as well as stress perturbation in association both with earthquake-earthquake interactions and aseismic slip migration (Vilarrasa et al., 2022). A specific challenge is to understand the processes causing post-injection induced seismicity in order to mitigate the seismic level and avoid the emergence of high-magnitude earthquakes after the stop of injection. Extensive work has been carried out in this respect, on the related processes and effects, but is still an open research topic given its complexity, through the direct or indirect coupling of multiple driving and increasing factors.

Here, we aim at providing a complete overview of all aspects of post-injection induced seismicity in EGS. The review is organized as follows. In Section 2.2, we present (1) the basic concepts of initiation of earthquakes and fault activation, (2) the main physical processes that trigger induced seismicity, and (3) the coupling between them. Next, in Section 2.3, we present EGS cases in which the LME has been observed after the stop of injection (Table 2.1). We differentiate between the early and the late (later than 2 days after shut-in) post-injection seismic activity in order to distinguish the processes triggering seismicity shortly after the stop of injection from the ones triggering the long-term seismicity. The lessons learned in each of these LME cases are discussed. We finally introduce the recent advances in terms of forecasting and mitigation of high-magnitude induced seismicity in Section 2.4. We lastly suggest some perspectives for future research to improve forecasting and mitigation of induced seismicity.

*Table 2.1: EGS cases for which the post-injection induced earthquakes have higher magnitude (M_w, M_l in certain cases annotated with *) than during the injection phase, sorted as a function of the delay between shut-in and the time of the maximum magnitude earthquake. Note that the largest magnitude earthquake is not always felt on surface ($M_w < 2$). SS: strike-slip; NF: normal faulting*

Year	EGS project	Injection type	Injected volume (m^3)	Depth (m)	Rheology	Regime	M during injection	M post-injection	Timing of LME after shut-in	Distance LME-well	References
Early post-injection induced seismicity											
2011	Paralana	multi-stimulation (acid)		3960	quartzite	SS	0.85	1.45	1 h	400m	(Albaric et al., 2014)
2009	Landau	circulation - 1.9 years	balanced	3000	granite/ sediments	SS/NF	1.9*	2.7*	2 h	1.5-2 km	(Evans et al., 2012; Groos et al., 2013)
2006	Basel	stimulation - 6 days	11 570	4630	granite	SS/NF	2.1	2.94	5 h	250m	(Deichmann et al., 2014; Häring et al., 2008)
2003	Habanero-1, Cooper Basin	restimulation - 9 days	20 000	4250	granite	SS	1.6	3.7	1 d	350m	(Asanuma et al., 2005; Baisch et al., 2015)
2004	GPK4 well, Soultz-sous-Forêts	stimulation - 3.5 + 4 days	21 800	4982	granite	SS/NF	2.0	2.3	1 d	300m	(Charléty et al., 2007; Dorbath et al., 2009)
2003	GPK3 well, Soultz-sous-Forêts	stimulation - 11 days	40 000	5091	granite	SS/NF	2.5	2.9	2 d	500m	(Charléty et al., 2007; Dorbath et al., 2009)
Late post-injection induced seismicity											
2000	GPK2 well, Soultz-sous-Forêts	stimulation - 7 days	23 000	4955	granite	SS/NF	2.5	2.6	7 d	500m	(Charléty et al., 2007; Dorbath et al., 2009)
1993	GPK1-GPK2 circulation, Soultz-sous-Forêts	circulation - 4 months	44 000	3600	granite	SS/NF	-	1.9	9 d	-	(Charléty et al., 2007; Dorbath et al., 2009)
2003	Berlin Field	production - 11 years (10 injection wells)	2 x 100 000	2240	volcanic rock	SS	1.7	4.4	14 d	2km	(Majer et al., 2007)
2017	Pohang	stimulation - 20 months	5663 + 7135	4340	granite	SS/NF	2.0	5.5	59 d	300m	(Ellsworth et al., 2019; Kim et al., 2018; Korean Government Commission, 2019)
2011	Cooper Basin Jolokia-1	stimulation -7 days	380	4160	granite	SS	1.0*	1.6*	127 d	-	(Asanuma et al., 2005; Baisch et al., 2015)
2021	Vendenheim	circulation – 3 months	85 126	~5000	granite	SS/NF	3.6*	3.9*	180 d	5 km	(Fiori et al., 2023; Lengliné et al., 2023; Schmittbuhl et al., 2022)

2.2. Physical processes of injection-induced seismicity in Enhanced Geothermal Systems

Mechanically, the occurrence of induced seismicity is intricately linked to both the shear strength and frictional stability of faults, which in-turn depends on the mineralogical composition of materials into the seismic slip zone (Collettini et al., 2009; Scuderi et al., 2017). Earthquakes occur when fault frictional resistance is overcome, releasing the elastic energy stored in the subsurface. In natural seismicity, the stress acting on faults progressively accumulates due to tectonic forces until it reaches a threshold associated with the fault resistance, leading to the triggering of an earthquake, with subsequent seismic slip propagation and arrest. Shear slip of the fault causes a shear stress drop along the slipped patch of the fault and stress redistribution around it, a process known as static stress transfer (King et al., 1994). In EGS, fault failure and consequent seismicity are triggered by subsurface stress changes caused by fluid injection and withdrawal. EGS also aims at dislocating fractures, to enhance their permeability. Although similar processes can occur on faults and fractures, they are different geological structures, because a fracture is a discontinuity without movement, and of smaller dimension. As a result, natural and induced seismicity is a complex process that depends on the initial stress before failure, fault strength, the stress drop and the temporal variability of loading on the plane (Kanamori & Brodsky, 2004). The size of the earthquake, i.e., the quantity of energy released with the seismic slip, depends on the amount and velocity of the slip, the size of the slipping area and the previously applied stresses on the fault plane (Brune & Thatcher, 2002). Seismic magnitude and frequency depend on multiple physical processes occurring at different scales, such as the fault frictional weakening or the fluid pressurization in the fault due to mechanical compression during frictional sliding, but also on tectonic structure geometries themselves (Kanamori & Brodsky, 2004; Rice & Cleary, 1976; Sibson, 1973).

To quantify the size of an earthquake, the Richter scale for local magnitude, M_l, (Richter, 1935) is widely used, but it can underestimate the magnitude of large earthquakes occurring at great depths. The current standard magnitude quantification is the moment magnitude, M_w (Hanks & Kanamori, 1979; Kanamori, 1977, 1978), which is not linked to the local magnitude, M_l, by a theoretical relation, although the ratio of M_w/M_l is estimated to vary between 2/3 to 4/3 (Mereu, 2020).

2.2.1. Fault activation causing induced seismicity in EGS

Seismicity is the result of fast slip (cm/s to m/s) due to stress changes on a geological fault, which is a pre-existing discontinuity that represents a zone of weakness in a volume of crustal rock (Scholz, 2002). In subsurface rock, faulting process is mainly found in the brittle regime. From the hydraulic viewpoint, a fault may behave as a barrier or a conduit for fluids, depending on the

infill material which determines its permeability (Caine et al., 1996). Fault failure often depends on whether the fault is behaving as a conduit or as a barrier for fluid flow (Cappa et al., 2022). In the former case, fluid migration can promote the fast pressurization of critical or weak fault portion, while in the latter case, stress variations can be large, making them more prone to induce seismicity (Wu, Fu, et al., 2021). Fault failure induces shear slip that is accompanied by dilation that permanently increases the aperture and permeability. Shear failure is a dominant mechanism in hydraulic stimulation of fractured rock (Pine & Batchelor, 1984) and concerns faults that reactivate when the friction resistance is overcome by the shear forces according to the Mohr-Coulomb failure criterion (Barton, 1976; Jaeger & Cook, 1979)

$$\tau = C + \mu(\sigma_n - \alpha P), \tag{2.1}$$

where τ is the shear stress acting on the fault plane and σ_n is the compressive stress normal to the fault orientation. C is the cohesion, μ is the coefficient of friction ($\mu = tan\,\varphi$, where φ is the angle of friction) and α represents the Biot-Willis coefficient. Fluid pressure, P, increase reduces the effective normal stress σ'_n ($\sigma'_n = \sigma_n - \alpha P$, in faults $\alpha = 1$), which directly affects the frictional resistance.

The occurrence of induced seismicity is generally related to the presence of critically stressed faults, with the initial stress tensor close to failure before injection. Critically-stressed faults may reactivate with minimal stress changes, while stable faults necessitate substantial stress alterations for reactivation. The Coulomb failure criterion of Equation (2.1) predicts the stress conditions for fault slip, but it does not address the question of frictional stability and whether slip will be seismic or aseismic. Once a fault is activated, the stability of frictional sliding depends on the local elastic stiffness of the rocks that surround the fault, the fault frictional properties and the rate of the reduction of shear strength (i.e., the frictional weakening) compared to the rate of elastic unloading on the fault (Garagash & Germanovich, 2012). In the theory of earthquake nucleation (Scholz, 1998, 2002), the frictional strength evolution can be described as function of slip velocity and slip history with the rate-and-state friction law (Dieterich, 1978; Marone, 1998; Ruina, 1983; Scholz, 1998). If the fault has rate-weakening properties and the reduction of shear strength is fast, an earthquake can occur once the slipping region reaches a critical size. Conversely, if the fault has rate-strengthening properties, slip is stable and aseismic. The factor that affects the rate-and-state friction parameters and consequently the fault rheological stiffness and frictional stability include the mineralogical compositions of gouges, contact area, fluid pressure and temperature (Scuderi & Collettini, 2016). According to the earthquake nucleation theory, an increase in fluid pressure will increase the critical size for unstable slip, thus promoting aseismic slip. Recent experimental studies of fluid injections on fault gouges in the laboratory have shown that the increase in fluid pressure can promote a transition of the parameters from velocity-

strengthening to velocity-neutral/weakening, or conversely, from velocity-weakening to velocity-strengthening depending on the nature of fault gouge materials (Cappa et al., 2019; Scuderi & Collettini, 2016). These observations demonstrate that frictional instability is a complex mechanism, and a large spectrum of fault slip behaviour can occur during fluid pressurization.

In addition, another mechanism of rock failure due to fluid injection is tensile failure, which occurs when the increase of pore fluid pressure reaches the sum of the least principal stress, σ_3, and the rock tensile strength, T_o, ($P = \sigma_3 + T_o$). Tensile failure occurs along planes normal to the least principal stress σ_3. Tensile opening is a consequence of hydraulic fracturing operations responsible of the creation of fresh fractures, generally without inducing seismicity (Clark, 1949; Scholz, 2002).

2.2.2. Stress changes driving fault activation

The fault orientation and the in-situ stress field are key parameters controlling the stress conditions acting on faults that ultimately drive fault activation. The stress tensor can be defined by the orientation and magnitude of the three principal stresses acting in the subsurface. The principal stresses ($\sigma_1 > \sigma_2 > \sigma_3$) are orthogonal to each other and are commonly assumed to be aligned with the vertical stress, σ_v, (lithostatic stress) and two horizontal directions, σ_H and σ_h. According to the Anderson's classification, faulting regime can be classified based on the in-situ stress regime: normal faulting in extensional regimes ($\sigma_v > \sigma_H > \sigma_h$), transform faulting in strike-slip regimes ($\sigma_H > \sigma_v > \sigma_h$) and reverse faulting in compressive regimes ($\sigma_H > \sigma_h > \sigma_v$) (Anderson, 1905; Heidbach et al., 2018). This classification allows to infer the required stress changes for a fault activation and its slip behaviour. The Mohr circle is a common method to represent the stress state at a point of a domain and the potential for fault activation, or reactivation, due to stress changes (Figure 2.1). The circle radius corresponds to the difference between the largest and the smallest principal effective stresses. The coordinates of each point of the circle correspond to the effective normal and shear stresses acting on differently oriented planes. The failure envelope of the rock represents the limit between failing and stable states, and it depends on the cohesion and the friction coefficient of the rock (see Equation 2.1), which increases with the fault surface roughness. Larger values of failure stress would require larger shear stress acting on fault planes to reach failure conditions (Jaeger et al., 2009). Fault activation occurs when the effective normal stress varies naturally, but, as previously introduced, can be triggered or induced by effective stress variations due to anthropic activities involving fluid pressure perturbation at depth. For instance, fluid injection increases the pore pressure in a rock and consequently decreases the effective stresses, which is graphically represented on the Mohr circle by the shift of the Mohr circle to the left (blue circle in Figure 2.1a). Poroelasticity changes the total stress tensor resulting in an increase or decrease of the size of the Mohr circle, which combined with the pore pressure increase is represented by the green circles in Figure 2.1a (a

more comprehensive description is given in Section 2.4.a). Thermal effects tend to shift the circle to the left, due to the cooling of the rock, and they can also lead to variation of the circle size (Figure 2.1b and Section 2.4.b for additional explanations). Geochemical interactions affect the cohesive and friction properties of the rock (Figure 2.1c and Section 2.4.c), while static stress transfer from an adjacent fault reactivation can change the total stress tensor acting on the fault, such that the circle changes its size and moves (Figure 2.1d and Section 2.4.d). Depending on the direction of the circle movement and on the variation of its size, these different mechanisms can destabilize or stabilize the fault. If the circle reaches the failure envelope, the intersection points correspond to failing fault planes. From geometrical observations, it is easily derived that the most critical fault planes are those oriented with an angle of $(\pi/4 \pm \varphi/2)^{\circ}$ with the direction of the maximum principal stress σ_1.

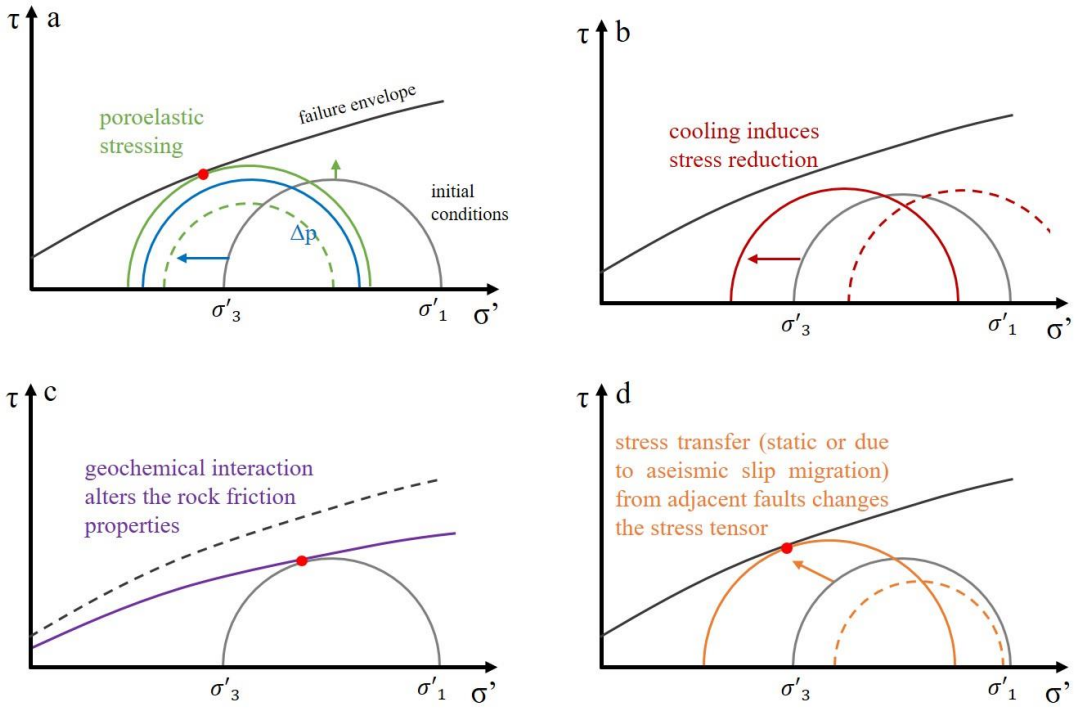

Figure 2.1: The Mohr circle represents the stress tensor, with every point corresponding to a different orientation. The grey circle illustrates the initial stress state. The red dot indicates the fault plane orientations that fail corresponding to the points where the Mohr circle touches the failure envelope. (a) Pressure-driven mechanisms modify the stress tensor: the blue circle corresponds to the shift of the grey circle in response to an increase of pore pressure Δp, while the green circle corresponds to the combination of pressure increase with variation of total stress due to poroelasticity. (b) Thermoelasticity induces the shift of the initial circle to the left or to the right, and it can also induce variation of the circle size. (c) Geochemical interactions alter fault strength, i.e., cohesion and friction, which can facilitate reaching failure conditions. d. Static stress transfer from adjacent faults lead to decrease or increase of the circle, which can stabilize or destabilize the faults.

2.2.3. Field and laboratory experiments

The behaviour of fault/fracture reactivation has been investigated and determined in rock laboratory and field experiments, such as fracture (Parisio, Tarokh, et al., 2019) and fault slip propagations (Cappa et al., 2022). Laboratory experiments highlighted that fault properties, and especially roughness, affect the seismic (or aseismic) potential of the fault slip (Ji et al., 2022). Aseismic slip has been recently studied and observed in experimental rock laboratory and in decametre-scale rock laboratories (Cappa et al., 2019; Guglielmi, et al., 2015a). Moreover, recent studies propose laboratory experiments to investigate the fracture behaviour, specifically under EGS conditions (thermal and pressure-wise), some analysed the response to different injection protocols and types of injected fluids (Frash et al., 2015; Hu et al., 2020; Hu & Ghassemi, 2020). Particularly, the interest in cyclic injection is currently increasing, and requires further studies to explore its efficiency in permeability enhancement while mitigating seismicity (Ji et al., 2022). The review by Ji et al. (2022) provides a complete and recent state-of-art on laboratory experiments of fault behaviour.

In the last decades, different field-scale laboratories have been developed to study in a wider scale the effects of fluid injection on fractured rock, e.g., the Äspö Hard Rock Laboratory in Sweden (see López-Comino et al., 2017), the Bedretto Underground Laboratory for Geosciences and Geoenergies (BULGG) in Switzerland (see Gischig et al. 2019), the Utah FORGE in the USA, the Grimsel Test Site (GTS) in Switzerland (see Amann et al., 2018; Gischig et al., 2020), the Low Noise Underground Laboratory in France (Cappa et al., 2019; Guglielmi, et al., 2015a), the Tournemire in France (De Barros et al., 2018; Guglielmi et al., 2015b), and the Mont Terri rock laboratory in Switzerland (Cappa et al., 2022; Guglielmi et al., 2020). Although Mont Terri currently partly works on CO_2 storage, it also investigates the thermo-hydro-mechanical behaviour of the rock matrix at a relatively large scale in space (meters) and time (4 to 10-20 years) during fluid injection, which is central in EGS applications. The Bedretto laboratory conditions are also very favourable to the investigation on induced seismicity. The great depth of the experiments and the dense instrumentation allow for experimenting fluid injection on a target fault. These experiments open up a large number of possibilities to better understand the processes involved in inducing seismicity and to fill scale-gaps between rock experiments and field-scale injections.

2.2.4. Triggering mechanisms of injection-induced seismicity in EGS

Multiple coupled processes are acknowledged to induce failure and potentially trigger seismicity in EGS (Ellsworth, 2013; Keranen & Weingarten, 2018). The increase in pressure, consequent to fluid injection, is one of the dominant triggering mechanism which induces deformations and poromechanical stress changes, with associated variations of rock and fault hydro-mechanical properties. Because the injection is non-isothermal, there is a temperature variation near the

injector, which propagates in the subsurface, mostly driven by fluid flow. Temperature changes affect fluid properties (density and viscosity) and may also accelerate geochemical reactions. Moreover, thermal contraction and thermoelastic stress may arise. These processes, in turn, affect the fluid flow and thus the pressure field, creating a thermo-hydro-mechanical coupling. Fault reactivation and fracture propagation create an increased level of coupling because the consequent permeability variation impacts the pressure distribution (Ellsworth, 2013; Ge & Saar, 2022; Keranen & Weingarten, 2018; Zareidarmiyan et al., 2020). Recently, field experiments and large-scale observations have also shown that injection-induced aseismic slip play an important role in the triggering of earthquakes (Cappa et al., 2019; Cornet, 2012; Guglielmi et al., 2015a; Vilarrasa et al., 2021; Wei et al., 2015). This subsection describes these mechanisms individually, and is concluded by an explanation of their coupling and combined effects both during and after injection in EGS.

2.2.4.a. Pressure-driven mechanisms and associated poroelastic stressing

Injection of fluid volumes causes an increase in pore pressure at the injection well. This pressure build-up is proportional to the injected fluid volume and inversely proportional to the hydraulic conductivity of the reservoir, i.e., the ratio between the rock permeability and the fluid flux. This pressure build-up propagates in the reservoir following a diffusive process. i.e., the pressure front $L(t)$ propagates in time as $L(t) = \sqrt{D_h t}$, where the hydraulic diffusivity D_h is directly proportional to the reservoir hydraulic conductivity and inversely proportional to its specific storage coefficient (Knudby & Carrera, 2006). Pore pressure increase causes the reduction of the effective normal stress and consequently of the shear resistance acting on a fault plane, which can reactivate the fault (Raleigh et al., 1976). The pressure front continues to propagate even after the stop of injection and can destabilize distant faults for a long period after the injection cessation (Bachmann et al., 2012; Hsieh & Bredehoeft, 1981; Segall & Lu, 2015). In fractured rocks, fluids diffuse through preferential flow paths, i.e., faults and fractures, and progressively increase their pore pressure. Critically-stressed faults have generally a higher permeability than other faults, because they slip periodically, which opens them up due to dilatancy effects, and thus they become preferential flow-path for the injected fluid (Barton et al., 1995; Ito & Zoback, 2000; Townend & Zoback, 2000). Consequently, fluid injection enhances the permeability of the most hydraulically-conductive faults (Ellsworth, 2013; Langenbruch et al., 2018; Zhang et al., 2013).

Apart from these direct effects of pressure on the effective stresses acting on fault planes, fluid injection also induces poroelastic strain and stress variation in the rock (Wang, 2000). Because the effective stresses change inside the pressurized rock volume, there is a differential deformation between the pressurized and the non-pressurized zones which may cause destabilization ahead of the pressurized area and can trigger seismicity on faults at larger distance from the injection well, sometimes greater than 10 km (De Simone & Carrera, 2017; Goebel et

al., 2017; Goebel & Brodsky, 2018; Segall & Fitzgerald, 1998). This effect is amplified by the presence of faults and fractures, which additionally cause stress changes along them, leading to anisotropic poroelastic stress variations (De Simone et al., 2017b; Segall, 1989; Zareidarmiyan et al., 2018). As a consequence, poroelasticity has the potential to improve or worsen the stability of faults depending on their orientation (Chang & Segall, 2016; De Simone et al., 2013; Segall & Lu, 2015). After the stop of injection, the pore pressure gradients rapidly attenuate and, thus, the forces that induce poroelastic stresses reduce, tending towards the homogenization of the stress tensor of the rock inside and outside the pressurized volume, diminishing the effects of poroelasticity (De Simone et al., 2017b). This poroelastic stress relaxation can be sufficient to reactivate faults that had been stabilized during injection (Boyet et al., 2023b).

2.2.4.b. Thermal effects

In EGS, the fluid is injected at ambient temperature (~20°C) into a rock at temperature between 120-180°C (at ~4-5-km depth). This thermal disparity spreads into the reservoir following heat transport processes. Given the low permeability of crystalline rock, heat transport is controlled by the coupling of thermal convection of the fluid through the fractures with the thermal conduction in the rock and the heat transfer between the fluid and the rock (Bödvarsson & Tsang, 1982; Gringarten et al., 1975). Cooling induces thermal rock contraction. Similar to the poroelastic process, the differential elastic strain in the cooled volume generates thermal stress reduction (Biot, 1956; Palciauskas & Domenico, 1982; Zimmerman, 2000). Thermoelasticity depends on the temperature drop, the rock stiffness and the tectonic structures in the subsurface. Although thermoelastic effects can be marked in stiff crystalline rock undergoing large temperature variation, they remain limited to the vicinity of the well during the duration of EGS hydraulic stimulation, affecting a much smaller area than the pressurized area (Ghassemi, 2012). Indeed, the thermal front propagates in the order of $\sim 10^{-3}\sqrt{t}$ meters (t in second) for typical values and continuous injection, while pore pressure propagates in the order of $\sim 10^{-2}\sqrt{t}$ meters (De Simone et al., 2023). However, long-term fluid circulation affects wider volume and thermal effects can become a major triggering mechanisms of induced seismicity, even for distant faults (Kivi et al., 2022). At The Geysers geothermal plant (USA), where fluid circulation and heat production have been active for over 50 years, reservoir cooling and associated thermal-elastic shrinkage of the rock are believed to be the dominant mechanism of injection-induced seismicity through cooling-induced shear slip (Rutqvist & Oldenburg, 2008).

2.2.4.c. Geochemical interactions

Fluid injection also disturbs the initial chemical equilibrium between the rock matrix and the resident fluid, promoting chemical interactions (Niemeijer et al., 2012). If the fluid has a lower/higher mineral content than the rock, mineral dissolution/precipitation is likely to occur (Pandey et al., 2018). These chemical interactions depend on the type of minerals, the pressure

and the temperature of the fluids and the host rock (Lasaga et al., 1994). EGS reservoirs are commonly constituted of crystalline rock and cold-water injection favours dissolution of calcite in fluid paths. In certain cases, the dissolved species diffuse and precipitate, reducing the permeability farther away in the fracture (Elsworth & Yasuhara, 2010; Min et al., 2009; S. Ogata et al., 2018). Precipitation of amorphous silica is also common in granitic rock due to its faster precipitation compared to other minerals, such as quartz and feldspar (Andre & Rajaram, 2005; Jing et al., 2002; Pandey et al., 2015; Taron & Elsworth, 2009). These dissolution and precipitation may degrade rock stiffness and strength, as well as affecting fault asperities that weaken the fault friction capacity, emphasizing the potential of fault activation. Mineral dissolution increases porosity and permeability of both fractures and rock. Variations in porosity and permeability, in turn, cause changes in pressure and temperature, and consequently stress variations in the stimulated rock.

2.2.4.d. Static stress transfer

Fault activation, triggered by any kind of mechanisms, causes permanent variations in the local stresses around the slipped area, which may promote additional seismicity (King et al., 1994; Stein, 2005; Toda et al., 2011). This effect has been observed both in natural and induced earthquakes. Static stress transfer causes stress redistribution that modifies the critical-orientation of faults for failure by rotating the stress tensor (De Simone et al, 2017b). The critical orientation depends on the initial stress state and on the ratio of the shear stress variation to the initial in-situ shear stress. When an earthquake is triggered, stress is redistributed over the sliding fault plane and adjacent faults in the network. The shear stress drop that occurs along the slipped area is proportional to the seismic magnitude, which is a function of the amount of slip and the rock stiffness, and inversely proportional to the slipping surface of the reactivated fault (Okada, 1992). Generally, the stress drop ranges from 0.1 to 10 MPa (Charléty et al., 2007). To give an idea of the order of magnitude, the 1992 Landers natural earthquake (Mw 7.4, USA) had a stress drop of 3.5 MPa, with aftershocks with a stress drop of 0.03 MPa (King et al., 1994). At the Basel EGS project in Switzerland, the median value of the stress drop of the induced seismicity has been estimated in 2.3 MPa (Goertz-Allmann & Wiemer, 2013). Stress drops of induced and tectonic earthquakes show a comparable range of values (Huang et al., 2017).

Fault activation induces antisymmetric variations of the stresses both in perpendicular and parallel directions to the fault (Figure 2.2). Local stress redistribution promotes failure of adjacent faults, while inhibiting slip of certain faults as a function of their location and orientation (Catalli et al., 2013; Kettlety et al., 2019; Schoenball et al., 2012). Fault slip can induce earthquake initiation, initiating a dynamic earthquake-earthquake interaction promoting aftershock events on the same reactivated fault (Okada, 1992). These earthquake-earthquake interactions have been studied in the 2011 Prague and 2016 Pawnee sequences in cases of wastewater disposals in Oklahoma, USA

(Ge & Saar, 2022). Even small seismic events influence fault stability and can become itself a triggering mechanism of induced seismicity (Brown & Ge, 2018).

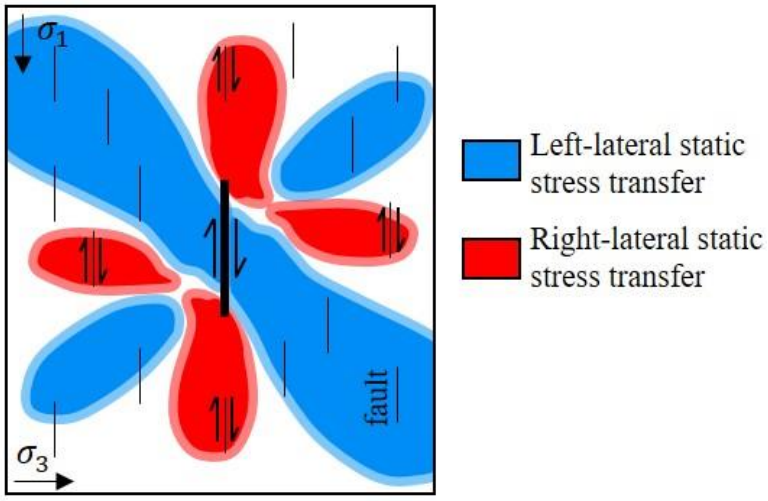

Figure 2.2: Asymmetric static stress transfer due to dextral fault reactivation. Left-lateral static stress transfer is shown in blue and right-lateral stress transfer in red. The magnitude of stress redistribution depends on the surface of the fault, the amount of slip, the initial stress state and on mechanical properties of the rock. Dextral faults affected by right-lateral static stress transfer could be reactivated.

2.2.4.e. Stress perturbation caused by aseismic slip

Recently, fluid injection-induced aseismic fault slip has been highlighted as an active triggering mechanism of induced seismicity (Bourouis & Bernard, 2007; Cappa et al., 2019; Cornet, 2012; Danré et al., 2022; Guglielmi et al., 2015a; Vilarrasa et al., 2021; Wei et al., 2015). During injection experiments, (Guglielmi et al., 2015a) and Cappa et al. (2019) have shown that fault aseismic slip and opening precede the fault slip acceleration that leads to seismicity. Thus, aseismic slip can migrate and potentially activates faults within and outside the pressurized area, redistributing stresses on asperities over the aseismically-slipping fault and on adjacent faults, promoting seismic activation (Figure 2.3) (Bhattacharya & Viesca, 2019; Cappa et al., 2019; De Barros et al., 2021; Vilarrasa et al., 2021). Generally, rough faults fail aseismically (Tal et al., 2020). The stress transfer caused by aseismic slip onto nearby faults is mechanically similar to the Coulomb static stress transfer discussed in Section 2.4.d. Moreover, the amount of aseismic slip depends mostly on the total injected volume (Yang & Dunham, 2021) and the criticality of initial fault stress to failure (Bhattacharya & Viesca, 2019; Wynants-Morel et al., 2020). It has been shown that aseismic slip over critically-stressed faults can trigger post-injection seismicity far away from the injection well (Cornet, 2016; De Barros et al., 2021; Sáez & Lecampion, 2023; Segall & Lu, 2015), for a duration proportional to the duration of injection with a self-propagation along the activating fault without any further fluid pressure increase (Jacquey & Viesca, 2023; Sáez et al., 2022).

A number of studies have pointed out that aseismic fault slip can precede seismic slip on a fault (Cappa et al., 2019; Cornet et al., 1997; De Barros et al., 2018; Guglielmi et al., 2015a). A fault

with initially rate-strengthening properties (see Section 2.2.1) could change to the velocity-weakening regime, capable of a seismic activation (Aretusini et al., 2021; Dal Zilio et al., 2022; De Barros et al., 2023). The observations of this process are quite novel and encourage new investigations to consider the possibility of mixed modes of friction slip in laboratory experiments and numerical model from fault failing first aseismically and then seismically. In addition, both aseismic and seismic slips degrade the frictional properties of the fault by deteriorating the fault asperities and reducing frictional resistance, promoting additional fault slip (Eyre et al., 2019; Wibberley & Shimamoto, 2005).

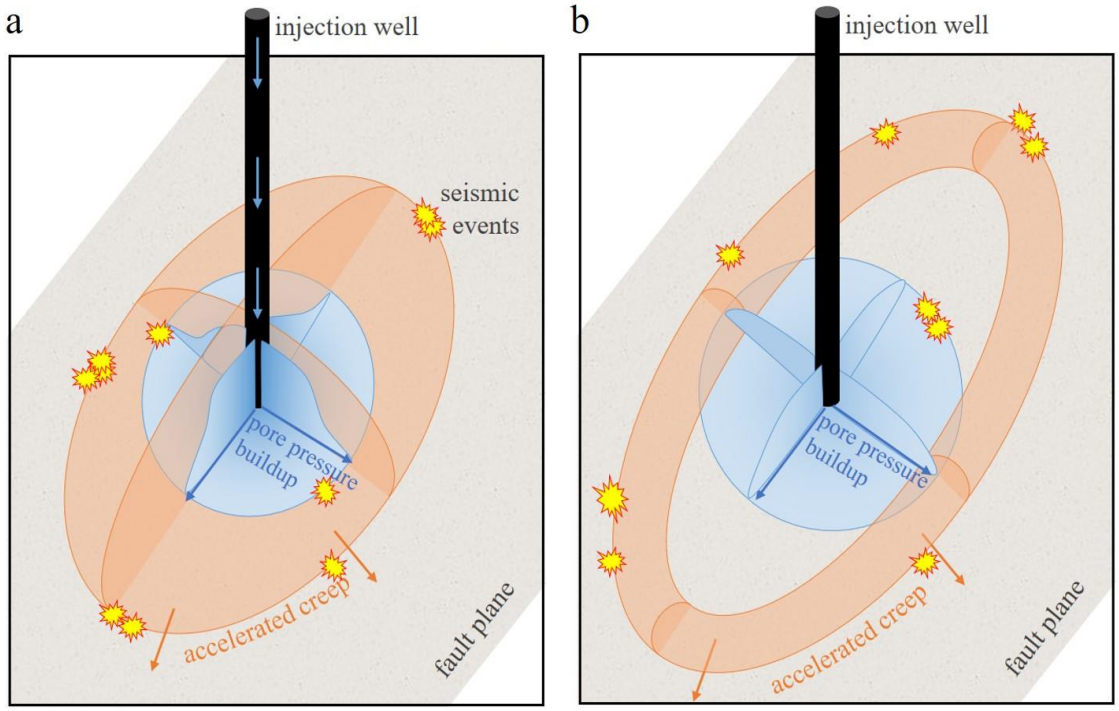

Figure 2.3: Fluid injection induces an aseismic creep propagation ahead of the pressurized front. (a) The stress perturbation due to creep can induce seismic activation on faults far from the injection well during the injection. (b) At the stop of injection, the aseismic creep is self-propagating without any further fluid pressure increase.

2.2.4.f. Coupled processes operating concurrently or consecutively both during co- and post-injection induced seismicity in EGS

Hydraulic stimulation aims to enhance the permeability of existing faults and fractures by increasing their aperture due to dilation during shear slip. To this end, a large volume of fluid is injected at high pressure, which modifies the stress conditions in the subsurface and initiates different physical mechanisms that are strictly interconnected (Ge & Saar, 2022; Majer et al., 2007).

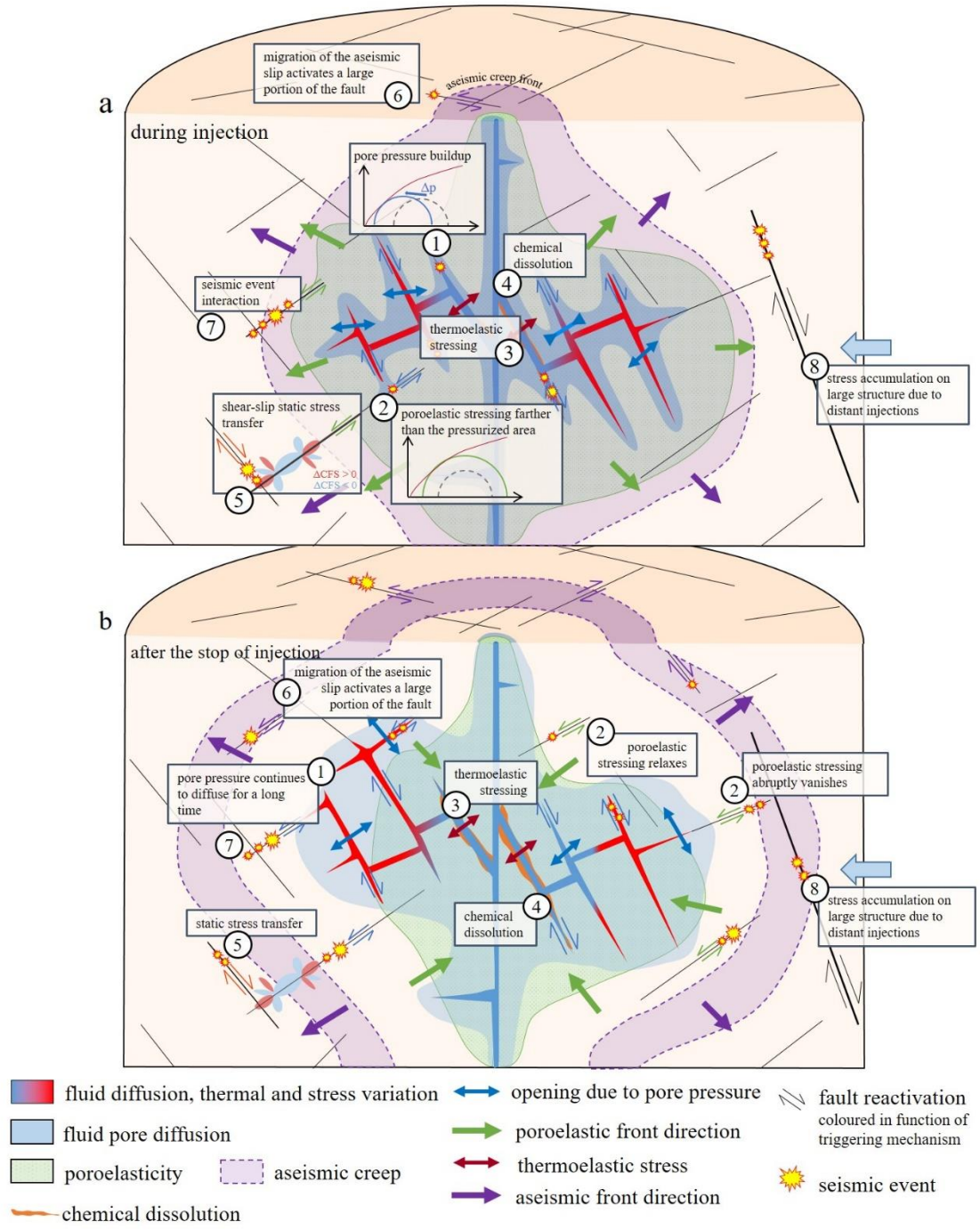

Figure 2.4: Conceptual illustration explaining (a) co-injection and (b) post-injection triggering mechanisms of fluid-injection induced seismicity. Fluid is injected along a well and circulated through fractures. (1) The increase of pore pressure opens fractures and enhances their permeability and consequently the circulation. (2). The deformation due to the pore pressure build-up in the vicinity of the well affects a wider area and produces poroelastic stress that can induce slip along distant faults. (3) Thermoelastic stressing affects the stability of fault from the start of injection. (4) Chemical interactions affect the frictional properties of faults. (5) The seismic, or aseismic, fault slips redistribute the stresses around the faults and can nucleate more seismicity and fault slips. (6) Aseismic creep diffuses from the injection well to the outside of the reservoir, even after the stop of injection. (7) Earthquake rupture induces others earthquakes on the same fault. (8) Stress accumulation on large faults due to distant and/or previous injections can induce high-magnitude seismic events.

During fluid injection (Figure 2.4a), the pore pressure build-up in the host rock decreases the effective stresses acting within the rock matrix and on the faults. The pore pressure build-up is the principal mechanism responsible for the tensile opening and shear activation of faults in the vicinity of the injection well (Process 1, Figure 2.4a). The differential elastic deformation between differently-pressurized rock volumes in the reservoir leads to variation of the total stress field, a phenomenon known as poroelasticity. As a consequence, fractures and faults located at the interfaces between non-pressurized and pressurized rock volumes may become destabilized. This poroelastic phenomenon may also have a marked effect in zones of the reservoir that are far from those affected by pore pressure build-up, because total stresses instantaneously propagate in the rock, especially in low-permeability rock due to their initial undrained response (Process 2, Figure 2.4a). Thermal disparities between the injected fluid and the rock also induce variations of elastic stress, pressure (due to variation of fluid density and viscosity) and volume deformation of the system. Thermal deformation affects the stability of the domain similarly to the poroelastic stressing (Process 3, Figure 2.4a). Geochemical interactions between the rock and the fluid also modify the equilibrium of the domain and affect rock properties, such as porosity, permeability and stiffness. (Process 4, Figure 2.4a). In particular, geochemical reactions, i.e., dissolution and/or precipitation, may degrade the mechanical strength, which may bring a fault to failure conditions even if the stress state remains constant. Thermal and geochemical processes are strictly coupled with the fluid flow process and they are also dependent on each other. In fact, transport of heat and chemicals is mostly driven by fluid advection in the system of connected fractures, and thermal- and chemical-induced porosity variation in turn affects the fluid flow and thus the pore pressure variation. Additionally, temperature variation can accelerate or delay geochemical reactions. Additionally, static stress transfer due to fault activation (Process 5, Figure 2.4a) causes a stress redistribution that may also trigger seismicity within and outside of the pressurized zone during injection. Aseismic creep propagates from the injection well into the host rock and can reactivate faults far away from the pressurized volume (Process 6, Figure 2.4a). Slip activation causes compressive deformation that also reflects into increase of pressure, potentially destabilizing nearby faults. This is in fact known as one of the mechanisms leading to triggering of aftershocks (Process 7, Figure 2.4a). In the case of long-term injections, the accumulation of pore pressure build-up and stresses acting on a pre-existing large structure can eventually trigger the activation of such structure, resulting in high-magnitude earthquakes (Process 8 in Figure 2.4).

After the cessation of injection, seismicity is still observed for days to months in many EGS sites (Figure 2.4b). Pore pressure build-up continues to diffuse into the reservoir for long time after the stop of injection (Process 1, Figure 2.4b). The post-injection normal closure of the fractures extends the pressurized front and amplifies the post-injection pressure diffusion (Ucar et al., 2017). Fluids in pressurized dead-end fractures backflow at the stop of injection and could

propagate the fractures, which may result in large magnitude induced seismicity (McClure, 2015). Poroelastic stress vanishes faster than pore pressure drop, which may lead to reactivation of faults that were stabilized during injection by poroelastic stress (Process 2, Figure 2.4b). Aseismic creep continues to propagate along the domain after the injection is stopped and may reactivate faults far from the injection well (Process 6, Figure 2.4b). Thermal and geochemical interaction, static stress transfer, slip propagation and earthquake interaction (Processes 3, 4, 5, 6 and 7, Figure 2.4b) are still acting after the stop of injection. Accumulation of pore pressure and stresses on major faulting structures can also induce seismicity for a long time after the stop of the injection (Process 8, Figure 2.4b). The pressure gradients, the injected volume, the pressurization rate, and the duration of injection play an important role in the destabilization of the subsurface reservoirs because of the induced stress and pressure accumulation. The delay of post-injection induced seismicity depends on the hydro-mechanical properties of the rock and faults and also on the diffusivity of the reservoir.

2.3. Identification of the potential mechanisms that triggered post-injection LME in EGS: summary of documented cases

EGS have been developed around the world for decades. However, the emergence of high-magnitude earthquake and post-injection seismicity are a hurdle for a positive perception on EGS projects by the authorities and population. In this section, we analyse the cases of post-injection LME in order to better understand the processes that control post-injection induced seismicity. We classify the studied cases into early and late post-injection induced seismicity, depending on whether the delay of occurrence of the LME is shorter or larger than 2 days (Table 2.1, Figure 2.5). We arbitrarily define the threshold of 2 days because the next delays observed beyond this threshold are larger than 7 days in the studied cases, which suggests that different triggering processes are involved. Additional information on these cases, and other cases of injection-induced seismicity can be found in Buijze et al. (2019), Foulger et al. (2018), Kivi et al. (2023), Majer et al. (2007) and De Simone et al. (2023).

For each case, we present the possible explanations of the post-injection induced seismicity that have been proposed by employing different methods. Among these methods, interpretation of the monitored seismicity is the first step to understand the evolution of the fault reactivations in the domain. Determination of focal mechanisms of monitored earthquakes allows to identify the potential orientation and dip of activated fault planes. Timing and location of the seismic activation are indicators of the evolution of the fluid diffusion path and the overpressurized front. Furthermore, the response of the subsurface to fluid injection can also be studied through mathematical modelling of coupled processes. Statistical models describe and forecast the seismicity using physical laws, e.g., the Gutenberg-Richter law, describing the frequency-magnitude distribution of earthquakes (Gutenberg & Richter, 1942), or the Omori's law

describing the decay activity rate of smaller events (aftershocks) occurring near the rupture zone after a large earthquake (mainshock) (Omori, 1895; Utsu, 1961). Numerical models are also widely used to study the response of rock and faults to fluid injection. Physics-based models, both empirical and deterministic, allow to reproduce the fault activation and/or the induced seismicity through the injection time. Coupled thermo-hydro-mechanical-chemical models are useful tools in the understanding of the seismicity that may potentially be induced by pressure-driven mechanisms, thermal interaction, geochemical reactions, and geomechanical responses of the medium due to fluid injection.

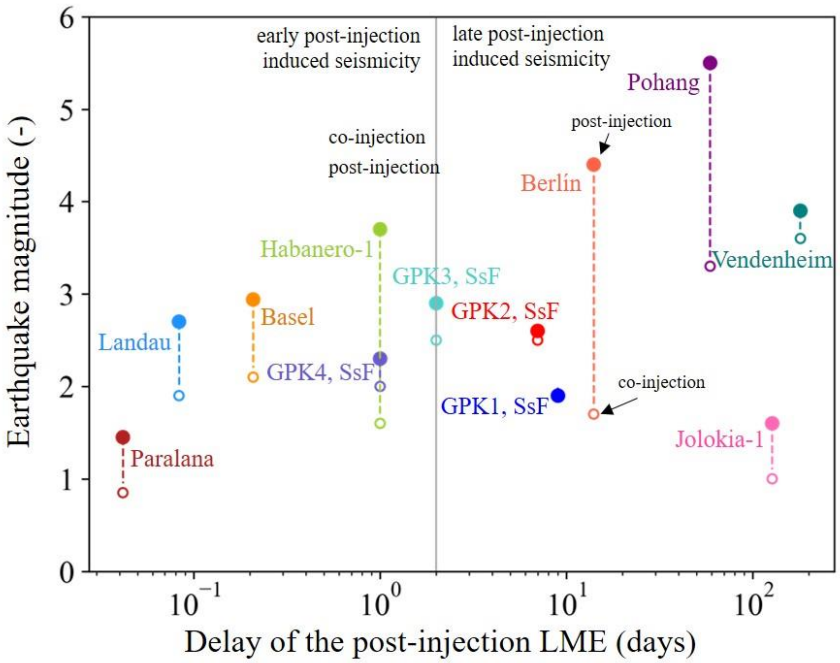

Figure 2.5: Temporal evolution of the largest magnitude earthquake (LME) monitored after the stop of injection (full circle), compared to the LME monitored during the fluid injection (empty circle). The grey vertical line separates cases with seismic delay shorter or longer than two days. SsF: Soultz-sous-Forêts.

2.3.1. EGS cases in which the largest magnitude earthquake occurs early in the post-injection stage

2.3.1.a. Paralana, Australia

The Paralana EGS, South Australia, was initiated to provide power to local mining developments, but currently provides electricity at the national scale. The ground exploration started in 2007, and the Paralana-2 well was drilled in 2009 (Albaric et al., 2014). The reservoir was subject to multiple stimulations. The first large-scale hydraulic acid-stimulation was done in July 2011 at the depth of 3960 m to enhance the permeability of the reservoir located between sedimentary and basement rocks, inducing microseismicity with maximum magnitude of 0.85. Less than one hour after the shut-in, a M_w1.45 earthquake occurred (Albaric et al., 2014).

Poroelasticity destabilized different areas in the reservoir during and after the stop of injection, as shown by means of a thermo-hydro-mechanical 3D model of the fluid injection at the EGS site (Riffault et al., 2016). The inversion of permeability from injectivity and monitored seismicity shows that the pressurized volume, estimated numerically as a result of injecting 3000 m^3 of water (Riffault et al., 2016), is smaller than the seismically active volume. This case shows that investigations should associate pore pressure diffusion and poroelastic stresses to explain the co- and post-injection seismicity at Paralana (Riffault et al., 2018).

2.3.1.b. Landau, Germany

Landau is located in the Upper Rhine Graben, in the western part of Germany, 4 kilometres away from the EGS project of Insheim (initiated in 2012). For both projects, their location in urban areas makes the induced seismicity a sensitive issue. The Landau EGS project is in activity since 2007 and the granitic reservoir was stimulated through a doublet of wells separated by 1.3 km at approximately 3000-m depth (Schindler et al., 2010). After a successful and seismically-quiet hydraulic stimulation and almost two years of production, the project was shut-in for maintenance in August 2009. One hour after the shut-in, a $M_l 2.7$ event occurred 1.5-2 km north of the site, estimated at 2300–3300-m depth (Evans et al., 2012). Seven more perceivable events were recorded after the LME. The location of the post-injection seismic events is not clear, as they could have nucleated either in the sediments, or the basement, or both (Groos et al., 2013). Due to the scarcity of information, the triggering mechanisms of post-injection LME have not been investigated in the published literature. The operations were resumed with a lower maximum injection pressure, reduced by 4.5 MPa, in November 2009.

2.3.1.c. Basel, Switzerland

Basel EGS is located in the southern part of the Upper Rhine Graben in Switzerland, at the borders with France and Germany. After only 6 days of hydraulic stimulation of the granitic basement (11570 m^3 of water injected at 4630-m depth) in December 2006, levels of observed seismicity higher than the traffic light system threshold ($M > 2$) led to the decision of stopping the injection (Häring et al., 2008). 5 hours later, the LME ($M_l 3.4$) occurred at the edge of the pressurized area (Deichmann et al., 2014; Herrmann et al., 2019; Kraft & Deichmann, 2014). The well was bled-off with the aim of mitigating the triggering of more high-magnitude events, but levels of seismicity higher than 1 were recorded for months, including three events with magnitude close to the LME. After investigations and consequent to the strong public concern, the project was cancelled, remaining as a marked example to highlight the importance of controlling the post-injection induced seismicity.

The Basel case attracted great interest of the scientific community and it has been analysed by means of different methods. Bachmann et al. (2012) employed a hybrid methodology comparing a simple model of pore pressure diffusion with the distribution of the monitored seismicity. The

study shows that, during injection, the pore pressure increases and induces seismicity in the vicinity of the well, while it decreases at the stop of injection. Far from the well, pore pressure increases slightly after the stop of injection, but not enough to trigger seismicity. The study suggests that static and dynamic stress changes may have triggered the post-injection and farther induced seismicity. Another proposed approach is the Focal Mechanism Tomography method (Terakawa 2014; Terakawa et al., 2012), which consists of an inverse method based on the monitored seismicity in order to estimate the pore pressure required to nucleate each seismic event. The method succeeds in explaining the co-injection and close-to-the-well earthquake initiation. However, post-injection LME located at 600 m from the injection well is estimated to nucleate with a required overpressure of 30 MPa, which is not possible because this overpressure coincides with the maximum injection pressure at the well (and overpressure drops away from the well). The analytical study of the stress redistribution from monitored earthquakes coupled with pore pressure diffusion by Catalli et al. (2013, 2016) highlighted the predominance of the effects of pore pressure on the initiation of co-injection induced seismicity, and more importantly, the predominance of static stress transfer on the triggering of the post-injection seismicity. Mukuhira et al. (2017) proposed that the post-injection LME was triggered by the shear slip of a large fault plane after the post-injection homogenization of the pressure gradient along a large fault. This conjecture is based on interpretations of the monitored seismicity, and the evaluation of the pressure required to trigger failure according to the Mohr-Coulomb criterion, compared to the actual pressure variation induced by the injection. Going beyond the pressure diffusion process, a thermo-hydro-mechanical model proposed by Andrés et al. (2019b) studied the effects of the injection on a discrete fault taking into account poroelastic and thermoelastic effects. However, this study is limited to the co-injection period while the post-injection seismicity triggering is not analysed. Nonetheless, De Simone et al. (2013) found that for the duration and injected volume of the stimulation at Basel, cooling did not propagate enough to induce significant contraction and thermal stress reduction that could destabilize faults. More recently, Boyet et al. (2023b) built a numerical hydro-mechanical model based on a faulting network geometry inferred from seismic observations to show that the combination of poroelastic stress relaxation at the moment of the shut-in and static stress transfer could explain the early post-injection LME at Basel (see Figure 2.6).

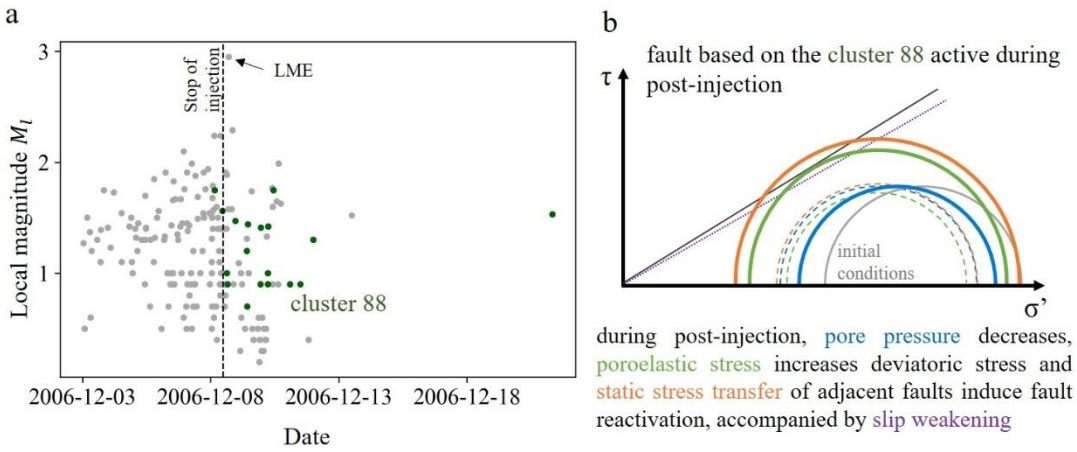

Figure 2.6: (a) Catalog of the clustered main events occurring during injection and after it stops at Basel, as reported by Deichmann et al. (2014). (b) Mohr circles for the fault build from the Cluster 88 in the hydro-mechanical model of a fault network (Boyet et al., 2023b). Dashed circle correspond to the co-injection stress tensor and solid circles for the post-injection stage. The blue circle corresponds to the effects of pore pressure build-up, the green to the poroelasticity and the orange to the static stress transfer. During injection, the fault is stabilized by poroelastic effects but the shut-in induces stress changes and the reactivation of the fault.

2.3.1.d. Habanero-1 well, Cooper Basin, Australia

The EGS project in the Cooper Basin, South Australia, was developed from 2000 to 2015. The project produced electricity for the mining industry of the Cooper Basin, and was thus subjected to little or no community concern for the risk of induced seismicity, accepting $M_w > 3$ earthquakes during injection. The main stimulation of the granitic basement (Big Lake Suite Granite) was initiated on November 30th 2003 on the Habanero-1 well, at 4254-m depth and 280°C. The stimulation lasted 9 days, injecting 20000 m^3 of water, with a maximum pumping rate of 48 l/s (Majer et al., 2007). One day after the stop of injection, the LME of M_w3.7 occurred. Most of the post-injection induced seismicity occurred on the outer-edge of the seismic cloud (Baisch et al., 2006).

Because no clear breakdown in the Habanero-1 wellhead pressure could be noticed at the occurrence of the largest seismic events, it was assumed that the post-injection seismicity was mainly induced by repeated slips on sub-horizontal fault asperities due to pressure-driven stress changes during injection (Asanuma et al., 2005; Baisch et al., 2006). It was also suggested that the seismicity was influenced by the different hydraulic stimulations from the multiple injection and production wells of the area (Baisch et al., 2006). A recent study (Wang & Dunham, 2022) used the case of the Cooper Basin history (stimulations and production of 6 wells from 2002 to 2013) to analyse the aseismic slip of a main fault (modelled with velocity-strengthening) and seismic slip on secondary faults (modelled with velocity-weakening). However, no particular finding is made in this study about the post-injection triggering mechanisms at the Habanero-1,

and for the stimulation of the Jolokia-1 well, also located in the Cooper Basin (Sections 2.3.1.d and 2.3.2.d).

2.3.1.e. GPK3 and GPK4 wells, Soultz-sous-Forêts, France

The EGS project of Soultz-Sous-Forêts led to the first successful circulation test between injection and production wells, and improved the knowledge on the mitigation of induced seismicity along nine consecutive circulation tests (Schill et al., 2017; Tischner et al., 2007). The project is located in the French part of the Upper Rhine Graben. The geothermal granitic reservoir lays between 3500 and 5000 m and was stimulated by multiple injections in multiple wells (Dorbath et al., 2009). The first injection test was made through the well GPK1, drilled down to 2002-m depth in 1987, reaching a temperature of 140°C (Majer et al., 2007), and was prolonged in 1992-1993 to reach the temperature of 160°C at the depth of 3590 m. Successively, additional deviated wells were drilled. The GPK2 well was drilled in 1995 at the depth of 3890 m and the first circulation test was done between GPK1 and GPK2 in 1997. The GPK2 well was then prolonged in 1999 at the depth of 5084 m to reach the temperature of 202 °C. In 2002-2003, the injection well GPK3 was drilled to the depth of 5000 m and, in 2004, the production well GPK4 to 5260 m.

The reservoir was subject to late (see Section 2.3.2.a for GPK1 and GPK2 stimulation and circulation) and to early post-injection seismicity. In 2003, the stimulation of the GPK3 well induced post-injection seismicity, with a magnitude $M_w 2.9$ occuring 2 days after its stop. During 11 days, 40000 m^3 of water were injected with an injection rate between 20 and 80 l/s. The injection design was then adapted with a stepped shut-in, after previous injection high-magnitude earthquakes (Gaucher et al., 2015). The following year, an earthquake of magnitude $M_w 2.3$ occurred 1 day after the shut-in of the stimulation of the GPK4 well. The stimulation was performed in two phases, 9300 m^3 of water injection in 3.5 days and then 12300 m^3 in 4 days.

The perceivable induced seismic events (more than 400 with a magnitude $M_w > 1$, 30 with $M_w > 2$) nucleating during the stimulation of the GPK3 well were assumed to occur along large structures, promoting or hindering fluid circulation (Charléty et al., 2007). The wells are hydraulically connected (Sanjuan et al., 2006), allowing a complex fluid circulation and complicating the identification of the triggering mechanisms of the induced seismicity. The early post-injection induced seismicity from the injections at GPK3 and GPK4 wells are not specifically detailed, but aseismic slip is recognized as a major triggering mechanism of induced seismicity in this EGS project (Bourouis & Bernard, 2007; Calò et al., 2011; Cornet et al., 1997; Lengliné et al., 2014) and could have an effect coupled to pressure-driven mechanisms on early post-injection induced seismicity. Moreover, a study based on the stimulation of the well GPK2 (Section 2.3.2.a) showed that the presence of unstable fractures induced seismicity shortly after the stop of injection (Langenbruch & Shapiro, 2010).

2.3.1.f. Comparison of cases with early post-injection LME

Early post-injection seismicity occurs both after short-duration stimulations and circulation (for the case of Landau). Post-injection seismicity is mostly localized in the surrounding of the pressurized volume. In cases of short-duration fluid injection and early seismicity occurrence, the effect of pore pressure build-up does not explain the triggering of the LME far from the injection well. Thus, poroelasticity was proposed as one of the main triggering mechanisms of the early seismicity in the EGS projects of Basel (Boyet et al., 2023b) and Paralana (Riffault et al., 2016, 2018). Slip of a large fault due to pressure and poroelastic stress changes was also suggested as a triggering mechanism for the cases of Habanero-1 stimulation (Baisch et al., 2006) and the Basel case (Mukuhira et al., 2017). Static stress transfer from seismic events and fault reactivation might have triggered co- and post-injection seismicity in the cases of Basel EGS and of Habanero-1 stimulation (Baisch et al., 2006; Catalli et al., 2013, 2016). Aseismic slip is also recognized as a triggering mechanism of co- and post-injection seismicity in the case of Soultz-sous-Forêts. Each study uses a different methodology and considers different coupled mechanisms, making the comparison between the cases difficult, especially because of the specific characteristics of each site in terms of geology and tectonic structures, and on their control on the induced seismicity. Yet, a common finding is that pore pressure changes are not the only triggering mechanism of post-injection seismicity and that other mechanisms contribute to induce the LME.

2.3.2. EGS cases at which the largest magnitude earthquake occurs lately in the post-injection stage

2.3.2.a. GPK1 and GPK2 wells, Soultz-sous-Forêts, France

The project of Soultz-sous-Forêts (see also Section 2.3.1.e.) is the first project that performed a successful forced circulation test, carried out in 1997 through the wells GPK1, drilled in 1987, and GPK2, drilled in 1995, during four months, in which 44000 m^3 of water were injected. A $M_w 1.9$ earthquake occurred 9 days after the shut-in of the circulation test (Dorbath et al., 2009; Majer et al., 2007). There is no published literature hypothesizing the mechanisms that triggered this post-injection earthquake.

The GPK2 was deepen in 2000 (4431–5084-m depth) and stimulated again through a progressive injection of 23000 m^3 of water in steps of 30, 40 and 50 l/s during 7 days, with the largest seismic event with magnitude $M_w 2.5$. 7 days after the shut-in, a $M_w 2.6$ earthquake occurred (Dorbath et al., 2009; Majer et al., 2007). The following studies are based on the stimulation of the GPK2 well. However, the correlation concerning the triggering mechanisms of the late post-injection injection seismicity can be made between the stimulations GPK1 and GPK2.

Induced seismicity has been recognized to occur along a large fault destabilized by fluid diffusion (Charléty et al., 2007; Dorbath et al., 2009). Identification of seismic multiplets corresponding to

the previously identified faults showed that induced seismicity is due to repeated rupture of faults, whose density is high in the EGS site (Bourouis & Bernard, 2007). Pore pressure is determined to have a minor role on the triggering of induced seismicity in the reservoir, but is effective for the propagation of aseismic creep along fault zones. The overpressure front diffused after the stop of injection along large critically-oriented faults that require small stress variations to be activated. Pressure diffusion and fault slips were confirmed as triggering mechanisms by a hydro-mechanical model reproducing the induced seismicity occurring on a subvertical fault zone crossing the injection well (Baisch et al., 2010). Calculations of the co-seismic stress changes resulting from monitored seismic events showed that static stress transfer could possibly explain post-injection induced earthquakes (Schoenball et al., 2012). The decay of induced seismicity followed the Omori law and was controlled by the strength of the fault (Langenbruch & Shapiro, 2010), meanwhile the presence of unstable fractures induced seismicity shortly after the stop of injection (see the cases of Section 2.3.1.e.). Late post-injection induced seismicity in Soultz-Sous-Forêts was assumed to be due to post-injection pore pressure diffusion along the pre-existing fractures, inducing static stress transfer that propagated preceding the overpressure front. Aseismic slip was identified to contribute to induced seismicity during the fluid injection at the EGS site, which could still propagate after the stop of injection (Bourouis & Bernard, 2007; Calò et al., 2011; Cornet et al., 1997; Lengliné et al., 2014).

2.3.2.b. TR8A well, Berlín, El Salvador

Berlín EGS is located on a flank of the Cerro Tecapa volcano, a very high-seismically active region for which the last eruption occurred in 1878. The project operated through 10 wells since 1992 (Majer et al., 2007). It was the first project coupled with built-in warning system for monitoring, quantifying and controlling the risks associated with induced seismicity (Bommer et al., 2006). In September 2003, 14 days after the shut-in of the second phase of the stimulation at the TR8A well at 2240-m depth (with maximum magnitude of $M_w 1.7$), a $M_w 4.4$ earthquake occurred 2 km away from the well.

The co-injection induced seismicity was spatio-temporally correlated to the stimulations and its seismic cloud was contained within 500 m from the injection well. Additional injections, performed southern to the well TR8A during the stimulation, have been suspected to be responsible of the distant LME (Bommer et al., 2006). However, interpretations of the source parameters of the seismicity did not find evidences that the post-injection induced seismicity was due to the multiple and simultaneous injections (Bommer et al., 2006; Kwiatek et al., 2014).The hypothesis that the injection might have disturbed the pore pressure distribution and initiated a fluid migration through the domain has been suggested (Kwiatek et al., 2014).

2.3.2.c. Pohang, South Korea

Fluid injection at the Pohang EGS was initiated in 2015 and it was the first attempt of performing a cyclic injection strategy (Hofmann et al., 2019). The project performed 5 hydraulic stimulations along 20 months carried out at wells PX1 and PX2 at 4340-m depth, within the basement. Two months after the stop of the 5th stimulation, an earthquake of magnitude $M_w 5.5$ occurred in November 2017, causing severe damages in the surrounding urban areas (Ellsworth et al., 2019; Grigoli et al., 2018; Kim et al., 2018). This induced earthquake, the highest magnitude recorded in the post-injection stage in an EGS, led to the cancellation of the project and posed critical questions about the safety of EGS projects.

The expected magnitude estimated by the magnitude-injected volume scaling relationships (Lee et al., 2019; McGarr, 2014) is significantly lower than the LME of magnitude $M_w 5.5$ that was registered at Pohang. To cause a $M_w 5.5$ earthquake, the required injection volume would be three orders of magnitude larger than what was injected. Sensitivity tests, done by Chang et al. (2020), comparing coupled and uncoupled hydro-mechanical models, highlighted the importance of poroelasticity and static stress transfer to better explain the post-injection seismicity of the EGS project of Pohang. By combining a hydro-mechanical model of pore pressure diffusion and a Coulomb Stress transfer model due to the large fault slip, Yeo et al. (2020) concluded that post-injection LME initiation is due to the stress redistribution of a large fault slip, associated with frictional slip weakening, while the co-injection seismicity is induced by pore pressure build-up. Hydro-mechanical simulations considering a simplified representation of the Pohang case including two faults, simulated with different fault permeability, showed that with a higher permeability of the fault, fluid would have propagated faster with major Coulomb failure changes; and post-injection events would have occurred earlier (Kim et al., 2022). The large delay of the post-injection LME was likely due to the low permeability of the major fault, in accordance to modelling studies, i.e., Yoo et al., 2021. The different studies also agree on the hypothesis that the long-duration injection caused accumulation of pore pressure and poroelastic stressing on a large, unmapped and low-permeable fault on which the late post-injection LME occurred.

2.3.2.d. Jolokia-1 well, Cooper basin, Australia

After years of production in the Cooper Basin, a new stimulation was made through the Jolokia-1 well in October 2010, 10 km away of the Habanero-1 well location (see Section 2.3.1.d.). A total volume of approximately 380 m^3 was injected at 4160-m depth during 7 days, with maximum magnitude of induced events of 1.0. Wells located in the Habanero reservoir area were simultaneously stimulated. Four months after the shut-in, a seismic event of magnitude $M_l 1.6$ occurred (Baisch et al., 2015). Fault mechanisms interpreted from the focal mechanisms of the induced seismicity differ from the in-situ thrust-faulting regime, suggesting the creation of new fractures in the reservoir due to large pressure changes (Baisch et al., 2015). Although the injected

volume was relatively small, it induced seismicity in the vicinity of the well, where the overpressure exceeded the least principal stress. However, this injected volume cannot explain the post-injection induced earthquake. It is suggested that the post-injection LME occurred due to the destabilization of the subsurface due to the many fluid injections in the region (Baisch et al., 2015).

2.3.2.e. Vendenheim, France

Located 30 km away from the EGS of Soultz-sous-Forêts, in the French part of the Upper Rhine Graben, the Vendenheim project was initiated in 2018 (Fiori et al., 2023; Lengliné et al., 2023; Schmittbuhl et al., 2022). Tests were carried out from February 2018 until November 2019, followed by fluid injection to develop the doublet between GT1 and GT2 wells. Circulation took place from October 2020 until the beginning of December 2020, during which 85126 m^3 of water were injected, causing the occurrence of an earthquake with local magnitude $M_l 3.6$, a value higher than the $M_l 2$ threshold established in the adopted Traffic Light System. Afterwards, a progressive bleed-off and shut-in was operated from mid-December to beginning of January, during which a $M_l 3.3$ earthquake was recorded 3 weeks after the stop of injection. In June 2021, 6 months after the stop of injection, the LME occurred with a magnitude of $M_l 3.9$. The late post-injection event is suggested to be triggered by poroelastic pressure changes and/or by aseismic slip of a large fault located at 5 km from the reservoir and hydraulically connected to it (Fiori et al., 2023).

2.3.2.f. Comparison of cases with late post-injection LME

Late post-injection induced seismicity occurs in cases of long-term stimulations, from either single or multiple wells in the region of the study cases. Seismic and aseismic slips redistribute the stresses along faults of the domain and are considered as triggering mechanisms for the cases of the stimulation of the GPK2 well at Soultz-Sous-Forêts (Baisch et al., 2010; Schoenball et al., 2012) and for the circulation in Vendenheim (Fiori et al., 2023). Yet, pore pressure diffusion and stress accumulations on large faults are the main triggering mechanism of induced seismicity in long-term stimulations. In, significant volumes of water are injected and consequently are expected to potentially induce high-magnitude seismic events (McGarr, 2014). The delay between shut-in and post-injection LMEs is related to diffusion, which is controlled by rock permeability and stiffness (Kim et al., 2022; Langenbruch & Shapiro, 2010). To sum up, late post-injection induced seismicity is due to long-term processes, such as diffusion of pore pressure, accumulation of stresses on major faults, and their strength weakening.

2.4. Recent advances in the mitigation of induced seismicity

2.4.1. Understanding of the post-injection induced seismicity

Recent studies focusing on the triggering mechanisms of induced seismicity in synthetic settings or in specific EGS cases had greatly improved the understanding of the emergence of post-

injection LME. The present review of the cases (Section 2.3), combining seismic interpretation and numerical analyses, showed that the delay of post-injection induced seismicity is dependent on the diffusion of the injected fluid, the migration of aseismic slip, and the fault hydro-mechanical properties. However, early post-injection induced seismicity generally seems to be due to mechanisms that have *immediate* effects, such as poroelasticity, slip of nearby faults and subsequent static stress transfer. Interestingly, the late post-injection induced seismicity seems to occur mostly in EGS projects located in regions where production lasted many years. Pore pressure diffusion, thermoelasticity and accumulation of stresses on large faults due to multiple injections both in the same well or in multiple wells may cause LME late after the cessation of injection. Challenging the traditional conceptualization in which induced seismicity is exclusively controlled by pore pressure changes, the triggering effects of poroelastic stressing were estimated with numerical simulations (De Simone et al., 2013; Segall & Lu, 2015), encouraging their consideration in recent modelling studies. Rock laboratory and field-scale experiments provide a unique opportunity to fill the knowledge gaps on induced seismicity in both space and time, as for example at Low Noise Underground Laboratory in France, the Mont Terri underground rock laboratory or the Bedretto Underground Laboratory for Geosciences and Geoenergies, both in Switzerland. Aseismic slip preceding the seismic slip during fault reactivation was recently observed and the modelling of the propagating aseismic creep showed its significant impact on the post-injection induced seismicity (Section 2.2.4.e.).

2.4.2. Real-time monitoring and mitigation of induced seismicity

Induced seismicity in EGS needs to be controlled both in frequency and magnitude. Monitoring systems are set to adjust injection parameters in response to the monitored seismicity. The Traffic Light System (TLS) is aimed to adapt the injection parameters (i.e., injection rate and pressure, injected volume) in response to the monitored seismic magnitude and frequency occurrence. The thresholds and instructions depend on the area of the projects, for instance as a function of local communities and specific infrastructures (Bentz et al., 2020; Gaucher et al., 2015). The TLS was first applied in 1992 in the EGS project of Berlín, El Salvador (see Section 2.3.2.b). Since then, this real-time monitoring system has been used in most of the EGS projects. Yet, this method is not robust concerning the control of post-injection induced seismicity. For instance, the hydraulic stimulation of the Basel EGS project, Switzerland, was operated in combination with a TLS, whose maximum acceptable magnitude was reached after only 6 days of injection. The adoption of the TLS instruction of shut-in failed to mitigate the occurrence of higher-magnitude earthquakes. Moreover, the LME occurring with a long-term delay after the stop of injection is beyond the potential of current TLS.

A more advanced technique has been recently adopted during the stimulation of the St1-EGS project near Helsinki, Finland, in 2019, namely a near-real-time monitoring of the induced

seismicity (Kwiatek et al., 2019). It consists in an automated system for the fast seismic interpretation but with low characterization of earthquake parameters; estimating for instance their location and magnitude and the evolution of the seismic and hydraulic energy. The stimulation was temporally stopped four times and did not reach the maximum magnitude threshold of $M_w 2.0$, and only few seismic events occurred until one week after the shut-in, the largest with a magnitude of $M_w 1.3$ (Kwiatek et al., 2019). The development of this type of TLS is promising for the future of EGS, especially for sites located in urban areas. Additionally, recent studies propose the development of new types of TLS, such as statistical, e.g., Adaptive Traffic Light Systems (ATLS) (Broccardo et al., 2017; Mignan et al., 2017; Ritz et al., 2023), or physics-based, e.g., Goertz-Allmann & Wiemer (2013), in which the parameters can be calibrated during the fluid injection, based on seismic monitoring and fast-computing models in order to improve the forecasting potential of the models. New technologies of monitoring seismicity are also developed to improve the seismic interpretation. This is the case of a new monitoring system that uses distributed fiber optic acoustic sensors above the reservoirs and in boreholes. Seismic detection and interpretation is also supported by novel artificial intelligence techniques, such as Machine Learning, with significant enrichment of the obtained catalogue (Beroza et al., 2021) . For instance, earthquake detection can be improved with the treatment of seismic signal by a template matching and repeating signal detection (Fasola & Brudzinski, 2023). Machine Learning can be also adopted to optimize the ATLS (He et al., 2020). Machine Learning training on tectonic and injection settings has been adopted to estimate the geological potential of induced seismicity in cases of hydraulic fracturing, and it could be adapted for EGS projects, although more refined data would be required for the local induced seismicity (Pawley et al., 2018; Wozniakowska & Eaton, 2020). The improvement of such techniques for real-time monitoring are a major challenge in the mitigation of induced seismicity.

2.4.3. Forecasting methodologies and mitigation of induced seismicity

Simple and more complex hybrid forecasting models, based on numerical models solving complete or partial coupled thermo-hydro-mechanical-chemical (THMC) problems, allows to simulate the response of the subsurface to fluid injection (e.g., Clasen Repolles et al., 2023; Luu et al., 2022). The model geometry and material properties, especially the structures of heterogeneities (i.e., faulting network or fault zones), are central to improve the model forecasting capacity (Boyet et al., 2023a). A thorough characterization of the project area should permit to determine the main properties of the site and of the reservoir rock, i.e., regional stresses, tectonic structures, rheology. Moreover, current challenges of forecasting models focus on the implementation of the processes of fracture propagation and of aseismic deformation, two major mechanisms resulting from fluid injection and potentially inducing seismicity. The coupling of the THMC processes further increases the computational complexity, which is also a challenge

for the forecasting of seismicity from the standpoint of computing efforts, which may, nonetheless, be overcome by current developments in high-performance computing (Folch et al., 2023).

2.4.4. Injection protocols to mitigate induced seismicity

Novel injection strategies have been also proposed in order to favour permeability enhancement while controlling the occurrence of induced seismicity above an undesired magnitude. For instance, a cyclic soft injection was applied at the EGS project of Pohang, South Korea, in 2017 (see Section 2.3.2.c.) in order to control the co-injection induced seismicity and keep it below the M_w2.0 threshold (Hofmann et al., 2019). This injection strategy consists in cycles of high-rate/low-rate injection of specific duration, typically in the order of minutes. It is based on the concept of fatigue hydraulic fracturing, in which pressure pulses weaken the rock resistance by inducing microcracks that anticipate large failures (Zang et al., 2019). The cyclic injection in the Pohang EGS project controlled the co-injection induced seismicity but did not avoid the occurrence of the high-magnitude earthquake two months after the shut-in of the latest stimulation. Moreover, innovative unconventional hydraulic stimulations, as for instance horizontal drilling or multi-stage fracturing in time and space, have been proposed to limit fault reactivation and to increase the volume of stimulated rock, improving the heat production (Jia et al., 2022). Their aim is to avoid the stress shadow effect, i.e., the stress redistribution due to previous injection stages that restrains the propagation of nearby fractures, preventing permeability enhancement in the affected fractures (Jia et al., 2022).

Furthermore, the protocol that defines how to stop the injection is important in the mitigation of post-injection induced seismicity. For example, an abrupt shut-in destabilizes faults more than a progressive decrease of injection pressure (Alghannam & Juanes, 2020; McClure & Horne, 2011). Injection strategies need to be adapted for each EGS project and need to be efficient in the control of the permeability enhancement. The development of injection strategies favouring tensile fracture (opening normal to the fault plane), and avoiding or limiting shear failure, and the development of injections that maintain the rock deformation aseismic, are currently studied by modelling, laboratory and field experiments.

2.5. Future perspectives

The major challenge of EGS development is the mitigation of both magnitude and frequency of the induced seismicity. The first suggestion is to adapt the injection protocols in response to the induced seismicity. Several types of injection protocols should be investigated to analyse their efficiency. It is specifically the case of the cyclic injection that is currently discussed regarding its efficiency to mitigate seismicity while simultaneously enhancing the permeability of the geothermal reservoir. The protocols for stopping injection, and the instructions given by TLS, are

also currently discussed, on whether shut-in or bleed-off is the safest way to control post-injection induced seismicity.

Furthermore, the review of the different cases of post-injection induced seismicity encourages the use of fully THMC numerical models to study the different mechanisms. Yet, many newly-developed forecasting models are still considering pore pressure build-up as the only triggering mechanism. This is partly due to the high computational cost of fully coupled THMC simulations, although the development of High-Performance Computing advances the development of robust THMC models that include fault reactivation and laboratory-derived friction laws. Their association with existing statistical forecasting tools is a perspective to better adapt the injection strategy to each EGS project. The combination of hybrid methods with a real-time monitoring is likely the way forward to control of induced seismicity in EGS projects.

At the same time, a new emerging application for preventing induced earthquakes is the possibility of using robust nonlinear control theory (Stefanou & Tzortzopoulos, 2022). The main idea is to design controllers, based on the mathematical theory of control, driving aseismically a fault system to a new equilibrium point of lower energy by tracking a slow reference signal. This new methodology opens new perspectives for the application of robust nonlinear control theory to complex geosystems. While additional advancements are needed before practical application in the field, it is anticipated that this methodology will serve as inspiration for the development of earthquake mitigation strategies, addressing both anthropogenic and natural seismicity.

Recent studies on observed and modelled fault behaviour have proposed new explanations on fault reactivation. The continuation of rock-laboratory and field-scale experiments is necessary to achieve a more comprehensive understanding of the processes involved in the reactivation of faults in deep and hot rocks. The recent observation of mixed slip-behaviour (velocity-weakening/strengthening) is currently investigated at the field-scale in the Bedretto Underground Laboratory for Geosciences and Geoenergies and in the Mont Terri research laboratory in Switzerland. Moreover, experiments over faults with heterogeneous hydro-mechanical properties, and unfavourably orientated faults, as much as including thermal components in the experiments, would enlarge the current understanding of the behaviour of different faults in highly-monitored environments subject to fluid injection.

Despite the difficulty to anticipate and control induced seismicity, a number of projects are still in production, as for the projects of Soultz-sous-Forêts (France), Landau and Insheim (Germany), and Berlín (El Salvador). Induced seismicity can hinder the widespread development of EGS, and managing the preparation phase of earthquakes both in time and magnitude is a cornerstone for its future deployment. In this sense, the future EGS project of Haute-Sorne, Switzerland, is currently under investigations and will be decisive for the public perception of EGS projects as an important low-carbon energetic resource to reach net-zero emissions.

Chapter 3: Physics-based modelling to understand and to propose forecasting methods of induced seismicity

3.1. Introduction

The production of long-term and secure green energy is a current challenge to reduce carbon emissions, and electricity production from geothermal resources hosted in deep hot rocks is a promising solution (IPCC, 2022). However, induced seismicity due to hydraulic stimulation to enhance the permeability of deep low-permeable crystalline rock can jeopardize the development of Enhanced Geothermal Systems (EGS). Despite significant advances in the understanding of the processes that induce seismicity during stimulation (Ellsworth, 2013; Ge & Saar, 2022; Keranen & Weingarten, 2018), post-injection seismicity is not well understood and raises worries about EGS viability (Baisch et al., 2019). Surprisingly, in many cases, the highest magnitude seismic events occur in the post-injection stage (Majer et al., 2007). For instance, a magnitude 5.5 earthquake was induced at Pohang EGS (South Korea) in November 2017, two months after the shut-in of the last hydraulic stimulation of a set of five stimulations distributed over 20 months (Ellsworth et al., 2019). It has been suggested that slip weakening of a fault placed between the two stimulated wells, combined with pore pressure build-up and earthquake interactions, led to the large magnitude event (Yeo et al., 2020). Another well-known case of induced seismicity in an EGS project is the Basel Deep Heat Mining Project (Switzerland), which was developed in 2006 in the Upper Rhine Graben. The project was shut down after six days of stimulation (11,570 m^3 of water was injected at 4,629-5,000-m depth) because the threshold of the traffic light system was reached by events with magnitude up to $M_w 2.3$ (Häring et al., 2008). Five hours after the stop of injection, the highest-magnitude event occurred ($M_w 2.95$), which led to the decision of bleeding off the well. Subsequently, more events with slightly lower magnitude were induced and the project was abandoned (Deichmann et al., 2014; Herrmann et al., 2019). These two cases of post-injection seismicity with higher magnitude than co-injection seismicity illustrate the challenging task of forecasting and managing post-injection induced seismicity.

Pore pressure is the most widely assumed triggering mechanism of induced seismicity. Pore pressure build-up decreases the effective normal stress on the surfaces of discontinuities, leading to their failure and consequent seismic or aseismic slip (Cornet et al., 1997; Raleigh et al., 1976; Wei et al., 2015). Unlike what is observed in reality, induced seismicity would be expected to decrease both in frequency and magnitude as pressure drops as a consequence of the stop of injection. In some occasions, post-injection seismicity can be explained by the fact that pore pressure diffusion continues after the stop of injection and could destabilize distant faults that had not been pressurized during injection (Bachmann et al., 2012; Segall & Lu, 2015), like at the Rocky Mountain Arsenal, Denver, Colorado, US (Hsieh & Bredehoeft, 1981). In cases in which

seismicity occurs farther away than the pressurization front, co- and post-injection seismicity may be induced by the stress changes induced by seismic and/or aseismic fronts, which may outpace the pressure diffusion front (Bhattacharya & Viesca, 2019; Guglielmi et al., 2015a; Sáez & Lecampion, 2023; Wynants-Morel et al., 2020; Yang & Dunham, 2021). Moreover, most faults that host large magnitude post-injection earthquakes are pressurized during injection, which should have brought them to fail. The delayed seismicity on these faults indicates that pressure diffusion alone cannot explain the high-magnitude post-injection seismicity, which is rather caused by more complex behaviours.

3.1.1. Pore pressure build-up alone is not enough to explain induced seismicity

Pore pressure is the most common triggering mechanism of induced seismicity but is often insufficient to explain the nucleation of earthquakes far from the injection well, or after the shut-in of the injection (Mukuhira et al., 2017; see also Section 3.3). It has been shown that other triggering mechanisms may induce seismicity. In particular, poroelastic stresses and static-stress transfer have been identified as relevant in certain cases of induced seismicity, such as Pohang EGS (Yeo et al., 2020), Soultz-sous-Forêts EGS (Schoenball et al., 2012) and Castor underground gas storage (Vilarrasa et al., 2021). On the one hand, poroelasticity affects the stability of a reservoir farther than the pressurized area, stabilizing or destabilizing pre-existing fractures depending on their orientation (De Simone et al., 2017b; Goebel et al., 2017; Goebel & Brodsky, 2018). Since poroelastic stressing is driven by the pressure gradients, it quickly vanishes with the stop of injection, when the pressure gradients relax. This abrupt removal of poroelastic stress associated with an abrupt stop of injection can be responsible of a sharp increase in the seismicity rate on those fractures that have been stabilized during the injection (Chang et al., 2018; Segall & Lu, 2015). On the other hand, static-stress transfer arises from the slip of a fault, whether seismic or aseismic. Shear slip causes a shear stress drop within the slipped surface and an antisymmetric variation of compressive stresses around the tips of the slipped surface, i.e., an increase and a decrease on opposite sides. This stress redistribution around the tips stabilizes or destabilizes nearby faults depending on their orientation and location. Slip may be inhibited in some areas and promoted in others, triggering new seismic events (Catalli et al., 2013; Kettlety et al., 2019; Schoenball et al., 2012).

3.1.2. Including geological structures in models

Accounting for subsurface heterogeneities is also important for accurately modelling and forecasting of induced seismicity (Birdsell et al., 2018; Candela et al., 2022; Dempsey & Suckale, 2017; Hager et al., 2021; McClure & Horne, 2014; Zareidarmiyan et al., 2018, 2021). Both at Pohang and at Basel EGS, the location and focal mechanisms of the seismic events indicate the presence of a planar fault structure, along which seismicity migrated during the stimulation (Deichmann et al., 2014; Häring et al., 2008; Mukuhira et al., 2013; Yeo et al., 2020).

The hydraulic conductivity and stiffness of such geological structures have a significant effect on the effective stress changes that may lead to induced seismicity (Wu, Vilarrasa, et al., 2021). Fault zones, in fact, act as preferential flow paths, which accelerate pressure diffusion and lead to pronounced stress anisotropy. This effect, combined with the contrast in mechanical properties, amplifies poroelastic effects (De Simone et al., 2013; De Simone et al., 2017b; Zareidarmiyan et al., 2021). Moreover, fault zones host a large number of fractures close to critical conditions, which increase the seismic risk (Ritz et al., 2022). Incorporating the presence of fault zone structures, in terms of hydraulic, poroelastic and seismogenic characteristics, improve predictive models of fluid-injection induced seismicity (Chang & Segall, 2016; Ritz et al., 2022).

The aim of this study is to propose a physically-sound, hydro-mechanical model to better understand the processes leading to seismicity induced by hydraulic stimulation, in order to improve the forecasting capability. Forecasting models can be used to anticipate seismic occurrence in the design of injection strategies for geothermal systems and other geo-energy applications (Smith et al., 2022), e.g., varying the injection rate to mitigate risks of induced seismicity (Alghannam & Juanes, 2020; V. S. Gischig & Wiemer, 2013; Passelègue et al., 2018; Ritz et al., 2022; Zhu et al., 2017). We consider pore pressure diffusion associated with poroelasticity and static-stress transfer as triggering mechanisms. We compare their triggering effects with the monitored seismic events at Basel EGS, making use of models based on the site characteristics. The first model assumes a domain with homogeneous rock, while the second model assumes a domain crossed by a fault zone with a lower stiffness and a higher permeability than the surrounding rock. For both models, we study the evolution of the destabilizing effects of pore pressure, poroelastic stressing and static-stress transfer, and the consequent evolution of the seismicity rate during and after injection. The pore pressure and poroelastic stress are quantified by numerically simulating the coupled hydro-mechanical processes activated by fluid injection. The stress variation consequent to earthquake activation is calculated according to the dislocation theory in elastic space. Finally, the seismicity rate is evaluated according to a model based on the rate and state friction law (Dieterich, 1994; Segall & Lu, 2015). The comparison between the outcomes from the two models emphasizes the importance of including faults and fractures in physics-based models to improve fluid-injection induced seismicity forecasting. Although we use the properties and monitored seismicity of the Basel EGS as a comparison tool, we do not aim at exactly reproducing the seismicity at Basel, which requires the adoption of a more complex system of faults (Boyet et al., 2023a).

3.2. Model settings

We adopt the measured and estimated properties of the Basel EGS site to build 2D models to numerically simulate hydraulic stimulation (Häring et al., 2008). The first model is based on the assumption that the domain is homogeneous and characterized by equivalent properties

representative of fractured granitic rock – porosity $\phi_d = 0.01$, Young's modulus $E_d = 45\ GPa$ and intrinsic permeability $k_d = 7.5 \times 10^{-18}\ m^2$. The second model consists of a domain comprising a rock matrix with the same properties of the homogeneous model, but crossed by a fault zone aligned with the fracture system, which can be inferred from the monitored seismicity (Mukuhira et al., 2013). The fault zone is 1200-meter long and 30-meter wide, with vertical dip and oriented at 20° from the maximum horizontal stress (Figure 3.1). Although, in reality, the basement may include a more complex fracture network, even this simple representation of the fault zone permits reproducing a preferential flow path that is more deformable than the surrounding rock. The fault zone is assumed to be characterized by – $\phi_f = 0.01$, $E_f = 4.5\ GPa$ and $k_f = 7.5 \times 10^{-14}\ m^2$. In both models, the maximum horizontal stress is orientated N114, which is aligned with the y-axis ($\sigma_{Hmax} = 160\ MPa$), the minimum horizontal stress is aligned with the x-axis ($\sigma_{hmin} = 84\ MPa$) and the vertical stress coincides with the out-of-plane direction ($\sigma_v = 115\ MPa$) (Figure 3.1). Plane strain conditions in the vertical direction are assumed. The initial temperature of the domain is 190 °C and the initial pore pressure of 45 MPa corresponds to the hydrostatic pressure at 4.6 km (Häring et al., 2008). The simulation is assumed as isothermal, thus thermoelastic effects such as rock contraction, cooling-induced fracture aperture increase and thermal stress changes are neglected (Gan & Lei, 2020; Ghassemi et al., 2008; Salimzadeh et al., 2018). These processes are known to have a major impact in long-term fluid circulation (Kivi et al., 2022; Majer & Peterson, 2007; Parisio, Vilarrasa, et al., 2019; Rutqvist et al., 2015), while in the case of short-term injection, like at Basel, they are limited to the vicinity of the injection well because heat transport is much slower than pressure diffusion (De Simone et al., 2017a; De Simone et al., 2017b; De Simone et al., 2013). We solve the fully-coupled hydro-mechanical problem using the finite element method simulator CODE_BRIGHT (Olivella et al., 1996), solving simultaneously the momentum balance and the mass balance of water for a fully saturated porous medium (detailed governing equations and mesh settings provided in Appendix A, Section A1). The model returns the pressure, deformation and stress variations.

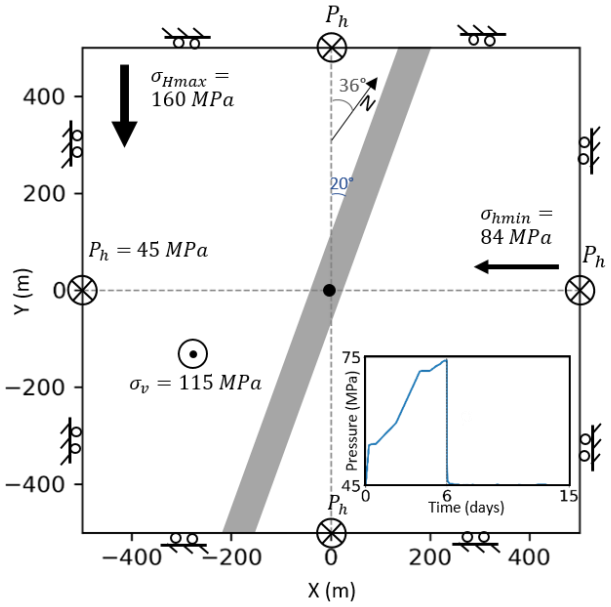

Figure 3.1: Schematic of the model setting. Injection pressure, plotted in the inset in the lower right part of the domain, is imposed at the centre of the domain (black dot). Initial stress conditions are aligned with the orthogonal axes. The fault zone is represented with the grey band. Fixed pressure and zero normal displacement conditions are applied to the boundaries.

We study the effects of pore pressure, poroelastic stressing and static-stress transfer at 185 locations corresponding to the main earthquakes observed at the Basel EGS during the injection, as reported by Deichmann et al. (2014) including their location, time of occurrence, magnitude and focal mechanism. Focal mechanisms are reliably derived from body-wave polarity and amplitude data thanks to the large number of monitoring stations and observations during the stimulation (Deichmann et al., 2014). We quantify the effects of the different triggering mechanisms by adopting the Mohr-Coulomb failure criterion (Jaeger et al., 2009) as an indicator of rock mechanical destabilization. We calculate the Coulomb Failure Stress (CFS) for each event, which takes positive values when failure conditions are reached, and it is given by

$$CFS = \tau - \sigma_n' \tan(\varphi) + \Delta CFS_{tr}\ , \qquad (3.1)$$

assuming the cohesion equal to 0. The effective normal and shear stresses, σ_n' and τ, respectively, acting on the orientation of the focal mechanism, at the time and location of the event occurrence, are estimated from the stress tensor calculated by the hydro-mechanical numerical simulations as detailed above. φ is the initial friction angle, typically equal to 30° for crystalline rock (Häring et al., 2008; Jaeger et al., 2009; Ohnaka, 1975). When the CFS exceeds 0, the fault reaches failure conditions and shear slip is activated, which we consider to correspond to earthquake nucleation as we disregard aseismic slip. Consequent to slip, the shear stress acting on the fault decreases. In our numerical model, we do not reproduce this stress drop for each fault slip, but we incorporate in our analysis the effects of the main static-stress transfer, ΔCFS_{tr}, i.e., the stress variation caused

by the activation of the main earthquakes of the clusters that have nucleated previously. Note that the stress changes associated to the main events are order of magnitude larger than those induced by the other events of smaller entity in the clusters, because the stress change scales with 10 to the power of the seismic moment M_w. We consider the seismic catalogue as reported by Deichmann et al. (2014) to build a simplified network of fractures on which seismic slip occurs (Figure SI A.1). For each cluster, we compute ΔCFS_{tr} by means of the Okada analytical solution (Okada, 1992), which is incorporated in the Coulomb3 tool (Toda et al., 2005). According to the dislocation theory (Steketee, 1958), Okada's solution quantifies the stress variation due to a uniform shear slip on a rectangular surface. The resulting ΔCFS_{tr} is inversely proportional to the dimension of the fault hosting the cluster and directly proportional to its slip d, which is calculated from the moment magnitude of the main event ($d = \frac{M_o}{G \times A}$ where G is the shear modulus, here equal to 21 MPa, and A is the surface area of the hosting fault, which we estimate based on the distribution in space of the cluster events, Figure SI A.1). We apply the calculated ΔCFS_{tr} at the time of occurrence of the main event in the cluster. Both the determination of the faults' location and slipping surfaces, and the attribution of the stress drop of the main event to the entire cluster increase the uncertainties of the estimation of ΔCFS_{tr}. To differentiate among the different triggering mechanisms of induced seismicity, we separately estimate the Coulomb Failure Stress changes (ΔCFS) associated with pore pressure variation,

$$\Delta CFS_{pp} = \Delta p \tan(\varphi), \tag{3.2}$$

and poroelasticity effects

$$\Delta CFS_{pe} = \Delta \tau - (\Delta \sigma_n - \Delta p) \tan(\varphi), \tag{3.3}$$

where Δp is the pressure change, whereas $\Delta \sigma_n$ and $\Delta \tau$ are the changes in normal and shear stress, respectively. Since the pressure variation is calculated by solving the coupled hydro-mechanical problem, it might be slightly affected by the poromechanical response of the domain.

3.3. Identification of the triggering mechanisms

To highlight the limitations of considering pore pressure as the only triggering mechanism of induced seismicity, we apply the critical pressure theory to both models. According to the critical pressure theory, faults would reach failure conditions at a certain pressure, depending on their friction, orientation and initial stress conditions (Shapiro, 2015). We derive the orientations of the reactivated faults considering the focal mechanisms of each event as fault plane solutions (Figure 3.2c and d). Once the fault orientation is established at each earthquake location, we determine the normal stress, $\sigma_{n_{init}}$, and the shear stress, τ_{init}, acting on the faults under the initial conditions, from the reported *in-situ* stress at Basel (Häring et al., 2008), and we calculate the critical pressure p_c for each monitored event at Basel EGS as

$$p_c = \sigma_{n_{init}} - \frac{\tau_{init}}{\tan(\varphi)}, \tag{3.4}$$

where φ is the initial friction angle, assumed equal to 30°. The comparison between the critical pressures and the pressure field consequent to fluid injection, which we numerically estimate, shows that this theory cannot explain most of the induced events (Figure 3.2a, b). Positive values (red) correspond to events for which pore pressure exceeds the critical pressure, i.e., pore pressure is the potential main triggering mechanism. Negative values (blue) in Figure 3.2 indicate that the critical pressure is not reached by the pressure variation, i.e., the critical pressure theory is not verified. Although incorporating a more-permeable fault zone into the model (Figure 3.2c and d) allows explaining a larger number of events, especially far from the injection well, most of the induced earthquakes are not explained by pore pressure diffusion. Pore pressure due to injection reaches the critical pressure solely for events located in the vicinity of the well and during the injection stage. Thus, most events in both the homogeneous and fault-crossed models do not obey the critical pressure theory, particularly the early-occurrence events located far from the well and the ones located away from the fault zone that cannot be triggered by pore pressure diffusion alone.

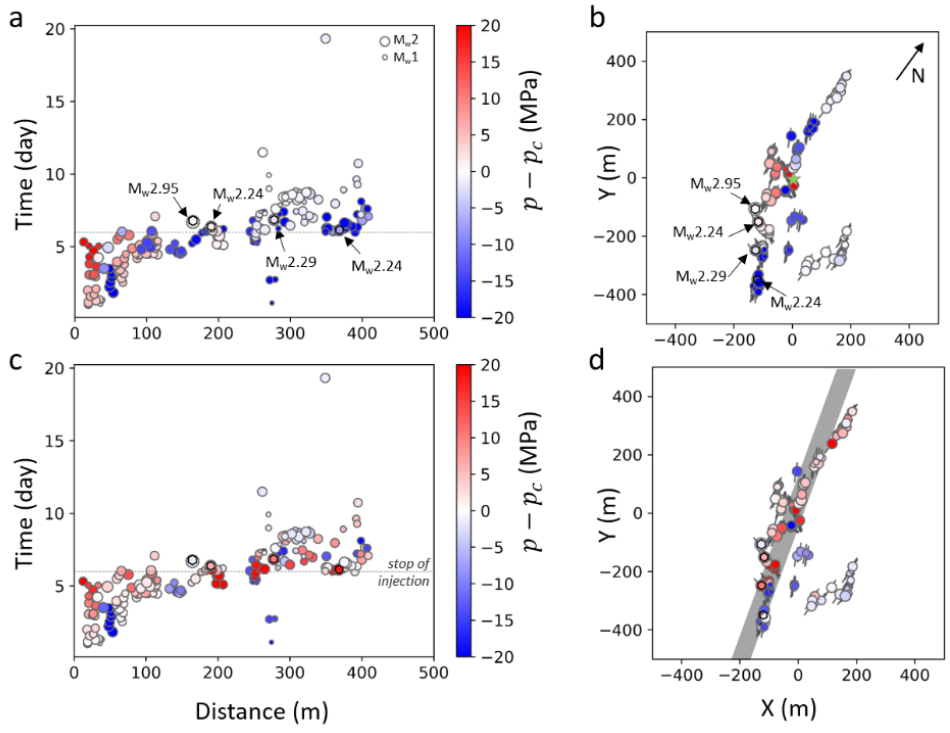

Figure 3.2: Difference between pore pressure due to fluid injection and critical pressure, $p - p_c$, at each Basel EGS seismic event location and time of occurrence in (a, b) the homogeneous domain [74 events out of 185 with positive values] and (c, d) the domain crossed by a fault zone (represented by the grey band in (d)) [111 events out of 185 with positive values]. In (a, c) results are plotted as a function of the distance from the injection well and time, while in (b, d) they are projected on a horizontal plane at the depth of the injection well. The magnitude of the largest events is indicated in (a) and (b). The orientation of the focal mechanisms is represented in (b) and (d).

We analyse the effects of the combination of pore pressure diffusion, poroelasticity and static-stress transfer using the Mohr-Coulomb failure criterion, calculated for each event. Positive values of Coulomb Failure Stress (CFS) indicate that at the time and location of occurrence, failure conditions are reached for the focal mechanism of the events (Figure 3.3). Coulomb Failure Stress changes (ΔCFS) illustrate the variation in fault stability of each mechanism. ΔCFS is used here to quantify the stabilizing or destabilizing effects, while CFS is an indicator of whether failure conditions are reached or not. ΔCFS_{pp}, induced by pore pressure, has high values for events located in the vicinity of the well and occurring during the injection for both the homogeneous and fault-crossed domain. Yet, in the fault-crossed domain (Figure 3.3b), pore pressure build-up destabilizes more and farther in the portion of the domain along the fault zone at the stop of injection, which confirms the results of Figure 3.2. Poroelastic stressing has stabilizing effects that counterbalance the destabilizing effects of pore pressure. Note, for example, that the number of events with $CFS > 0$ is smaller than the number of events with $CFS_{pp} > 0$ for the fault-crossed domain, which implies that the stabilizing effect of poroelastic stressing during injection prevents the occurrence of some events. However, poroelastic stressing tends to destabilize the areas outside the fault zone in the fault-crossed domain. Static-stress transfer ΔCFS_{tr} is higher for events located in the vicinity of the well than for the rest of the seismic cloud. Differences in ΔCFS_{tr} and in the focal mechanisms of the events are responsible of the uneven spatial distribution of the CFS in the homogeneous domain (Figure 3.3a). The combination of the pore pressure with the poroelasticity and the static-stress transfer permits explaining more and farther events occurring after the stop of injection (compare the number of locations with CFS>0 as reported in Figure 3.3a and b).

The fault-crossed model better explains the events at Basel EGS as shown by the difference of the CFS calculated for the two models (Figure 3.3c). In particular, for the post-injection events located far from the well, larger CFS values are observed in the fault-crossed domain. In fact, the larger hydraulic conductivity of the fault zone facilitates the faster propagation of overpressure, which amplifies the diffusive effects of pore pressure build-up after the stop of injection. Moreover, poroelastic stressing also has a larger impact in the fault-crossed domain than in the homogeneous one. As a result of the differential deformation of rock and fault zone due to the stiffness contrast and differential pressurization, the stress field variation is such that regions located slightly outside of the fault zone are destabilized ($\Delta CFS > 0$), although pore pressure build-up in these regions is insufficient to cause the nucleation of the monitored seismicity.

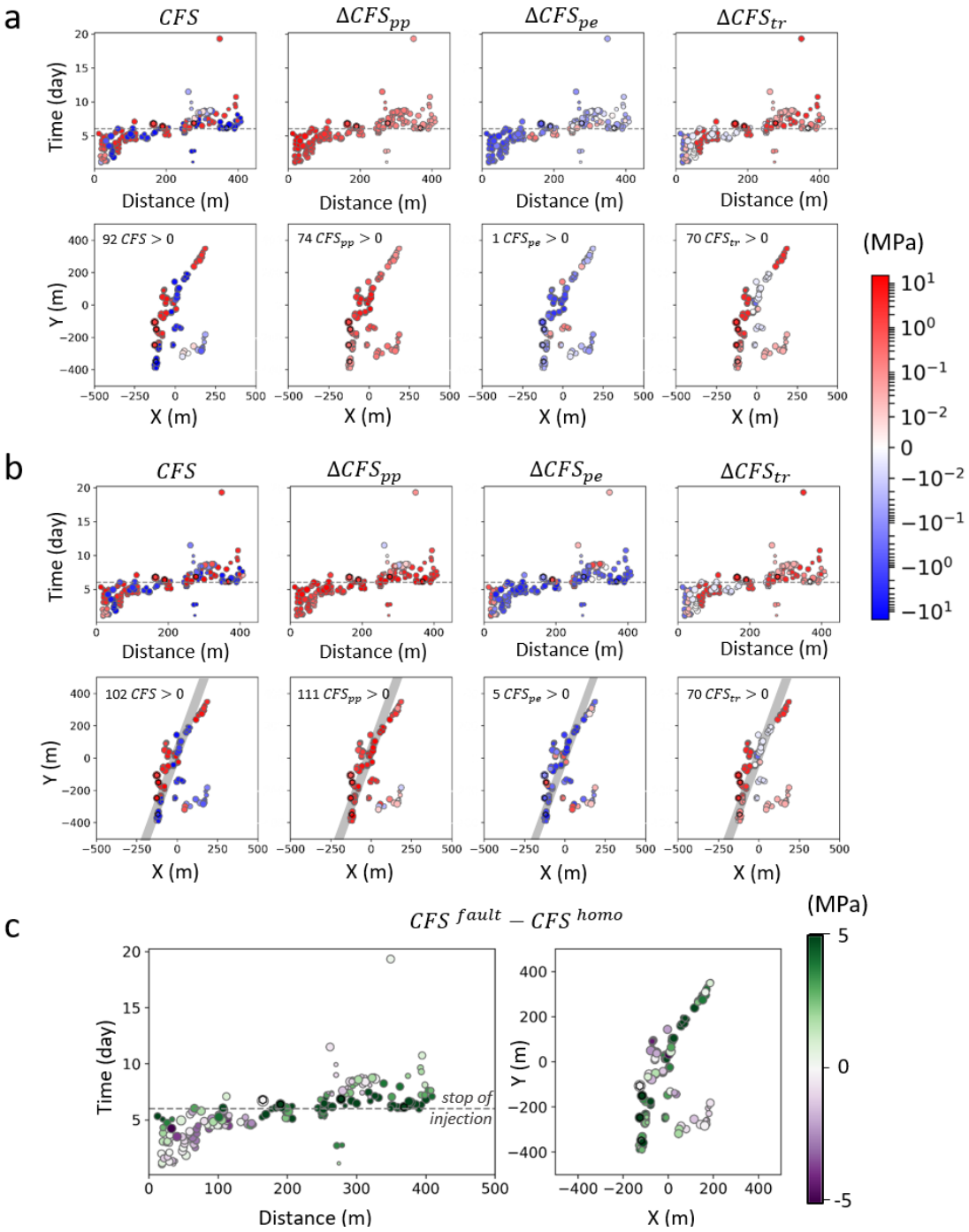

Figure 3.3: CFS and ΔCFS due to the effects, combined and individually, of pore pressure diffusion (ΔCFS_{pp}), poroelastic stressing (ΔCFS_{pe}) and static-stress transfer (ΔCFS_{tr}) at the time and location of occurrence of seismic events at Basel EGS in (a) homogeneous and (b) fault-crossed domains. Results are plotted as a function of distance from the injection well and time in the top row, while their spatial distribution is shown in the bottom row, where they are projected on a horizontal plane at the depth of the injection well. Positive values (red) indicate mechanical destabilization, while negative values (blue) indicate mechanical stabilization. The number of events for which we estimate a CFS>0 is reported for each mechanism. (c) The difference between the CFS estimated for the fault-crossed and homogeneous models highlights that the fault-crossed model is more capable to simulate the observed seismicity as it reproduces a larger destabilization than the homogeneous domain (green tones, positive values), which is also equivalent to the difference of DCFS of the two models.

3.4. Evolution of the destabilizing effects of pore pressure and poroelastic stressing

The combination of pore pressure diffusion, poroelastic stressing and static-stress transfer explains the activation of most of the monitored seismicity at Basel EGS (Figure 3.3). In this section, we analyse the evolution of the stability of both the homogeneous and fault-crossed models without referring specifically to the seismicity observed in Basel. We calculate the destabilizing effects of pore pressure and poroelastic stressing on the most critical orientation, which forms an angle of 30° with the direction of the maximum principal stress if a friction angle of 30° is assumed. Static-stress transfer is not considered in this general analysis because it refers to the specific magnitude and focal mechanism of seismic events.

The evolution of the CFS is calculated for the most critical orientation at the stop of injection and two days later, taking into consideration the combined effects of pore pressure diffusion and poroelastic stressing, indicated by CFS_{pp+pe} , and the effects induced separately by pore pressure diffusion and poroelastic stress, respectively indicated by ΔCFS_{pp} and ΔCFS_{pe} (Figure 3.4). Positive values of CFS_{pp+pe}, which indicate that failure conditions are met for the most critical orientation, are concentrated in the vicinity of the well in the homogeneous domain because the effects of the limited hydraulic conductivity prevail over the poroelastic effects (Figure 3.4a). Pore pressure continues to diffuse after the stop of injection, while poroelastic stressing vanishes, destabilizing a more spherical and smaller area than in the fault-crossed domain. The fault-crossed domain is also controlled by this process, but high ΔCFS_{pp} values spread along the fault zone (Figure 3.4b). ΔCFS_{pe} values are smaller than the ΔCFS_{pp} ones for both models. Poroelastic stressing destabilizes small zones, near the well and at the tips of the fault zone, and stabilizes the rest of the domain. These stabilizing poroelastic effects vanish fast at the stop of injection, while pore pressure continues to dissipate and leads to the failure of the areas located around the fault zone that were stabilized during injection by poroelastic stressing (Figure 3.4b).

The fault-crossed model exhibits a wider area with positive CFS_{pp+pe} during and after the stop of injection than the homogeneous domain (Figure 3.4c). High values (higher than 5 and 10 MPa) vanish at the stop of injection in the homogeneous model, while they persist for 2 days after the stop of injection in the fault-crossed model. The former reaches stability ($CFS_{pp+pe} < 0$) 8 days after the stop of injection, while the fault-crossed model remains unstable in a large area in and around the fault zone even 14 days after the stop of injection, as pore pressure destabilizes the domain. Pore pressure diffusion and poroelastic stressing have more impact on the stability of a fault-crossed model, for which post-injection instabilities are better explained.

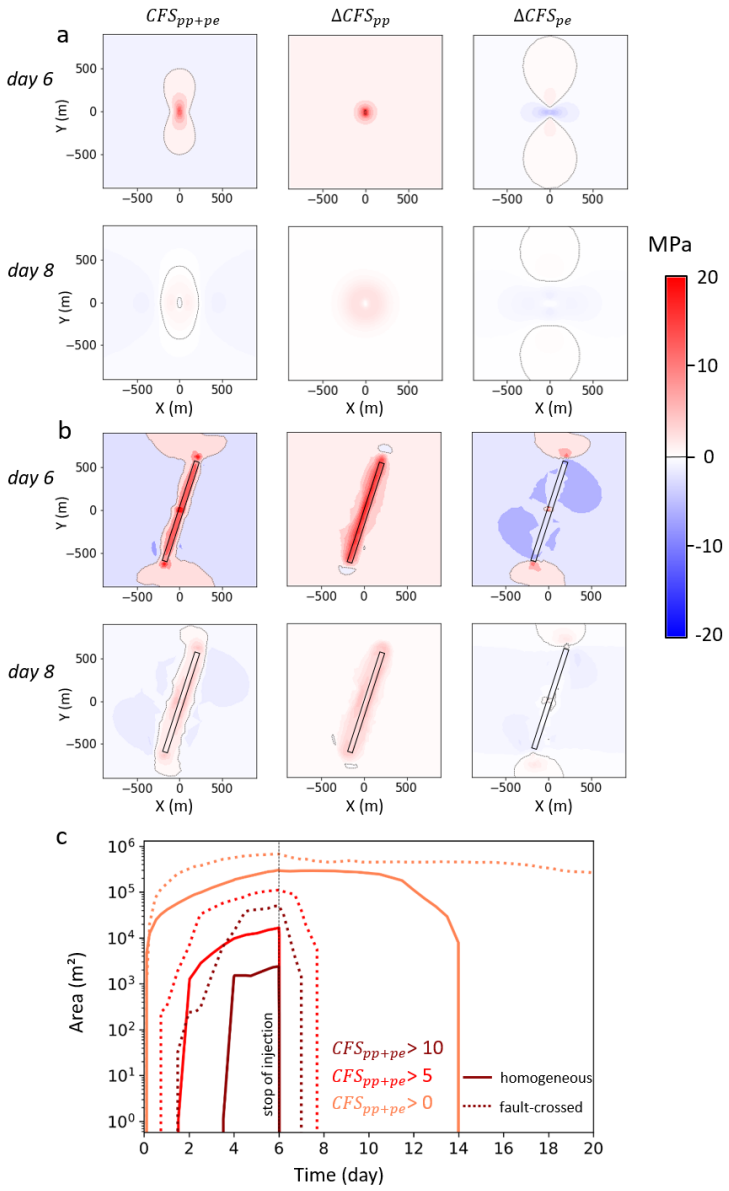

Figure 3.4: CFS variation at the stop of injection (day 6) and 2 days after (day 8) caused by the individual effects of pore pressure variation, ΔCFS_{pp}, and poroelastic stressing, ΔCFS_{pe}, and caused by their combined effects, CFS_{pp+pe}, in (a) the homogeneous and (b) the fault-crossed models for the most critical orientation. The contour line corresponds to the value 0. Areas with positive CFS are in failure conditions. (c) Temporal evolution, in the homogeneous (solid lines) and in the fault-crossed domains (dashed lines), of the surface area (in m²) with positive CFS (orange lines), with $CFS > 5\ MPa$ (red lines) and $CFS > 10\ MPa$ (dark red lines).

3.5. Effect of geological structures on the seismicity rate

Mechanical instabilities are linked to seismicity. We adopt the seismicity rate model proposed by Dieterich (1994), which relates Coulomb stress changes and seismicity rate. The model considers independent earthquakes sources governed by the rate-and-state friction law. It admits steady-state solution and predicts the Omori-like decay of nucleation after a rapid increase of CFS (Dieterich, 1994; Segall & Lu, 2015). The seismicity rate R is described by

$$\frac{dR}{dt} = \frac{R}{t_c}\left(\frac{\dot{\tau}}{\dot{\tau_0}} - R\right). \qquad (3.5)$$

This ordinary differential equation includes the Coulomb and background stressing rates, $\dot{\tau}$ and $\dot{\tau_0}$, and the characteristic relaxation time, which is defined as $t_c = \bar{A}\sigma/\dot{\tau_0}$. We assume $\bar{A}\sigma = 1.8$ MPa, the free parameter of the equation ($\bar{A}$ is a constitutive parameter quantifying the direct effect on slip rate in the rate-state friction law, and σ is the background effective normal stress) and $\dot{\tau_0} =$

3×10^{-6} MPa/year based on a calibration aimed at reproducing the cumulative number of monitored earthquakes in Basel EGS (2,420 earthquakes with a magnitude higher than -1.5 after declustering the aftershocks (Herrmann et al., 2019)). We are not interested in reproducing exactly the observed seismicity at Basel, but we aim at showing the seismic potential associated to the different mechanisms. The absolute seismicity rate SR, in events per year, is equal to $R \times r_0$, where the background seismicity rate for Basel is $r_0 = 0.123$ events/year (Bachmann et al., 2011). We calculate the evolution of the absolute seismicity rate SR along a central part of the domain ($1000\text{m} \times 1000\text{m}$) by assuming that each element of the central mesh hosts a portion of fracture with a probability

$$p_{f_{elem}} = p_f \times \frac{S}{S_{max}} \tag{3.6}$$

where p_f is the probability of having a fracture in a square meter, S is the surface area of the element and S_{max} is the surface area of the largest element in the mesh. We assume that p_f is proportional to the areal fracture intensity P21, i.e., $p_f = c \times P21$, where c is a constant of proportionality that we assume here to equal 0.361 m in order to normalize p_f such that its maximum value is 1. We estimate the areal fracture intensity P21, which expresses the length of fracture traces per unit area, from the observations of the linear fracture intensity P10 at Basel borehole, where P10 expresses the number of fracture traces per unit length (see Dershowitz & Herda (1992) for more details on the classification of fracture intensity in one, two and three dimensions). We consider the borehole unit transversal surface and assume that the mean length of fracture traces is equal to the borehole diameter divided by the cosine of the fracture dip, which has been reported as equal to 70° for Basel, i.e., $P21 = P10 \,/\cos(70°)$. For the homogeneous domain, we adopt the value $P10_{homo} = 0.25$ m^{-1} , as measured by acoustic borehole imager at Basel (Häring et al., 2008). In the fault-crossed domain, we assume a large value of $P21_{fault}$ for the fault zone, which is calculated from the value of $P10_{fault} = 0.95$ m^{-1}, as reported by Haring (2008) for the most intensely fractured zone. The rest of the domain around the fault zone has a value of $P21_{matrix}$ such that the total length of fractures of the fault-crossed model is comparable with the one of the homogeneous model ($P10_{matrix} = 0.22$ m^{-1}). Based on the observed dominant strike of the pre-existing fractures in the network (Häring et al., 2008), we randomly assign to the mesh elements a fracture orientation of N160 or N40 with probability of 0.6 and 0.4, respectively. The Coulomb stressing rate $\dot{\tau} = \frac{\Delta CFS}{\Delta t}$ is calculated for these orientations for each time step of the hydro-mechanical model, and is introduced in Eq. (3.5) to estimate the absolute seismicity rate SR of each element. The ordinary differential equation Eq. (3.5) is solved numerically by means of the tool BRUCES (Luu, 2022; Luu et al., 2022). The SR calculated for each element is then multiplied by the estimated probability $p_{f_{elem}}$ (Eq. (3.6)) to take into

consideration the probability of having a fracture portion in the element, which gives the probable seismicity rate PSR for each element in the domain (Figure 3.5a and b). The cumulative probable seismicity rate of the domain is the sum of the PSR of each element. Note that this corresponds to the integral of SR over the domain surface multiplied by the probability of fracture presence per square meter p_f and normalized by the maximum element area.

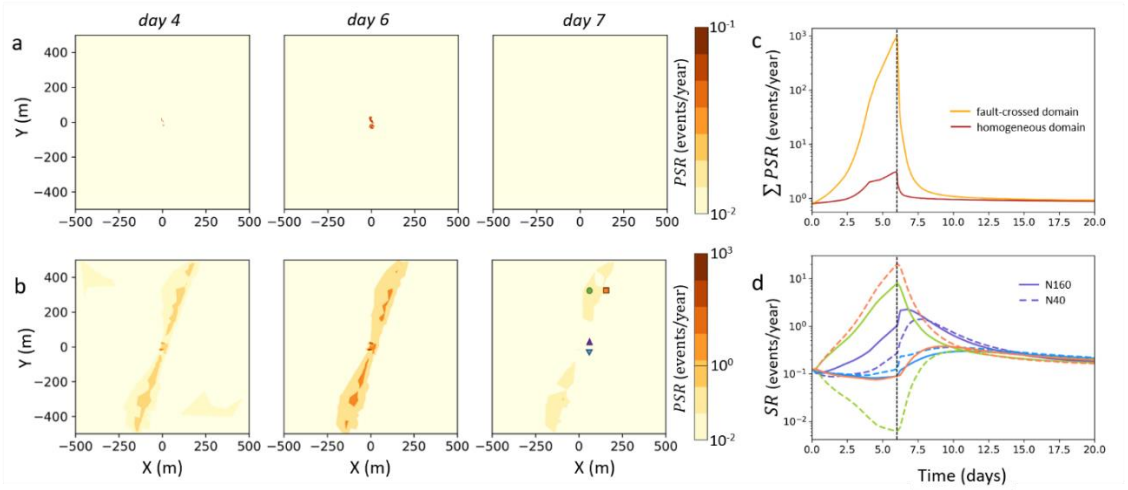

Figure 3.5: Evolution of the probable induced seismicity rate PSR during injection (day 4), at the stop of injection (day 6) and 1 day after (day 7) in (a) the homogeneous and (b) the fault-crossed models. (c) Temporal evolution of the cumulative PSR ($\sum PSR$) in the homogeneous (dark orange) and fault-crossed (light orange) domains, and (d) temporal evolution of the absolute seismicity rate SR at four points of the fault-cross domain for both dominant strikes of the fracture network (colors corresponding to the colored markers shown on the day-7 plots). The vertical dashed lines in (c) and (d) indicate the stop of injection.

The evolution of the probable seismicity rate is barely observable in the homogeneous domain, which emphasizes the importance of a more complex model including the major geological structures. Following the same trend as the CFS_{pp+pe}, the fault-crossed model exhibits a probable seismicity rate orders of magnitude larger than in the homogeneous model (Figure 3.5c). During injection, the potential events are concentrated in the vicinity of the injection well for both models, and along the fault zone for the fault-crossed model. The post-injection spatial repartition of the seismicity rate in both models is very limited. Beside the difference in the number of events, the fault-crossed model requires a longer period after the stop of the injection to reach the initial values (Figure 3.5c). Moreover, we observe post-injection spikes of absolute seismicity rate SR at different locations of the fault-crossed domain, for both dominant orientations of fractures (Figure 3.5d). The behaviour at these points, which are located close to the interface with the fault zone, highlights the effects of fluid injection on stress tensor rotation when different materials are in contact. The presence of geological structures, like fractures or fault zones, enhances the effects of pore pressure build-up and poroelasticity on the destabilization of the domain, and induces a

potential higher magnitude post-injection seismicity in the fault-crossed domain, assuming that the probability of high- magnitude occurrence is proportional to the seismicity rate.

3.6. Discussion

3.6.1. Beyond pore pressure diffusion

The application of the critical pressure theory (Shapiro, 2015) on the monitored events at Basel EGS, using models of simplified homogeneous and fault-crossed domains, demonstrates the limitations of considering the pore pressure diffusion as the unique triggering mechanism (Figure 3.2). Pore pressure build-up explains the triggering of the monitored seismicity nearby the injection well, and along the fault zone during injection. The pressurization front continues to diffuse after the stop of injection and destabilizes a wider area. However, events located far from the co-injection pressurized area and early events far from the injection well cannot be explained by pore pressure diffusion alone. Its combination with poroelastic stressing and static-stress transfer better justifies the occurrence of induced seismicity in the case of Basel (Figure 3.3).

Poroelastic stressing has a larger spatial influence than pore pressure on both the homogeneous and the fault-crossed models. It stabilizes and destabilizes specific zones of the domain, including the non-pressurized region (Figure 3.4). For instance, the tips of the fault zone are destabilized in the fault-crossed model (Figure 3.4b). Regarding post-injection seismicity, poroelastic stress relaxes quickly at the stop of injection and, combined with post-injection pore pressure diffusion, leads to failure conditions in zones that had been stabilized during injection. The poroelastic response varies as a function of the heterogeneities of a domain, with strong effects at the tips of faults. It also changes with the in-situ stress conditions. For instance, when the maximum horizontal stress is orientated parallel to the y-axis, the poroelasticity destabilizes the upper and lower zones of the domain, rather than the left and right zones. Poroelastic effects can be inverted by the stop of injection, inducing a longer positive seismicity rate after the stop of injection in the fault-crossed domain (Figure 3.5d).

Studies of the monitored seismicity at Basel EGS highlight the importance of the triggering role of the static-stress transfer and earthquake interaction both during injection and after its stop (Catalli et al., 2013, 2016). Even isolated clusters could be destabilized by previous seismicity despite their distance from the seismicity cloud. Yet, static-stress transfer cannot be calculated without previous knowledge of the occurrence of earthquakes, especially when little is known about the fracture system in the reservoir. Nonetheless, the effect of static-stress transfer can be incorporated into real-time forecasts of induced seismicity by computing it, analytically (Okada, 1992; Schoenball et al., 2012), from the estimation of the orientation, dip, rake, slipped area and mean slip obtained with moment tensor inversion of induced events.

Our model improves previous explanations of the induced seismicity at Basel EGS by combining pore pressure diffusion, poroelastic stressing and static-stress transfer resulting from hydraulic stimulation; each mechanism having its spatial and temporal particularities (Figure 3.3).

In absence of structures of hydraulic connectivity in the model, the effects are local to the injection well, whereas with the inclusion of a fault zone or a fracture network, the pore pressure can affect a larger area/volume of the domain. Additionally, poroelasticity destabilizes upper and lower zones of the domain due to the initial stress conditions, while it destabilizes the fault zone and its tips in the fault-crossed domain. The shut-in of injection abruptly relaxes the poroelasticity, inducing a short post-injection poroelastic strain and stress redistribution. Static-stress transfer is an important triggering mechanism, both during and after the stop of injection, as it can destabilize faults that would not be reactivated by pore pressure and poroelastic effects. The combination of these three triggering mechanisms permits explaining a larger number of induced seismic events at Basel EGS, especially those occurring in the post-injection stage (Figure 3.3). To account for the relevant triggering mechanisms of induced seismicity at every site, physics-based models are necessary (Dempsey & Suckale, 2023; Dieterich et al., 2015). Besides the mechanisms analysed here, thermoelasticity effects, geochemical effects and stress variation due to aseismic slips could be integrated in the modelling of the rock response during a fluid injection to improve the forecasting of seismicity.

3.6.2. Adding relevant geological structures into models

Explicitly including geological structures or heterogeneities into physics-based modelling improves the induced seismicity forecasting capability (Figure 3.3-Figure 3.5) (Zareidarmiyan et al., 2021). On the one hand, preferential flow paths enhance pore pressure diffusion. On the other hand, the stiffness contrast in the fault-crossed domain amplifies poroelastic stressing caused by the differential pressure-induced deformation. The two mechanisms have larger effects on the stability of a fault-crossed model, especially during the post-injection stage (Figure 3.4c). As a result, the absolute seismicity rate is orders of magnitude larger in the fault-crossed model, presenting a longer post-injection decrease. Quantifying the seismicity rate allows identifying the regions where the potential seismicity could occur during injection and after its stop. The methods proposed here can guide the development of more accurate forecasting tool. Moreover, this work suggests possible strategies for seismicity control. On the one hand, a threshold can be set for the absolute seismicity rate (i.e., if background seismicity is $r_0 = 1$ event/year, it may be convenient to limit it to $PSR = 2$ events/year during injection). On the other hand, the change in the seismicity rate may be a more efficient indicator of probable future large magnitude earthquakes occurrence (i.e., if the SR changes rapidly, more frequent and larger seismicity will occur). In spite of the fact that we have idealized the complex fracture network of the crystalline basement at Basel with a linear fault zone, the improvement in the forecasting capability with respect to the

homogeneous model is significant (Figure 3.3c). This improvement highlights the importance of performing a detailed characterization of the fracture network and faults to incorporate these structures in physics-based models to achieve accurate forecasts of induced seismicity.

3.7. Conclusions

Pore pressure diffusion is not the only triggering mechanism during hydraulic stimulation at Basel EGS, as it fails to explain certain induced seismicity, especially the one occurring in the post-injection stage. Poroelasticity and static-stress transfer should be considered in physics-based modelling of induced seismicity to reproduce most events. Accounting for relevant geological structures, such as fault zones, improves the model capability of identifying potential destabilized regions and thus, induced seismicity, especially in the post-injection stage. Even a simplification of the in-situ fracture network into a fault zone yields improved forecasts of induced seismicity at Basel EGS.

To improve the reliability and accuracy of current forecasting tools, it is required to improve our understanding of the processes that induce seismicity due to fluid injection. We show that even simple-geometry models can be sufficient to study the induced seismicity evolution by using a hydro-mechanical model and a seismicity rate model. By continuously characterizing the subsurface by interpreting monitoring data in real time, unidentified geological structures can be incorporated into the model, improving forecasting accuracy. Utilizing real-time monitoring of induced seismicity to incorporate the static-stress transfer in forecasting tools permits explaining a larger number of events. Identifying all the dominant triggering mechanisms of induced seismicity is key to develop reliable physics-based forecasting models that assist decision-makers in managing induced seismicity.

Chapter 4: Poroelastic stress relaxation, slip stress transfer and friction weakening controlled post-injection seismicity at the Basel Enhanced Geothermal System

4.1. Introduction

Induced seismicity represents one of the main obstacles to the development of geothermal energy, which is a key low-carbon technology to reach mid-century net-zero carbon emission targets (IEA, 2017). In Enhanced Geothermal Systems (EGS), a fluid is circulated through a newly created and/or stimulated fracture network carrying heat through fluid circulation to the production well, increasing the generation of electricity. Seismicity of small magnitude (M<2) is in general observed, especially during the stimulation phase, in which a massive fluid injection is performed to enhance the permeability of pre-existing fractures such that the flow rates are sufficient for geothermal power production. This injection-induced seismicity has occasionally reached magnitudes large enough to be felt on the surface (Majer et al., 2007). Felt induced earthquakes are undesirable not only because they may injure people and damage buildings and infrastructure, but also because they cause a negative effect on public perception that may lead to project cancellation, as occurred at the EGS projects at Basel, Switzerland (Häring et al., 2008), and Pohang, South Korea (Ellsworth et al., 2019). For these two cases, an intriguing common characteristic of induced seismicity by EGS stimulation is that the largest earthquakes take place after the stop of injection, when the induced seismicity potential is supposed to decrease because pore pressure drops.

Following these and other cases of poorly-understood induced seismicity (Evans et al., 2012; Grigoli et al., 2017), the last two decades of research activity have extensively discussed the existence of multiple triggering mechanisms, including pore pressure build-up, poromechanical stress changes, and aseismic or seismic slip stress transfer (Ellsworth, 2013; Ge & Saar, 2022; Keranen & Weingarten, 2018; Vilarrasa et al., 2021). By increasing the pore pressure, the effective normal stress acting on pre-existing fault surfaces, and consequently the shear resistance, reduces and may induce slip on these surfaces (Raleigh et al., 1976). Despite being the most common causal mechanism, pore pressure build-up may not be the only cause of induced seismicity, and in some cases large increases in pore pressure would be required to reach failure conditions. During hydraulic stimulation, fluid injection alters the pore pressure and temperature of the rock. The low temperature of the injected fluid (compared to the in-situ temperature) progressively cools down the vicinity of the injection well, becoming particularly significant during long-term fluid circulation (Parisio, Vilarrasa, et al., 2019). Poroelastic stresses propagate much ahead of the pressurized region and can trigger seismicity at large distance from the

injection well (Goebel et al., 2017; Goebel & Brodsky, 2018). Because these stresses are anisotropic, they can improve or worsen the mechanical stability of pre-existing faults depending on fault orientation (Andrés et al., 2019a; De Simone et al., 2013; Segall & Lu, 2015). Moreover, fluids flowing along preferential pathways have an anisotropic impact on the local stress tensor, leading to more pronounced anisotropy in the poroelastic stress redistribution (De Simone et al., 2017b).

Pore pressure diffusion is also considered as a mechanism of post-injection induced seismicity (Bachmann et al., 2012; Segall & Lu, 2015), as pore pressure continues to propagate in the reservoir after the stop of injection. Earthquake interaction is another potential mechanism (King et al., 1994). The stress variation caused by shear slip activation near the injection well may promote failure on nearby faults. This shear-slip stress transfer may be the result of both seismic and aseismic slip. Aseismic slip generated by pore pressure diffusion may precede seismic slip (Bhattacharya & Viesca, 2019; Cappa et al., 2019) and its associated shear-slip stress transfer may seismically reactivate nearby or distant faults, including faults placed outside the pressurized area after injection stops (De Barros et al., 2021), like in the case of the underground gas storage of Castor, Spain (Vilarrasa et al., 2021). Yet, the cumulative stress transfer due to small events near the injection well is often insufficient to explain the reactivation of nearby or distant faults (Catalli et al., 2013; Kettlety et al., 2019; Schoenball et al., 2012). In some cases, only the combination of slip-induced stress redistribution, poro-thermo-elastic effects, pressure diffusion and fault weakening may explain the seismicity observed in the post-injection period (De Simone et al., 2017b; Yeo et al., 2020). Additionally, fluid injection impacts the geomechanical properties of the rock, especially in the fault zones which concentrate preferential flow paths. The activation of both seismic and aseismic shear slips degrades the fault frictional properties because part of the asperities at the fracture walls are deteriorated (Wibberley & Shimamoto, 2005). This slip weakening further reduces the frictional resistance, promoting additional fault slip. Models taking into account this slip weakening allow to reproduce seismicity with larger events than models without friction weakening (Eyre et al., 2019). The above-mentioned processes are highly influenced by the local stress field, fracture distribution and connection, rock mechanical properties, hydrologic factors and historical natural seismicity, which makes it a complex phenomenon to understand in detail (Majer et al., 2007).

Despite the progress in deepening the understanding of these processes, the ultimate causes of the high-magnitude post-injection seismicity remain not fully understood. In particular, the causes of the post-injection seismicity at the Deep Heat Mining Project at Basel (Switzerland) are not clear. During hydraulic stimulation in December 2006, event magnitudes up to $M_L 2.6$ were recorded. Operations were then stopped, but an event of $M_L 3.4$ (M_W 2.95) occurred 5 hours after shut-in in the stimulation well (Häring et al., 2008). Subsequently, the well was bled off, i.e., the wellhead

was opened and hydrostatic pressure was imposed along the well. This felt post-injection induced seismicity led to the abandonment of the project. Numerous conjectures and studies have been developed since then to explain the observed seismic response, most of them focusing on pressure and stress redistribution consequent to fluid injection. Pressure diffusion has been shown to be the causal mechanism for part of the seismicity occurred during injection at Basel. Mukuhira et al. (2017) compared the injection-induced pressure build-up, estimated by considering a homogeneous domain, with the critical pressure required for fault failure (Shapiro, 2015). Similarly, Terakawa et al. (2012) and Terakawa (2014) used the observed seismicity and critical pressure considerations to map the overpressure distribution in three dimensions, which was obtained exclusively by invoking the existence of preferential diffusion through pre-existing faults. They found that the inferred pressure is consistent with the wellhead pressure history. However, the values of overpressure necessary to explain seismicity are often unrealistically high and they only partially explain the co-injection seismicity. Slip-induced stress redistribution as a triggering mechanism at Basel EGS has been highlighted by showing that the seismicity rate is correlated with the interactions between seismic events (Catalli et al., 2013, 2016; Goertz-Allmann et al., 2011). It has been suggested that co-injection induced seismicity was triggered by pore pressure diffusion (Bachmann et al., 2012), while stress redistribution dominates in the post-injection induced seismicity (Catalli et al., 2016). Andrés et al. (2019b) proposed a conceptual poroelastic 3D-model of fault reactivation to evaluate the potential causal mechanisms of induced seismicity at Basel. Although this was the first attempt to reproduce the seismicity at Basel acknowledging coupled hydro-mechanical (HM) effects, Andrés et al. (2019b) were only able to reproduce the temporal evolution of reactivation of a conceptual single fault plane. Moreover, the respective role of the different mechanisms and their combination were not deeply analysed. After more than 15 years from the halting of the Basel EGS operations, a description of the main triggering mechanisms at Basel to reproduce the spatio-temporal observation of seismicity is still missing.

In this study, we simultaneously simulate pressure diffusion, poroelastic stress redistribution and shear slip-induced stress interactions, to understand their impacts on induced seismicity during and after injection at Basel. We build an explicit faulting model which is based on the seismic observations at Basel, and we solve the coupled HM problem associated with the hydraulic stimulation. We aim at identifying the mechanisms responsible of failure at different reservoir locations. We analyse the role of pressure diffusion, poromechanical stressing, stress variation due to shear slip activation and friction weakening consequent to shear slip activation, on the activation of post-injection seismic activity.

4.2. Methods

4.2.1. Fault network

To construct the geometry of the fault system, we use the Basel seismic database provided by Deichmann et al. (2014), in which different seismic events are grouped on the basis of their focal mechanism, location and timing of occurrence. We assume that each cluster corresponds to a fault plane obtaining a network of 11 faults with different orientations and locations. To simplify the geometry, we combine a few clusters on the basis of similarities of focal mechanism, location and timing. This operation is applied to two sets of three clusters each, which allows us to reduce the original network of 11 faults to a simplified network of 7 faults (Figure SI B.4 and Table SI B.1). To the representativeness of this simplification, we compare the failure-induced static stress redistribution in the simplified fault system and in the original fault system, i.e., in which each cluster is represented by a fault. We use Coulomb3 (Lin & Stein, 2004; Toda et al., 2005) to calculate the static stresses induced by fault slip according to linear elastic behaviour of rock. A net slip d is imposed on each fault plane, calculated as (Steketee, 1958)

$$d = \frac{M_o}{G \times A}, \qquad (4.1)$$

where $G = E/(2(1+\nu))$ is the shear modulus, which we assume to equal 21 GPa, E is Young's modulus , ν is the Poisson ratio, and A is the area of the slipping surface of the fault plane, which we estimate from the seismic cloud of the cluster. M_o is the moment magnitude of the largest event of the cluster, derived from the magnitude of the seismic event M_w, and calculated by (Kanamori & Brodsky, 2004)

$$M_o = 10^{1.5M_w + 6.07}. \qquad (4.2)$$

Results of the slip-induced stress variation in the simplified and original systems are comparable, which confirms the effectiveness of the simplified fault network to model the case of Basel EGS (see Figure SI B.4). Next, we simplify the three-dimensional model to a two-dimensional one by considering the projection of the cluster surfaces on the two-dimensional plane. It should be noted that Coulomb3 considers three dimensions, thus comparisons with the shear-slip stress transfer estimated by the two-dimensional HM numerical model have to be made carefully. Similarly, we can only qualitatively compare the net slip estimated through Eq. (4.1) with the shear slip displacements calculated by the HM numerical simulations to verify the consistency of the HM model.

4.2.2. Hydro-mechanical problem

We calculate the stress and pore pressure variations consequent to fluid injection by means of CODE_BRIGHT, a Finite Element Method (FEM) simulator that solves the fully coupled hydro-mechanical problem (Olivella et al., 1996). Faults are modelled by finite-thickness elements, yet

governed by a Mohr-Coulomb failure criterion together with a friction law. To reduce computational effort, we assume this continuum approach instead of an interface model with discontinuous displacement. The two methods may lead to equivalent results if a correct parametrization is performed (Cappa & Rutqvist, 2011; Zareidarmiyan et al., 2021). The mechanical governing equation to be solved is the momentum balance for the medium, expressed by

$$\nabla \cdot \boldsymbol{\sigma} + \mathbf{b} = 0 \,, \tag{4.3}$$

where **σ** is the stress tensor and **b** is the vector of body forces. The hydraulic governing equation is the mass balance of water, which for a fully saturated porous medium is expressed by

$$\phi\beta \frac{\partial P}{\partial t} + \frac{\partial}{\partial \mathrm{t}} \varepsilon_v + \nabla \cdot \mathbf{q} = f^w \,, \tag{4.4}$$

where ϕ is the rock porosity, β is the fluid compressibility, ε_v represents the volumetric strain, and f^w is an external supply of water. **q** is the water mass flux and is expressed by Darcy's law

$$\mathbf{q} = -\frac{k}{\gamma}(\nabla P - \rho \mathbf{g}) \,, \tag{4.5}$$

where γ and ρ are the fluid viscosity and density, respectively, **g** is the gravity vector and k is the rock intrinsic permeability, considered as isotropic. The intrinsic permeability of the intact rock is considered to be a function of porosity by means of Kozeny's model

$$k = k_o \frac{\phi^3}{(1-\phi)^2} \frac{(1-\phi_o)^2}{{\phi_o}^3} \,, \tag{4.6}$$

with k_o and ϕ_o being the reference values for intrinsic permeability and porosity of the rock matrix, respectively. Fault permeability variations are instead calculated as a function of the undergone deformations, adopting the "embedded model" proposed by Olivella and Alonso (2008), with fractures defined by their aperture embedded in a continuous finite element composed of rock matrix. The model assumes that variations of permeability are proportional to the square of the fault aperture variation, in agreement with the cubic law.

The coupling between Eq. (4.3) and Eq. (4.4) is built through the elastic constitutive law, which relates stress tensor, **σ,** strain tensor, **ε**, and pressure as

$$\Delta\boldsymbol{\sigma} = K\varepsilon_v \mathbf{I} + 2G\left(\boldsymbol{\varepsilon} - \frac{\varepsilon_v}{3}\mathbf{I}\right) - \Delta P \mathbf{I} \,, \tag{4.7}$$

where $K = E/[3(1-2\nu)]$ is the rock bulk modulus and **I** is the first invariant of the stress tensor. While the intact rock is assumed to follow the standard linear elasticity model, the fault elements may present a non-elastic behaviour according to a visco-plastic constitutive law, following a Mohr-Coulomb failure criterion, as expressed by (Vilarrasa et al., 2010)

$$\frac{d\varepsilon_p}{dt} = \Gamma\langle\Phi(F)\rangle\frac{\partial\xi}{\partial\sigma}, \quad (4.8)$$

where ε_p is the visco-plastic strain, Γ is the fluidity set at 1.00E-4 $s^{-1}MPa^{-m}$, F is the yield function, ξ is the flow rule and $\Phi(F)$ is the overstress function, which are defined as

$$F = \sigma_m \cdot \sin\varphi(\eta) + \left[\cos\theta - \frac{1}{\sqrt{3}}sin\theta \cdot \sin\varphi(\eta)\right] \cdot \sqrt{J_2} - c(\eta) \cdot cos\varphi(\eta), \quad (4.9)$$

$$\xi = \alpha \cdot \sigma_m \cdot \sin\psi + \left(\cos\theta - \frac{1}{\sqrt{3}}sin\theta \cdot \sin\psi\right) \cdot \sqrt{J_2} - c(\eta) \cdot cos\,\psi(\eta), \quad (4.10)$$

$$\Phi(F) = \begin{cases} 0, & if\ F \le 0 \\ F^m, & if\ F > 0 \end{cases}, \quad (4.11)$$

where c is cohesion equal to 2 MPa, η is the weakening parameter of 0.01, α is a parameter for the plastic potential set at 1, J_2 is the second invariant of the deviatoric stress tensor and ψ is the dilatancy angle, set at 3° for the faults. The invariants of the equations are σ_m, the effective mean stress, and θ, Lode's angle. m is a constant power to define the overstress function, set as 3 in the model. Fault elements are deformed elastically until stresses reach the shear yield surface ($F = 0$). When the yield surface is exceeded the fault begins to slip irreversibly, but stresses are allowed to remain beyond the yield surface for a range determined by the overstress function. To reproduce the degradation of frictional resistance consequent to the shear slip, we apply a friction weakening on fault C. The friction coefficient decreases linearly from the initial value, φ^{init}, to the residual one, φ^{res}, over a critical shear strain η^*

$$\varphi(\eta) = \begin{cases} \varphi^{init}, & \eta \le 0 \\ \varphi^{init} + \frac{\varphi^{res} - \varphi^{init}}{\eta^*} \cdot \eta, & 0 \le \eta \le \eta^* \\ \varphi^{res}, & \eta^* \le \eta \end{cases}. \quad (4.12)$$

The described model is able to reproduce the HM response to fluid injection and the activation of shear slip along the pre-existing fractures in the network.

4.3. Modelling approach

4.3.1. Conceptual model

We reproduce the setting of Basel EGS by building a numerical model of fluid injection into a fault network embedded in the crystalline basement. The network geometry is based on the interpretation of the seismic event clustering performed by Deichmann et al. (2014). The faults are explicitly represented in our model, reproducing the pre-existing faults in the reservoir that were seismically activated (Figure 4.1b). The faults may reactivate in shear mode as a result of water injection, but we disregard fracture creation or propagation during the hydraulic stimulation. The model domain consists of a plane strain 2D horizontal section intersected by a vertical injection well. This simplification of the reservoir is supported by the long open-hole

section of the injection well (more than 300 meters) and by the fact that most of the monitored events exhibits a focal mechanism with strike-slip movement and vertical dip (Deichmann et al., 2014; Häring et al., 2008; Kraft & Deichmann, 2014). These conditions imply that poroelastic stress and deformation are constant along the depth and that plane-strain conditions can be assumed on a horizontal section. We solve the fully coupled HM problem to estimate the pore pressure and stress variations, as well as fault reactivation, both during injection and after the stop of injection, including the bleed-off period after shut-in.

Pore pressure diffusion, poroelastic stressing and shear-slip stress transfer are analysed as potential causal mechanisms of induced seismicity. Initially, we assess fault stability with purely hydraulic considerations, i.e., neglecting poromechanical effects. The direct effects of pore pressure diffusion on the stability of the faults are determined by applying the critical pressure theory (Shapiro, 2015). For each fault, the critical pressure, P_c, corresponds to the maximum pressure value that the fault can sustain before reaching failure conditions, as expressed by

$$P_c = \sigma_n - \frac{\tau}{\mu}, \qquad (4.13)$$

where σ_n and τ are, respectively, the normal and shear stresses acting on the fault and μ is the friction coefficient. The normal and shear stresses define the fault slip tendency, and are calculated from the orientation of the fault and the regional stress field, which is assumed to remain constant during injection. The friction coefficient μ is an intrinsic property of the fault, which typically takes values around 0.6 in crystalline rocks (Ohnaka, 1975). At Basel, since there are data of the onset of induced seismicity of each fault, i.e., fault activation, we can calibrate which is the actual friction coefficient μ_φ (the friction coefficient being the tangent of the frictional angle φ) for each fault. The obtained critical pressure P_{c_φ} from the calibrated friction angles results in values that are more coherent with the pressure build-up and observed induced seismicity (Table 4.1). We compare the numerically simulated pressure variations in the vicinity of the faults with their critical pressure values to identify the direct impact of pore pressure diffusion on fault reactivation.

Following this simplified analysis, we analyse the fully coupled HM stress variation and consequent failure conditions in two modelling scenarios with elastic and visco-plastic fault mechanical behaviour, respectively (see the section 4.2. Methods). In the elastic scenario, fault deformation is reversible, and the shear displacement is small with no permanent static stress transfer and inversely proportional to the fault stiffness. In the visco-plastic scenario, faults respond to a Mohr-Coulomb failure criterion. When failure conditions are met, irreversible and abrupt shear slip occurs, with consequent irreversible stress redistribution, i.e., shear-slip stress

transfer. The comparison of the two scenarios allows us to distinguish the effects of poroelastic stress from those of shear-slip stress transfer.

Table 4.1: Characteristics and estimated parameters for each fault in the numerical model of the Basel EGS project. M_w is the seismic event magnitude of the largest event of the cluster group associated with the corresponding fault. Friction angle φ is calibrated to reproduce fault reactivation occurrence. Critical pressure P_c is calculated with Equation (4.13), using a friction coefficient of $\mu = 0.6$ (corresponding to $\varphi = 30°$), while critical pressure P_{c_φ} using the friction coefficient that leads to failure at the time of the onset of induced seismicity for each fault, i.e., $\mu_\varphi = tan(\varphi)$. Net slip is calculated with Equation (4.1).

Fault	Strike (°)	Dip (°)	Rake (°)	M_w	φ(°)	P_c (MPa)	P_{c_φ} (MPa)	Net slip (m)	Slip area (m²)
A	160	88	-165	1.75	27.5	54	48	0.0087	1 946
B	170	50	- 50	2.10	19.5	66	53	0.0212	14 236
C	160	88	-155	2.95	24.5	59	49	0.0090	8 019
D	198	88	10	2.24	29	50	46	0.0124	846
E	206	71	- 43	1.91	29.5	50	48	0.0101	1 403
F	200	85	14	1.75	28	52	47	0.0035	5 308
G	204	48	- 22	1.99	30.5	50	49	0.0036	8 878

4.3.2. Numerical Model setup

The 2D geometry represents a horizontal plane of 3.61 km^2 located at approximately 4,630-m deep, coinciding with the injection depth in the crystalline basement at Basel. A set of faults is embedded in the rock matrix, with the fault network derived from the induced seismicity registered in the range from 3,750 to 4,750-m deep. We make use of the open-data seismic catalogue by Deichmann et al. (2014), which proposes a clustering of events occurring during injection and short-term post-injection stages that is based on their locations and focal mechanisms (Figure 4.1a). We translate these clusters into fault planes that constitute the fault network of the domain. From the 11 clusters proposed by Deichmann et al. (2014), we simplify the fault network into an equivalent network composed of 7 pre-existing faults (Figure 4.1b, Table 4.1 and Table SI B.1) by considering the microseismicity focal mechanisms, location, timing and magnitude (see section 4.2).

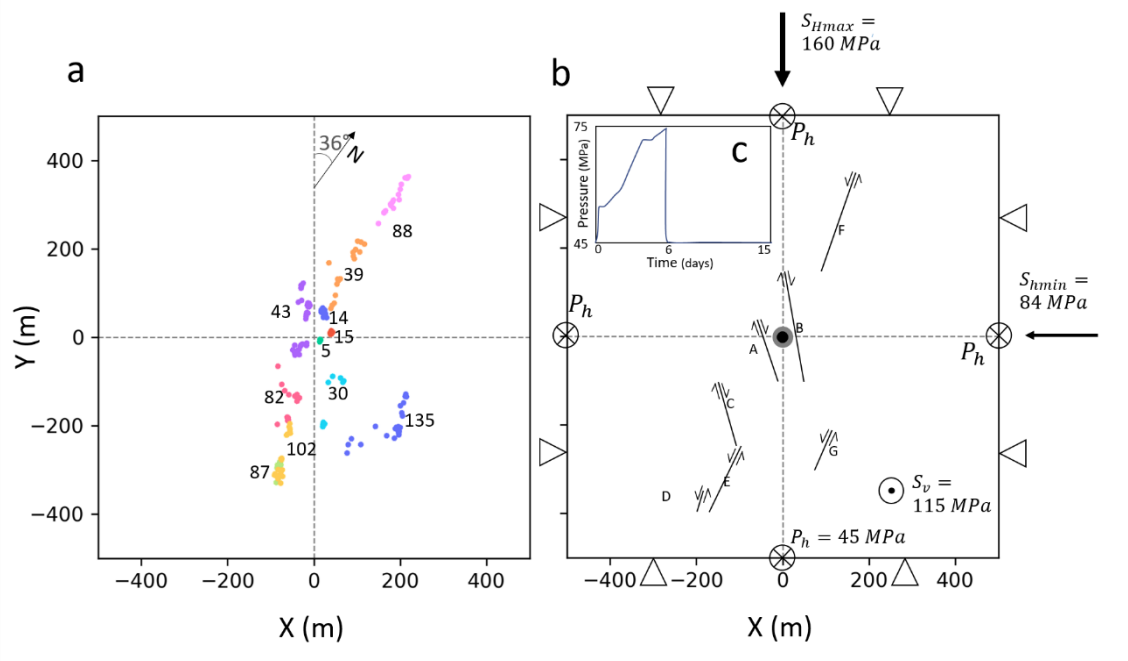

Figure 4.1: Geometry and conditions of the model. a) Plan view of the location of seismic events at Basel, sorted by clusters according to Deichmann et al. (2014). Colours correspond to different clusters as indicated by the numbers. b) Model setup showing geometry, fault network and boundary conditions. The central black dot represents the injection well and the grey area the damaged zone. Initial values of principal stresses and pore pressure are indicated, along with the boundary conditions of constant pressure prescribed at the outer boundaries (represented by the crossed circle) and no displacement perpendicular to the boundaries (represented by the triangles). Note the (b) represents the central region of the model containing the faults, but that boundaries are actually at 950 m away from the well. The direction of shear slip is also indicated for each fault. c) Pressure evolution in time at the well location, according to Häring et al. (2008)

The granitic rock is described as a porous isotropic material with linear elastic mechanical behaviour. A damaged zone, with diameter of 20 meters, with a higher permeability and a lower stiffness surrounds the well to mimic an intensely altered region (Figure 4.1). Faults are represented by continuous material elements with a thickness of 10 centimetres. For all materials, the values assigned to the hydraulic and mechanical parameters are the results of literature reviews and model calibration against field data of injection rate, wellhead pressure and seismicity activation (Deichmann et al., 2014; Häring et al., 2008). In particular, we calibrate the permeability of the rock matrix for a range from 10^{-18} to 10^{-16} m^2 and choose the value with the best fit between the monitored induced seismicity and pore pressure diffusion. The fault intrinsic permeability varies with fracture aperture following the cubic law as faults are deformed, with an initial value that is several orders of magnitude larger than the rock matrix permeability. Large permeability increase at the fault reactivation is important to model pressure diffusion through the domain (Miller, 2016). The specific friction coefficient for each fault is calibrated according to the slip tendency analysis, which is performed using the regional stress field (Häring et al.,

2008) and the focal mechanisms (Table 4.1) to match the fault reactivation with the monitored seismicity. In addition, a slip-weakening of the friction angle of 5° is assigned to fault C.

We set the initial conditions as defined by Häring et al. (2008), with the maximum principal stress aligned with the y-axis after a rotation of 36°, S_{Hmax} having a strike of 144°N, and values of stresses and hydrostatic pressure as indicated in Figure 4.1b. Constant pressure boundaries are set at 45 MPa, to match the hydrostatic pressure. Yet, the nature of the hydraulic boundary condition does not affect the results if pore pressure diffusion does not approach the domain boundaries during the simulated time. Normal displacement perpendicular to the boundary is constrained to zero on all boundaries of the domain. The temperature at the depth of the reservoir is 190°C and the injection fluid is water. We assume isothermal conditions, i.e., the injected fluid is in thermal equilibrium with the reservoir. To correctly reproduce the injection-induced overpressure of the real 3D domain into a 2D domain, we do not impose a fluid injection rate at the injection well, but we directly assign pressure variations as reported by Häring et al. (2008), after smoothing out the oscillations for computing purposes (see Figure 4.1c). At day 6 after the start of the hydraulic stimulation, the well pressure is set to 45 MPa to reproduce the bleed-off.

Table 4.2: Hydro-mechanical properties of the materials composing the numerical model.

	Rock matrix	Damaged zone	Faults
Young's modulus, E (GPa)	52	50	43
Poisson's ratio, ν (-)	0.25	0.25	0.25
Permeability, k (m^2)	$7.50 \cdot 10^{-17}$	$1.00 \cdot 10^{-14}$	$2.30 \cdot 10^{-13}$
Porosity, ϕ (-)	0.01	0.01	0.1

4.4. Results

4.4.1. Comparison of modelled slip with Basel microseismicity

We examine the spatial and temporal reactivation of the faults by observing their visco-plastic deviatoric strain (ε_p), which is a measure of irreversible shear deformations. The temporal evolution of ε_p at three locations, at the centre and close to the extremities of each fault, is analysed together with the cumulative seismic moment, calculated (Eq. 4.2) from the registered events (Deichmann et al., 2014) at the clusters associated with each fault (Figure 4.2). ε_p variations are observed during both co- and post-injection. For most faults, there is a remarkable correspondence between the numerically estimated values of ε_p and the cumulative seismic moment of the cluster related to the fault, which highlights the ability of our model to capture the seismicity observed at Basel EGS.

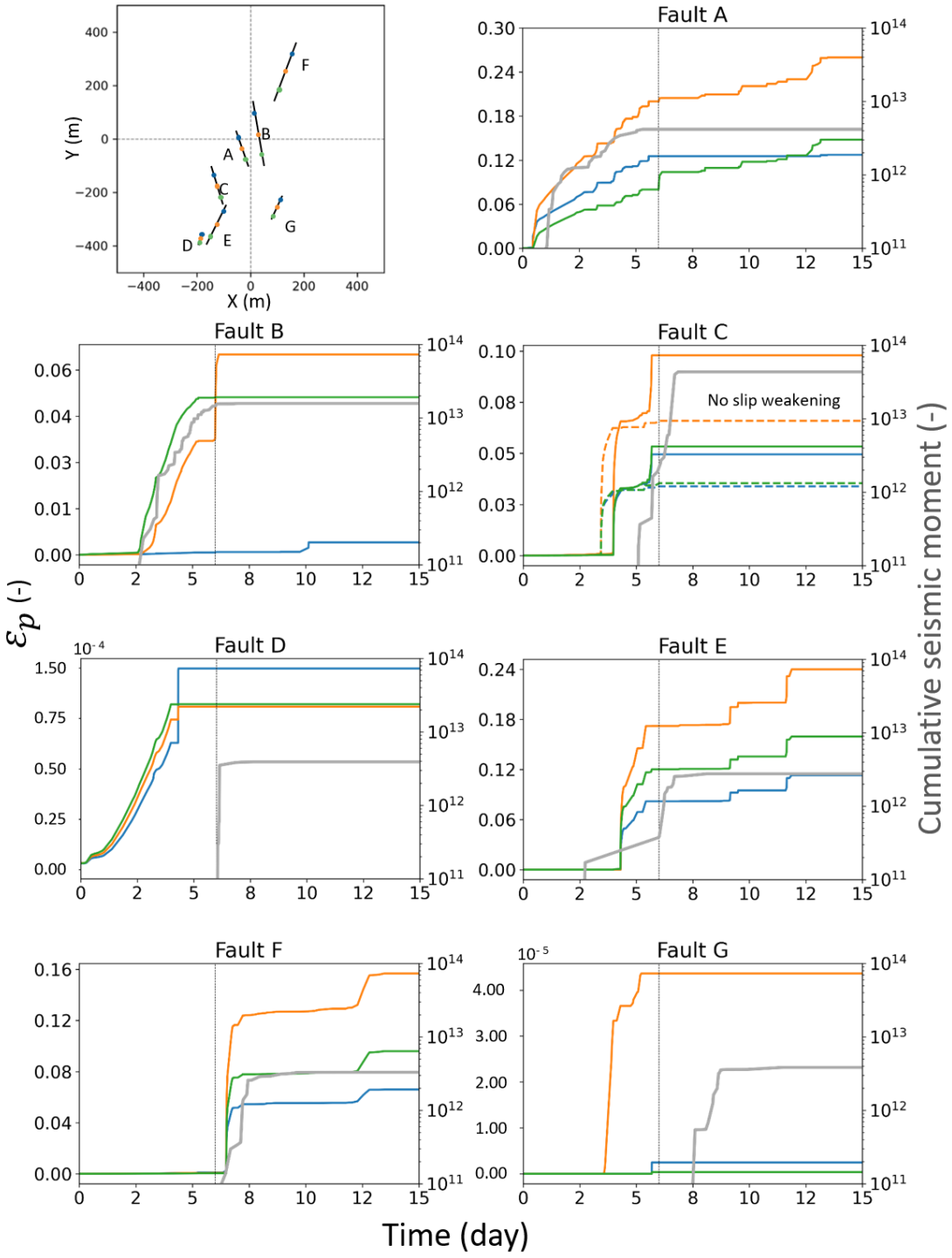

Figure 4.2: *Temporal evolution of modelled plastic strain, ε_p (solid lines), at different locations on each fault (represented by different colors as indicated in the top-left plot), and of the cumulative seismic moment Mo (grey solid lines) of the observed seismic events as reported by Deichmann et al. (2014). At fault C, ε_p for the case without friction coefficient weakening is represented by the dashed lines. The vertical grey line represents the stop of injection at day 6. Note that the scale of the plastic strain is different for each fault.*

Faults A and C are activated during the injection period. Fault A undergoes a progressive failure during co- and post-injection, while fault C undergoes two failures during injection. To better understand the role of friction weakening assigned to fault C, we repeat the simulations disabling this option. We observe that fault C fails only once if friction weakening is disabled (dashed lines in Figure 4.2), i.e., the second failure does not occur. The effect of not considering friction weakening in fault C on the behaviour of the other faults is significant for the multiple subsequent reactivations of faults A and E, located next to fault C (Figure SI B.1). Ruptures occur both during and after injection for faults B and E, while fault F exclusively fails during the post-injection period. Values of visco-plastic strains at faults D and G are not large enough to interpret them as fault failures. We compare the scales of the numerically simulated displacements with the net slip estimated from the recorded magnitude of seismic events (Table 4.1, see also Methods) to verify the coherence of our model with the seismicity of the Basel EGS. Although it is not straightforward to differentiate between aseismic and seismic slip, the model results are overall temporally and spatially consistent with the monitored seismicity at Basel EGS (Deichmann et al., 2014). In Section 4.3.3, we analyse in detail the different patterns of failure to identify the triggering mechanisms.

4.4.2. Pore pressure diffusion

Injection-induced pressure build-up spreads radially in the reservoir until reaching faults A and B, which are located around the injection well and alter the radial pressure propagation because they represent preferential pathways for pressure along their directions (Figure 4.3a – observe the change of pressure gradient corresponding to fault A on day 2 in Figure 4.3c). Pore pressure propagation is affected by the strain-dependent permeability of the faults, which causes an irreversible permeability enhancement up to four orders of magnitude upon failure (see Figure SI B.2). After the stop of injection and subsequent bleed-off on day 6, pore pressure decreases drastically in the reservoir tending to recover the initial hydrostatic value of 45 MPa (Figure 4.3b). However, residual fluid overpressure continues diffusing and it may trigger failure during the post-injection phase, as shown by the pressure variations along a cross-section at different times (Figure 4.3c). Indeed, the peak of pore pressure propagates farther in the reservoir, as shown at fault C, where pore pressure is higher on day 8 than at the stop of injection on day 6.

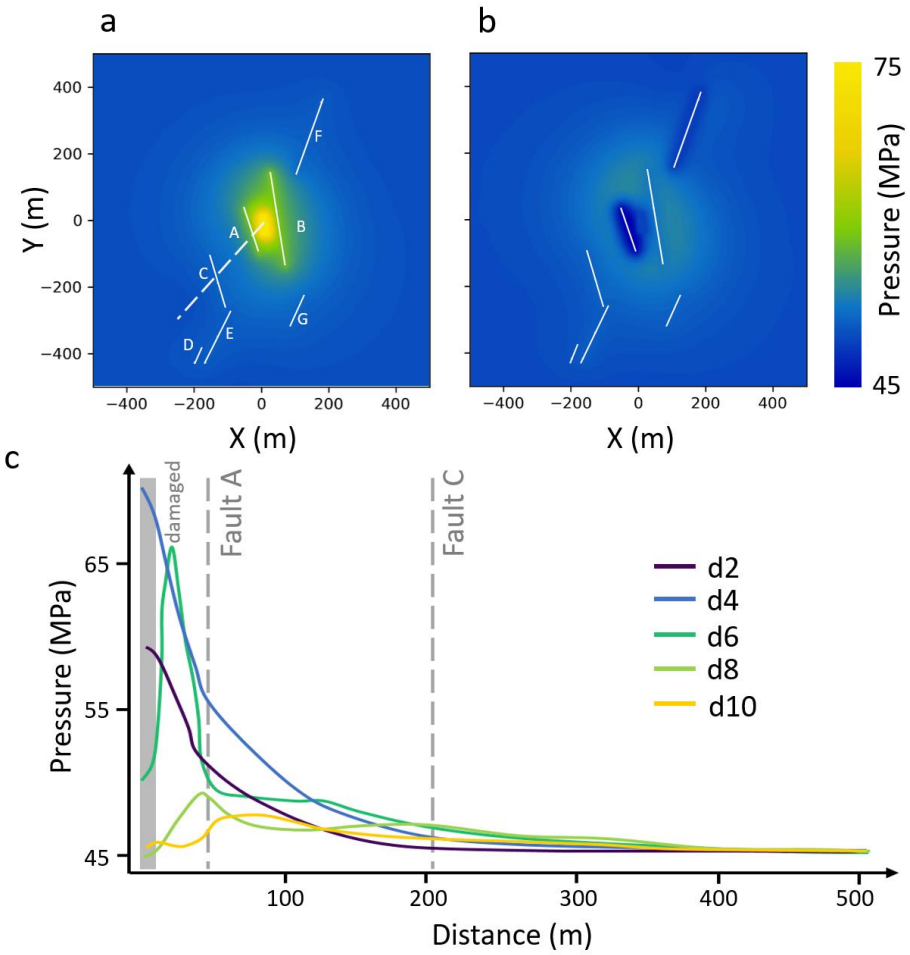

Figure 4.3: Pore pressure evolution in the domain. a) Contour plot of pressure at the end of injection (day 6), b) contour plot of pressure in the post-injection stage (day 7), c) spatial distribution of pressure at different days from day 2 to day 10 along a cross-section extending from the injection well to the bottom-left corner of the domain, which crosses faults A and C, as represented by the dashed white line in (a). The damaged zone is represented by the grey band in Figure 4.3c.

To determine the triggering role of pore pressure diffusion, we compare the estimated critical pressure (Table 4.1) with the pressure reached for each fault (Figure 4.4). We observe that, in some cases, the pressure increase is not sufficient to initiate rupture at the time of the observed seismicity. For example, at fault A, the critical pressure is only reached after 2 days of injection, whereas the fault is activated at the start of injection. The extreme situation of this case occurs in faults that are reactivated while the critical pressure is not reached, e.g., faults B, C and E (Figure 4.4). In contrast, other faults are reactivated after the critical pressure is exceeded. For instance, the critical pressure is reached at fault F after 4 days of injection, but the fault is reactivated after the stop of injection, at day 7. These observations highlight that triggering mechanisms other than pore pressure build-up control induced seismicity.

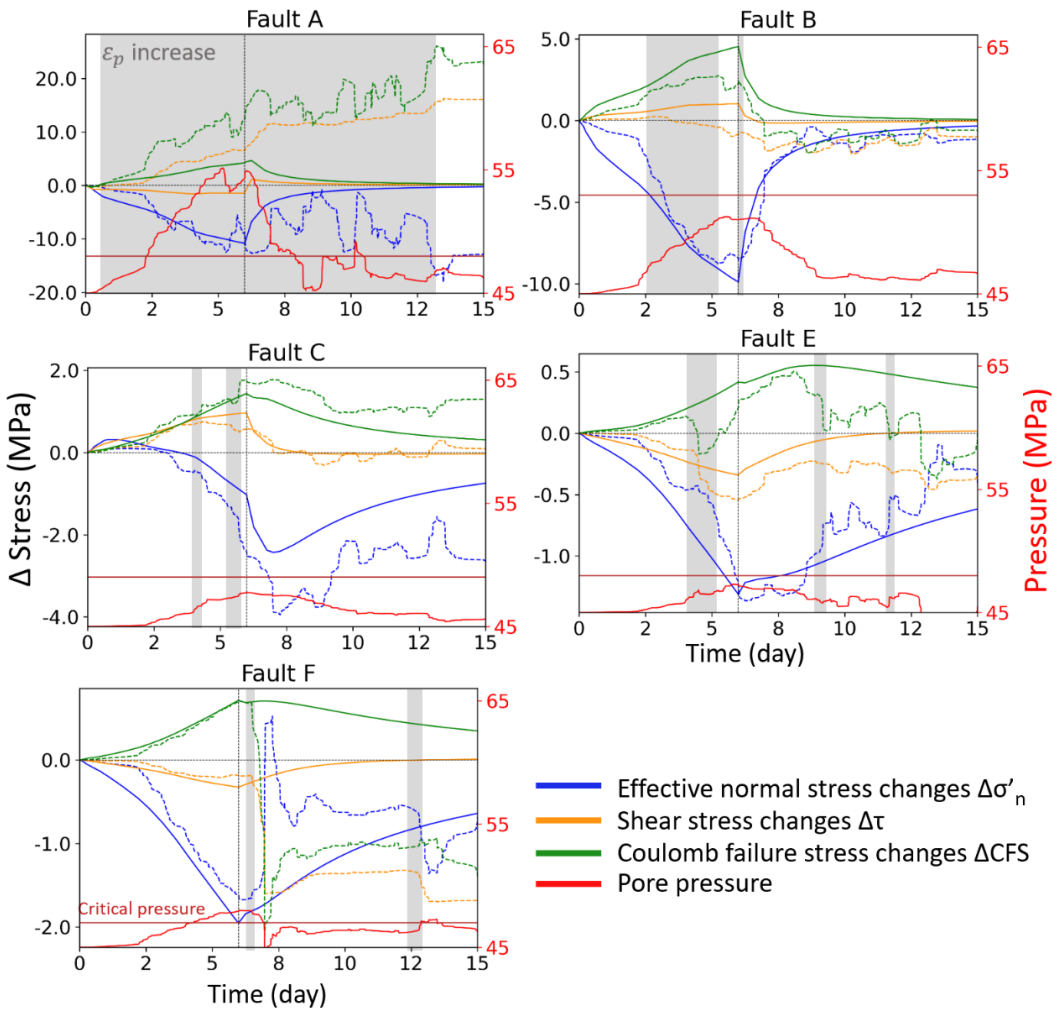

Figure 4.4: Temporal evolution of effective normal and shear stresses changes (blue and yellow lines, respectively), Coulomb Failure Stress changes (green lines) and pore pressure (red line) under elastic (solid lines) and visco-plastic (dashed lines) behaviour at the central location of the selected faults. The critical pressure for failure is represented by the horizontal dark red line. The grey shadowed regions correspond to times with increasing ε_p for each fault according to Figure 4.2. Note that the scale of stress variation is different in each plot. The behaviour of the rest of the faults is shown in Figure SI B.5.

4.4.3. Stress variations

We focus on five faults and we analyse the evolution of the effective normal stress σ_n' and shear stress τ acting on these faults, which allow us to illustrate different rupture patterns (Figure 4.4). To facilitate the analysis, we show the variations of stresses with respect to their initial values. The failure potential along a given fault is expressed by the Coulomb Failure Stress (CFS), calculated as (Jaeger et al., 2009)

$$CFS = |\tau| - \sigma_n' \tan(\varphi) , \qquad (4.14)$$

where φ being the initial friction angle. CFS depends on the stresses acting on the fault plane, and thus, on its orientation. A positive CFS indicates that failure conditions are reached along the

fault. Here, we analyse the CFS variations with respect to the initial conditions, ΔCFS, which illustrate the evolution of fault stability, i.e., a fault becomes less stable when ΔCFS is positive. The elastic model indicates the effect of the poroelastic stressing, while the differences between the visco-plastic and the elastic models quantify the effect of the shear-slip stress transfer.

Both faults A and B undergo a significant increase of pore pressure (5-10 MPa) due to their proximity to the injection well. The pore pressure build-up leads to the decrease in the effective normal stress in both the elastic and visco-plastic scenarios. Concerning the shear stress variation, it is interesting to note that in the elastic scenario, $\Delta\tau$ is reduced during injection in fault A, whereas it increases in fault B. However, the opposite occurs when considering visco-plasticity of the faults as a result of the shear stress drop that takes places during slip. Before failure occurs, fluid injection causes a poromechanical response of the rock in which the rock expands and, as a result, total stress components increase accordingly. The lower portion of the block of rock comprised between faults A and B, i.e., the half space with negative values of the y-coordinate, which contains the central point of these two faults whose results are plotted in Figure 4.4, is compressed against fault A. Such deformation promotes a right-lateral movement of fault A (negative values of the shear stress) and a left-lateral movement of fault B (positive values of the shear stress). Since faults A and B undergo a right-lateral slip because of their orientation with respect to the principal stresses, fault A is destabilized by the poromechanical effect, while the upper part of fault B is destabilized and its lower part stabilized (in which lower and upper refer to the reference axis Y). This poromechanically-induced destabilization of fault A explains why failure is reached before its critical pressure is reached. The activation of shear slip, and the consequent stress redistribution, amplify failure on fault A (Figure 4.2) and mitigate failure on fault B (compare the dashed and solid green lines in Figure 4.4). These opposite effects, despite the similar orientation of the two faults, are due to the different location of the faults with respect to the antisymmetric variation of shear stress caused by poroelastic expansion (Figure 4.5). Although critical pressure is not reached on faults A and B at the time of their activation, their rupture is mostly initiated by direct pressure effects and partially by the poroelastic effects. Once failure is initiated, shear-slip stress transfer plays a major role on fault stability, as shown by the lower reduction in the effective normal stress in fault B during the first two days of injection that stabilizes it. Furthermore, slip causes the fault to open up because of dilatancy, which causes undrained pore pressure drops that are subsequently recovered by diffusion. These dilatancy-induced pore pressure changes perturb the smooth evolution of pore pressure, stresses and fault stability observed when only elasticity is considered. Right after the stop of injection and subsequent bleed-off, poromechanical effects vanish. Therefore, fault A temporarily improves its stability and fault B fails for the second time coinciding with the immediate stop of poroelastic volume expansion (see also Figure 4.2). By bleeding off the well, i.e., opening the wellhead and

achieving hydrostatic conditions within the well, poromechanical effects disappear almost completely, which may be the cause of the sudden second reactivation of fault B.

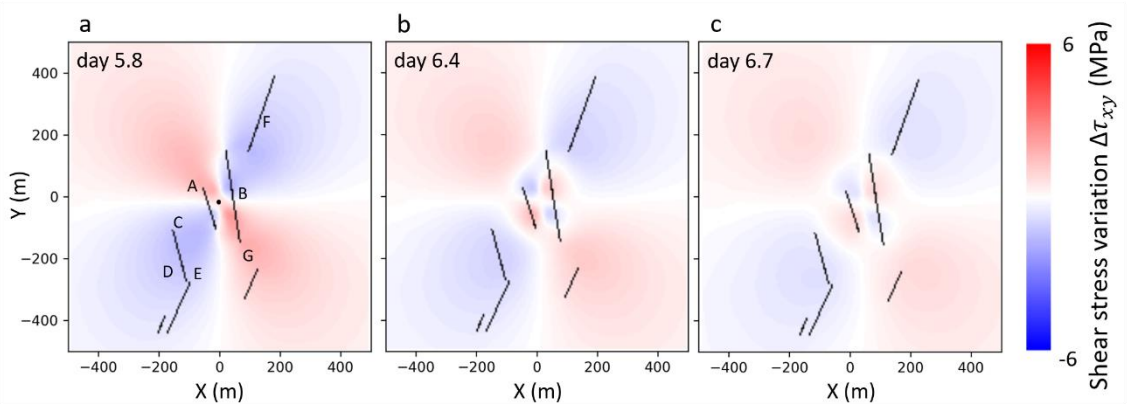

Figure 4.5: Shear stress variation $\Delta\tau_{xy}$ in the elastic scenario before and after the stop of injection. Observe the spatial distribution of the poroelastic stressing due to the injection-driven volume expansion during injection (a) and volume contraction during bleed-off (b and c), evolving as four antisymmetric lobes with respect to the injection well (black dot). Positive shear stress indicates left-lateral movement.

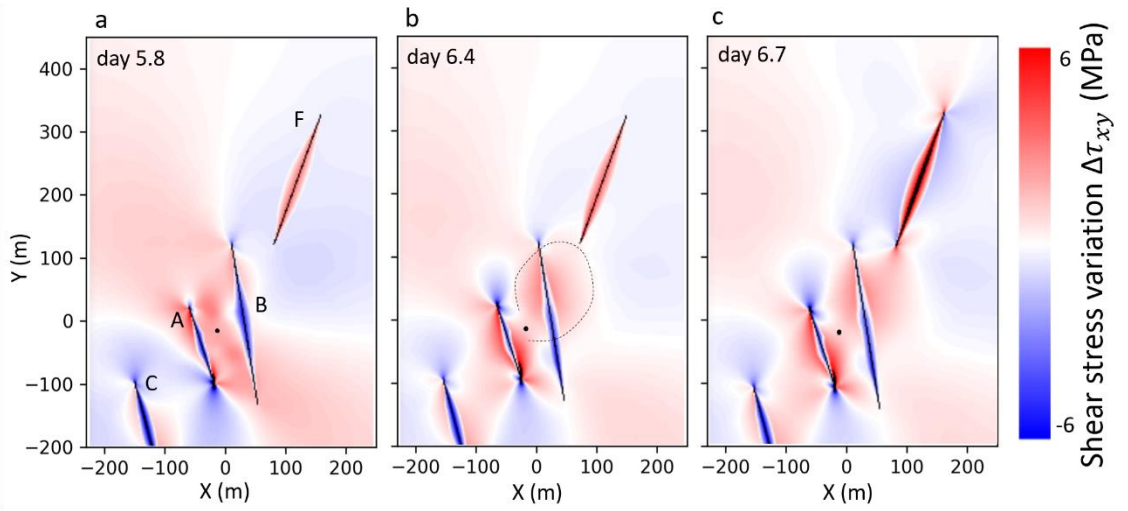

Figure 4.6: Shear stress variation $\Delta\tau_{xy}$ in the visco-plastic scenario at different times. a) At day 5.8, fault B is affected by the injection. b) At day 6.4, the rupture of fault B induces stress transfer, and amplifies the stress redistribution caused by poroelastic contraction due to bleed-off. (c) At day 6.7, fault F yields due to the combination of the shear-slip stress transfer and poroelastic mechanisms. Observe the evolution of the positive small lobe from poroelastic stressing after the bleed-off at day 6 that affects fault B. Note that the figure shows a close-up of the domain focusing on the area of interaction between faults B and F.

Fault C reactivates twice at day 4 and day 5. Both reactivations of fault C are due to pore pressure diffusion, poroelasticity and stress transfer from faults A and E, as shown by the difference between elastic and plastic Coulomb Failure Stress changes (compare the solid and dashed green lines in the Figure 4.4). Fault E fails for the first time during the injection and then twice during post-injection. Pore pressure variations are not sufficient to activate the fault, which is located

outside of the pressurized region (Figure 4.3). Additionally, poroelastic expansion has a stabilizing effect during injection because the induced right-lateral shear stress (Figure 4.4) opposes to the left-lateral slip originated from the regional stress. On the other hand, elastic $\Delta\sigma'_n$ slightly reduces and it tends to return to initial values after bleed-off, without completely recovering because residual overpressure continues propagating. Resulting from these variations, ΔCFS increases even after bleed-off and slightly starts decreasing at day 9 in the elastic case. Stresses in the visco-plastic scenario follow the same trends with a more complex behaviour because each failure on the fault itself causes a drop in shear stress, and a drop in pore pressure that increases the effective normal stress, both contributing to improve stability. To better understand the role of shear-slip stress transfer, we run additional simulations in which alternatively each fault is the only one following a plastic-behaviour, while the others follow an elastic behaviour. We observe that without slip activation on fault C, fault E does not reach failure conditions. Overall, fault E is triggered by the combination of poroelastic stressing and shear-slip stress transfer during injection, and by the combination of stress transfer from the distant fault C and the poroelastic stressing relaxation due to the stop of injection and bleed-off in the post-injection stage.

Fault F is of special interest because it fails solely after the stop of injection. Pore pressure reaches the critical pressure at day 4. But similar to fault E, during the injection, poroelastically-induced right-lateral movement opposes to the left-lateral slip caused by the regional stress state and prevents the failure due to the pore pressure increase. The first rupture of fault F, which occurs one day after the stop of injection, is caused by the combination of poroelastic stress relaxation and shear-slip stress transfer caused by the reactivation of fault B with the pore pressure diffusion, as shown by the comparison with the simulation in which only fault F has a visco-plastic behaviour (fault F never reaches failure conditions if fault B is not activated, see Figure SI B.3). Figure 4.6 shows the spatial evolution of the shear stress τ_{xy} around faults B and F. The reactivation of fault B creates a local shear stress variation at the tips of fault F (Figure 4.6b) that destabilizes it (Figure 4.6c). The rupture of fault F stabilizes it due to the shear stress drop and an increase in the effective normal stress caused by the dilatancy-induced pore pressure drop. The second failure of fault F is caused by stress transfer from the reactivation of a portion of fault B.

4.5. Discussion and conclusions

We have revisited the intriguing case of co- and post-injection induced seismicity at Basel EGS and we have identified the triggering mechanisms by making use of coupled fluid flow and geomechanics numerical simulations in a model that explicitly includes a set of pre-existing faults based on *in-situ* observed seismicity. We simulate fault reactivation, which is a necessary condition for induced seismic events to occur, by considering the non-elastic response of the faults. Despite a few simplifying assumptions, simulation results are remarkably coherent with

the observed induced seismicity, both temporally and spatially. Our results illustrate that accounting for poroelastic stressing and non-elastic behaviour, i.e., shear-slip stress transfer, is crucial to reproduce the reactivation of certain faults.

In general, pore pressure diffusion is accepted as the main triggering mechanism in EGS. Yet, this vision may be oversimplifying, leading to inaccurate forecasting of induced seismicity, especially of post-injection seismicity. We estimate values of critical pressures which are similar to the ones proposed by other studies (Mukuhira et al., 2017; Terakawa, 2014; Terakawa et al., 2012). However, the simulation of the hydraulic stimulation shows that pore pressure does not reach the critical pressure for most of the faults. Thus, even though pore pressure build-up has a direct effect on faults, especially in those in the vicinity of the well, other triggering mechanisms are relevant and should be taken into account to enable reliable estimates of induced seismicity (Zareidarmiyan et al., 2021).

Poromechanical volume expansion exhibits a wider and faster front than pore pressure diffusion during co-injection, in accordance with previous works by Duboeuf et al. (2017) and Krietsch et al. (2020). This poroelastic effect, driven by fluid injection that acts as a compressive loading, can improve or worsen the stability of faults depending on their orientation (De Simone et al., 2017b; Segall & Lu, 2015). After the stop of injection, and more pronounced if bleed-off is applied, pressure gradients dissipate fast and poroelastic stress vanishes. Therefore, faults on which stability is enhanced by poroelastic stressing during injection are destabilized by volume contraction caused by bleed-off, e.g., faults B, E and F. The abrupt decrease of pore pressure and poroelastic stress are responsible for the immediate post-injection induced seismicity in certain zones of the reservoir, e.g., fault F. Lastly, shear-slip stress transfer affects the stability of nearby-faults and amplifies the induced seismicity (Figure 4.6). Catalli et al. (2016) suggested that the seismicity rate in the post-injection period is higher when stress transfer is taken into account than with pressure-induced seismicity only, enabling a better fitting of the observed seismicity. Our study confirms this finding, as we observe that only two faults in the vicinity of the well (faults A and B) fail when stress transfer is neglected while shear-slip stress transfer is required to reach shear failure conditions on the rest of the faults. The combination of pore pressure diffusion, poroelastic stress and shear-slip stress transfer (De Simone et al., 2017b ; Yeo et al., 2020) explains the fault rupture patterns underpinning the co-injection and post-injection induced seismicity at Basel. A quantification of the effects of the reactivation capacity of each mechanism, or combination of mechanisms, is presented in Figure 4.7, where we estimate the portion of each fault reactivated by direct pore pressure effects, poroelastic effects, i.e., pore pressure changes and induced poromechanical stresses, or the combination of poroelastic effects and stress transfer during injection and post-injection stages. To do so, we analyse the behaviour of each fault mesh element. If pore pressure, estimated by the hydro-mechanical elastic model, reaches the critical

pressure, we consider that fault portion as reactivated by direct pore pressure effects. If the Coulomb Failure Stress, estimated by the hydro-mechanical elastic model, is positive, we consider that fault portion as reactivated by the combination of pore pressure and poroelasticity. Finally, if a positive increment of the plastic strain is estimated by the hydro-mechanical visco-plastic model (and if the plastic strain has a value higher than 1e-3), we consider that fault portion as reactivated by the combination of all the mechanisms. Pore pressure has a major impact on the stability of the faults located near the injection well before shut-in, and a minor impact after shut-in. Poroelasticity affects a wider region, but depending on the orientation and location of the faults, it can promote (faults B and C) or hinder (faults A and F) fault reactivation. Note that fault F is reactivated if pore pressure is considered as the only triggering mechanism. However, poroelasticity hinders failure because it stabilizes the fault. Static stress transfer is responsible for the reactivation of faults that are not destabilized by the effects of pore pressure and poromechanical stresses (faults C and E). Fault D does not have a sufficient plastic strain increase and is not considered as reactivated, even if pore pressure alone, and its combination with poroelasticity could trigger fault reactivation. Post-injection fault reactivations are due to the fact that poroelasticity vanishes abruptly, and stabilization effects are quickly reversed; while pore pressure still diffuses after shut-in (fault F). These mechanisms are combined to the continuous stress redistribution from fault reactivation during and after the stimulation, which trigger the post-injection induced seismicity.

Despite our modelling approach permitting to identify the triggering mechanisms of the induced seismicity at Basel, simulation results cannot fully explain the reactivation of all faults. In particular, faults D and G, even though they reach failure conditions in our model, present a plastic strain that is too small to explain the observed cumulative seismic moment at these faults (Figure 4.2). For the rest of the faults, the spatio-temporal evolution of faults reactivation correlates well with the observed seismic events. Yet, the largest event, which occurred at fault C shortly after the stop of injection, is not captured by our numerical model that reproduce two reactivations at times earlier than the reported ones in the injection stage (Figure 4.2). This is probably due to our simplification of the fracture network into a few faults. It is possible that aseismic slip occurred on smaller fracture connecting the seismogenic faults, but no data is available to confirm this hypothesis. Our model identifies that multiple reactivations of fault C only occur with a slip-weakening friction, but the weakening, and reactivation of the real fault may have obeyed to a behaviour different than just the linear strain-weakening assumed in our model.

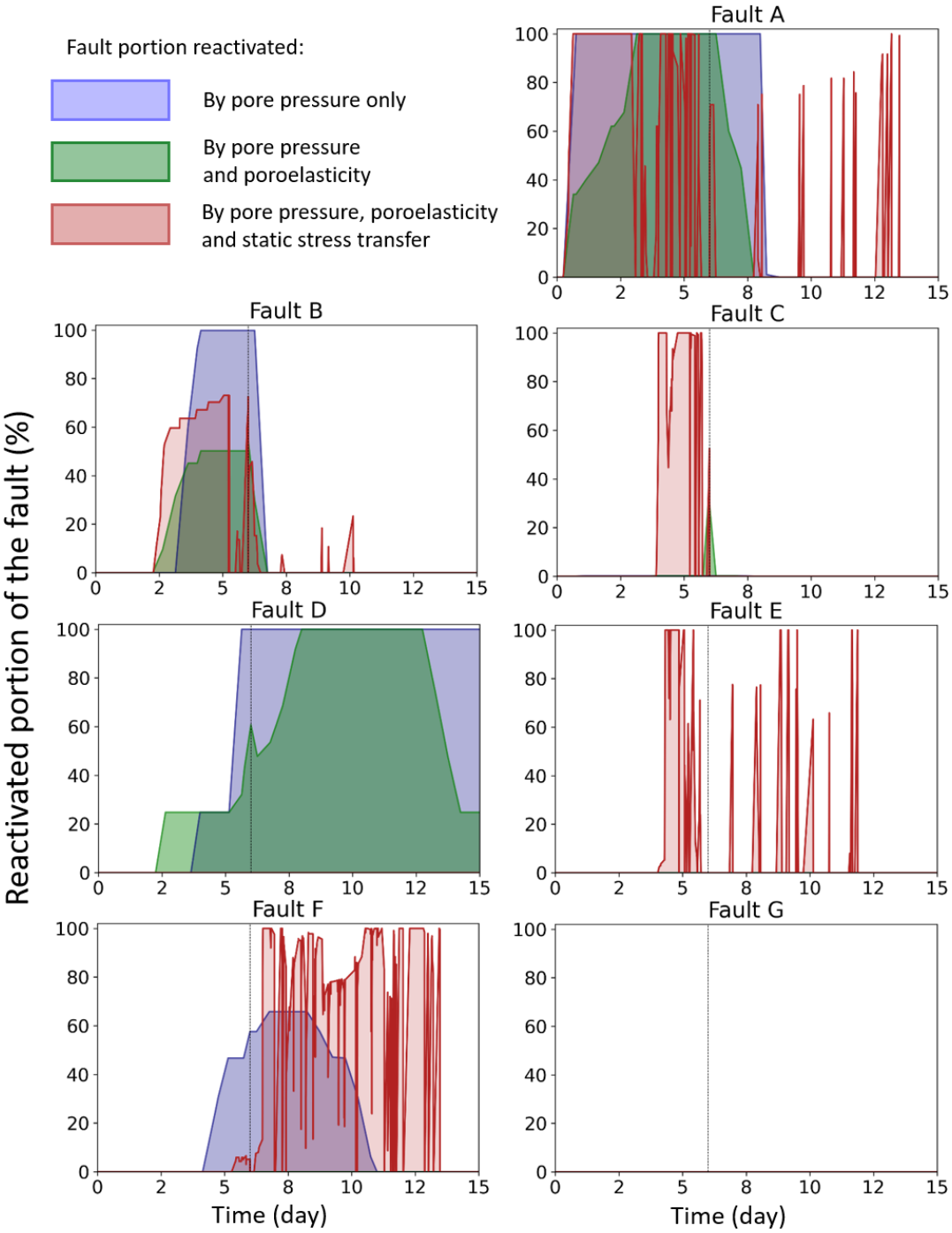

Figure 4.7: Temporal evolution of the portion of each fault reactivated by the different combinations of triggering mechanisms. Faults G is not reactivated by any mechanisms.

For faults A, B, E and F, our 2D hydro-mechanical model of the Basel EGS is able to qualitatively reproduce the timing of fault reactivation. Although the adopted constitutive visco-plastic model does not allow to quantify the seismic magnitude, we compare the observed cumulative seismic moment with the numerically estimated plastic strain, which is proportional to slip and, therefore, to the moment magnitude. Interestingly, the temporal evolution of the numerically estimated plastic strains qualitatively corresponds to the one of the observed seismicity for most of the

faults. Therefore, our results are relevant to identify the triggering effects of the multiple processes represented in the model.

Another simplification of our modelling resides in the adoption of a 2D domain. Although the monitored seismic events – exhibiting focal mechanisms with strike-slip movement and vertical dip – combined with the long open-hole section of the injection well – ensuring that overpressure field and poroelastic deformation are constant along the depth – suggest that a 2D horizontal section that crosses the vertical faults is reasonable to represent fault reactivation, static stress transfer is limited by this assumption. Indeed, stress redistribution from fault slip and earthquake-interactions are more complex in a 3D domain than in a 2D model. Improvements of our model could be achieved by modelling the 3D geometry of the fractured network, but such representation is extremely computationally challenging.

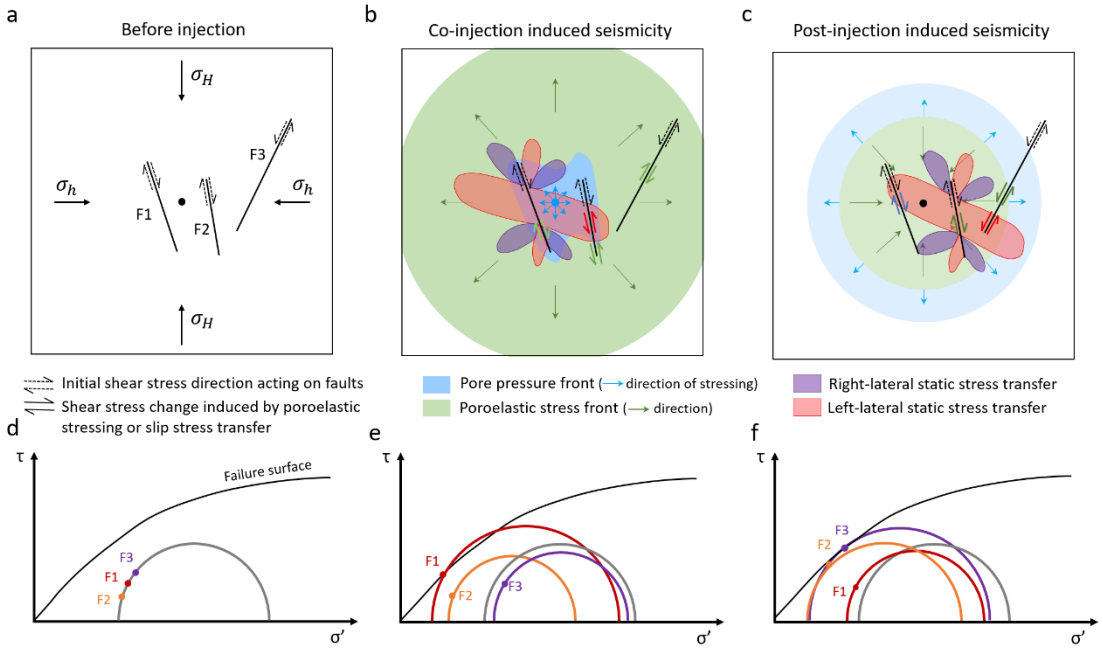

Figure 4.8: Schematic illustration of the triggering mechanisms of induced seismicity. (a)-(c) Evolution of pore pressure, poroelastic stress and shear-slip stress transfer, respectively, before, during and after injection in a simplified generic fault network. The black dot in the centre represents the injection well. (d)-(f) Mohr circles illustrating the stress state of the faults at each stage. (a) At initial conditions, faults F1 and F2 undergo right-lateral slip while fault F3 undergoes left-lateral slip (dashed arrows), in accordance with the maximum (σ_H) and minimum (σ_h) horizontal stresses. (b) During injection, pore pressure diffuses in the vicinity of the well. Poroelastic stressing extends farther and faster, and it exerts an inversed stress than the initial shear stress on F2 and F3, which are thus stabilized during injection. Combined with pore pressure, poroelastic stressing triggers the reactivation of F1, with the decrease of normal stress and the increase of the shear stress (e). Subsequently, F1 is stabilized by the shear stress drop (c and f). After the stop of injection, the pore pressure front continues to diffuse, while poroelastic stress relaxes (c). This change of direction leads to the increase of shear stress at the previously stabilized F2 and F3, which reach the failure envelope (f). The shear-slip stress transfer due to the reactivation of F2 affects F3, emphasizing the poroelastic effects until reaching failure.

This novel analysis of the induced seismicity at Basel provides a substantial step forward in the general understanding of the physical processes that induce seismicity in the context of EGS hydraulic stimulation. Fault failures occurring during and after injection are located close to the well and farther away in the reservoir, respectively. Pore pressure diffusion and poromechanical stress combined are the main triggering mechanisms during injection. Poromechanical effects extend farther and faster than pressure diffusion during injection (Figure 4.8b). Furthermore, poroelastic stresses, depending on fault orientation with respect to the injection well, stabilize or destabilize faults during injection, and cause the opposite effect after the stop of injection as they rapidly diminish with pore pressure drop. After the stop of injection, pore pressure continues to advance further, leading to pore pressure increase far away from the well, which may induce some seismic events. Shear-slip stress transfer becomes dominant after the stop of injection, especially in faults far away from the injection well (Figure 4.8c). In brittle rock, like the crystalline rock that is the target of most EGS projects, faults may present a slip-weakening friction, which may enhance the magnitude and frequency of induced seismic events (Kirkpatrick & Shipton, 2009). An analysis of the real-time monitored seismicity could allow calibrating the actual friction angle of the reactivated faults to improve the accuracy of the predictions of the reservoir stability. This improved understanding of the causal mechanisms of induced seismicity in EGS will contribute to have a better forecasting capability of induced seismicity and to come up with stimulation protocols that mitigate induced earthquakes, which are key points for the widespread development and management of geothermal projects.

Chapter 5: Forecasting fluid-injection induced seismicity to choose the best injection strategy for safety and efficiency

5.1. Introduction

Low-carbon emission geo-applications are a major instrument in the reduction of carbon emissions to reach the 2050-IPCC goals (IPCC, 2023). Current investigations focus on the development of geological carbon and hydrogen storage and geothermal energy projects. The principal obstacles to these applications reside in the hydraulic constrains of the geological reservoir and subsequent induced seismicity. Fluid injection and extraction disturb the effective stress field in the subsurface, leading to the reactivation of pre-existing faults and to the creation of new ones. Each geo-energy application has its characteristics and limitations, depending on the thermal and geochemical interactions between the injected fluid, the rock and the fluids initially present in the rock. Enhanced geothermal systems (EGS) aim to produce electricity by exploiting the heat from the deep and hot crystalline basement. Because of the low permeability of the rock, the reservoirs are engineered to enhance the permeability of the natural fractures, in order to improve fluid circulation between the injection and the production wells, via hydraulic or acid stimulations (Tester et al., 2007). This technology has been developed since the 1980s in many locations in the world (Buijze et al., 2019; Evans et al., 2012; Majer et al., 2007; Pine & Batchelor, 1984; Zang et al., 2014). Yet, economic viability and public perception hinder the exploitation of new EGS projects. Induced seismicity is expected during hydraulic stimulation and production, with a magnitude generally lower than $M_w < 2$. Nevertheless, larger magnitude induced seismicity has been felt by local population in different cases of EGS. Probably the most controversial and studied case is the Basel Deep Heat Mining project in Switzerland, 2006, where after only 6 days of injection (11570 m^3 of water at 4630-m depth), the magnitude of the induced seismicity reached the threshold of the Traffic Light System ($M_w 2.3$). The injection was consequently stopped, but 5 hours later the largest magnitude earthquake occurred ($M_l 3.4 - M_w 2.9$) and led to the decision of bleeding-off the well (Häring et al., 2008). Perceivable induced seismicity kept occurring for months after the cancellation of the project. The recent case of Pohang EGS, South Korea, in 2017 further questioned the safety of EGS in urban areas. A $M_w 5.4$ earthquake occurred two months after the stop of injection and caused damages in the surrounding urban areas, leading to the cancelation of the project (Ellsworth et al., 2019; Grigoli et al., 2018; Kim et al., 2018). More recently, in 2021, a $M_l 3.9$ earthquake occurred six months after the stop of a circulation test in Vendenheim, France, and led to the cancellation of the EGS project (Fiori et al., 2023; Lengliné et al., 2023; Schmittbuhl et al., 2022).

The triggering mechanisms of induced seismicity are difficult to apprehend and their coupling make it difficult to model and forecast (Ellsworth, 2013; Ge & Saar, 2022; Majer et al., 2007).

Fluid injection increases the pressure in the reservoir, which induces poromechanical deformations and stress changes. These pressure-driven processes affect the hydro-mechanical properties of the rock and faults. Fault reactivation and fracture propagation modify the permeability of the rock, consequently affecting the fluid flow. Fault slips, which can be aseismic or seismic, can also further destabilize the reservoir due to processes of static stress transfer (Cornet, 2012; Guglielmi et al., 2015a; Wei et al., 2015). These triggering mechanisms continue to occur after the stop of injection. Pressure-driven processes continue to diffuse for a long duration, while poroelasticity and static stress transfer rather continue to occur for a shorter time scale.

Because all these processes are initiated by fluid injection, they are affected by the injection protocol, which can vary in terms of applied pressure, injection rate and duration. New strategies are investigated in order to mitigate the frequency and magnitude of earthquake nucleation. For example, cyclic injection is currently seen as a promising solution to enhance the permeability of EGS reservoirs while controlling the seismicity based on the concept of fatigue hydraulic fracturing, as shown by numerical studies (Yoon et al., 2014, 2015), validated in rock laboratory experiments (Ji, Fang, et al., 2021; Ji, Yoon, et al., 2021; Zhu et al., 2021). On the contrary, Noël et al. (2019) showed that the stable slip from a displacement-driven fault can become unstable and induce seismicity also during cyclic injection. Cyclic injection was also applied during the EGS projects of Pohang, South Korea, (Hofmann et al., 2019) and of Helsinki, Finland (Kwiatek et al., 2019). In the Pohang EGS, the co-injection magnitude threshold of $M_w 2.0$ was never reached, but the largest magnitude ($M_w 5.4$) earthquake ever induced in a EGS occurred two months after the stop of the fifth stimulation (Ellsworth et al., 2019; Grigoli et al., 2018; Kim et al., 2018). The Helsinki EGS project also successfully controlled the induced seismicity under the magnitude threshold set by the local authorities, but permeability enhancement was insufficient (Kwiatek et al., 2019). Hydraulic fatigue in cyclic injection is also considered as a mitigation injection strategy, by inducing microcracks to avoid large failures (Zang et al., 2019, 2023). Strategies for stopping injection are also investigated in the perspective of controlling the post-injection induced seismicity that occasionally occurs with larger magnitude than the co-injection seismicity. For example, progressive stop of injection have been proposed to mitigate the post-injection induced seismicity (Alghannam & Juanes, 2020; McClure & Horne, 2011). Effectively, a progressive decrease of injection lessens the effects of pore pressure changes and mitigate the destabilizations of early-post-injection stage (Boyet et al., 2023a).

Currently, numerical models are developed to understand, simulate and forecast fluid-injection induced seismicity. Numerical models, also called physics-based models, are the best tool to solve coupled problems of pressure-driven, thermal, geochemical and geomechanical processes due to fluid injection and extraction on the subsurface. These models require a characterization of the

reservoir, including rock properties, in-situ pressure and stress conditions, and geological settings, which are difficult data to measure. Analytical and statistical models fill the lack of data by applying different statistical laws on the observed problems. Many statistical models have been developed to forecast seismicity (e.g., Broccardo et al. 2017, Ritz et al., 2023, Shapiro et al., 2007, 2010). For instance, the Seismogenic Index forecasts the induced seismicity rate mainly as a function of the injected volume (Mignan et al., 2017, 2021). Hybrid models actually combine physics-based models with statistical laws to develop robust tools to forecast induced seismicity. Different methodologies have been proposed, building on seed models (e.g., Clasen Repolles et al., 2023; Dempsey & Riffault, 2019; Goertz-Allmann & Wiemer, 2013), or based on discrete faulting models (e.g., Karvounis & Wiemer, 2022; Luu et al., 2022). All models have their strengths and weaknesses: seed models have the advantage of providing fast computations but they lack of representation of the physical and mechanical processes, while discrete models solve more complex problems, but with a too high computational cost to be used as an efficient forecasting tool.

In this chapter, we propose a hybrid methodology based on a hydro-mechanical model of a discrete fault network associated to a seismicity rate model and statistical seismological laws. We apply the methodology to the case of the Deep Heat Mining Project in Basel, Switzerland. Induced seismicity in Basel EGS has been intensively studied in the last two decades. Seismic interpretations provide a rich and accurate catalogue of earthquakes (Deichmann et al., 2014; Herrmann et al., 2019; Kraft & Deichmann, 2014). Pore pressure build-up was suggested as the triggering mechanism of the induced seismicity due to the short-duration injection, but this assumption is insufficient to explain the nucleation of earthquakes far from the injection well and shortly after the stop of injection (Bachmann et al., 2012; Terakawa, 2014). Mukuhira et al. (2017) explained this far post-injection seismicity to be induced by means of the homogenisation of pore pressure build-up along a large fault when the injection was stopped. The diffusion of the pore pressure would have reached the critical pressure along the fault plane. Moreover, the triggering effects of static stress transfer due to nucleation stress drop was measured and defined as partly triggering the post-injection induced seismicity (Catalli et al., 2013, 2016). This latter study proposed a decoupling of a hydraulic model with the stress drop calculation. A few coupled models with discrete faults propose more convincing explanations concerning the fluid-injection effects on the induced seismicity in Basel EGS. Andrés et al. (2019b) provided a thermo-hydro-mechanical model of one large discrete fault and Boyet et al. (2023b) used a hydro-mechanical model to study the reactivation of a fault network. The post-injection induced seismicity at Basel can be reproduced by the combination of the poroelastic relaxation due to the shut-in of injection with the static stress transfer of reactivating faults (Boyet et al., 2023b). In this study, we adopt the same physics-based model of Boyet et al. (2023b) to analyse the response to different injection

strategies and to forecast the best strategy in term of permeability enhancement and inducing seismicity.

5.2. Hybrid method to forecast induced seismicity

The hybrid method is based on the combination of a hydro-mechanical model of a discrete fault network with a seismicity rate model (Figure 5.1). The seismicity rate estimates the number of mainshocks occurring during the simulation, as a function of the Coulomb stressing rate calculated in the hydro-mechanical model. Their magnitude and their aftershocks sequence are then respectively estimated by the Gutenberg-Richer law (GR) (Gutenberg & Richter, 1942) and the Epidemic Type Aftershock Sequence (ETAS) model (Y. Ogata, 1988).

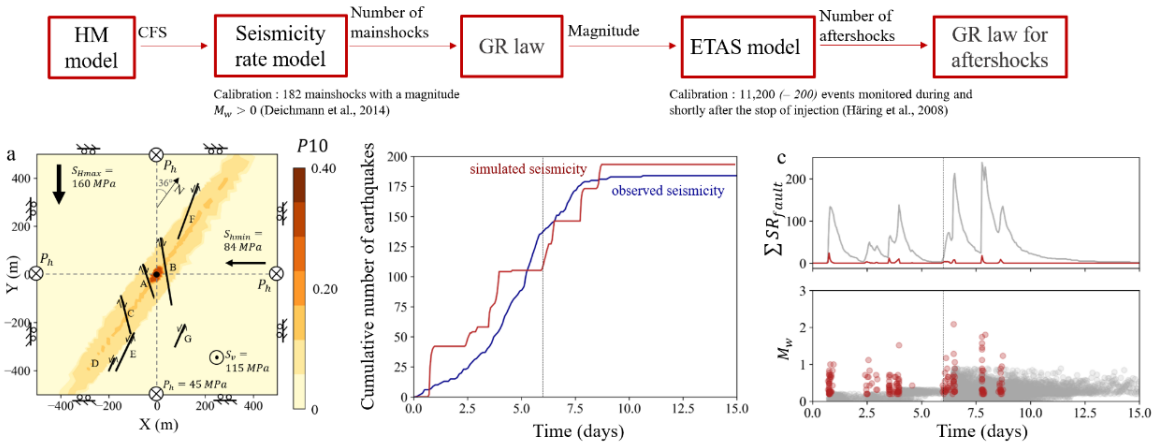

Figure 5.1: Hybrid methodology: The CFS outputted from the hydro-mechanical (HM) model is the main input of the seismicity rate model. The Gutenberg-Richter law and the ETAS model estimate the magnitude and the aftershock-sequence of the mainshocks. (a) Hydro-mechanical model with the fault network. Note that the x- and y-axes are not aligned with the north but with the principal stresses. The injection well is represented by the black dot in the centre. Colours refer to the probability of hosting a fracture, which is equal to 1 on faults A to G. (b) Temporal evolution of cumulative number of observed mainshocks from the catalogue of Deichmann et al. (2014) (blue line) and of simulated mainshocks in the injection scenario used for calibration, which reproduces the operations at Basel (injection during 6 days followed by 5-hour shut-in and a bleed-off until the end) (red line). (c) Time evolution of number of mainshocks (red) and aftershocks (grey); and time evolution of the magnitude of seismic events in the domain during the calibration injection case.

5.2.1. Hydro-mechanical model

The hydro-mechanical problem is solved by means of the Finite Element Method simulator CODE_BRIGHT (Olivella et al., 1996) with the adoption of a continuum approach. The model of this study is limited to two dimensions due to the complexity of the discrete fault network and to the computation time. The hydro-mechanical problem is solved in a fully coupled way, solving the momentum balance and the water mass balance simultaneously. The former reads

$$\nabla \cdot \boldsymbol{\sigma} + \mathbf{b} = \mathbf{0}\,, \qquad (5.1)$$

where **σ** is the stress tensor and **b** is the vector of body forces. The latter is expressed as

$$\phi\beta\frac{\partial P}{\partial t}+\frac{\partial}{\partial \mathrm{t}}\varepsilon_v+\nabla\cdot\mathbf{q}=f^w\,, \qquad (5.2)$$

where ϕ is the rock porosity, β is water compressibility, P is water pressure, ε_v represents the volumetric strain, t is time and f^w is an external supply of water. **q** is the water volumetric flux and is expressed by Darcy's law

$$\mathbf{q}=-\frac{k}{\gamma}(\nabla P-\rho\mathbf{g})\,, \qquad (5.3)$$

where γ and ρ are water viscosity and density, respectively, **g** is the gravity vector and $k=k_o\frac{\phi^3}{(1-\phi)^2}\frac{(1-\phi_o)^2}{{\phi_o}^3}$ is the rock intrinsic permeability calculated by the Kozeny's model, with k_o and ϕ_o being respectively the reference values for intrinsic permeability and porosity of the rock matrix. The permeability of the matrix is assumed as isotropic. The coupling of the governing equations (1) and (2) is expressed through the elastic constitutive law of the matrix

$$\Delta\boldsymbol{\sigma}=K\varepsilon_v\,\mathbf{I}+2G\left(\boldsymbol{\varepsilon}-\frac{\varepsilon_v}{3}\mathbf{I}\right)-\Delta P\mathbf{I}\,, \qquad (5.4)$$

where $K=E/[3(1-2\nu)]$ is the rock bulk modulus, $G=E/[2(1+\nu)]$ is the shear modulus, E is Young's modulus, ν is Poisson's ratio, **ε** is the strain tensor and **I** is the identity matrix. Note that the volumetric strain ε_v is the first invariant of the strain tensor, i.e., $\varepsilon_v=\mathrm{tr}(\boldsymbol{\varepsilon})$. The effective stress law is enclosed in Eq. (5.4) with Biot coefficient equal to 1.

Discrete faults are represented by finite-thickness elements following the "embedded model" proposed by Olivella and Alonso (2008). In this model, faults are defined by their aperture embedded in a continuous finite element composed of rock matrix. The permeability of the faults varies as a function of deformation. Fault aperture changes are computed from the volumetric strain of the fault elements and permeability variation is proportional to the square of the fault aperture change based on the cubic law. Fault elements are subject to the visco-plastic constitutive law

$$\frac{d\varepsilon_p}{dt}=\Gamma\langle\Phi(F)\rangle\frac{\partial\xi}{\partial\sigma}\,, \qquad (5.5)$$

where ε_p is the visco-plastic strain and Γ is the fluidity, a parameter of the deformation of the medium, set at 1.00E-4 $MPa^{-m}\,s^{-1}$. ξ is the flow rule, which reads

$$\xi=\alpha\cdot\sigma_m\cdot\sin\psi+\left(\cos\theta-\frac{1}{\sqrt{3}}sin\theta\cdot\sin\psi\right)\cdot\sqrt{J_2}-c\cdot\cos\psi, \qquad (5.6)$$

where α is a parameter for the plastic potential, set at 1, ψ is the dilatancy angle, set as 3°. σ_m, the mean stress, J_2 and θ, Lode's angle, are invariants of the deviatoric stress tensor. c is the cohesion, in our model equal to 0 MPa. $\Phi(F)$ is the overstress function

$$\Phi(F) = \begin{cases} 0, & if\ F \leq 0 \\ F^m, & if\ F > 0 \end{cases}, \quad (5.7)$$

where m is a constant power to define the overstress function and is set to be equal to 3 in the model. F is the yield function, which is defined as

$$F = \sigma_m \cdot \sin\varphi(\eta) + \left(\cos\theta - \frac{1}{\sqrt{3}} sin\theta \cdot \sin\varphi\right) \cdot \sqrt{J_2} - c \cdot cos\varphi \quad (5.8)$$

with φ the friction angle, calibrated for each fault to reproduce the timing of reactivation. The deformation of the fault element is elastic until the stresses reach the shear yield surface, $F = 0$. During the elastic regime, a constitutive law similar to Eq. (5.4) holds. When the yield surface is exceeded, the fault element deforms irreversibly according to the visco-plastic behaviour described in Eqs. (5.5)-(5.8), but stresses can remain beyond the yield surface for a range determined by the overstress function. The permeability enhancement mostly occurs when the fault element deforms plastically.

In this hydro-mechanical model, the effects of pressure-driven processes, i.e., pressure build-up and poroelasticity, are combined with the static stress transfer due to fault reactivation. To measure the mechanical stability of discrete faults, the Coulomb Failure Stress (CFS) is calculated as

$$CFS = \tau - \sigma_n' \times \mu + c, \quad (5.9)$$

where τ and σ_n' are the shear and normal effective stress acting on the fault, respectively. μ is the friction coefficient ($\mu = \tan\varphi$) and c is the cohesion. The Coulomb Failure Stress of the elements CFS_p are the main inputs of the seismicity rate model.

5.2.2. Seismicity rate model

The seismicity rate is estimated by the rate-and-state friction model, which is based on the theory of earthquake nucleation (Dieterich, 1994; Meyer et al., 2023; Scholz, 1998, 2002). The friction of a fault depends on the slip rate and on the state variable of re-strengthening of the fault after a slip. Unstable and seismic slip occurs on faults with rate-weakening properties when the shear strength reduces fast (Dieterich, 1978; Marone, 1998; Ruina, 1983; Scholz, 1998).

The number of mainshocks that are likely induced by stress variations is expressed by the relative seismicity rate R (Dieterich, 1994; Segall & Lu, 2015)

$$\frac{dR}{dt} = \frac{R}{t_c}\left(\frac{\dot{\tau}}{\dot{\tau_0}} - R\right), \quad (5.10)$$

where the stressing rate is $\dot{\tau} = \frac{dCFS}{dt}$ and $\dot{\tau_0}$ is the initial stressing rate. $t_c = A\sigma/\dot{\tau_0}$ is the characteristic relaxation time. $A\sigma$ is a free parameter calibrated to reproduce the total number of monitored mainshocks, or expected in a region of fluid injection. The ordinary differential equation (5.10) is solved using a fifth-order adaptive time step Runge-Kutta-Fehlberg algorithm through the BRUCES tool (Luu, 2022; Luu et al., 2022). The absolute seismicity rate SR (the number of independent earthquakes in a certain time window) is then calculated as a function of the relative seismicity rate R and the background seismicity rate r_0 (Table 5.1) as

$$SR = R \times r_0 . \quad (5.11)$$

The Coulomb failure stress CFS is calculated for each element of the mesh according to equation (9). The number of independent earthquakes for each mesh element, SR_{elem}, is estimated by multiplying the seismicity rate based on CFS by the surface area of the element S_{elem} and by the probability that the element hosts a portion of fracture, $p_{f_{elem}}$, such as

$$SR_{elem} = SR(CFS_{elem}) \times S_{elem} \times p_{f_{elem}} \quad (5.12)$$

We assume $p_{f_{elem}} = 1$ for the fault elements. Because the matrix elements cannot be considered as important as the fault elements in the estimation of the seismicity rate of the domain SR_{dom} (matrix and fault elements), we define $p_{f_{elem}} = p_f \cdot \frac{S}{S_{max}}$ where p_f is the probability of having a fracture in a square meter and S_{max} is the surface area of the largest element in the mesh, equal to 10,300 m^2.

The seismicity rate of a fault SR_{fault} is the sum of the SR_{elem} of the elements of the faults. We measure the evolution of $\sum SR_{fault}$ to compare the seismicity rate of the discrete faulting domain of the three injection protocols (see Section 5.4, Figure 5.2a). We consider the seismicity rate of the whole domain SR_{dom} when forecasting seismicity in the 2 dimensions, corresponding to the sum of the seismicity rate of all the elements of the model (faults and matrix) (see Section 5.5).

5.2.3. Magnitude attribution with Gutenberg-Richter law

Once the seismicity rate, i.e., the number of earthquakes for a period of time, is estimated, we use the Gutenberg-Richter (G-R) law to relate the earthquake frequency to the magnitude. The G-R law can be used to attribute magnitude to each forecasted earthquake (Gutenberg & Richter, 1942; Navas-Portella et al., 2020). For a specific location, it forecasts the number of earthquakes N with a magnitude greater than or equal to M according to

$$log\, N\,(M) = a - b \cdot M, \quad (5.13)$$

where a and b are constants. We adopt this stochastic law for both the mainshock and the aftershocks. We first derive a and b from the observed seismic catalogues of the study case for both co-injection and post-injection stages (Table 5.1). The magnitude of the aftershocks, estimated by the ETAS model, is also attributed with the G-R law with the maximum magnitude of the aftershock sequence set as $M = M_i - 1.2$, where M_i is the mainshock magnitude (Båth, 1965). Note that a and b are typically different in the injection and post-injection stages (Bachmann et al., 2011; Ruiz-Barajas et al., 2017).

5.2.4. The Epidemic Type Aftershock Sequence model

The seismicity rate model only forecasts mainshocks, i.e., independent earthquakes. To better forecast fluid-injection induced seismicity, we adopt the Epidemic Type Aftershock Sequence (ETAS) model based on the Omori law (Omori, 1895; Utsu, 1961). The ETAS model estimates the aftershocks sequence associated to each mainshock of magnitude M_i, i.e., the number of aftershocks per unit of time as (Y. Ogata, 1988)

$$\lambda(t) = \frac{K_{As}}{(c_{As}+t-t_i)^{p_{As}}}\ 10^{\alpha_{As}(M_i - M_{min})}\ , \qquad (5.14)$$

where c_{As} is an empirical constant and p_{As} is the power of the Omori law, while K_{As} and α_{As} are describing parameters of the seismic sequence (Table 5.1). Note that this procedure does not include any spatial reference for the forecasted aftershocks, aftershocks are forecasted at the centre of the host element, same location as the mainshock.

5.3. Calibration and application of the hybrid method to the case of the Basel EGS

The hydro-mechanical model is designed to reproduce the fault reactivation due to fluid injection at the Basel EGS. The geometry, hydraulic and mechanical properties of the model have been defined in a previous study whose aim was to understand the triggering mechanisms of each fault reactivation, with special emphasis on the post-injection induced seismicity (Boyet et al., 2023b). The domain consists of a 7-fault network which is based on the cluster characterisation of the monitored seismicity proposed by Deichmann et al. (2014). The reproduction of the reactivation of the faults is modelled on a 2D horizontal domain acknowledging that most of the focal mechanisms exhibit strike-slip movement on faults with vertical dip (Figure *5.1*a). The location and orientation of the faults were chosen accordingly to the orientation of the focal mechanisms and the location of the cluster swarms. Mechanical properties of the subsurface and of the initial stress conditions were inferred from different studies of the Basel EGS and/or from a calibration process (Table 5.2) (Bachmann et al., 2011; Häring et al., 2008; Herrmann et al., 2019; Mukuhira et al., 2013). The calibration is based on a simulation reproducing the injection and well pressure

response in the Basel EGS project, which lasts 6 days, followed by a 5-hour shut-in and a bleed-off for the rest of the simulation, which we stop at day 15 (Figure 5.1b and 1c, Table 5.1).

The initial stressing rate $\dot{\tau_0}$ is a parameter difficult to estimate, here set it from an estimation made for the case of the EGS of Soultz-Sous-Forêts (Hossein Hakimhashemi et al., 2014). The free parameter $A\sigma$ of the seismicity rate model is calibrated for each fault in order to reproduce the cumulative number of monitored earthquakes constituting the cluster used to design each fault, in total 185 mainshocks with magnitude $M_w > 0$ that were monitored during and after the hydraulic stimulation (Deichmann et al., 2014). To assign a magnitude to the forecasted earthquakes, a and b parameters of the G-R law are assumed as estimated by Bachmann et al. (2011) (Table 5.1). Bachmann et al. (2011) also confirmed that the Basel sequence follows the Omori law and used the ETAS model in order to forecast the lasting of the sequence, and we use the same values. The free parameter K_{As} of the ETAS model is calibrated in order to estimate a total number of earthquakes (mainshock and aftershocks) equal to 11,200 events, as monitored during and shortly after the stop of injection at Basel (Häring et al., 2008). Once all the parameters of the seismic and hydro-mechanical models are calibrated, the hybrid model is applied to forecast the seismicity under different protocols of injection.

Table 5.1: Parameters of the seismic models, with values for natural earthquakes and for the case of Basel EGS project. Bold values are calibrated so that the models reproduce the monitored number of mainshocks (185 earthquakes with a magnitude $M_w > 0$ (Deichmann et al., 2014)) and the total number of monitored earthquakes (11,200 events during and shortly after the stop of injection (Häring et al., 2008)).

Parameters	Natural earthquakes	References	Basel EGS	References
Seismicity rate model				
$\dot{\tau_0}$ (MPa/yr)	Background stressing rate		$\mathbf{3 \times 10^{-6}}$	10^{-7} for Soultz-Sous-Forêts (Hossein Hakimhashemi et al., 2014)
$A\sigma$ (MPa)	Free parameter		$\mathbf{0.09 - 0.25}$	calibrated for each fault
r_0 (events/yr)	Background seismicity rate		0.123	(Bachmann et al., 2011)
Gutenberg-Richter law				
a			$a_{co} = 6.08$, $a_{post} = 3.32$	(Bachmann et al., 2011)
b	1	(Wiemer & Wyss, 2002)	$b_{co} = 1.57$, $b_{post} = 1.14$	(Bachmann et al., 2011)
M_w	Minimum value similar as the monitored		$[\mathbf{0}; \mathbf{3}]$	
ETAS model				
K_{as}	Free parameter		$\mathbf{0.035}$	
c_{as}	$0.003 - 1.1$	(Y. Ogata, 1992)	0.38 ± 0.06	(Bachmann et al., 2011)
p_{as}	$0.9 - 1.9$	(Y. Ogata, 1992)	1.33 ± 0.06	(Bachmann et al., 2011)
α_{as}	$0.3 - 3.1$	(Y. Ogata, 1992)	0.8 ± 0.06	(Bachmann et al., 2011)

Table 5.2: Material properties of matrix and fault elements of the hydro-mechanical model (Boyet et al., 2023b)

Parameters	Matrix	Fault element
Porosity, ϕ (-)	0.01	0.1
Permeability, k (m^2)	7.50×10^{-17}	2.30×10^{-13}
Young's modulus, E (GPa)	52	43
Poisson's ratio, ν (-)	0.25	0.25
Cohesion	0	0
Friction coefficient	0.6	0.35-0.58 (from calibration of reactivation)

5.4. Effects of different injection protocols on the stability of discrete faults

We simulate three injection protocols in the hydro-mechanical model of Basel EGS, which is successively linked to the seismic models through the CFS parameter. We use a progressive step-rate injection during 6 days, similar to the measured pressure at the injection wellhead of Basel EGS, but followed by a 5-hour shut-in and then a bleed-off, to calibrate the models. Then, using the calibrated parameters (Table 5.1) and properties (Table 5.2), we simulate a progressive step-rate injection, a constant injection and a cyclic injection followed by simple shut-in (Figure 5.2a). To systematically compare the enhancement of permeability of faults and the induced seismicity of the three protocols, the same total volume of water is injected and the maximum applied pressure is set at 75 MPa, as the monitored maximum wellhead pressure in Basel EGS. For the constant injection, the applied pressure is set at 75 MPa and lasts 4.5 days. The cyclic injection is based on the cyclic soft injection protocol that was applied at Pohang EGS (Hofmann et al., 2019), considering the long-term cycle of one day with 6 medium-term cycles per day. The maximum applied pressure is 75 MPa and the stimulation lasts 8 days (Figure 5.2a, note that the simulated pressure is plotted, not the one applied at the injection well in the hydro-mechanical model).

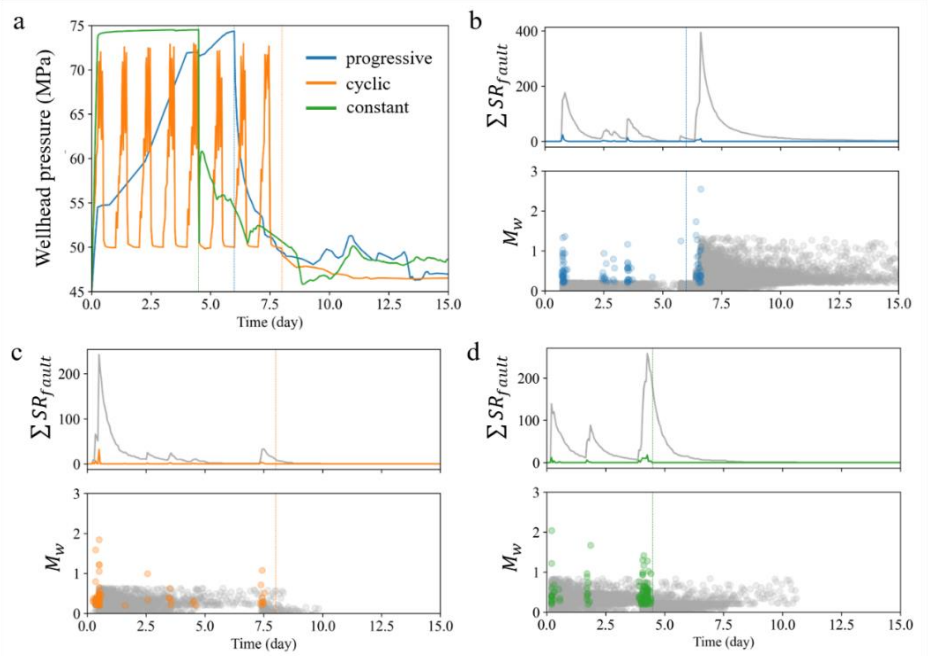

Figure 5.2: (a) Simulated wellhead pressure for the different injection protocols in the hydro-mechanical model. (b), (c) and (d) show, on top, the forecasted seismicity rate in the domain $\sum SR_{fault}$ through time, and on the bottom, the estimated magnitude M_w of the forecasted earthquakes for the progressive, cyclic and constant injection protocols, respectively. The mainshock seismicity rate and earthquakes follow the same colour code that in figure (a), while the aftershocks are in grey. Vertical lines correspond to the stop of the injections.

5.4.1. Permeability enhancement

As previously introduced, the aim of the hydraulic stimulation in EGS projects is to enhance the permeability of pre-existing fractures and faults in low-permeability rock. The permeability enhancement is mostly observed when faults reach shear failure conditions (Figure 5.3a). The permeability of Faults A, B and C increases for the three injection protocols. The permeability of farther faults (E and F) is enhanced only with the constant and the progressive injections, and the one of Fault G only with the constant injection. The faults that are reactivated with the constant and progressive are not significantly pressurized during injection, which implies that poroelastic stress and static stress transfer are dominant triggering mechanisms of these distant faults. The effects of cyclic injection are limited to the faults in the vicinity of the injection well. In this protocol, the pressure build-up and consequent mechanisms are insufficient to activate shear failure on the distant faults (Figure 5.4). Therefore, the constant and the progressive injection protocols similarly enhance the permeability of the discrete faults, while the cyclic protocol leads to a limited permeability enhancement. The delay in fault permeability enhancement of approximatively two days between the constant and progressive protocols is due to the time difference in the diffusion of the pressure sufficient to enhance permeability of faults in the domain – the progressive injection injects at low pressures at early times. Interestingly, the

reactivation and permeability enhancement of Fault F during progressive injection is the unique reactivation that occurs after the stop of injection in all the cases.

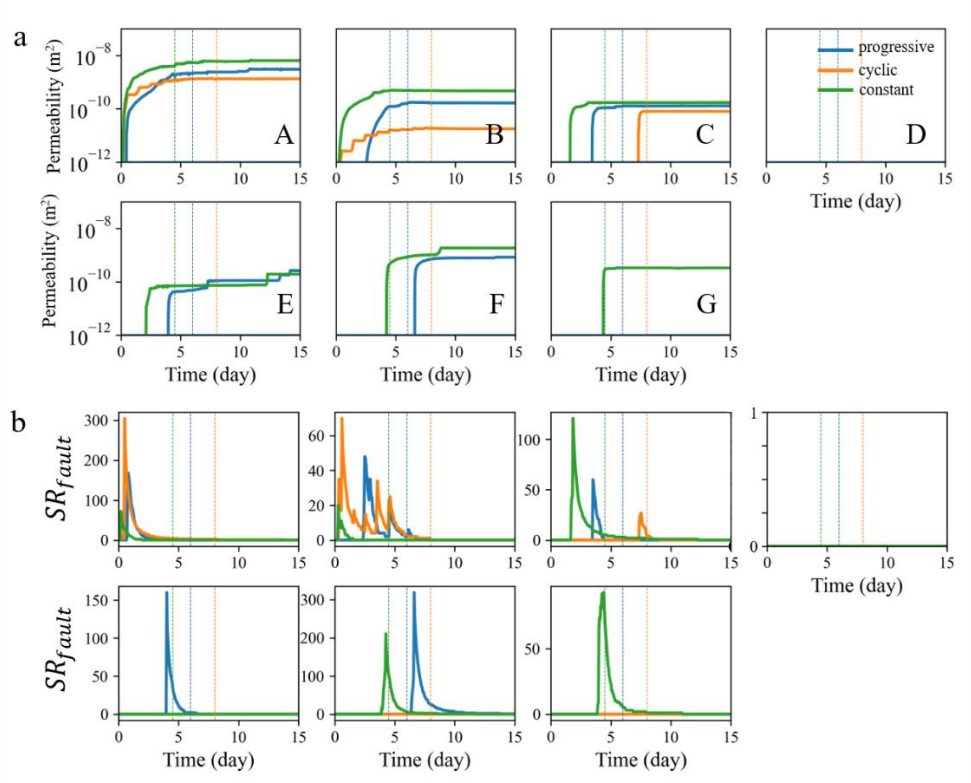

Figure 5.3: (a) Evolution of the permeability of the faults outputted from the hydro-mechanical model. The permeability varies when the fault fails is shear mode. (b) Seismicity rate of each fault, SR_{fault}, through time for each of the injection strategies. Although some faults reach failure conditions in the hydro-mechanical model, their CFS is too low to forecast the reactivation of the faults as seismic according to the calibrated seismicity rate model. Vertical lines correspond to the stop of the injections.

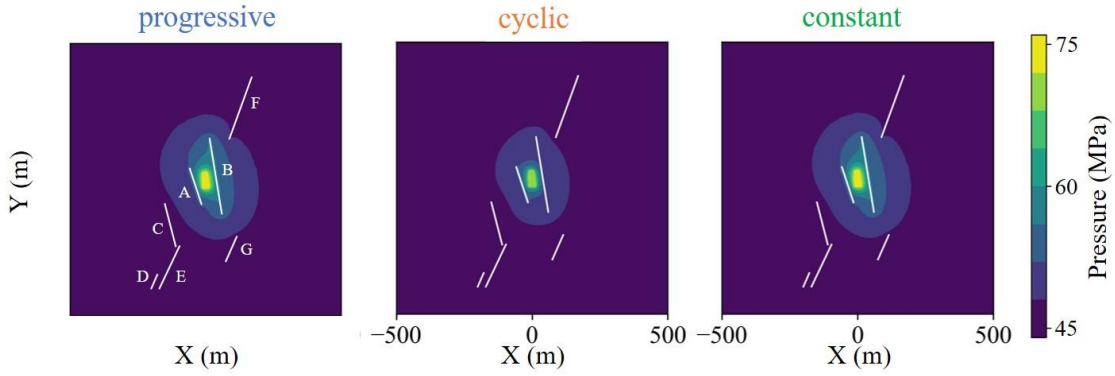

Figure 5.4: Pressure at the stop of injection for each strategy (day 6 for progressive injection, day 7.5 for cyclic injection (peak of injection of the last long-term cycle) and day 4.5 for constant injection) in the domain, outputted from the hydro-mechanical model.

5.4.2. Forecasted seismicity

The hybrid method based on the hydro-mechanical simulations forecasts the mainshocks and aftershocks for the three injections. The progressive injection is the one inducing the most mainshocks, due to the reactivation of the Faults A, B, C, E and F. Fault F reactivation occurs after the stop of injection and translates into a large peak of the seismicity rate of the faults $\sum SR_{fault}$ for the case of the progressive injection. Constant injection, which reactivates similar faults (A, B, C, F and G) during injection than the progressive injection, has nonetheless smaller peaks of the seismicity rate SR_{fault} for most faults (Figure 5.2b and 2d, and Figure 5.3b). Cyclic injection induces the largest peak of the seismicity rate of the faults $\sum SR_{fault}$ at the start of the stimulation, when Faults A and B reactivate simultaneously, and their permeability is enhanced (Figure 5.2c and Figure 5.3b).

In our simulations, the magnitude of forecasted seismic events does not reach the magnitude of the monitored seismicity of Basel EGS. Nonetheless, the trend of the magnitude of the events in the progressive injection is similar to Basel EGS, with the largest event occurring after the stop of injection (Figure 5.2b). The seismicity rate indicates in all cases the destabilization of the reservoir. The constant and cyclic protocols induce seismicity from the start of injection, while the onset of seismicity in the progressive injection is delayed for a few hours (Figure 5.2 and Figure 5.5a). Despite the progressive injection presents the largest total number of mainshocks (progressive: 147, cyclic: 64 and constant: 111 mainshocks), its cumulative seismic moment is the lowest, presenting steps caused by the different timings of fault reactivations (Figure 5.5a). Interestingly, the cumulative seismic moment at the end of the stimulation is similar for the cyclic and constant injections (Figure 5.5a), but the permeability enhancement is much lower in the cyclic than in the constant injection (Figure 5.3a). It is worth noting that there is no correlation between the injected volume and the forecasted magnitude, and that the maximum magnitude M_{max} is induced towards the beginning of injection in the three protocols (Figure 5.5b). This result contradicts relationships that estimate the maximum expected magnitude as a function of the injected volume (e.g., McGarr, 2014) and highlights the importance of triggering mechanisms other than pore pressure changes (Boyet et al., 2023b; Vilarrasa et al., 2021).

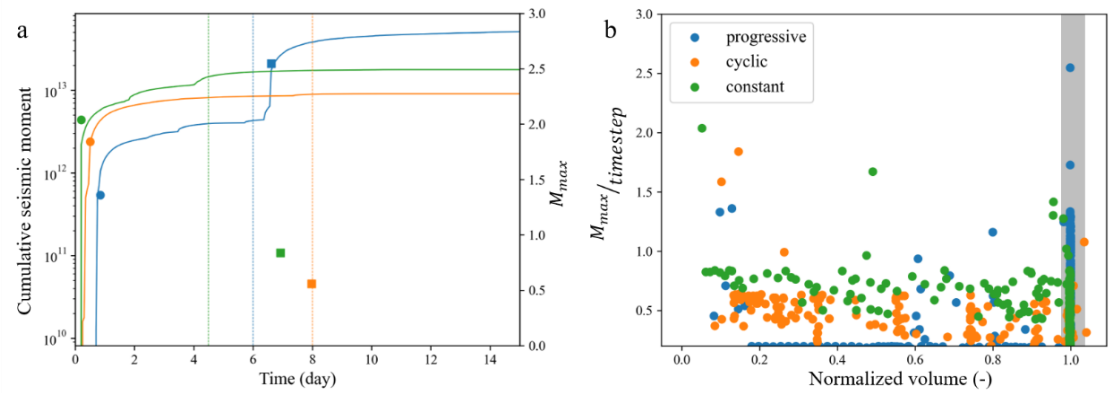

Figure 5.5: (a) Cumulative seismic moment $M_o = 10^{1.5M_w+6.07}$ (Kanamori & Brodsky, 2004) of the forecasted earthquakes (lines) and maximum magnitude M_{max} for both co-injection (circle) and post-injection (square) stages. Vertical lines correspond to the stop of injections. (b) Maximum earthquake magnitude as a function on the normalized injected volume for each timestep. The grey band corresponds to the time after the stop of injection.

As far as post-injection seismicity is concerned, the progressive injection strategy induces the largest magnitude earthquake at the stop of injection, as it was the case of the Basel EGS (Figure 5.2b and Figure 5.5a). This large event is due to the reactivation and permeability enhancement of Fault F. Cyclic and constant injections do not induce mainshocks after the stop of injection, but the co-injection largest magnitude earthquake occurs at the beginning of the stimulation with similar magnitude to that of the progressive post-injection earthquake (Figure 5.5a). The mainshocks forecasted after the end of injection in the progressive injection lead to a significant aftershock sequence.

To sum up, different protocols injecting the same volume of water show different responses of the subsurface. Cyclic injection is very limited enhancing fault permeability. Progressive injection delays seismicity and accumulates stresses at the faults that induce larger stress drops, inducing larger peaks of SR_{fault} and $\sum SR_{fault}$, meaning larger risk of high-magnitude earthquake nucleation. Progressive injection is also the only scenario with post-injection simulated mainshocks. The best strategy seems to be the constant injection, which reactivates the faults from its start, enhancing permeability in most faults, and that limits the post-injection seismicity on pre-existing faults.

5.5. Spatially forecasting the seismicity

The proposed hybrid methodology can be used to spatially forecast the seismicity rate in the whole domain SR_{dom}, including the matrix elements (Figure 5.6). For the matrix, we set $A\sigma$ equal to 0.25, the largest value for the fault calibration. We assume a spatial distribution of the probability of having a fracture in a square meter, p_f, in order to better represent the presence of conjugate fractures in the vicinity of the well (Mukuhira et al., 2013). We consider $p_f = u \times P21$, where $u = 3 \times 10^{-6}$ in order to calibrate the forecast of more or less 50 mainshocks in the matrix

elements. $P21$ is the areal fracture intensity, which expresses the length of fracture traces per unit area (Dershowitz & Herda, 1992). $P21$ is estimated by field observations of the linear fracture intensity, expressed by the number of fracture traces per unit length $P10$. Because the mean length of fracture traces is equal to the borehole diameter divided by the cosine of the fracture dip, 70° in the study case of Basel EGS, the real fracture intensity is

$$P21 = P10\ /cos(70°). \qquad (5.15)$$

For Basel EGS, values of $P10_{low} = 0.25$ m^{-1} and $P10_{high} = 0.95$ m^{-1} have been estimated for the least and the most intensely fractured zones, respectively (Häring et al., 2008). However, we set $P10$ of the matrix elements between 0.10 and 0.25 m^{-1} to forecast a coherent number of mainshocks, less than 250 mainshocks in total, in both fault and matrix elements (Figure 5.1a). In order to estimate the Coulomb Failure Stress rate of the matrix elements, we randomly assign to each of the mesh elements a fracture orientation of N160 or N40, which correspond to the main conjugate faults with probability of 0.6 and 0.4, respectively (Mukuhira et al., 2013). The seismicity rate of the whole domain SR_{dom} is similar to the seismicity rate of the domain $\sum SR_{fault}$ (calculated from the discrete faults only) (Figure 5.2b,c,d and Figure 5.6a,c,e), but the 2D forecasting allows to simulate the potential induced seismicity in different areas of the reservoir without mapped faults (Figure 5.6). With the forecasting of seismicity in the matrix, the constant injection induces a mainshock late after the stop of injection.

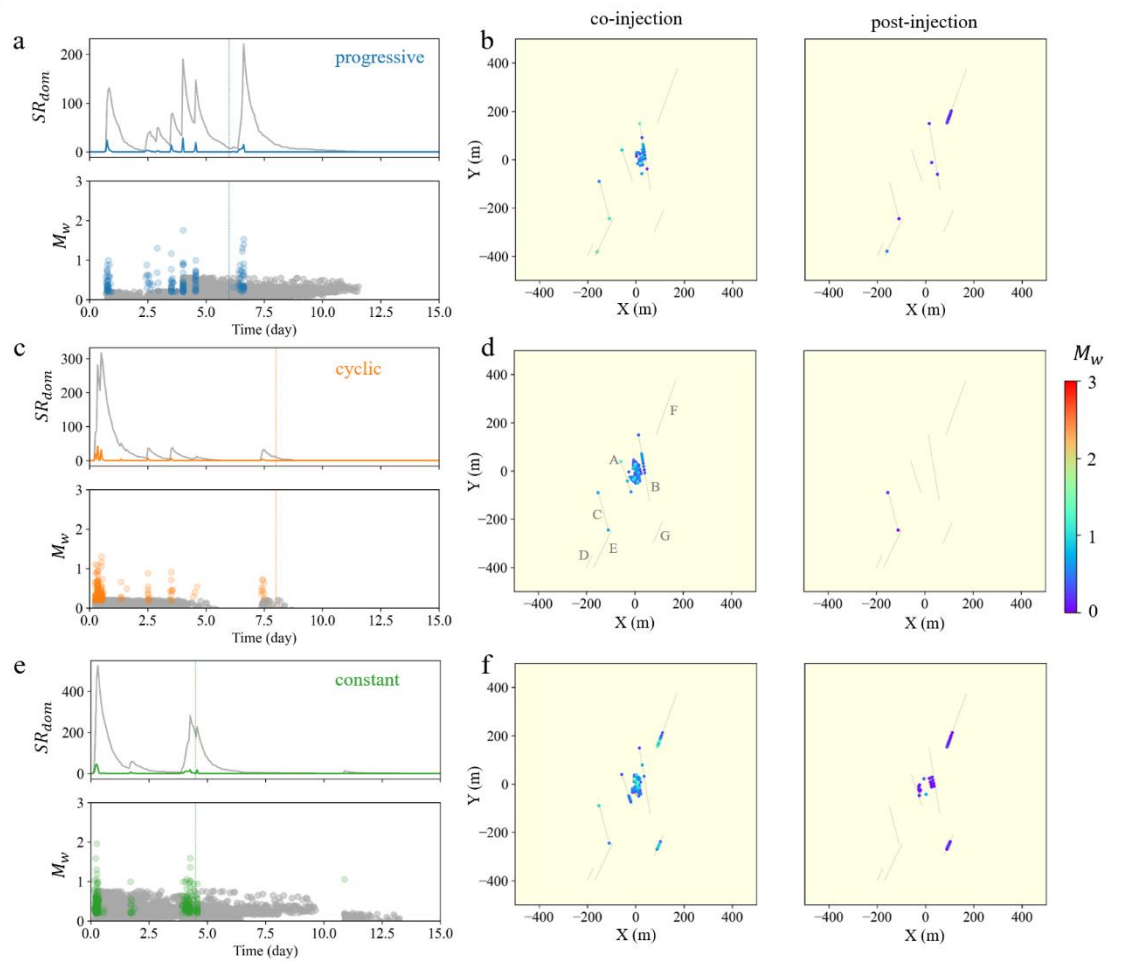

Figure 5.6: Time evolution of forecasted seismicity rate of the whole domain SR_{dom} and corresponding magnitude for the (a) progressive, (c) cyclic and (e) constant injections. Colours represent the mainshock seismicity rate and magnitude while grey represents the aftershocks. (b), (d) and (f) the 2D spatial distribution of the co- and the post-injection seismicity plotted for the three protocols. The colour scale represents the magnitude of the estimated earthquakes. For plotting purpose, the location of the earthquakes within the faults and in the matrix are adjusted to avoid overlapping.

5.6. Discussion

The proposed hybrid methodology allows to estimate the seismicity nucleation induced by different injection protocols. The implementation of the seismicity rate and the ETAS models combined with a numerical model is efficient to forecast fluid-injection induced seismicity. Hydro-mechanical models simulate the pressure and stress variations due to fluid injection and extraction in hot rock. In cases of discrete faults, it can also simulate stress redistribution from fault reactivations. The strength of numerical models is the possibility to understand and reproduce the complex and coupled triggering processes (e.g., pressure-driven processes, thermal interactions and mechanical behaviours) and the possibility to investigate their mitigation. Our model is limited to the hydro-mechanical problem due to the negligible effect of the thermal coupling as cooling does not significantly propagate away from the injection well during the short duration of the stimulation (De Simone et al., 2013). Our discrete-fault hydro-mechanical model

of the case of Basel EGS is however complex enough to forecast seismicity induced by hydraulic stimulation as both poromechanical stresses and static stress transfer are simulated in addition to pore pressure diffusion. We are optimistic that models will be developed to solve the coupled thermo-hydro-mechanical-chemical problems faster and more efficiently in the future with the development of the High-Performance Computing, allowing to forecast induced seismicity both during hydraulic stimulation and operation of EGS.

One of the weaknesses of the hybrid methodology is the estimation of large magnitude earthquakes. Because the G-R law depends on the number of seismic events, the model does not estimate magnitudes as large as the monitored earthquakes in Basel EGS. We favoured the calibration on the seismicity rate rather than the calibration of the magnitude attribution model. Moreover, the G-R law attributes stochastically the magnitude, which can impact the forecasting of the aftershocks via the ETAS model. It also affects the interpretation of the cumulative seismic moment. The second limitation of the methodology is that the ETAS model is used here to attribute an aftershock-sequence to each mainshock without spatial distribution. This aspect affects the 2D spatial forecasting, but more importantly the effects of stress drop that differ with the location of the nucleation of each earthquake, mainshocks and aftershocks. Moreover, the construction of the model was possible thanks to seismic interpretations posterior to the injection itself. In the case of development of new EGS projects, the fault network is usually not yet known. Yet, a simple fault zone could already be sufficient to initiate the model (Boyet et al., 2023b). This hybrid methodology could be associated to a real-time forecasting model that could update the simplified fault network as a function of real-time seismic interpretation; in the same dynamics than the Adaptive Traffic Light Systems adjustments with real-time monitoring (Mignan et al., 2017; Ritz et al., 2023).

Co-injection induced seismicity is partly controlled by the injection parameters. The comparison between three simple protocols (progressive, constant and cyclic injections) shows their different effects on the stability of the subsurface. Cyclic injection, designed on the cyclic soft stimulation performed at the Pohang EGS (Hofmann et al., 2019), results in a limited pore pressure build-up, as the periods with low-pressure injection cause pressure drop in the whole domain. The limited pressure build-up in the domain restricts fault reactivation to the vicinity of the injection well. Cyclic injection, investigated with the proposed methodology, does not significantly enhance the permeability of the faults and relatively large-magnitude induced seismicity is not prevented, two decisive objectives for economic viability and public perception of EGS projects. On the other hand, constant and progressive injections seem to be similar in enhancing fault permeability, with a time difference due to the time required to inject the same volume. The main difference between the two is that constant injection disturbs the stress conditions abruptly at the start of the injection which induces the peak of seismicity early in the stimulation. Progressive injection in our model

has a larger peak due to the simultaneous reactivations of two large faults. In addition, the reactivations of the faults induce larger stress drops than the case of the constant injection. Constant injection accumulates less stresses on the faults and for a shorter period of time, which mitigate large seismicity rate, and so large-magnitude earthquakes. Because the seismicity rate is sensitive to abrupt stress changes, constant injection induces less forecasted seismicity through smaller pressure changes during the stimulation. Moreover, the duration of injection affects the evolution of aseismic slip, and a shorter injection duration limits the duration of the post-injection aseismic slip propagation (Jacquey & Viesca, 2023). With all these arguments, constant injection seems the most promising stimulation protocol.

5.7. Conclusions

EGS need to be deployed to facilitate the low-carbon energy transition. The enhancement of permeability and the mitigation of co- and post-injection induced seismicity are the current principal challenges to improve the public perception and the economic viability of EGS projects. Constant injection seems to be the most efficient strategy, based on the comparison with cyclic and progressive (with the same injected volume) injection, to both enhance the permeability of pre-existing faults and control the induced seismicity. Its short duration limits the stress accumulation on faults and the post-injection aseismic slip. Cyclic injection, which is one of the most recent developed protocols, based on our hybrid method, does not enhance the permeability of the discrete faults outside of the vicinity of the injection well. The hybrid model, based on a strong and complex coupled hydro-mechanical model associated with the seismicity rate and aftershock-sequence models, allows to simulate the different known triggering mechanisms of induced seismicity and give liberty on the simulations of different injection protocols. Its coupling with a real-time monitoring in order to adjust the fault network and mechanical parameters could forecast and mitigate the seismicity during the hydraulic stimulations and production stages of EGS projects.

Chapter 6: To bleed-off or not to bleed-off?

6.1. Introduction

Geo-energy applications play a crucial role in advancing new technologies within the context of the energy transition, like enabling the generation of decarbonized energy with Enhanced Geothermal Systems (EGS). Fluid injection in the subsurface disturbs pressure and stress conditions, and induces seismicity (Ellsworth, 2013; Ge & Saar, 2022; Majer et al., 2007; Kivi et al., 2023). The pore pressure variation diffuses in the rock and reactivates pre-existing faults and fractures by decreasing the effective stress acting on their planes (Jaeger et al., 2009). At the same time, the rock deforms and the differential pressurization of rock volumes results in poroelastic effects that especially destabilize faults and fractures located close to interfaces between different rock types, also outside of the pressurized area. These pressure-driven mechanisms, i.e., pore pressure build-up and poroelasticity, are considered as the dominant processes triggering seismicity during fluid injection. The reactivation of faults may be seismic or aseismic (De Barros et al., 2018; Guglielmi et al., 2015). In either case, shear-slip stress transfer and earthquake interaction are other triggering mechanisms of induced seismicity (Brown & Ge, 2018; King et al., 1994; Okada, 1992). Fluid injection also induces aseismic creep propagation that deforms rocks in the reservoir, and which continue even after the stop of injection and can induced post-injection seismicity (Jacquey & Viesca, 2023; Sáez & Lecampion, 2023).

While induced seismicity is usually registered during operations of fluid injection at depth, it can also occur after the stop of injection, and in some cases with magnitude perceivable by local inhabitants. The abrupt stop of injection rapidly attenuates the pore pressure gradient, which neutralizes the effects of poroelasticity, homogenizing the stress tensor of the material inside and outside the pressurized volume and potentially triggering new fault reactivations (De Simone et al., 2017; Goebel et al., 2017). At the Castor Underground Gas Storage, Spain, a large number of earthquakes occurred 20 days after the stop of injection in 2013, with three events of magnitude $M_w > 4$ (Vilarrasa et al., 2021, 2022). In some cases of EGS, the seismicity monitored after the stop of the injection operations is of higher magnitude than the one registered during the injection. EGS are geothermal reservoirs located in deep and hot rock, often granites, which are engineered to enhance their permeability, by shearing fractures and thus inducing seismicity, in order to improve the fluid circulation and the production of hot water. The largest induced earthquake monitored in EGS occurred at the Pohang EGS, South Korea, in 2017. The $M_w 5.5$ earthquake was monitored two months after the shut-in of a cyclic injection (Ellsworth et al., 2019; Grigoli et al., 2018; Kim et al., 2018). The delay of occurrence of the large magnitude earthquakes depends on each EGS, from hours to months, and can be located both within and outside of the pressurized area (Kim et al., 2022).

Protocols associated to Traffic Light Systems (TLS) have been implemented to mitigate the seismic magnitude and frequency during the injection, by modifying the injection pressure and flow rate. However, post-injection induced seismicity seems to be out of the scope of TLS. The current protocols of stop of injection entail shut-in and bleed-off of the well. The first corresponds to the shut-down of the fluid injection which retains the injection fluids in the reservoir. It assumes that overpressure slowly decays according to pressure diffusion process in the reservoir, but in the same time mitigate the short-term occurrence of large magnitude earthquake due to abrupt pressure and stress changes and poroelastic relaxation. The second, the bleed-off, involves the opening of the well to extract the injected fluid still located in the vicinity of the well decreasing the post-injection pore pressure diffusion, and the risk of a late post-injection induced seismicity.

Both are widely used since the deployment of EGS. For instance, a bleed-off procedure was firstly applied at the Vendenheim EGS, France 2021, when a large magnitude earthquake $M_w 3.6$ reached the TLS threshold during the injection phase. After three weeks of bleed-off, a $M_w 3.3$ earthquake led to the decision of shutting-in the well (Fiori et al., 2023; Lengliné et al., 2023). Yet, the largest earthquake ($M_w 3.9$) occurred six months after the shut-in. In the case of Basel EGS, Switzerland 2006, the well was shut-in when the maximum threshold $M_l 2.6$ of the TLS was reached after only 6 days of hydraulic stimulation (Häring et al., 2008). Five hours later, the largest earthquake occurred with a local magnitude of $M_l 3.4 (M_w 2.95)$ and led to the decision of bleeding-off the well. For months after the cancellation of the project, induced seismicity kept being monitored. A number of works have investigated the effects of different mechanisms in order to identify the processes inducing the post-injection seismicity at the Basel EGS. These studies have found that the pore pressure build-up remains the most important triggering mechanism during injection (Bachmann et al., 2011; Mukuhira et al., 2017), but stress transfer and earthquake interactions drive the post-injection seismicity initiation (Catalli et al., 2013, 2016). Recently, the effects of poroelastic stress relaxation and shear-slip stress transfer were highlighted as the main triggers of the post-injection reactivation of faults that were stabilized during the injection (Boyet et al., 2023). The EGS cases of Vendenheim and Basel illustrate the complexity of seismicity forecasting and mitigation through the stop of injection.

A number of studies argue that a bleed-off is the best solution to hinder post-injection seismicity, but these studies only consider pore pressure as a triggering mechanisms (e.g., Karvounis & Wiemer, 2022). In contrast, other studies propose progressive injection rate changes in order to control the induced seismicity. Smaller rates of injection have been proven to induce less seismicity during the injection stage (Almakari et al., 2019; Dempsey & Riffault, 2019). Moreover, progressive decreases of injection rate mitigate the post-injection induced seismicity (Alghannam & Juanes, 2020; McClure & Horne, 2011; Segall & Lu, 2015). Because the

seismicity rate is correlated to injection rate, a smaller decrease of pressure injection flattens the peak of the seismicity rate at the stop of injection (Segall & Lu, 2015).

This study aims at identifying the most effective protocol between shut-in and bleed-off to reduce the post-injection seismicity rate at the case of Basel EGS. We also simulate the effects of continuous and step-wise progressive decrease of injection rates. We combine a hydro-mechanical model based on a discrete-faulting geometry, which estimates pressure and stress variations due to fluid injection, with the seismicity rate model. We also analyse the reactivation of the discrete faults and found that the best protocol mitigating the post-injection induced seismicity is shut-in.

6.2. Methodology for forecasting seismicity rate

We use the combination of a hydro-mechanical model with a seismicity rate model to forecast induced seismicity. In the hydro-mechanical model, we simulate the fluid injection and consequent pressure variation, rock deformation, and stress perturbation in the reservoir which allows to reproduce the induced seismicity observed at the Basel EGS. This model is based on a model calibrated in a previous study by Boyet et al. (2023). The geometry contains a discrete faulting network based on the cluster characterization of the Basel seismicity proposed by Deichmann et al. (2014), which is estimated from the focal mechanisms and the cluster swarms. We assume a 2D horizontal plane to reproduce fault reactivation because focal mechanisms of most of the earthquakes show strike-slip movements with a vertical dip. An injection pressure is applied at the centre of the domain, according to the pressure monitored at the injection wellhead at Basel (Figure 6.1). The properties of the rock matrix and the faults are determined by previous studies and models, and they are presented in Appendix C (Andrés et al., 2019; Bachmann et al., 2011; Boyet et al., 2023; Häring et al., 2008; Herrmann et al., 2019; Mukuhira et al., 2013). The discrete faults follow a visco-plastic constitutive law, and their permeability is especially enhanced when they reach the conditions of plastic failure due to dilatancy (see the Appendix C). Intact rock is modelled as an elastic porous material. The hydro-mechanical model couples the effects of pressure-driven processes, pore pressure build-up and poroelasticity, and stress transfer due to fault reactivation. The momentum balance for the medium and the mass balance of water for a fully saturated porous medium are solved through the means of the finite-element solver CODE_BRIGHT (see Appendix C). Once stress variations are computed in the domain, the Coulomb Failure Stress for each fault element is calculated as

$$CFS = \tau - \sigma_n' \times \mu - c \tag{6.1}$$

where τ and σ_n' are the shear and normal effective stresses acting on the fault, respectively, μ is the friction coefficient, calibrated for each fault, and c is the cohesion, equal to 0 in the model.

The seismicity rate model is based on the rate-and-state friction model (Dieterich, 1994; Segall & Lu, 2015). Based on the theory of earthquake nucleation, seismic events occur on faults with rate-weakening properties when the shear strength reduces fast (Dieterich, 1978; Marone, 1998; Ruina, 1983; Scholz, 1998). The number of independent events that are likely induced by a certain stress variation is expressed by the relative seismicity rate R and is governed by the rate-and-state friction law (Dieterich, 1994; Segall & Lu, 2015)

$$\frac{dR}{dt} = \frac{R}{t_c}\left(\frac{\dot{\tau}}{\dot{\tau_0}} - R\right) \tag{6.2}$$

where the stressing rate is $\dot{\tau} = \frac{dCFS}{dt}$ and $\dot{\tau_0}$ is the initial stressing rate which is assumed as 3×10^{-6} MPa/yr based on estimations made for the EGS case of Soultz-Sous-Forêts, France, also located in the Upper Rhine Graben, not far away from Basel (Hossein Hakimhashemi et al., 2014). t_c is the characteristic relaxation time, which is defined as $A\sigma/\dot{\tau_0}$. $A\sigma$ is a free parameter calibrated to reproduce the total numbers of mainshocks monitored in the study case. The calibration of $A\sigma$ is independently performed for each fault to reproduce the number of earthquakes in the clusters defining each fault (in total 185 earthquakes with a magnitude $M_w > 0$ (Deichmann et al., 2014), see Figure SI C.2.). The relative seismicity rate R is found by solving the ordinary differential Equation (6.2), which is calculated using fifth-order adaptive time step Runge-Kutta-Fehlberg algorithm through BRUCES functions (Luu, 2022; Luu et al., 2022). The absolute seismicity rate SR (in events per year) is successively calculated as $R \cdot r_0$, where r_0 is the background seismicity rate and equal to 0.123 events/year (Bachmann et al., 2011). We calculate the Coulomb failure stress at the centre of each fault element CFS_p using Equation (6.1), as a function of the fault orientation. We estimate the number of independent earthquakes for each fault element SR_{elem} by multiplying the seismicity rate based on CFS_p with the surface area of the fault element. We study the seismicity rate of the fault SR_{fault} by summing the SR_{elem} of the elements constituting each fault.

The Gutenberg-Richter (G-R) law is then used to attribute a magnitude to each forecasted earthquake at each time step (Navas-Portella et al., 2020). For a location, it forecasts the number of earthquakes N with a magnitude greater than or equal to M (Gutenberg & Richter, 1942):

$$log\, N\,(M) = a - b \cdot M, \tag{6.3}$$

where a and b are constants to be estimated from the seismic catalogues. We distinguish co- ($a_{co} = 6.8$ and $b_{co} = 1.57$) and post-injection ($a_{post} = 3.32$ and $b_{post} = 1.14$) parameters, as suggested by Bachmann et al. (2011).

Because the seismicity rate model only forecasts independent earthquakes, i.e., mainshocks, we use the Epidemic Type Aftershock Sequence (ETAS) model (Ogata, 1988) to calculate the number of aftershocks at each time step, $\lambda(t)$, from each mainshock of magnitude M_i

$$\lambda(t) = \frac{K_{As}}{(c_{As}+t-t_i)^{p_{As}}}\ 10^{\alpha_{As}(M_i-M_{min})}\ , \tag{6.4}$$

where $c_{As} = 0.38 \pm 0.06$ and $p_{As} = 1.33 \pm 0.06$ are empirical parameters and K_{As} and $\alpha_{As} = 0.8 \pm 0.06$ are describing parameters of the seismic sequence (Bachmann et al., 2011). We also calibrate the parameter $\mathrm{K_{As}} = 0.035$ to estimate the aftershocks in order to reach the total of 11,200 events monitored during and shortly after the stop of injection (Häring et al., 2008). When estimating the magnitude of the aftershocks, we set their magnitude with the order of minus 1.2 from the mainshock magnitude following Båth's law (Båth, 1965).

6.3. Bleed-off or shut-in?

The main mitigation protocols of post-injection seismicity are currently the bleed-off and the shut-in of the well. The two scenarios are simulated with the hydro-mechanical model of Basel that consider pore pressure, poroelasticity and shear-slip stress transfer as potential triggering mechanisms. We make use of the methods described in the previous section to compare the seismicity rate occurring under the bleed-off scenario (represented in blue in Figures 6.1, 6.2 and 6.3) and the shut-in scenario (represented in orange). At two days after the stop of injection, the shut-in scenario exhibits a higher pore pressure than in the bleed-off scenario, with a slower decrease of pore pressure in the overpressurized rock volume. At the end of the simulation, pressure returns to initial conditions in both scenarios (Figure 6.1c). The evolution of pore pressure at two locations, one in the vicinity of the well and the other farther in the domain (plotted in Figure 6.1c) highlights the effects of the bleed-off with an abrupt decrease of pore pressure in the vicinity of the well, and the slower and progressive decrease of pore pressure for the shut-in scenario (Figure 6.1b). For the location far in the domain, we even observe the peak of pore pressure at day 7 due to the post-injection pore pressure diffusion. Yet, in both scenarios, the pore pressure reaches back the initial conditions before the end of the simulations.

We also compare the two scenarios studying both early and late post-injection induced seismicity. Considering the seismicity rate of the faults, SR_{fault}, we observe that both scenarios forecast a peak of seismicity at Fault B immediately at the moment of the stop, larger for the bleed-off scenario (Figure 6.2). Additionally, Fault F would reactivate in both scenarios, as observed in our previous model of the Basel EGS where a 5-hour shut-in followed by a long-term bleed-off was applied (Boyet et al., 2023). However, the shut-in scenario induces slightly more seismicity at Fault F than the bleed-off scenario (Figure 6.2).

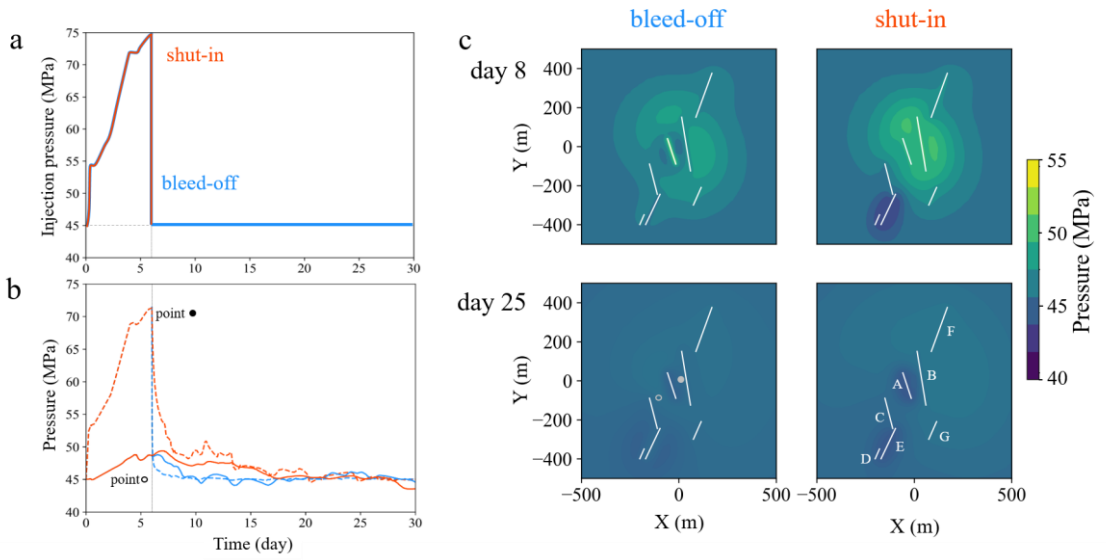

Figure 6.1: (a) Pressure applied at the injection well, similar to the monitored wellhead pressure at Basel. The stop of injection is represented in blue for the bleed-off scenario and in orange for the shut-in scenario. (b) Pressure at the two different points, plotted in the subplot (c) during the simulation of both scenarios. (c) Pressure simulated by the hydro-mechanical model at day 8, 2 days after the stops of injection, and at day 25 for the two stop scenarios.

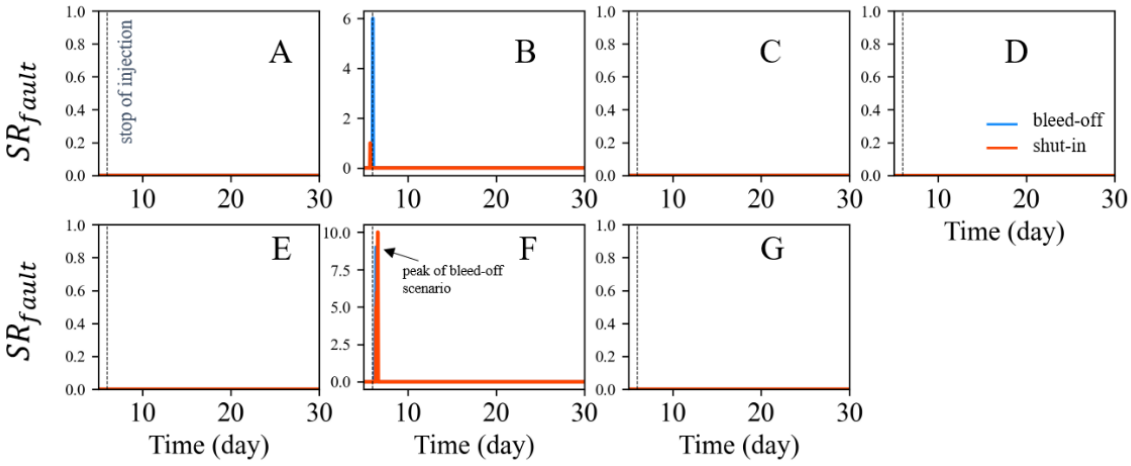

Figure 6.2: Seismicity rate of each fault, SR_{fault}, through time, for each fault under the two scenarios of bleed-off (blue lines) and shut-in (orange lines). Vertical dotted lines correspond to the stop of injection.

Because the seismicity rate model is sensitive to the calibration, we compare the scenarios by looking at both the seismicity rate of the faults SR_{fault} (Figure 6.2) and the plastic strain rate $\frac{d\varepsilon_p}{dt}$, outputted by the hydro-mechanical models (Figure 6.3). We can observe that even if the seismicity rate model does not forecast any seismicity on Faults A, C, D, E and G, they do reach failure conditions after the stop of injection, as expressed by the plastic strain rate (Figure 6.3). Overall, the bleed-off scenario induces peaks of plastic strain rates in different faults shortly after the stop (before day 10), while the shut-in scenario induces later peaks on faults located farther from the injection well, like Faults D, E and G. These plastic reactivations confirm that bleeding-

off the well mitigates pore pressure diffusion, but enhances poroelastic stress relaxation because of the generation of pressure gradients in the opposite direction as during fluid injection. Such enhancement can reactivate faults that were stabilized by poroelastic stresses or that were already seismically-active during injection. On the other hand, the shut-in scenario seems to mitigate the seismic activity of the active faults in the vicinity of the well, but it permits a greater pore pressure diffusion in the reservoir, leading to late activation of distant faults. Nevertheless, whereas the hydro-mechanical model reproduces the reactivation of farther faults, the stress changes are not sufficient to forecast seismicity according to the seismic model adopted here.

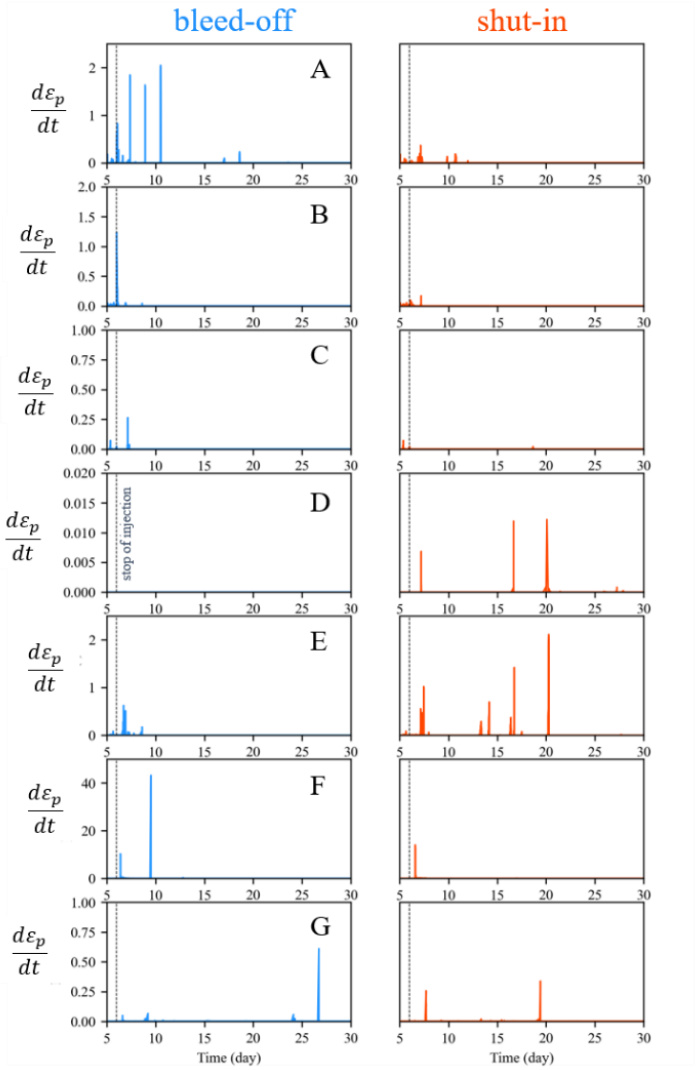

Figure 6.3: Plastic strain rate evolution of each fault, $\frac{d\varepsilon_p}{dt}$, for each fault under the two scenarios of bleed-off (blue lines) and shut-in (orange lines). Vertical dotted lines correspond to the stop of injection.

6.4. The importance of a progressive decrease of pressure rate at the stop of injection

We also analyse the seismic response under different strategies of injection tapering as alternative to the shut-in. As represented in Figure 6.4a, we simulate four scenarios with a progressive continuous (greens) and step-wise (pinks) decrease of injection rate during a time of two (light colours) and four days (dark colours), which we compare with the shut-in scenario (represented

again in orange). For all scenarios, the injection stage is the same as discussed in the previous section, and results for this time window (day 0 to 6) are not represented in Figure 6.4.

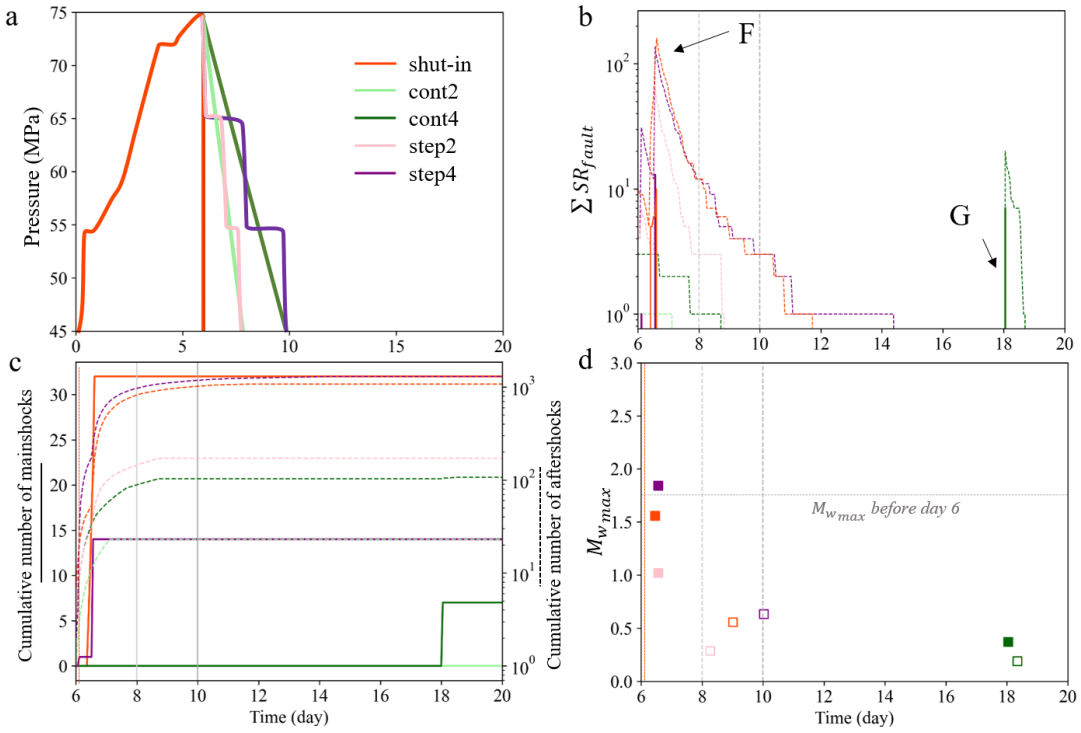

Figure 6.4: (a) Pressure applied at the injection well for the scenarios with progressive (greens) and stepping (pinks) stop of injection; the standard shut-in scenario is represented in orange. (b) Total seismicity rate (sum of the seismicity rate of the Faults A to G) through time. (c) Cumulative number of mainshocks (solid lines and left axis) and cumulative number of aftershocks (dashed lines and right axis) through time for each scenario. (d) Maximum forecasted magnitude of mainshocks (filled squares) and aftershocks (empty squares) in the post-injection stage. The vertical lines at day 8 and 10 mark the end of the injection reduction.

Firstly, we observe that mainshocks are only forecasted for the two stepping and shut-in scenarios. The combined seismicity rate of the faults, expressed by their sum in $\sum SR_{fault}$, peaks at day 7 due to the reactivation of Fault F. This reactivation also occurred in the stepping and shut-in scenarios, but it is mitigated under the two scenarios of progressive continuous decrease of injection rate (Figure 6.4b). Yet, the four-day decrease of injection rate (cont4) scenario induces one mainshock at day 18, due to the reactivation of Fault G, located far from the injection well (Figure 6.4b and d). Since a longer progressive decrease of injection implies injecting a larger volume of water into the system, pore pressure diffusion has larger effects than a shorter progressive decrease of injection. It is important to note that the attribution of magnitude to the mainshock events is controlled by a stochastic process (GR law, Section 2), and it impacts the calculation of the aftershocks sequences (ETAS model, Section 2). The shut-in scenario induces more mainshocks than the stepping scenarios, increasing the probability of having a high magnitude (Figure 6.4c). The largest earthquakes of the post-injection stage are forecasted, in

general, to have a magnitude smaller than the co-injection largest earthquakes. Although, involving a larger injected volume, the continuous decrease of injection rate mitigates post-injection induced seismicity better than the shut-in scenario, confirming the findings of previous studies (Alghannam & Juanes, 2020; McClure & Horne, 2011; Segall & Lu, 2015).

6.5. Conclusions

Induced seismicity is controlled by fluid injection. Post-injection induced seismicity can persist long after the stop of injection. Bleed-offs reverse the strains forcing critically stressed faults in the vicinity of the injection well during the injection, which induces immediate post-injection seismicity. An abrupt shut-in scenario does not trigger immediate reactivation of the faults in the wellbore surroundings, but it affects faults located far from the injection well on the long term as pressure diffuses. Despite the fault reactivation is reproduced by our numerical HM model and the calibration of the seismicity rate model, our hybrid methodology does not forecast much seismicity at the faults during the post-injection stage. The two scenarios of progressive continuous decrease of injection rate mitigate fault reactivation right after the initiation of the stop of injection. This behaviour is observed because by progressively decreasing the injection pressure, the poroelastic stress relaxation occurs gradually, giving time to pressure to drop and stabilize faults, in accordance with the studies of Alghannam & Juanes (2020), McClure & Horne (2011) and Segall & Lu (2015). We argue that current TLS should be revised and tested to include progressive decreases of injection rates lasting a relatively longer time than the current "emergency" protocols, in order to control the immediate post-injection induced seismicity.

Chapter 7: Conclusions

This thesis contributes to improving the understanding of the mechanisms that trigger induced seismicity and specifically addresses the counterintuitive occurrence of post-injection large magnitude earthquakes in EGS. The analysis of several cases of observed seismicity in EGS and the potential triggering mechanisms suggests that he delay of post-injection induced seismicity depends on the diffusion process in the reservoir and the fault mechanical properties. Early post-injection induced seismicity generally is likely to be due to mechanisms that have immediate effects, as poroelasticity, static stress transfer and fault slips. Pore pressure build-up diffuses for a long time and further triggers seismicity. Late induced seismicity tends to occur in EGS projects located in regions where production lasted many years in the same well, or on multiple wells; in these cases, pore pressure diffusion, thermoelasticity and the accumulation of stresses on large faults are prominent.

Due to the complex and coupled mechanisms inducing seismicity during and after injection, the adoption of physics-based models solving coupled thermo-hydro-mechanical-chemical problems is required. By adopting 2D models, homogeneous and crossed by a fault, to simulate pressure-driven mechanisms due to the applied injection, this thesis highlights the importance of implementing models including structural heterogeneities and reproducing the effects of coupled HM mechanisms to forecast induced seismicity. The identification of the triggering mechanisms of plastic reactivations of each fault is possible by a complex study using the critical pressure theory and the Coulomb Failure Stress, and comparing models with plastic and elastic-behaviour faults. The quality and abundance of studies documenting the case of Basel EGS allows the construction of a robust hydro-mechanical model incorporating seven discrete major faults. Simulation results show that co-injection fault reactivation is due to the pore pressure build-up and consequent poromechanical stress changes in the vicinity of the well, and is induced farther by the shear-slip stress transfer of adjacent fault reactivation. Yet, the main novelty of the thesis is actually the observation of the impacts of poroelastic relaxation on the short-term post-injection reactivation of a fault located relatively far from the injection well, and outside of the pressurized rock volume. The use of this coupled hydro-mechanical model emphasises even more the importance of complex physics-based models in studying and forecasting induced seismicity.

The second main contribution of the thesis is the proposition of a forecasting methodology, one of the current challenges of geo-energy applications. The methodology combines a coupled hydro-mechanical model with a seismicity rate model. This hybrid model is applied again to the case of Basel EGS, where we observe that constant injection, instead of a progressive, and longer, injection, reactivates the faults from the start of the stimulation, and consequently enhances their permeability, avoiding large pressure and stress accumulation and controlling post-injection

induced seismicity. Additionally, the effects of cyclic injection are explored and they result to be limited to the vicinity of the well while not useful in enhancing the permeability of faults in the reservoir, which is the aim of hydraulic stimulation. Based on simulation results, the thesis provides a best-strategy to control post-injection induced seismicity. It is recommendable to operate the cessation of the injection through a progressive decrease of injection rate followed by a shut-in to mitigate the induced seismicity in early and late post-injection stages. Although this thesis focuses on EGS, its findings and proposed methods could be applied to understand, forecast and mitigate induced seismicity in any geo-application involving fluid injection.

Appendices

A. Supplementary information for Chapter 3

This appendix provides further explanations of the modelling tools used in the Chapter 3, CODE_BRIGHT, COULOMB3 and BRUCES. We provide here detailed explanations about the governing equations, the methods and the calibration of the models.

A.1. Hydro-mechanical problem

We solve the fully coupled hydro-mechanical problem using CODE_BRIGHT, a Finite Element Method (FEM) simulator (Olivella et al., 1996) to calculate the pressure and stress variation due to fluid injection. The momentum balance for the medium is expressed by

$$\nabla \cdot \boldsymbol{\sigma} + \mathbf{b} = 0 \,, \tag{SI A.1}$$

where $\boldsymbol{\sigma}$ is the stress tensor and $\mathbf{b}$ is the vector of body forces. The mass balance of water for a fully saturated porous medium is expressed by

$$\phi\beta \frac{\partial P}{\partial t} + \frac{\partial}{\partial \mathrm{t}}\varepsilon_v + \nabla \cdot \mathbf{q} = f^w \,, \tag{SI A.2}$$

where ϕ is the rock porosity, β is the fluid compressibility, ε_v represents the volumetric deformation, P is pore pressure, t is time and f^w is an external supply of water. $\mathbf{q}$ is the water mass flux and is expressed by Darcy's law

$$\mathbf{q} = -\frac{k}{\gamma}(\nabla P - \rho \mathbf{g}) \,, \tag{SI A.3}$$

where γ and ρ are the fluid viscosity and density, respectively, $\mathbf{g}$ is the gravity vector and k is the rock intrinsic permeability, considered as isotropic. The intrinsic permeability of the intact rock is considered to be a function of porosity by means of Kozeny's model

$$k = k_o \frac{\phi^3}{(1-\phi)^2}\frac{(1-\phi)^2}{{\phi_o}^3} \,, \tag{SI A.4}$$

with k_o and ϕ_o being the reference values for intrinsic permeability and porosity of the rock matrix, respectively.

The coupling between Eq. (SI A.1) and Eq. (SI A.2) is built through the elastic constitutive law, which relates stress tensor $\boldsymbol{\sigma}$, strain tensor $\boldsymbol{\varepsilon}$, and pressure as

$$\Delta\boldsymbol{\sigma} = K\varepsilon_v \mathbf{I} + 2G\left(\boldsymbol{\varepsilon} - \frac{\varepsilon_v}{3}\mathbf{I}\right) + \Delta P \mathbf{I} \,, \tag{SI A.5}$$

where $K = E/[3(1-2v)]$ is the rock bulk modulus, E is Young's modulus, v is the Poisson ratio and $\boldsymbol{I}$ is the identity matrix. The rock is assumed to follow the standard linear elasticity model.

The grid mesh is composed by rectangular elements with maximum size 20 m^2. A refinement is applied close to the injection well and the fault zone, with elements of size of 2 m^2. Numerical tests have been performed to confirm that results do not significantly differ if a more refined mesh is adopted.

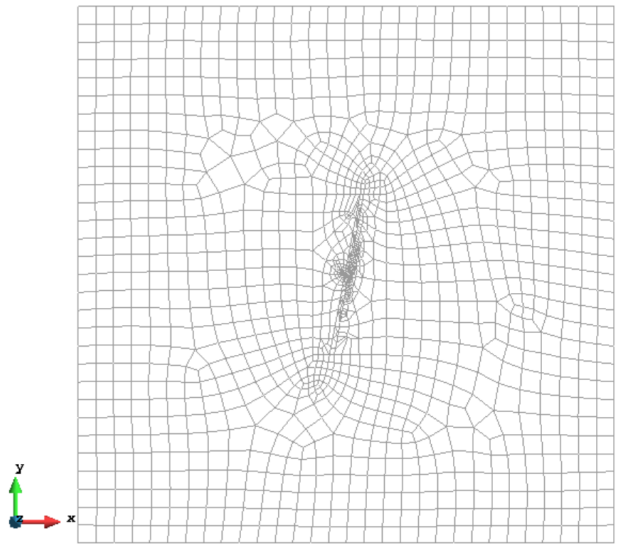

Figure SI A.1: Mesh of the models. The mesh is bigger (4 x4 km^2) than the studied area (500 x 500 m^2) in order to avoid any boundary computing issues. For both models, the mesh is similar, only the material properties differ.

A.2. Calculation of the static stress transfer

We consider the seismic clusters as reported by Deichmann et al. (2014), and we represent each of the clusters as a fault (Figure SI A.2) in order to estimate the stress redistribution induced by each cluster as the stress variation induced by the fault reactivation. We use Coulomb3 (Lin & Stein, 2004; Toda et al., 2005) to calculate the static stresses induced by fault slip according to linear elastic behaviour of rock.

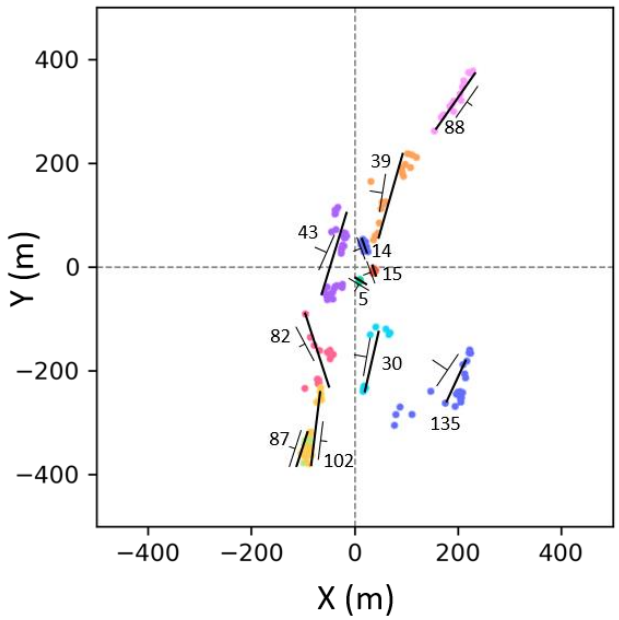

Figure SI A.2 Projection of location of the main seismic events grouped by cluster (Deichmann et al., 2014) and the synthetic faults representing the clusters on a horizontal plane placed at the depth of the injection (4630m). Clusters are located between 3750 to 4750-m deep. The orientation and dip of the focal mechanism of the main event of each cluster are represented by the T-symbol.

The net slip d for each fault is estimated as a function of the moment magnitude M_o of the main event of the corresponding cluster and the slipping surface of the fault plane A, such as (Steketee, 1958)

$$d = \frac{M_o}{G \times A}, \qquad \text{(SI A.6)}$$

where $G = E/(2(1+\nu))$ is the shear modulus, which we assume to be equal to 21 GPa. Coulomb3 calculates the static stress transfer in a three dimensional domain. The stress changes are projected in the 2D plan of the model. We apply to each event the amount of stress change resulting from the nucleation of the main seismic event of clusters anterior to the event.

A.3. Seismicity rate model

We adopt the seismicity rate model developed by Dieterich (1994), which relates Coulomb stress changes and seismicity rate as

$$\frac{dR}{dt} = \frac{R}{t_c}\left(\frac{\dot{\tau}}{\dot{\tau_0}} - R\right). \qquad \text{(SI A.7)}$$

Where $\dot{\tau}$ and $\dot{\tau_0}$ are the Coulomb and background stressing rates, and $t_c = \bar{A}\sigma/\dot{\tau_0}$ the characteristic relaxation time, which is defined as. $\bar{A}\sigma$ is a free parameter of the equation ($\bar{A}$ is a constitutive parameter quantifying the direct effect on slip rate in the rate-state friction law, and σ is the background effective normal stress). The earthquakes sources are governed by a rate-and-state friction law. The model admits steady-state solution and predict the Omori-like decay of

seismic occurrence after a rapid increase in Coulomb Failure Stress (Segall & Lu, 2015). We calculate the seismicity rate induced by the stress variation of our hydro-mechanical model by numerically solving the ordinary differential equation SI A.7 by means of the BRUCES code developed by Luu (2022).

B. Supplementary information for Chapter 4

This Appendix provides the temporal evolution of the numerically estimated plastic strain at the faults in the cases with fault C friction weakening enabled and disabled (Figure SI B.1). We also present the temporal evolution of the permeability at the faults (Figure SI B.2); and the temporal evolution of the plastic strain at the faults when each fault is the only one following a visco-plastic-behaviour (Figure SI B.3). In Figure SI B.4, we show the difference of Coulomb Failure Stress changes caused by the activation of the original clusters and the simplified fault network, calculated by means of COULOMB3 (Lin and Stein, 2004; Toda et al., 2005). Figure SI B.5 shows the temporal evolution of the normal, shear and Coulomb Failure Stresses at faults D and G, which are not plotted in Figure 4.4 of the Chapter 4. In Table SI B.1, we present the correspondence between the faults and the seismic clusters, and their main characteristics.

Table SI B.1: Correspondence between the faults included in the simplified geometry adopted for the numerical model and the full set of seismic clusters, as reported by Deichmann et al. (2014), for which the main characteristics (focal mechanisms, magnitude M_w and time of occurrence) are shown.

FAULT	CLUSTER	STRIKE	DIP	RAKE	M_W	TIME	
	14	124	88	-178	1.27	03/12/2006	0:59
A	15	125	88	-167	1.30	03/12/2006	6:41
	5	85	86	154	1.80	03/12/2006	19:51
	43	168	50	-67	1.90	04/12/2006	12:37
B	39	153	45	-63	2.10	05/12/2006	18:56
	30	154	58	-27	1.70	06/12/2006	12:42
C	82	116	88	-155	1.80	07/12/2006	1:12
D	87	168	88	10	2.20	08/12/2006	0:45
E	102	331	71	-43	1.90	08/12/2006	4:54
F	88	359	85	14	1.80	08/12/2006	3:43
G	135	178	48	-22	1.70	09/12/2006	14:17

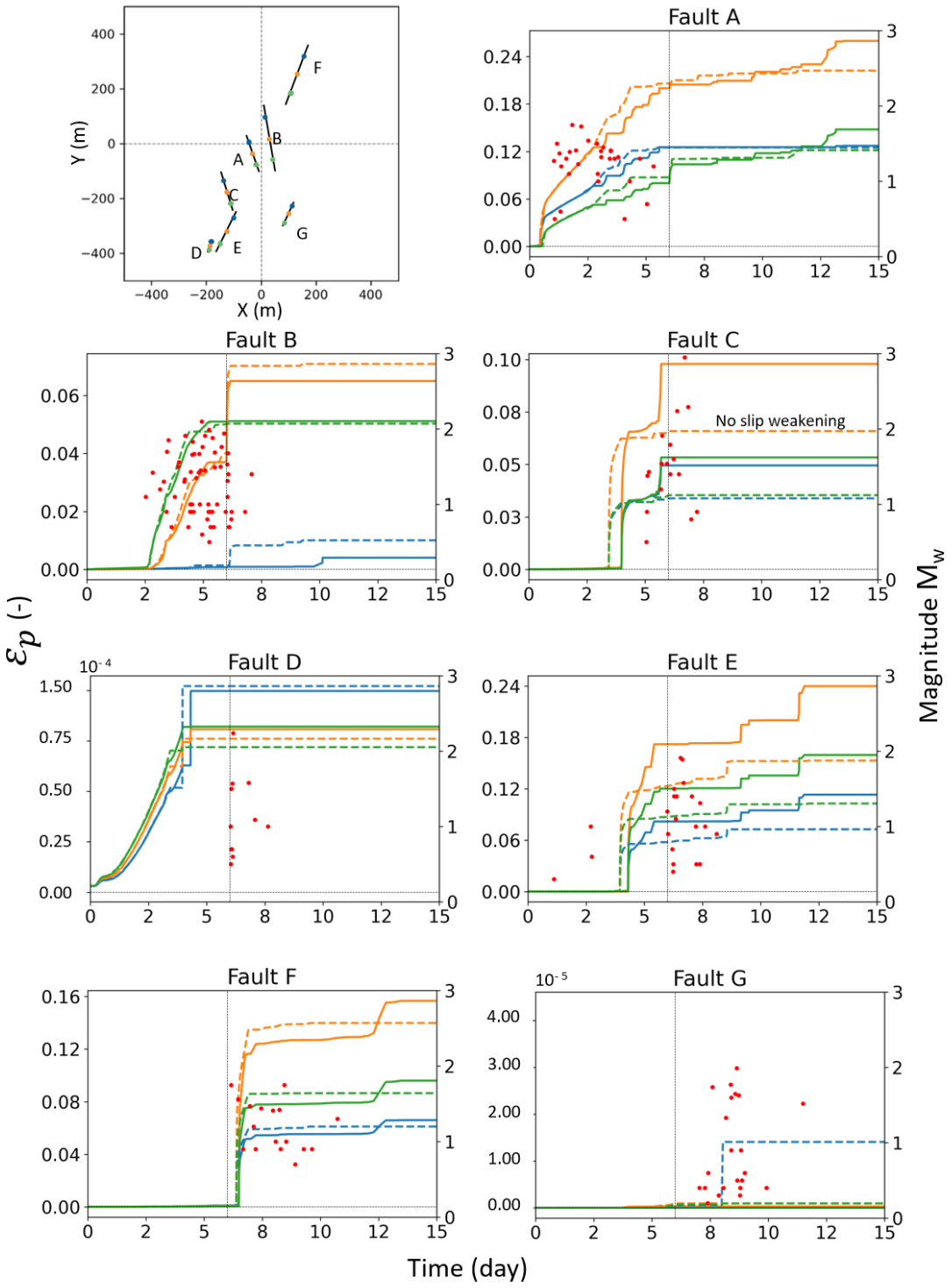

Figure SI B.1 Temporal evolution of numerically estimated plastic strain, ε_p (solid lines), at different locations on each fault as indicated in the upper left figure, and of the magnitude M_w of observed seismic events (dots) as reported by Deichmann et al. (2014). Solid and dashed lines correspond, respectively, to the cases with fault C friction weakening enabled and disabled. Fault C friction weakening affects the failure of the other faults in the reservoir, especially fault E. Note that Faults D and G have a different scale.

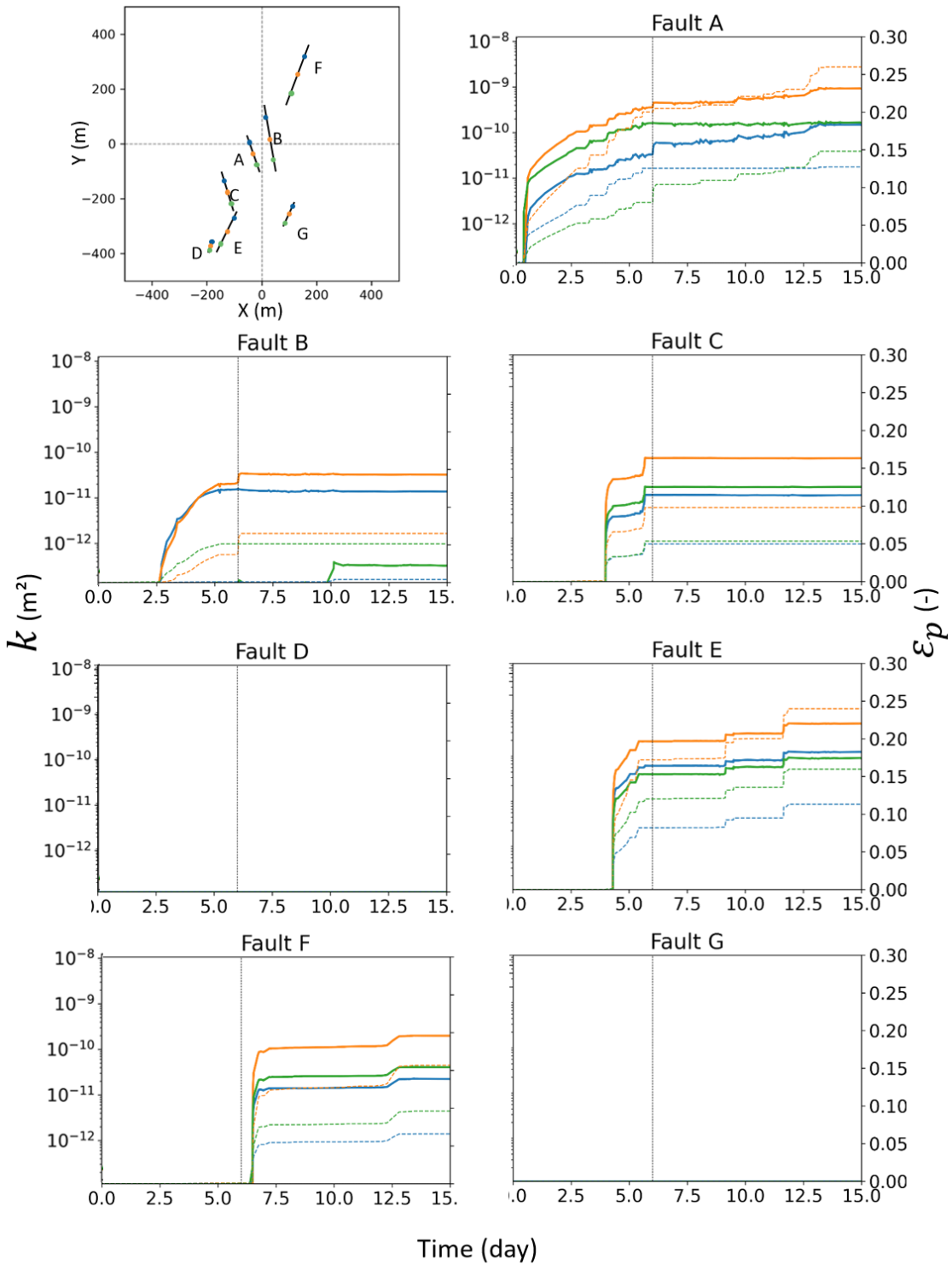

Figure SI B.2: Temporal evolution of numerically estimated permeability, k (continuous lines), and plastic strain, ε_p (dashed lines), at different locations on each fault as indicated in the first plot. Permeability variation evolves in agreement with ε_p and it is irreversible. Permeability and plastic stain of faults D and G vary with very small increments.

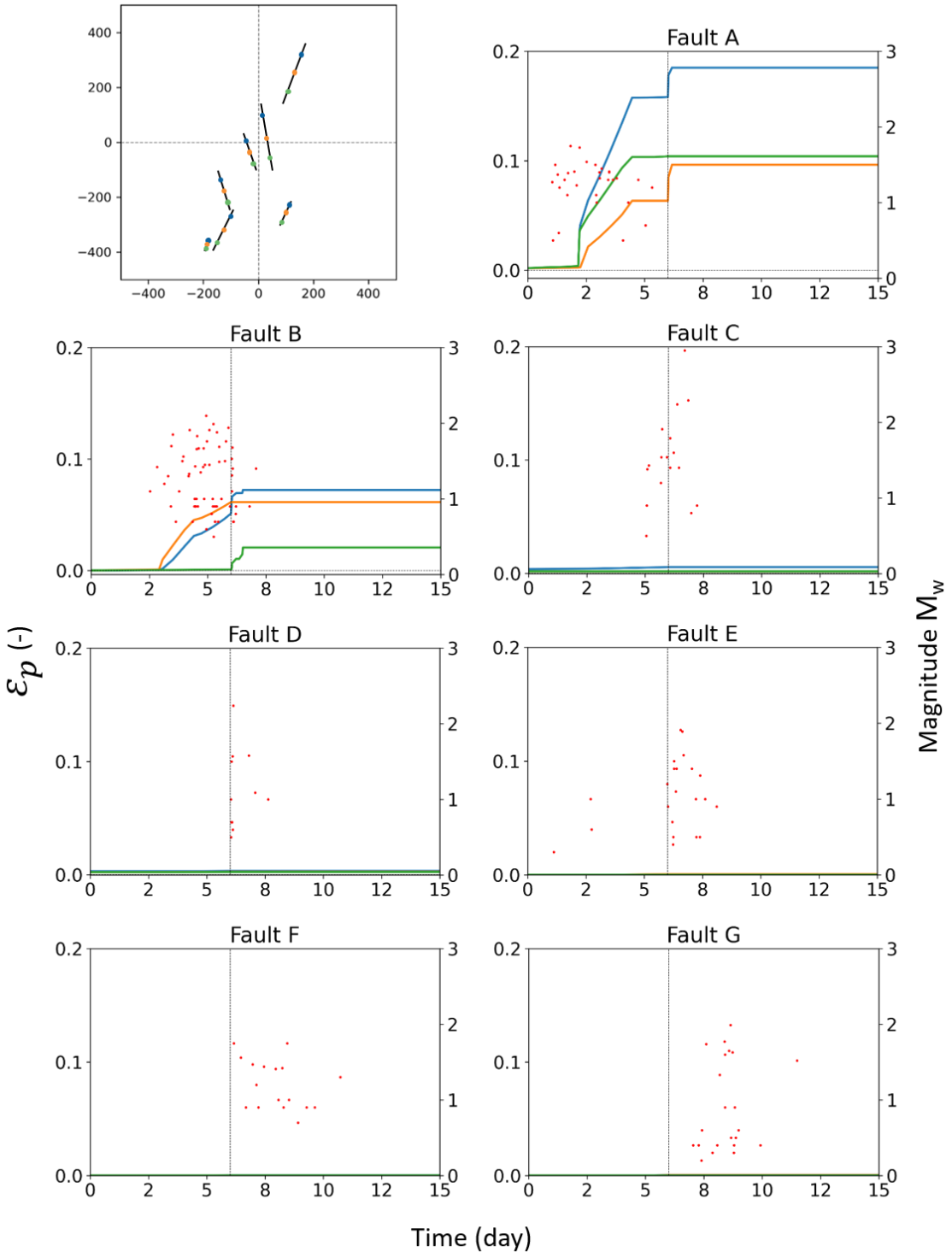

Figure SI B.3: Temporal evolution of numerically estimated plastic strain, ε_p (solid lines), at different locations on each fault when each fault is the only one following a visco-plastic-behaviour, i.e., the stability of the fault is not influenced by shear-slip stress transfer of the other faults, and of the magnitude M_w of observed seismic events (dots) as reported by Deichmann et al. (2014). Note that ε_p is equal to 0 or close to 0 for most faults.

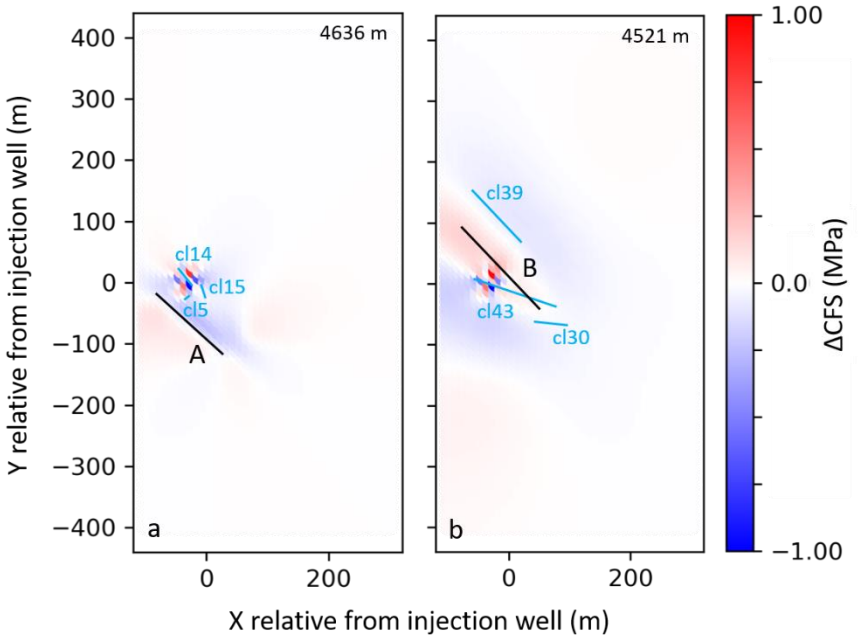

Figure SI B.4: Difference between the Coulomb Failure Stress (CFS) changes caused by the activation of the original clusters (from Deichmann et al.,2014) and the simplified fault network reconstructed from the original clusters. Estimations are performed with Coulom3. (a) Difference between the CFS changes (calculated on the orientation 120/88/-170) due to the activation of clusters 14, 15, and 5, and the activation of fault A. (b) Difference between the CFS changes (calculated on the orientation 155/50/-50) due to the activation of clusters 43, 39, and 30 and the activation of fault B. Both results exhibit absolute values much smaller than 1, confirming that the combination of three clusters into one fault is valid. Values close to 1 MPa are due to estimations tending to infinity at singular points, corresponding with fault tips in the three-dimensional domain, which we disregard. Note that the Y axis here refers to the North direction, and it does not correspond to the Y-direction considered in the hydro-mechanical model. Panels show two-dimensional sections of the three-dimensional domain, placed at 4636m and 4521m depth, respectively.

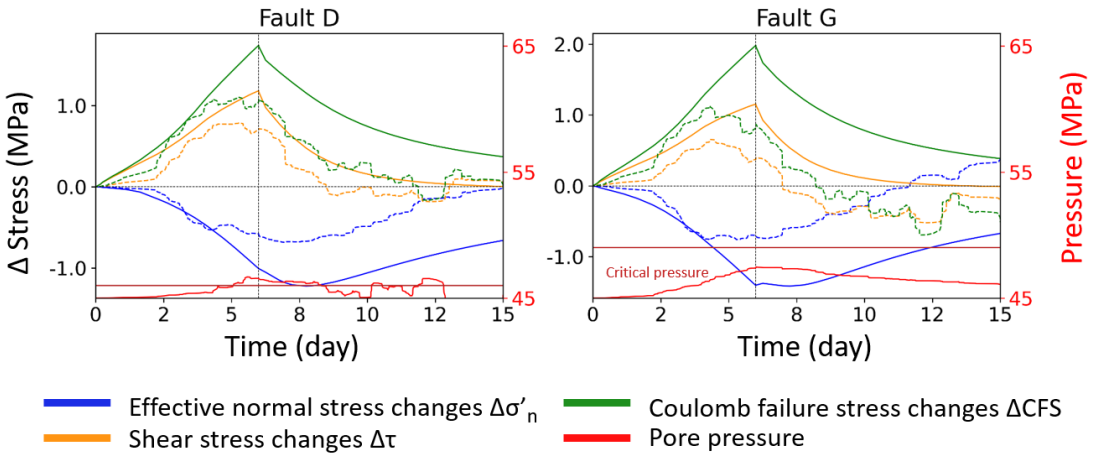

Figure SI B.5: Temporal evolution of effective normal and shear stresses changes (blue and yellow lines, respectively), Coulomb Failure Stress changes (green lines) and pore pressure (red line) under elastic (solid lines) and visco-plastic (dashed lines) behaviour at the central location of selected faults. The critical pressure for failure is represented by the horizontal dark red line. The grey vertical line marks the time of end of injection.

C. Supplementary information for Chapter 6

The hydro-mechanical problem is calculated by the Finite Element Method solver CODE_BRIGHT with a continuum approach, instead of an interface model with discontinuous displacement. The model of the discrete faulting network is limited to two dimensions because of computing duration, even if the solver can solve coupled thermo-hydro-mechanical problems in 3 dimensions. In the used hydro-mechanical model, the governing equations are the momentum balance for the medium

$$\nabla \cdot \sigma + b = 0 \,, \qquad \text{(SI C.1)}$$

where **σ** is the stress tensor and **b** is the vector of body forces, and the hydraulic governing equation is the mass balance of water for a fully saturated porous medium

$$\phi\beta \frac{\partial P}{\partial t} + \frac{\partial}{\partial \mathrm{t}} \varepsilon_v + \nabla \cdot \mathbf{q} = f^w \,, \qquad \text{(SI C.2)}$$

where ϕ is the rock porosity, β is the fluid compressibility, ε_v represents the volumetric strain, and f^w is an external supply of water. $\mathbf{q} = -\frac{k}{\gamma}(\nabla P - \rho \mathbf{g})$ is the water mass flux and is expressed by Darcy's law, where γ and ρ are the fluid viscosity and density, respectively, **g** is the gravity vector and $k = k_o \frac{\phi^3}{(1-\phi)^2} \frac{(1-\phi_o)^2}{{\phi_o}^3}$ is the rock intrinsic permeability calculated by the Kozeny's model, with k_o and ϕ_o being the reference values for intrinsic permeability and porosity of the rock matrix, respectively. The permeability of the matrix is isotropic. The coupling of the governing equations (SI 1) and (SI 2) constitute the elastic constitutive law of the matrix

$$\Delta \boldsymbol{\sigma} = K \varepsilon_v \, \mathbf{I} + 2G \left(\boldsymbol{\varepsilon} - \frac{\varepsilon_v}{3} \mathbf{I} \right) - \Delta P \mathbf{I} \,, \qquad \text{(SI C.3)}$$

where **σ** is the stress tensor, $K = E/[3(1-2\nu)]$ the rock bulk modulus, **ε** the strain tensor, P the pressure and **I** is the first invariant of the stress tensor.

Fault element are defined by finite-thickness elements following the "embedded model" proposed by Olivella and Alonso (2008). The faults are defined by their aperture embedded in a continuous finite element composed of rock matrix. The permeability of the faults varies as a function of the deformations, proportional to the square of the fault aperture variation based on the cubic law. Fault elements are subject to the visco-plastic constitutive law:

$$\frac{d\varepsilon_p}{dt} = \Gamma \langle \Phi(F) \rangle \frac{\partial \xi}{\partial \sigma} \,, \qquad \text{(SI C.4)}$$

where ε_p is the visco-plastic strain and Γ is the fluidity set at 1.00E-4 $s^{-1}MPa^{-m}$. ξ is the flow rule:

$$\xi = \alpha \cdot \sigma_m \cdot \sin\psi + \left(\cos\theta - \frac{1}{\sqrt{3}} sin\theta \cdot \sin\psi \right) \cdot \sqrt{J_2} - c(\eta) \cdot cos\, \psi(\eta) \,, \qquad \text{(SI C.5)}$$

where α is a parameter for the plastic potential set at 1, ψ is the dilatancy angle, set at 3° for the faults, and J_2 is the second invariant of the deviatoric stress tensor. σ_m, the effective mean stress, and θ, Lode's angle are invariant in the equations. m is a constant power to define the overstress function and is set to be equal to 3 in the model. $\Phi(F)$ is the overstress function:

$$\Phi(F) = \begin{cases} 0, & if\ F \leq 0 \\ F^m, & if\ F > 0 \end{cases}, \qquad \text{(SI C.6)}$$

With F is the yield function as

$$F = \sigma_m \cdot \sin\varphi(\eta) + \left[\cos\theta - \frac{1}{\sqrt{3}} sin\theta \cdot \sin\varphi(\eta)\right] \cdot \sqrt{J_2} - c(\eta) \cdot cos\varphi(\eta)\,, \qquad \text{(SI C.7)}$$

where c is the cohesion, in our model equal to 0 MPa, η is the weakening parameter of 0.01. The deformation of the fault element is elastic until the stresses reach the shear yield surface, $F = 0$. When the yield surface is exceeded, the fault element deforms irreversibly, but stresses can remain beyond the yield surface for a range determined by the overstress function.

The model is based on the case of Basel EGS. The faulting network is design as a function of the clustering of the monitored seismicity (Deichmann et al., 2014; Kraft & Deichmann, 2014). The material properties are defined as general values for a crystalline basement rock (Table SI C.1). The initial stress conditions are presented in the study of Häring et al. (2008) (Figure SI C.1:).

Table SI C.1: Material properties of the hydro-mechanical model

Parameters	Fault element	Matrix
Porosity, ϕ (-)	0.1	0.01
Permeability, k (m^2)	$2.30 \cdot 10^{-13}$	$7.50 \cdot 10^{-17}$
Young's modulus, E (GPa)	43	52
Poisson's ratio, ν (-)	0.25	0.25
Cohesion	0	0
Friction coefficient	0.35-0.58 (from calibration of reactivation)	0.6

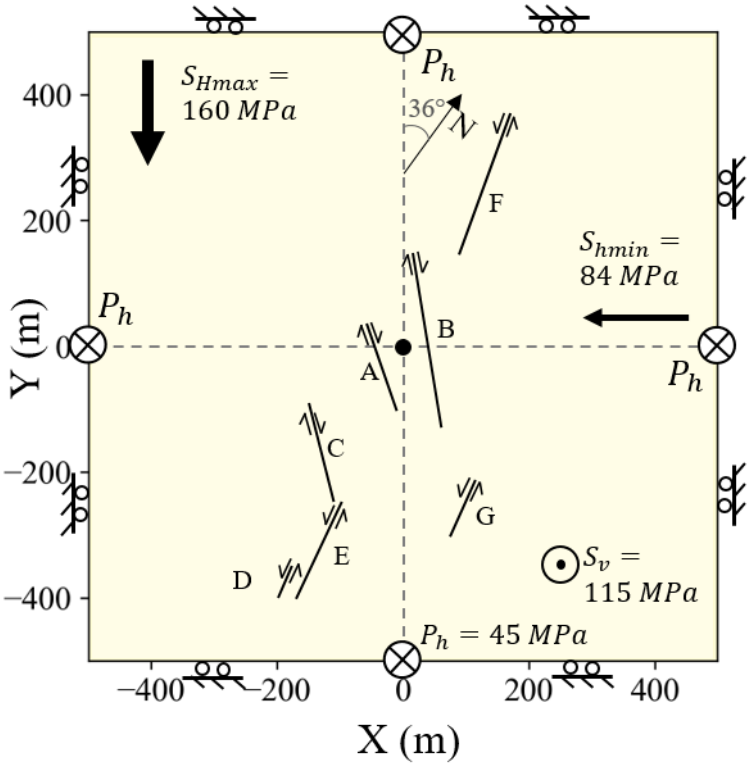

Figure SI C.1: Setting of the hydroechanical model. Initial stress conditions are described in Häring et al. (2008): maximum $S_{H_{max}}$ and minimum $S_{h_{min}}$ horizontal stresses, S_v vertical stress and P_h hydrostatic pressure. The injection well is at the centre of the domain.

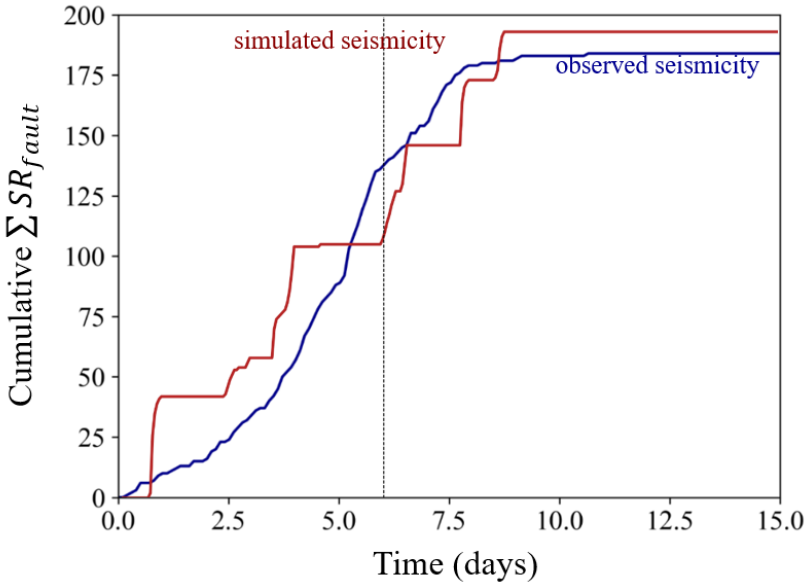

Figure SI C.2: Temporal evolution of cumulative number of observed mainshocks from the catalogue of Deichmann et al. (2014) (blue line) and of simulated mainshocks in the injection scenario used for calibration, which reproduces the operations at Basel (injection during 6 days followed by 5-hour shut-in and a bleed-off until the end) (orange line).

D. Publications and conference presentations

Publications in scientific journals

2023

Boyet, A., De Simone, S., Ge, S. and Vilarrasa, V. (2023). Poroelastic stress relaxation, slip stress transfer and friction weakening controlled post-injection seismicity at the Basel Enhanced Geothermal System. *Nature Communications Earth and Environment* 4, 104. https://doi.org/10.1038/s43247-023-00764-y

Kivi, I. R., **Boyet, A.**, Wu, H., Walter, L., Hanson-Hedgecock, S., Parisio, F., and Vilarrasa, V. (2023). Global physics-based database of injection-induced seismicity, *Earth Syst. Sci. Data*, 15, 3163–3182, https://doi.org/10.5194/essd-15-3163-2023, 2023.

Boyet, A., De Simone, S., Ge, S. and Vilarrasa, V. (2023). Physics-Based Modeling to Understand and to Propose Forecasting Methods of Induced Seismicity. *Seismological Research Letters,* 94 (6), 2666–2678. https://doi.org/10.1785/0220230109

Presentations in Congresses

2021

Boyet, A., De Simone, S., and Vilarrasa, V. Reconsidering the Causes of the Post-Injection Induced Seismicity at the Enhanced Geothermal System of Basel (Switzerland). Poster presentation, *American Geophysical Union, AGU Fall Meeting, Vienna*, December 2021.

2022

Boyet, A., De Simone, S., and Vilarrasa, V. Identification of The Processes Triggering Induced Seismicity at the Enhanced Geothermal System of Basel (Switzerland). *European Geosciences Union, EGU General Assembly, Vienna*, April 2022. DOI: 10.5194/egusphere-egu22-2160

Boyet, A., De Simone, S., and Vilarrasa, V. Coupled Hydromechanical Modeling of the hydraulic stimulation in an Enhanced Geothermal System to Determine Triggering Mechanisms of Post-Injection Induced Seismicity. *CouFrac 2022, Berkeley*, November 2022

2023

Boyet, A., De Simone, S., Ge, S., and Vilarrasa, V. Coupled Hydromechanical Modeling of the Induced Seismicity at the Enhanced Geothermal System of Basel (Switzerland). *CODE_BRIGHT Users workshop 2023, Barcelona,* April 2023.

Boyet, A., De Simone, S., Ge, S., and Vilarrasa, V. Triggering mechanisms of Post-Injection Induced Seismicity using the Enhanced Geothermal System of Basel (Switzerland). *European Geosciences Union, EGU General Assembly, Vienna,* April 2023. https://doi.org/10.5194/egusphere-egu23-3100

Boyet, A., De Simone, S., Ge, S., and Vilarrasa, V. Hydro-mechanical Modeling of Injection-induced Seismicity at The Deep Heat Mining Project of Basel, Switzerland. *European Geosciences Union, Solid Earth and Geohazards in the Exascale Era, Barcelona,* May 2023

References

Aki, K., Fehler, M., Aamodt, R. L., Albright, J. N., Potter, R. M., Pearson, C. M., & Tester, J. W. (1982). Interpretation of seismic data from hydraulic fracturing experiments at the Fenton Hill, New Mexico, hot dry rock geothermal site. *Journal of Geophysical Research: Solid Earth*, *87*(B2), 936–944. https://doi.org/10.1029/JB087iB02p00936

Albaric, J., Oye, V., Langet, N., Hasting, M., Lecomte, I., Iranpour, K., Messeiller, M., & Reid, P. (2014). Monitoring of induced seismicity during the first geothermal reservoir stimulation at Paralana, Australia. *Geothermics*, *52*, 120–131. https://doi.org/10.1016/j.geothermics.2013.10.013

Alghannam, M., & Juanes, R. (2020). Understanding rate effects in injection-induced earthquakes. *Nature Communications*, *11*(1), 3053. https://doi.org/10.1038/s41467-020-16860-y

Almakari, M., Dublanchet, P., Chauris, H., & Pellet, F. (2019). Effect of the Injection Scenario on the Rate and Magnitude Content of Injection-Induced Seismicity: Case of a Heterogeneous Fault. *Journal of Geophysical Research: Solid Earth*, *124*(8), 8426–8448. https://doi.org/10.1029/2019JB017898

Amann, F., Gischig, V., Evans, K., Doetsch, J., Jalali, R., Valley, B., Krietsch, H., Dutler, N., Villiger, L., Brixel, B., Klepikova, M., Kittilä, A., Madonna, C., Wiemer, S., Saar, M. O., Loew, S., Driesner, T., Maurer, H., & Giardini, D. (2018). The seismo-hydromechanical behavior during deep geothermal reservoir stimulations: Open questions tackled in a decameter-scale in situ stimulation experiment. *Solid Earth*, *9*(1), 115–137. https://doi.org/10.5194/se-9-115-2018

Anderson, E. M. (1905). The dynamics of faulting. *Transactions of the Edinburgh Geological Society*, *8*(3), 387–402. https://doi.org/10.1144/transed.8.3.387

Andre, B. J., & Rajaram, H. (2005). Dissolution of limestone fractures by cooling waters: Early development of hypogene karst systems: DISSOLUTION OF LIMESTONE FRACTURES BY COOLING WATERS. *Water Resources Research*, *41*(1). https://doi.org/10.1029/2004WR003331

Andrés, S., Santillán, D., Mosquera, J. C., & Cueto-Felgueroso, L. (2019a). Delayed Weakening and Reactivation of Rate-and-State Faults Driven by Pressure Changes Due to Fluid Injection. *Journal of Geophysical Research: Solid Earth*, *124*(11), 11917–11937. https://doi.org/10.1029/2019JB018109

Andrés, S., Santillán, D., Mosquera, J. C., & Cueto-Felgueroso, L. (2019b). Thermo-Poroelastic Analysis of Induced Seismicity at the Basel Enhanced Geothermal System. *Sustainability*, *11*(24), 6904. https://doi.org/10.3390/su11246904

Aretusini, S., Meneghini, F., Spagnuolo, E., Harbord, C. W., & Di Toro, G. (2021). Fluid pressurisation and earthquake propagation in the Hikurangi subduction zone. *Nature Communications*, *12*(1), 2481. https://doi.org/10.1038/s41467-021-22805-w

Asanuma, H., Nozaki, H., Niitsuma, H., & Wyborn, D. (2005). Interpretation of microseismic events with larger magnitude collected at Cooper Basin, Australia. *GRC Trans.*, *29*, 87–91.

Bachmann, C. E., Wiemer, S., Goertz-Allmann, B. P., & Woessner, J. (2012). Influence of pore-pressure on the event-size distribution of induced earthquakes: Pore pressure and earthquake size distribution. *Geophysical Research Letters*, *39*(9). https://doi.org/10.1029/2012GL051480

Bachmann, C. E., Wiemer, S., Woessner, J., & Hainzl, S. (2011). Statistical analysis of the induced Basel 2006 earthquake sequence: Introducing a probability-based monitoring approach for Enhanced Geothermal Systems: Probability-based monitoring approach for EGS. *Geophysical Journal International*, *186*(2), 793–807. https://doi.org/10.1111/j.1365-246X.2011.05068.x

Baisch, S., Koch, C., & Muntendam-Bos, A. (2019). Traffic Light Systems: To What Extent Can Induced Seismicity Be Controlled? *Seismological Research Letters*, *90*(3), 1145–1154. https://doi.org/10.1785/0220180337

Baisch, S., Rothert, E., Stang, H., Vörös, R., Koch, C., & McMahon, A. (2015). Continued Geothermal Reservoir Stimulation Experiments in the Cooper Basin (Australia). *Bulletin of the Seismological Society of America*, *105*(1), 198–209. https://doi.org/10.1785/0120140208

Baisch, S., Vörös, R., Rothert, E., Stang, H., Jung, R., & Schellschmidt, R. (2010). A numerical model for fluid injection induced seismicity at Soultz-sous-Forêts. *International Journal of Rock Mechanics and Mining Sciences*, *47*(3), 405–413. https://doi.org/10.1016/j.ijrmms.2009.10.001

Baisch, S., Weidler, R., Voros, R., Wyborn, D., & de Graaf, L. (2006). Induced Seismicity during the Stimulation of a Geothermal HFR Reservoir in the Cooper Basin, Australia. *Bulletin of the Seismological Society of America*, *96*(6), 2242–2256. https://doi.org/10.1785/0120050255

Bao, X., & Eaton, D. W. (2016). Fault activation by hydraulic fracturing in western Canada. *Science*, *354*(6318), 1406–1409. https://doi.org/10.1126/science.aag2583

Barton, C. A., Zoback, M. D., & Moos, D. (1995). Fluid flow along potentially active faults in crystalline rock. *Geology*, *23*(8), 683. https://doi.org/10.1130/0091-7613(1995)023<0683:FFAPAF>2.3.CO;2

Barton, N. (1976). The shear strength of rock and rock joints. *International Journal of Rock Mechanics and Mining Sciences & Geomechanics Abstracts*, *13*(9), 255–279. https://doi.org/10.1016/0148-9062(76)90003-6

Båth, M. (1965). Lateral inhomogeneities of the upper mantle. *Tectonophysics*, *2*(6), 483–514. https://doi.org/10.1016/0040-1951(65)90003-X

Bentz, S., Kwiatek, G., Martínez-Garzón, P., Bohnhoff, M., & Dresen, G. (2020). Seismic Moment Evolution During Hydraulic Stimulations. *Geophysical Research Letters*, *47*(5). https://doi.org/10.1029/2019GL086185

Beroza, G. C., Segou, M., & Mostafa Mousavi, S. (2021). Machine learning and earthquake forecasting—Next steps. *Nature Communications*, *12*(1), 4761. https://doi.org/10.1038/s41467-021-24952-6

Bhattacharya, P., & Viesca, R. C. (2019). Fluid-induced aseismic fault slip outpaces pore-fluid migration. *Science*, *364*(6439), 464–468. https://doi.org/10.1126/science.aaw7354

Biot, M. A. (1956). Thermoelasticity and Irreversible Thermodynamics. *Journal of Applied Physics*, *27*(3), 240–253. https://doi.org/10.1063/1.1722351

Birdsell, D., Rajaram, H., & Karra, S. (2018). *Code Development for Modeling Induced Seismicity With Flow and Mechanics Using a Discrete Fracture Network and Matrix Formulation With Evolving Hydraulic Diffusivity*. D023S012R004.

Bödvarsson, G. S., & Tsang, C. F. (1982). Injection and Thermal Breakthrough in Fractured Geothermal Reservoirs. *Journal of Geophysical Research: Solid Earth*, *87*(B2), 1031–1048. https://doi.org/10.1029/JB087iB02p01031

Bommer, J. J., Oates, S., Cepeda, J. M., Lindholm, C., Bird, J., Torres, R., Marroquín, G., & Rivas, J. (2006). Control of hazard due to seismicity induced by a hot fractured rock geothermal project. *Engineering Geology*, *83*(4), 287–306. https://doi.org/10.1016/j.enggeo.2005.11.002

Bourouis, S., & Bernard, P. (2007). Evidence for coupled seismic and aseismic fault slip during water injection in the geothermal site of Soultz (France), and implications for seismogenic transients. *Geophysical Journal International*, *169*(2), 723–732. https://doi.org/10.1111/j.1365-246X.2006.03325.x

Boyet, A., De Simone, S., & Vilarrasa, V. (2023a). Physics-based modeling to understand and to propose forecasting methods of induced seismicity. *Seismological Research Letters*. https://doi.org/10.1785/0220230109

Boyet, A., De Simone, S., Vilarrasa, V., & Ge, S. (2023b). Poroelastic stress relaxation, slip stress transfer and friction weakening controlled post-injection seismicity at the Basel Enhanced Geothermal System. *Communications Earth & Environment*. https://doi.org/10.1038/s43247-023-00764-y

Broccardo, M., Mignan, A., Wiemer, S., Stojadinovic, B., & Giardini, D. (2017). Hierarchical Bayesian Modeling of Fluid-Induced Seismicity. *Geophysical Research Letters*, *44*(22), 11,357-11,367. https://doi.org/10.1002/2017GL075251

Brown, M. R. M., & Ge, S. (2018). Small Earthquakes Matter in Injection-Induced Seismicity. *Geophysical Research Letters*, *45*(11), 5445–5453. https://doi.org/10.1029/2018GL077472

Brune, J., & Thatcher, W. (2002). *International Handbook of Earthquake and Engineering Seismology International* (Association of Seismology and Physics of Earth's Interior, Committee on Education, Vol. 81A).

Buijze, L., van Bijsterveldt, L., Cremer, H., Paap, B., Veldkamp, H., Wassing, B. B. T., van Wees, J.-D., van Yperen, G. C. N., ter Heege, J. H., & Jaarsma, B. (2019). Review of induced seismicity in geothermal systems worldwide and implications for geothermal systems in the Netherlands. *Netherlands Journal of Geosciences*, *98*, e13. https://doi.org/10.1017/njg.2019.6

Byrne, H., Silva, J. A., Plesch, A., Juanes, R., & Shaw, J. H. (2020). The Groundbreaking Experiment in Earthquake Control at Rangely, Colorado, Revisited. *Geophysical Research Letters*, *47*(11), e2020GL088257. https://doi.org/10.1029/2020GL088257

Caine, J. S., Evans, J. P., & Forster, C. B. (1996). Fault zone architecture and permeability structure. *Geology*, *24*(11), 1025. https://doi.org/10.1130/0091-7613(1996)024<1025:FZAAPS>2.3.CO;2

Calò, M., Dorbath, C., Cornet, F. H., & Cuenot, N. (2011). Large-scale aseismic motion identified through 4-D P-wave tomography: Temporal subsetting of the stimulation period. *Geophysical Journal International*, *186*(3), 1295–1314. https://doi.org/10.1111/j.1365-246X.2011.05108.x

Candela, T., Pluymaekers, M., Ampuero, J.-P., van Wees, J.-D., Buijze, L., Wassing, B., Osinga, S., Grobbe, N., & Muntendam-Bos, A. G. (2022). Controls on the spatio-temporal patterns of induced seismicity in Groningen constrained by physics-based modelling with Ensemble-Smoother data assimilation. *Geophysical Journal International*, *229*(2), 1282–1308. https://doi.org/10.1093/gji/ggab497

Cappa, F., Guglielmi, Y., Nussbaum, C., De Barros, L., & Birkholzer, J. (2022). Fluid migration in low-permeability faults driven by decoupling of fault slip and opening. *Nature Geoscience*, *15*(9), 747–751. https://doi.org/10.1038/s41561-022-00993-4

Cappa, F., & Rutqvist, J. (2011). Modeling of coupled deformation and permeability evolution during fault reactivation induced by deep underground injection of CO2. *International Journal of Greenhouse Gas Control*, *5*(2), 336–346. https://doi.org/10.1016/j.ijggc.2010.08.005

Cappa, F., Scuderi, M. M., Collettini, C., Guglielmi, Y., & Avouac, J.-P. (2019). Stabilization of fault slip by fluid injection in the laboratory and in situ. *Science Advances*, *5*(3), eaau4065. https://doi.org/10.1126/sciadv.aau4065

Catalli, F., Meier, M.-A., & Wiemer, S. (2013). The role of Coulomb stress changes for injection-induced seismicity: The Basel enhanced geothermal system: The Basel Enhanced Geothermal System. *Geophysical Research Letters*, *40*(1), 72–77. https://doi.org/10.1029/2012GL054147

Catalli, F., Rinaldi, A. P., Gischig, V., Nespoli, M., & Wiemer, S. (2016). The importance of earthquake interactions for injection-induced seismicity: Retrospective modeling of the Basel Enhanced Geothermal System. *Geophysical Research Letters*, *43*(10), 4992–4999. https://doi.org/10.1002/2016GL068932

Chang, K. W., & Segall, P. (2016). Injection-induced seismicity on basement faults including poroelastic stressing: Induced seismicity on basement faults. *Journal of Geophysical Research: Solid Earth*, *121*(4), 2708–2726. https://doi.org/10.1002/2015JB012561

Chang, K. W., Yoon, H., Kim, Y., & Lee, M. Y. (2020). Operational and geological controls of coupled poroelastic stressing and pore-pressure accumulation along faults: Induced earthquakes in Pohang, South Korea. *Scientific Reports*, *10*(1), 2073. https://doi.org/10.1038/s41598-020-58881-z

Chang, K. W., Yoon, H., & Martinez, M. J. (2018). Seismicity Rate Surge on Faults after Shut-in: Poroelastic Response to Fluid Injection. *Bulletin of the Seismological Society of America*, *108*(4), 1889–1904. https://doi.org/10.1785/0120180054

Charléty, J., Cuenot, N., Dorbath, L., Dorbath, C., Haessler, H., & Frogneux, M. (2007). Large earthquakes during hydraulic stimulations at the geothermal site of Soultz-sous-Forêts. *International Journal of Rock Mechanics and Mining Sciences*, *44*(8), 1091–1105. https://doi.org/10.1016/j.ijrmms.2007.06.003

Clark, J. B. (1949). A Hydraulic Process for Increasing the Productivity of Wells. *Journal of Petroleum Technology*, *1*(01), 1–8. https://doi.org/10.2118/949001-G

Clasen Repolles, V., Rinaldi, A. P., Ciardo, F., Passarelli, L., Wiemer, S., & Bedretto Team. (2023). *Performance comparison of newly developed hydro-mechanical (hybrid) models for real-time induced seismicity forecasting* [Other]. oral. https://doi.org/10.5194/egusphere-egu23-12783

Collettini, C., Niemeijer, A., Viti, C., & Marone, C. (2009). Fault zone fabric and fault weakness. *Nature*, *462*(7275), 907–910. https://doi.org/10.1038/nature08585

Cornet, F. H. (2012). The relationship between seismic and aseismic motions induced by forced fluid injections. *Hydrogeology Journal*, *20*(8), 1463–1466. https://doi.org/10.1007/s10040-012-0901-z

Cornet, F. H. (2016). Seismic and aseismic motions generated by fluid injections. *Geomechanics for Energy and the Environment*, *5*, 42–54. https://doi.org/10.1016/j.gete.2015.12.003

Cornet, F. H., Helm, J., Poitrenaud, H., & Etchecopar, A. (1997). Seismic and Aseismic Slips Induced by Large-scale Fluid Injections. In S. Talebi (Ed.), *Seismicity Associated with Mines, Reservoirs and Fluid Injections* (pp. 563–583). Birkhäuser Basel. https://doi.org/10.1007/978-3-0348-8814-1_12

Dahm, T., Cesca, S., Hainzl, S., Braun, T., & Krüger, F. (2015). Discrimination between induced, triggered, and natural earthquakes close to hydrocarbon reservoirs: A probabilistic approach based on the modeling of depletion-induced stress changes and seismological source parameters. *Journal of Geophysical Research: Solid Earth*, *120*(4), 2491–2509. https://doi.org/10.1002/2014JB011778

Dal Zilio, L., Hegyi, B., Behr, W., & Gerya, T. (2022). Hydro-mechanical earthquake cycles in a poro-visco-elasto-plastic fluid-bearing fault structure. *Tectonophysics*, *838*, 229516. https://doi.org/10.1016/j.tecto.2022.229516

Danré, P., De Barros, L., Cappa, F., & Ampuero, J. (2022). Prevalence of Aseismic Slip Linking Fluid Injection to Natural and Anthropogenic Seismic Swarms. *Journal of Geophysical Research: Solid Earth*, *127*(12), e2022JB025571. https://doi.org/10.1029/2022JB025571

De Barros, L., Cappa, F., Guglielmi, Y., Duboeuf, L., & Grasso, J.-R. (2019). Energy of injection-induced seismicity predicted from in-situ experiments. *Scientific Reports*, *9*(1), 4999. https://doi.org/10.1038/s41598-019-41306-x

De Barros, L., Guglielmi, Y., Rivet, D., Cappa, F., & Duboeuf, L. (2018). Seismicity and fault aseismic deformation caused by fluid injection in decametric in-situ experiments. *Comptes Rendus Geoscience*, *350*(8), 464–475. https://doi.org/10.1016/j.crte.2018.08.002

De Barros, L., Wynants-Morel, N., Cappa, F., & Danré, P. (2021). Migration of Fluid-Induced Seismicity Reveals the Seismogenic State of Faults. *Journal of Geophysical Research: Solid Earth*, *126*(11). https://doi.org/10.1029/2021JB022767

De Simone, S., & Carrera, J. (2017). Analytical Solutions to Coupled HM Problems to Highlight the Nonlocal Nature of Aquifer Storage: NONLOCAL STORAGE. *Water Resources Research*, *53*(11), 9580–9599. https://doi.org/10.1002/2017WR020824

De Simone, S., Carrera, J., & Gómez-Castro, B. M. (2017a). A practical solution to the mechanical perturbations induced by non-isothermal injection into a permeable medium. *International Journal of Rock Mechanics and Mining Sciences*, *91*, 7–17. https://doi.org/10.1016/j.ijrmms.2016.11.001

De Simone, S., Carrera, J., & Vilarrasa, V. (2017b). Superposition approach to understand triggering mechanisms of post-injection induced seismicity. *Geothermics*, *70*, 85–97. https://doi.org/10.1016/j.geothermics.2017.05.011

De Simone, S., Kivi, I. R., Min, K.-B., & Rutqvist, J. (2023). Chapter 9: Induced seismicity in EGS: observations and triggering mechanisms. In *Enhanced Geothermal Systems (EGS)* (1st Edition, p. 39). CRC Press.

De Simone, S., Vilarrasa, V., Carrera, J., Alcolea, A., & Meier, P. (2013). Thermal coupling may control mechanical stability of geothermal reservoirs during cold water injection. *Physics and Chemistry of the Earth, Parts A/B/C*, *64*, 117–126. https://doi.org/10.1016/j.pce.2013.01.001

De Barros, L., Guglielmi, Y., Cappa, F., Nussbaum, C., & Birkholzer, J. (2023). Induced microseismicity and tremor signatures illuminate different slip behaviours in a natural shale fault reactivated by a fluid pressure stimulation (Mont Terri). *Geophysical Journal International*, *235*(1), 531–541. https://doi.org/10.1093/gji/ggad231

Deichmann, N., & Giardini, D. (2009). Earthquakes Induced by the Stimulation of an Enhanced Geothermal System below Basel (Switzerland). *Seismological Research Letters*, *80*(5), 784–798. https://doi.org/10.1785/gssrl.80.5.784

Deichmann, N., Kraft, T., & Evans, K. F. (2014). Identification of faults activated during the stimulation of the Basel geothermal project from cluster analysis and focal mechanisms of the larger magnitude events. *Geothermics*, *52*, 84–97. https://doi.org/10.1016/j.geothermics.2014.04.001

Dempsey, D., & Riffault, J. (2019). Response of Induced Seismicity to Injection Rate Reduction: Models of Delay, Decay, Quiescence, Recovery, and Oklahoma. *Water Resources Research*, *55*(1), 656–681. https://doi.org/10.1029/2018WR023587

Dempsey, D., & Suckale, J. (2017). Physics-based forecasting of induced seismicity at Groningen gas field, the Netherlands: Forecasting Groningen seismicity. *Geophysical Research Letters*, *44*(15), 7773–7782. https://doi.org/10.1002/2017GL073878

Dempsey, D., & Suckale, J. (2023). Physics-Based Forecasting of Induced Seismicity at Groningen Gas Field, The Netherlands: Post Hoc Evaluation and Forecast Update. *Seismological Research Letters*. https://doi.org/10.1785/0220220317

Dershowitz, W. S., & Herda, H. H. (1992). *Interpretation of fracture spacing and intensity*. The 33rd US Symposium on Rock Mechanics (USRMS).

Dieterich, J. (1978). Time-Dependent Friction and the Mechanics of Stick-Slip. In J. Byerlee & M. Wyss (Eds.), *Rock Friction and Earthquake Prediction* (pp. 790–806). Birkhäuser Basel. https://doi.org/10.1007/978-3-0348-7182-2_15

Dieterich, J. (1994). A constitutive law for rate of earthquake production and its application to earthquake clustering. *Journal of Geophysical Research: Solid Earth*, *99*(B2), 2601–2618. https://doi.org/10.1029/93JB02581

Dieterich, J., Richards-Dinger, K. B., & Kroll, K. A. (2015). Modeling Injection-Induced Seismicity with the Physics-Based Earthquake Simulator RSQSim. *Seismological Research Letters*, *86*(4), 1102–1109. https://doi.org/10.1785/0220150057

Dorbath, L., Cuenot, N., Genter, A., & Frogneux, M. (2009). Seismic response of the fractured and faulted granite of Soultz-sous-Forêts (France) to 5 km deep massive water injections. *Geophysical Journal International*, *177*(2), 653–675. https://doi.org/10.1111/j.1365-246X.2009.04030.x

Duboeuf, L., De Barros, L., Cappa, F., Guglielmi, Y., Deschamps, A., & Seguy, S. (2017). Aseismic Motions Drive a Sparse Seismicity During Fluid Injections Into a Fractured Zone in a Carbonate Reservoir: Injection-Induced (A)Seismic Motions. *Journal of Geophysical Research: Solid Earth*, *122*(10), 8285–8304. https://doi.org/10.1002/2017JB014535

Ellsworth, W. L. (2013). Injection-Induced Earthquakes. *Science*, *341*(6142), 1225942. https://doi.org/10.1126/science.1225942

Ellsworth, W. L., Giardini, D., Townend, J., Ge, S., & Shimamoto, T. (2019). Triggering of the Pohang, Korea, Earthquake (Mw 5.5) by Enhanced Geothermal System Stimulation. *Seismological Research Letters*. https://doi.org/10.1785/0220190102

Elsworth, D., Spiers, C. J., & Niemeijer, A. R. (2016). Understanding induced seismicity. *Science*, *354*(6318), 1380–1381. https://doi.org/10.1126/science.aal2584

Elsworth, D., & Yasuhara, H. (2010). Mechanical and transport constitutive models for fractures subject to dissolution and precipitation: MECHANICAL AND TRANSPORT CONSTITUTIVE MODELS. *International Journal for Numerical and Analytical Methods in Geomechanics*, *34*(5), 533–549. https://doi.org/10.1002/nag.831

Evans, K. F., Zappone, A., Kraft, T., Deichmann, N., & Moia, F. (2012). A survey of the induced seismic responses to fluid injection in geothermal and CO2 reservoirs in Europe. *Geothermics*, *41*, 30–54. https://doi.org/10.1016/j.geothermics.2011.08.002

Eyre, T. S., Eaton, D. W., Garagash, D. I., Zecevic, M., Venieri, M., Weir, R., & Lawton, D. C. (2019). The role of aseismic slip in hydraulic fracturing–induced seismicity. *Science Advances*, *5*(8), eaav7172. https://doi.org/10.1126/sciadv.aav7172

Fasola, S. L., & Brudzinski, M. R. (2023). Machine Learning Reveals Additional Hydraulic Fracture-Induced Seismicity in the Eagle Ford Shale. *Journal of Geophysical Research: Solid Earth*, *128*(2), e2022JB025436. https://doi.org/10.1029/2022JB025436

Fiori, R., Vergne, J., Schmittbuhl, J., & Zigone, D. (2023). Monitoring induced microseismicity in an urban context using very small seismic arrays: The case study of the Vendenheim EGS project. *GEOPHYSICS*, *88*(5), WB71–WB87. https://doi.org/10.1190/geo2022-0620.1

Folch, A., Bhihe, C., Caviedes-Vouillième, D., De La Puente, J., Esposti Ongaro, T., Garg, D., Gibbons, S. J., Kaus, B., Monterrubio, M., Räss, L., Reis, C., Scaini, C., Srivastava, N., Vilarrasa, V., & Zwinger, T. (2023). *11th EGU Galileo Conference: Solid Earth and Geohazards in the Exascale Era Consensual Document* [Application/pdf]. https://doi.org/10.20350/DIGITALCSIC/15439

Foulger, G. R., Wilson, M. P., Gluyas, J. G., Julian, B. R., & Davies, R. J. (2018). Global review of human-induced earthquakes. *Earth-Science Reviews*, *178*, 438–514. https://doi.org/10.1016/j.earscirev.2017.07.008

Frash, L. P., Gutierrez, M., Hampton, J., & Hood, J. (2015). Laboratory simulation of binary and triple well EGS in large granite blocks using AE events for drilling guidance. *Geothermics*, *55*, 1–15. https://doi.org/10.1016/j.geothermics.2015.01.002

Gan, Q., & Lei, Q. (2020). Induced fault reactivation by thermal perturbation in enhanced geothermal systems. *Geothermics*, *86*, 101814. https://doi.org/10.1016/j.geothermics.2020.101814

Garagash, D. I., & Germanovich, L. N. (2012). Nucleation and arrest of dynamic slip on a pressurized fault. *Journal of Geophysical Research: Solid Earth*, *117*(B10), 2012JB009209. https://doi.org/10.1029/2012JB009209

Gaucher, E., Schoenball, M., Heidbach, O., Zang, A., Fokker, P. A., van Wees, J.-D., & Kohl, T. (2015). Induced seismicity in geothermal reservoirs: A review of forecasting approaches. *Renewable and Sustainable Energy Reviews*, *52*, 1473–1490. https://doi.org/10.1016/j.rser.2015.08.026

Ge, S., & Saar, M. O. (2022). Review: Induced Seismicity During Geoenergy Development—A Hydromechanical Perspective. *Journal of Geophysical Research: Solid Earth*, *127*(3). https://doi.org/10.1029/2021JB023141

Ghassemi, A. (2012). A Review of Some Rock Mechanics Issues in Geothermal Reservoir Development. *Geotechnical and Geological Engineering*, *30*(3), 647–664. https://doi.org/10.1007/s10706-012-9508-3

Ghassemi, A., Nygren, A., & Cheng, A. (2008). Effects of heat extraction on fracture aperture: A poro–thermoelastic analysis. *Geothermics*, *37*(5), 525–539. https://doi.org/10.1016/j.geothermics.2008.06.001

Gischig, V., Bethmann, F., Hertrich, M., Wiemer, S., Mignan, A., Broccardo, M., Villiger, L., Obermann, A., & Diehl, T. (2019). *Induced seismic hazard and risk analysis of hydraulic stimulation experiments at the Bedretto Underground Laboratory for Geosciences and Geoenergies (BULGG)* [Application/pdf,40 p.; 56 p. updated version]. ETH Zurich. https://doi.org/10.3929/ETHZ-B-000384348

Gischig, V. S., Giardini, D., Amann, F., Hertrich, M., Krietsch, H., Loew, S., Maurer, H., Villiger, L., Wiemer, S., Bethmann, F., Brixel, B., Doetsch, J., Doonechaly, N. G., Driesner, T.,

Dutler, N., Evans, K. F., Jalali, M., Jordan, D., Kittilä, A., … Valley, B. (2020). Hydraulic stimulation and fluid circulation experiments in underground laboratories: Stepping up the scale towards engineered geothermal systems. *Geomechanics for Energy and the Environment*, *24*, 100175. https://doi.org/10.1016/j.gete.2019.100175

Gischig, V. S., & Wiemer, S. (2013). A stochastic model for induced seismicity based on non-linear pressure diffusion and irreversible permeability enhancement. *Geophysical Journal International*, *194*(2), 1229–1249. https://doi.org/10.1093/gji/ggt164

Goebel, T. H. W., & Brodsky, E. E. (2018). The spatial footprint of injection wells in a global compilation of induced earthquake sequences. *Science*, *361*(6405), 899–904. https://doi.org/10.1126/science.aat5449

Goebel, T. H. W., Weingarten, M., Chen, X., Haffener, J., & Brodsky, E. E. (2017). The 2016 Mw5.1 Fairview, Oklahoma earthquakes: Evidence for long-range poroelastic triggering at >40 km from fluid disposal wells. *Earth and Planetary Science Letters*, *472*, 50–61. https://doi.org/10.1016/j.epsl.2017.05.011

Goertz-Allmann, B. P., Goertz, A., & Wiemer, S. (2011). Stress drop variations of induced earthquakes at the Basel geothermal site. *Geophysical Research Letters*, *38*(9), 2011GL047498. https://doi.org/10.1029/2011GL047498

Goertz-Allmann, B. P., & Wiemer, S. (2013). Geomechanical modeling of induced seismicity source parameters and implications for seismic hazard assessment. *GEOPHYSICS*, *78*(1), KS25–KS39. https://doi.org/10.1190/geo2012-0102.1

Grigoli, F., Cesca, S., Priolo, E., Rinaldi, A. P., Clinton, J. F., Stabile, T. A., Dost, B., Fernandez, M. G., Wiemer, S., & Dahm, T. (2017). Current challenges in monitoring, discrimination, and management of induced seismicity related to underground industrial activities: A European perspective: Challenges in induced seismicity. *Reviews of Geophysics*, *55*(2), 310–340. https://doi.org/10.1002/2016RG000542

Grigoli, F., Cesca, S., Rinaldi, A. P., Manconi, A., López-Comino, J. A., Clinton, J. F., Westaway, R., Cauzzi, C., Dahm, T., & Wiemer, S. (2018). The November 2017 M_w 5.5 Pohang earthquake: A possible case of induced seismicity in South Korea. *Science*, *360*(6392), 1003–1006. https://doi.org/10.1126/science.aat2010

Gringarten, A. C., Witherspoon, P. A., & Ohnishi, Y. (1975). Theory of heat extraction from fractured hot dry rock. *Journal of Geophysical Research*, *80*(8), 1120–1124. https://doi.org/10.1029/JB080i008p01120

Groos, J., Zeiß, J., Grund, M., & Ritter, J. (2013). *Microseismicity at two geothermal power plants at Landau and Insheim in the Upper Rhine Graben, Germany*. EGU2013-2742.

Guglielmi, Y., Cappa, F., Avouac, J.-P., Henry, P., & Elsworth, D. (2015). Seismicity triggered by fluid injection–induced aseismic slip. *Science*, *348*(6240), 1224–1226. https://doi.org/10.1126/science.aab0476

Guglielmi, Y., Elsworth, D., Cappa, F., Henry, P., Gout, C., Dick, P., & Durand, J. (2015). In situ observations on the coupling between hydraulic diffusivity and displacements during fault reactivation in shales. *Journal of Geophysical Research: Solid Earth*, *120*(11), 7729–7748. https://doi.org/10.1002/2015JB012158

Guglielmi, Y., Nussbaum, C., Jeanne, P., Rutqvist, J., Cappa, F., & Birkholzer, J. (2020). Complexity of Fault Rupture and Fluid Leakage in Shale: Insights From a Controlled Fault Activation Experiment. *Journal of Geophysical Research: Solid Earth*, *125*(2), e2019JB017781. https://doi.org/10.1029/2019JB017781

Gutenberg, B., & Richter, C. F. (1942). Earthquake magnitude, intensity, energy, and acceleration*. *Bulletin of the Seismological Society of America*, *32*(3), 163–191. https://doi.org/10.1785/BSSA0320030163

Hager, B. H., Dieterich, J., Frohlich, C., Juanes, R., Mantica, S., Shaw, J. H., Bottazzi, F., Caresani, F., Castineira, D., Cominelli, A., Meda, M., Osculati, L., Petroselli, S., & Plesch, A. (2021). A process-based approach to understanding and managing triggered seismicity. *Nature*, *595*(7869), 684–689. https://doi.org/10.1038/s41586-021-03668-z

Hanks, T. C., & Kanamori, H. (1979). A moment magnitude scale. *J. Geophys. Res.*, *84*.

Häring, M. O., Schanz, U., Ladner, F., & Dyer, B. C. (2008). Characterisation of the Basel 1 enhanced geothermal system. *Geothermics*, *37*(5), 469–495. https://doi.org/10.1016/j.geothermics.2008.06.002

He, M., Li, Q., & Li, X. (2020). Injection-Induced Seismic Risk Management Using Machine Learning Methodology – A Perspective Study. *Frontiers in Earth Science*, *8*, 227. https://doi.org/10.3389/feart.2020.00227

Heidbach, O., Rajabi, M., Cui, X., Fuchs, K., Müller, B., Reinecker, J., Reiter, K., Tingay, M., Wenzel, F., Xie, F., Ziegler, M. O., Zoback, M.-L., & Zoback, M. (2018). The World Stress Map database release 2016: Crustal stress pattern across scales. *Tectonophysics*, *744*, 484–498. https://doi.org/10.1016/j.tecto.2018.07.007

Herrmann, M., Kraft, T., Tormann, T., Scarabello, L., & Wiemer, S. (2019). A Consistent High-Resolution Catalog of Induced Seismicity in Basel Based on Matched Filter Detection and Tailored Post-Processing. *Journal of Geophysical Research: Solid Earth*, *124*(8), 8449–8477. https://doi.org/10.1029/2019JB017468

Hofmann, H., Zimmermann, G., Farkas, M., Huenges, E., Zang, A., Leonhardt, M., Kwiatek, G., Martinez-Garzon, P., Bohnhoff, M., Min, K.-B., Fokker, P., Westaway, R., Bethmann, F., Meier, P., Yoon, K. S., Choi, J. W., Lee, T. J., & Kim, K. Y. (2019). First field application of cyclic soft stimulation at the Pohang Enhanced Geothermal System site in Korea. *Geophysical Journal International*, *217*(2), 926–949. https://doi.org/10.1093/gji/ggz058

Hossein Hakimhashemi, A., Schoenball, M., Heidbach, O., Zang, A., & Grünthal, G. (2014). Forward modelling of seismicity rate changes in georeservoirs with a hybrid geomechanical–statistical prototype model. *Geothermics*, *52*, 185–194. https://doi.org/10.1016/j.geothermics.2014.01.001

Hsieh, P. A., & Bredehoeft, J. D. (1981). A reservoir analysis of the Denver earthquakes: A case of induced seismicity. *Journal of Geophysical Research: Solid Earth*, *86*(B2), 903–920. https://doi.org/10.1029/JB086iB02p00903

Hu, L., & Ghassemi, A. (2020). Heat production from lab-scale enhanced geothermal systems in granite and gabbro. *International Journal of Rock Mechanics and Mining Sciences*, *126*, 104205. https://doi.org/10.1016/j.ijrmms.2019.104205

Hu, L., Ghassemi, A., Pritchett, J., & Garg, S. (2020). Characterization of laboratory-scale hydraulic fracturing for EGS. *Geothermics*, *83*, 101706. https://doi.org/10.1016/j.geothermics.2019.07.004

Huang, Y., Ellsworth, W. L., & Beroza, G. C. (2017). Stress drops of induced and tectonic earthquakes in the central United States are indistinguishable. *Science Advances*, *3*(8), e1700772. https://doi.org/10.1126/sciadv.1700772

IEA. (2017). *World Energy Outlook 2017*.

IPCC. (2022). *Climate Change 2022: Impacts, adaptation, and Vulnerability. Contribution of Working Group II to the Sixth Assessment Report of the Intergovernmental Panel on Climate Change*.

IPCC. (2023). *Climate Change 2023: Synthesis Report. A Report of the Intergovernmental Panel on Climate Change. Contribution of Working Groups I, II and III to the Sixth Assessment Report of the Intergovernmental Panel on Climate Change [Core Writing Team, H. Lee and J. Romero (eds.)]*. (p. (in press)).

Ito, T., & Zoback, M. D. (2000). Fracture permeability and in situ stress to 7 km depth in the KTB scientific drillhole. *Geophysical Research Letters*, *27*(7), 1045–1048. https://doi.org/10.1029/1999GL011068

Jacquey, A. B., & Viesca, R. C. (2023). Nucleation and Arrest of Fluid-Induced Aseismic Slip. *Geophysical Research Letters*, *50*(4). https://doi.org/10.1029/2022GL101228

Jaeger, J. C., & Cook, N. G. (1979). *Fundamentals of Rock Mechanics* (Chapman&Hall).

Jaeger, J. C., Cook, N. G., & Zimmerman, R. (2009). *Fundamentals of rock mechanics*. John Wiley & Sons.

Ji, Y., Fang, Z., & Wu, W. (2021). Fluid Overpressurization of Rock Fractures: Experimental Investigation and Analytical Modeling. *Rock Mechanics and Rock Engineering*, *54*(6), 3039–3050. https://doi.org/10.1007/s00603-021-02453-8

Ji, Y., Hofmann, H., Duan, K., & Zang, A. (2022). Laboratory experiments on fault behavior towards better understanding of injection-induced seismicity in geoenergy systems. *Earth-Science Reviews*, *226*, 103916. https://doi.org/10.1016/j.earscirev.2021.103916

Ji, Y., Yoon, J. S., Zang, A., & Wu, W. (2021). Mitigation of injection-induced seismicity on undrained faults in granite using cyclic fluid injection: A laboratory study. *International Journal of Rock Mechanics and Mining Sciences*, *146*, 104881. https://doi.org/10.1016/j.ijrmms.2021.104881

Jia, Y., Tsang, C.-F., Hammar, A., & Niemi, A. (2022). Hydraulic stimulation strategies in enhanced geothermal systems (EGS): A review. *Geomechanics and Geophysics for Geo-Energy and Geo-Resources*, *8*(6), 211. https://doi.org/10.1007/s40948-022-00516-w

Jing, Z., Watanabe, K., Willis-Richards, J., & Hashida, T. (2002). A 3-D water/rock chemical interaction model for prediction of HDR/HWR geothermal reservoir performance. *Geothermics*, *31*(1), 1–28. https://doi.org/10.1016/S0375-6505(00)00059-6

Jung, R. (2013). EGS — Goodbye or Back to the Future 95. In R. Jeffrey (Ed.), *Effective and Sustainable Hydraulic Fracturing*. InTech. https://doi.org/10.5772/56458

Kanamori, H. (1977). The energy release in great earthquakes. *Journal of Geophysical Research*, *82*(20), 2981–2987. https://doi.org/10.1029/JB082i020p02981

Kanamori, H. (1978). Quantification of Earthquakes. *Nature*, *271*, 411–414.

Kanamori, H., & Brodsky, E. E. (2004). The physics of earthquakes. *Reports on Progress in Physics*, *67*(8), 1429–1496. https://doi.org/10.1088/0034-4885/67/8/R03

Karvounis, D., & Wiemer, S. (2022). A discrete fracture hybrid model for forecasting diffusion-induced seismicity and power generation in enhanced geothermal systems. *Geophysical Journal International*, *230*(1), 84–113. https://doi.org/10.1093/gji/ggac056

Keranen, K. M., & Weingarten, M. (2018). Induced Seismicity. *Annual Review of Earth and Planetary Sciences*, *46*(1), 149–174. https://doi.org/10.1146/annurev-earth-082517-010054

Kettlety, T., Verdon, J. P., Werner, M. J., Kendall, J. M., & Budge, J. (2019). Investigating the role of elastostatic stress transfer during hydraulic fracturing-induced fault activation. *Geophysical Journal International*. https://doi.org/10.1093/gji/ggz080

Kim, K.-H., Ree, J.-H., Kim, Y., Kim, S., Kang, S. Y., & Seo, W. (2018). Assessing whether the 2017 M_w 5.4 Pohang earthquake in South Korea was an induced event. *Science*, *360*(6392), 1007–1009. https://doi.org/10.1126/science.aat6081

Kim, K.-I., Yoo, H., Park, S., Yim, J., Xie, L., Min, K.-B., & Rutqvist, J. (2022). Induced and triggered seismicity by immediate stress transfer and delayed fluid migration in a fractured geothermal reservoir at Pohang, South Korea. *International Journal of Rock Mechanics and Mining Sciences*, *153*, 105098. https://doi.org/10.1016/j.ijrmms.2022.105098

King, G. C. P., Stein, R. S., & Lin, J. (1994). Static stress changes and the triggering of earthquakes. *Bulletin of the Seismological Society of America*, *84*(3), 935–953.

Kirkpatrick, J. D., & Shipton, Z. K. (2009). Geologic evidence for multiple slip weakening mechanisms during seismic slip in crystalline rock. *Journal of Geophysical Research*, *114*(B12), B12401. https://doi.org/10.1029/2008JB006037

Kivi, I. R., Boyet, A., Wu, H., Walter, L., Hanson-Hedgecock, S., Parisio, F., & Vilarrasa, V. (2023). Global physics-based database of injection-induced seismicity. *Earth System Science Data*, *15*(7), 3163–3182. https://doi.org/10.5194/essd-15-3163-2023

Kivi, I. R., Pujades, E., Rutqvist, J., & Vilarrasa, V. (2022). Cooling-induced reactivation of distant faults during long-term geothermal energy production in hot sedimentary aquifers. *Scientific Reports*, *12*(1), 2065. https://doi.org/10.1038/s41598-022-06067-0

Knudby, C., & Carrera, J. (2006). On the use of apparent hydraulic diffusivity as an indicator of connectivity. *Journal of Hydrology*, *329*(3–4), 377–389. https://doi.org/10.1016/j.jhydrol.2006.02.026

Korean Government Commission. (2019). Summary report of the Korean Government Commission on relations between the 2017 Pohang Earthquake and EGS Project. *Geological Society of Korea*.

Kraft, T., & Deichmann, N. (2014). High-precision relocation and focal mechanism of the injection-induced seismicity at the Basel EGS. *Geothermics*, *52*, 59–73. https://doi.org/10.1016/j.geothermics.2014.05.014

Krietsch, H., Gischig, V. S., Doetsch, J., Evans, K. F., Villiger, L., Jalali, M., Valley, B., Löw, S., & Amann, F. (2020). Hydromechanical processes and their influence on the stimulation effected volume: Observations from a decameter-scale hydraulic stimulation project. *Solid Earth*, *11*(5), 1699–1729. https://doi.org/10.5194/se-11-1699-2020

Kwiatek, G., Bulut, F., Bohnhoff, M., & Dresen, G. (2014). High-resolution analysis of seismicity induced at Berlín geothermal field, El Salvador. *Geothermics*, *52*, 98–111. https://doi.org/10.1016/j.geothermics.2013.09.008

Kwiatek, G., Saarno, T., Ader, T., Bluemle, F., Bohnhoff, M., Chendorain, M., Dresen, G., Heikkinen, P., Kukkonen, I., Leary, P., Leonhardt, M., Malin, P., Martínez-Garzón, P., Passmore, K., Passmore, P., Valenzuela, S., & Wollin, C. (2019). Controlling fluid-induced seismicity during a 6.1-km-deep geothermal stimulation in Finland. *Science Advances*, *5*(5), eaav7224. https://doi.org/10.1126/sciadv.aav7224

Langenbruch, C., & Shapiro, S. A. (2010). Decay rate of fluid-induced seismicity after termination of reservoir stimulations. *GEOPHYSICS*, *75*(6), MA53–MA62. https://doi.org/10.1190/1.3506005

Langenbruch, C., Weingarten, M., & Zoback, M. D. (2018). Physics-based forecasting of man-made earthquake hazards in Oklahoma and Kansas. *Nature Communications*, *9*(1), 3946. https://doi.org/10.1038/s41467-018-06167-4

Lasaga, A. C., Soler, J. M., Ganor, J., Burch, T. E., & Nagy, K. L. (1994). Chemical weathering rate laws and global geochemical cycles. *Geochimica et Cosmochimica Acta*, *58*(10), 2361–2386. https://doi.org/10.1016/0016-7037(94)90016-7

Lee, K.-K., Ellsworth, W. L., Giardini, D., Townend, J., Ge, S., Shimamoto, T., Yeo, I.-W., Kang, T.-S., Rhie, J., Sheen, D.-H., Chang, C., Woo, J.-U., & Langenbruch, C. (2019). Managing injection-induced seismic risks. *Science*, *364*(6442), 730–732. https://doi.org/10.1126/science.aax1878

Lengliné, O., Lamourette, L., Vivin, L., Cuenot, N., & Schmittbuhl, J. (2014). Fluid-induced earthquakes with variable stress drop. *Journal of Geophysical Research: Solid Earth*, *119*(12), 8900–8913. https://doi.org/10.1002/2014JB011282

Lengliné, O., Schmittbuhl, J., Drif, K., Lambotte, S., Grunberg, M., Kinscher, J., Sira, C., Schlupp, A., Schaming, M., Jund, H., & Masson, F. (2023). The largest induced earthquakes during the GEOVEN deep geothermal project, Strasbourg, 2018–2022: From source parameters to intensity maps. *Geophysical Journal International*, *234*(3), 2445–2457. https://doi.org/10.1093/gji/ggad255

Lin, J., & Stein, R. S. (2004). Stress triggering in thrust and subduction earthquakes and stress interaction between the southern San Andreas and nearby thrust and strike-slip faults: Stress triggering and fault interaction. *Journal of Geophysical Research: Solid Earth*, *109*(B2). https://doi.org/10.1029/2003JB002607

López-Comino, J. A., Cesca, S., Heimann, S., Grigoli, F., Milkereit, C., Dahm, T., & Zang, A. (2017). Characterization of Hydraulic Fractures Growth During the Äspö Hard Rock Laboratory Experiment (Sweden). *Rock Mechanics and Rock Engineering*, *50*(11), 2985–3001. https://doi.org/10.1007/s00603-017-1285-0

Luu, K. (2022). *bruces: A bunch of really useful codes for earthquake stuff* (v0.5.0) [Computer software]. Zenodo. https://doi.org/10.5281/ZENODO.6422572

Luu, K., Schoenball, M., Oldenburg, C. M., & Rutqvist, J. (2022). Coupled Hydromechanical Modeling of Induced Seismicity From CO_2 Injection in the Illinois Basin. *Journal of Geophysical Research: Solid Earth*, *127*(5). https://doi.org/10.1029/2021JB023496

Majer, E. L., Baria, R., Stark, M., Oates, S., Bommer, J., Smith, B., & Asanuma, H. (2007). Induced seismicity associated with Enhanced Geothermal Systems. *Geothermics*, *36*(3), 185–222. https://doi.org/10.1016/j.geothermics.2007.03.003

Majer, E. L., & Peterson, J. E. (2007). The impact of injection on seismicity at The Geysers, California Geothermal Field. *International Journal of Rock Mechanics and Mining Sciences*, *44*(8), 1079–1090. https://doi.org/10.1016/j.ijrmms.2007.07.023

Marone, C. (1998). The effect of loading rate on static friction and the rate of fault healing during the earthquake cycle. *Nature*, *391*(6662), 69–72. https://doi.org/10.1038/34157

McClure, M. W. (2015). Generation of large postinjection-induced seismic events by backflow from dead-end faults and fractures. *Geophysical Research Letters*, *42*(16), 6647–6654. https://doi.org/10.1002/2015GL065028

McClure, M. W., & Horne, R. N. (2011). Investigation of injection-induced seismicity using a coupled fluid flow and rate/state friction model. *GEOPHYSICS*, *76*(6), WC181–WC198. https://doi.org/10.1190/geo2011-0064.1

McClure, M. W., & Horne, R. N. (2014). An investigation of stimulation mechanisms in Enhanced Geothermal Systems. *International Journal of Rock Mechanics and Mining Sciences*, *72*, 242–260. https://doi.org/10.1016/j.ijrmms.2014.07.011

McGarr, A. (1976). Seismic moments and volume changes. *Journal of Geophysical Research*, *81*(8), 1487–1494. https://doi.org/10.1029/JB081i008p01487

McGarr, A. (2014). Maximum magnitude earthquakes induced by fluid injection: Limits on fluid injection earthquakes. *Journal of Geophysical Research: Solid Earth*, *119*(2), 1008–1019. https://doi.org/10.1002/2013JB010597

McGarr, A., Simpson, D., Seeber, L., & Lee, W. (2002). Case histories of induced and triggered seismicity. *International Geophysics Series*, *81*, 647–664.

Mereu, R. F. (2020). A study of the relations between ML, Me, Mw, apparent stress, and fault aspect ratio. *Physics of the Earth and Planetary Interiors*, *298*, 106278. https://doi.org/10.1016/j.pepi.2019.106278

Meyer, H., Smith, J. D., Bourne, S., & Avouac, J.-P. (2023). An integrated framework for surface deformation modelling and induced seismicity forecasting due to reservoir operations. *Geological Society, London, Special Publications*, *528*(1), SP528-2022–2169. https://doi.org/10.1144/SP528-2022-169

Mignan, A., Broccardo, M., & Wang, Z. (2021). Comprehensive Survey of Seismic Hazard at Geothermal Sites by a Meta-Analysis of the Underground Feedback Activation Parameter afb. *Energies*, *14*(23), 7998. https://doi.org/10.3390/en14237998

Mignan, A., Broccardo, M., Wiemer, S., & Giardini, D. (2017). Induced seismicity closed-form traffic light system for actuarial decision-making during deep fluid injections. *Scientific Reports*, *7*(1), 13607. https://doi.org/10.1038/s41598-017-13585-9

Miller, S. A. (2016). Modeling enhanced geothermal systems and the essential nature of large-scale changes in permeability at the onset of slip. In T. Gleeson & S. E. Ingebritse (Eds.), *Crustal Permeability* (pp. 353–362). John Wiley & Sons, Ltd. https://doi.org/10.1002/9781119166573.ch27

Min, K.-B., Rutqvist, J., & Elsworth, D. (2009). Chemically and mechanically mediated influences on the transport and mechanical characteristics of rock fractures. *International*

Journal of Rock Mechanics and Mining Sciences, *46*(1), 80–89. https://doi.org/10.1016/j.ijrmms.2008.04.002

Mukuhira, Y., Asanuma, H., Niitsuma, H., & Häring, M. O. (2013). Characteristics of large-magnitude microseismic events recorded during and after stimulation of a geothermal reservoir at Basel, Switzerland. *Geothermics*, *45*, 1–17. https://doi.org/10.1016/j.geothermics.2012.07.005

Mukuhira, Y., Dinske, C., Asanuma, H., Ito, T., & Häring, M. O. (2017). Pore pressure behavior at the shut-in phase and causality of large induced seismicity at Basel, Switzerland. *Journal of Geophysical Research: Solid Earth*, *122*(1), 411–435. https://doi.org/10.1002/2016JB013338

Navas-Portella, V., Jiménez, A., & Corral, Á. (2020). No Significant Effect of Coulomb Stress on the Gutenberg-Richter Law after the Landers Earthquake. *Scientific Reports*, *10*(1), 2901. https://doi.org/10.1038/s41598-020-59416-2

Niemeijer, A., Di Toro, G., Griffith, W. A., Bistacchi, A., Smith, S. A. F., & Nielsen, S. (2012). Inferring earthquake physics and chemistry using an integrated field and laboratory approach. *Journal of Structural Geology*, *39*, 2–36. https://doi.org/10.1016/j.jsg.2012.02.018

Noël, C., Passelègue, F. X., Giorgetti, C., & Violay, M. (2019). Fault Reactivation During Fluid Pressure Oscillations: Transition From Stable to Unstable Slip. *Journal of Geophysical Research: Solid Earth*, *124*(11), 10940–10953. https://doi.org/10.1029/2019JB018517

Norbeck, J. H., McClure, M. W., & Horne, R. N. (2018). Field observations at the Fenton Hill enhanced geothermal system test site support mixed-mechanism stimulation. *Geothermics*, *74*, 135–149. https://doi.org/10.1016/j.geothermics.2018.03.003

Ogata, S., Yasuhara, H., Kinoshita, N., Cheon, D.-S., & Kishida, K. (2018). Modeling of coupled thermal-hydraulic-mechanical-chemical processes for predicting the evolution in permeability and reactive transport behavior within single rock fractures. *International Journal of Rock Mechanics and Mining Sciences*, *107*, 271–281. https://doi.org/10.1016/j.ijrmms.2018.04.015

Ogata, Y. (1988). Statistical models for earthquake occurrences and residual analysis for point processes. *Journal of the American Statistical Association*, *83*, 9–27.

Ogata, Y. (1992). Detection of precursory relative quiescence before great earthquakes through a statistical model. *Journal of Geophysical Research*, *97*(B13), 19845. https://doi.org/10.1029/92JB00708

Ohnaka, M. (1975). Frictional characteristics of typical rocks. *Journal of Physics of the Earth*, *23*(1), 87–112. https://doi.org/10.4294/jpe1952.23.87

Okada, Y. (1992). Internal deformation due to shear and tensile faults in a half-space. *Bulletin of the Seismological Society of America*, *82*(2), 1018–1040. https://doi.org/10.1785/BSSA0820021018

Olivella, S., & Alonso, E. E. (2008). Gas flow through clay barriers. *Géotechnique*, *58*(3), 157–176. https://doi.org/10.1680/geot.2008.58.3.157

Olivella, S., Gens, A., Carrera, J., & Alonso, E. E. (1996). Numerical formulation for a simulator (CODE_BRIGHT) for the coupled analysis of saline media. *Engineering Computations*, *13*(7), 87–112. https://doi.org/10.1108/02644409610151575

Omori, F. (n.d.). On after-shocks. *Seismological Journal of Japan, p. 71–80, 1894.*, 71–80.

Omori, F. (1895). *On the After-shocks of Earthquakes*. College of Science, Imperial University. https://doi.org/10.15083/00037562

Palciauskas, V. V., & Domenico, P. A. (1982). Characterization of drained and undrained response of thermally loaded repository rocks. *Water Resources Research*, *18*(2), 281–290. https://doi.org/10.1029/WR018i002p00281

Pandey, S. N., Chaudhuri, A., Rajaram, H., & Kelkar, S. (2015). Fracture transmissivity evolution due to silica dissolution/precipitation during geothermal heat extraction. *Geothermics*, *57*, 111–126. https://doi.org/10.1016/j.geothermics.2015.06.011

Pandey, S. N., Vishal, V., & Chaudhuri, A. (2018). Geothermal reservoir modeling in a coupled thermo-hydro-mechanical-chemical approach: A review. *Earth-Science Reviews*, *185*, 1157–1169. https://doi.org/10.1016/j.earscirev.2018.09.004

Parisio, F., Tarokh, A., Makhnenko, R., Naumov, D., Miao, X.-Y., Kolditz, O., & Nagel, T. (2019). Experimental characterization and numerical modelling of fracture processes in granite. *International Journal of Solids and Structures*, *163*, 102–116. https://doi.org/10.1016/j.ijsolstr.2018.12.019

Parisio, F., Vilarrasa, V., Wang, W., Kolditz, O., & Nagel, T. (2019). The risks of long-term re-injection in supercritical geothermal systems. *Nature Communications*, *10*(1), 4391. https://doi.org/10.1038/s41467-019-12146-0

Parker, R. (1999). The Rosemanowes HDR project 1983–1991. *Geothermics*, *28*(4–5), 603–615. https://doi.org/10.1016/S0375-6505(99)00031-0

Passelègue, François. X., Brantut, N., & Mitchell, T. M. (2018). Fault Reactivation by Fluid Injection: Controls From Stress State and Injection Rate. *Geophysical Research Letters*, *45*(23). https://doi.org/10.1029/2018GL080470

Pawley, S., Schultz, R., Playter, T., Corlett, H., Shipman, T., Lyster, S., & Hauck, T. (2018). The Geological Susceptibility of Induced Earthquakes in the Duvernay Play. *Geophysical Research Letters*, *45*(4), 1786–1793. https://doi.org/10.1002/2017GL076100

Pine, R. J., & Batchelor, A. S. (1984). Downward migration of shearing in jointed rock during hydraulic injections. *International Journal of Rock Mechanics and Mining Sciences &*

Geomechanics Abstracts, *21*(5), 249–263. https://doi.org/10.1016/0148-9062(84)92681-0

Raleigh, C. B., Healy, J. H., & Bredehoeft, J. D. (1976). An Experiment in Earthquake Control at Rangely, Colorado. *Science*, *191*(4233), 1230–1237. https://doi.org/10.1126/science.191.4233.1230

Rice, J. R., & Cleary, M. P. (1976). Some basic stress diffusion solutions for fluid-saturated elastic porous media with compressible constituents. *Reviews of Geophysics*, *14*(2), 227. https://doi.org/10.1029/RG014i002p00227

Richards, H. G., Parker, R. H., Green, A. S. P., Jones, R. H., Nicholls, J. D. M., Nicol, D. A. C., Randall, M. M., Richards, S., Stewart, R. C., & Willis-Richards, J. (1994). The performance and characteristics of the experimental hot dry rock geothermal reservoir at Rosemanowes, Cornwall (1985–1988). *Geothermics*, *23*(2), 73–109. https://doi.org/10.1016/0375-6505(94)90032-9

Richter, C. F. (1935). An instrumental earthquake magnitude scale. *Bulletin of the Seismological Society of America*, *25*(1), 1–32.

Riffault, J., Dempsey, D., Archer, R., Kelkar, S., & Karra, S. (2016). Understanding poroelastic stressing and induced seismicity with a stochastic/deterministic model: An application to an EGS stimulation at Paralana, South Australia, 2011. *41st Workshop on Geothermal Reservoir Engineering*, *SGP-TR-209*.

Riffault, J., Dempsey, D., Karra, S., & Archer, R. (2018). Microseismicity Cloud Can Be Substantially Larger Than the Associated Stimulated Fracture Volume: The Case of the Paralana Enhanced Geothermal System. *Journal of Geophysical Research: Solid Earth*. https://doi.org/10.1029/2017JB015299

Ritz, V. A., Mizrahi, L., Repollés, V. C., Rinaldi, A. P., Hjörleifsdóttir, V., & Wiemer, S. (2023). *Pseudo-prospective forecasting of induced and natural seismicity in the Hengill geothermal field* [Preprint]. Preprints. https://doi.org/10.22541/essoar.168500354.49240043/v1

Ritz, V. A., Rinaldi, A. P., & Wiemer, S. (2022). Transient evolution of the relative size distribution of earthquakes as a risk indicator for induced seismicity. *Communications Earth & Environment*, *3*(1), 249. https://doi.org/10.1038/s43247-022-00581-9

Ruina, A. (1983). Slip instability and state variable friction laws. *Journal of Geophysical Research: Solid Earth*, *88*(B12), 10359–10370. https://doi.org/10.1029/JB088iB12p10359

Ruiz-Barajas, S., Sharma, N., Convertito, V., Zollo, A., & Benito, B. (2017). Temporal evolution of a seismic sequence induced by a gas injection in the Eastern coast of Spain. *Scientific Reports*, *7*(1), 2901. https://doi.org/10.1038/s41598-017-02773-2

Rutqvist, J., Dobson, P. F., Garcia, J., Hartline, C., Jeanne, P., Oldenburg, C. M., Vasco, D. W., & Walters, M. (2015). The Northwest Geysers EGS Demonstration Project, California: Pre-stimulation Modeling and Interpretation of the Stimulation. *Mathematical Geosciences*, *47*(1), 3–29. https://doi.org/10.1007/s11004-013-9493-y

Rutqvist, J., & Oldenburg, C. M. (2008). Analysis of Injection-Induced Micro-Earthquakes in a Geothermal Steam Reservoir, The Geysers Geothermal Field, California. *Proceedings of the 42th US Rock Mechanics Symposium, Paper No. 151*. http://escholarship.org/uc/item/4qg7v6qz.pdf.

Sáez, A., & Lecampion, B. (2023). Post-injection aseismic slip as a mechanism for the delayed triggering of seismicity. *Proceedings of the Royal Society A: Mathematical, Physical and Engineering Sciences*, *479*(2273), 20220810. https://doi.org/10.1098/rspa.2022.0810

Sáez, A., Lecampion, B., Bhattacharya, P., & Viesca, R. C. (2022). Three-dimensional fluid-driven stable frictional ruptures. *Journal of the Mechanics and Physics of Solids*, *160*, 104754. https://doi.org/10.1016/j.jmps.2021.104754

Salimzadeh, S., Paluszny, A., Nick, H. M., & Zimmerman, R. W. (2018). A three-dimensional coupled thermo-hydro-mechanical model for deformable fractured geothermal systems. *Geothermics*, *71*, 212–224. https://doi.org/10.1016/j.geothermics.2017.09.012

Sanjuan, B., Pinault, J.-L., Rose, P., Gérard, A., Brach, M., Braibant, G., Crouzet, C., Foucher, J.-C., Gautier, A., & Touzelet, S. (2006). Tracer testing of the geothermal heat exchanger at Soultz-sous-Forêts (France) between 2000 and 2005. *Geothermics*, *35*(5–6), 622–653. https://doi.org/10.1016/j.geothermics.2006.09.007

Sasaki, S. (1998). Characteristics of microseismic events induced during hydraulic fracturing experiments at the Hijiori hot dry rock geothermal energy site, Yamagata, Japan. *Tectonophysics*, *289*(1–3), 171–188. https://doi.org/10.1016/S0040-1951(97)00314-4

Schill, E., Genter, A., Cuenot, N., & Kohl, T. (2017). Hydraulic performance history at the Soultz EGS reservoirs from stimulation and long-term circulation tests. *Geothermics*, *70*, 110–124. https://doi.org/10.1016/j.geothermics.2017.06.003

Schindler, M., Baumgärtner, J., Gandy, T., Hauffe, P., Hettkamp, T., Menzel, H., Penzkofer, P., Teza, D., Tischner, T., & Wahl, G. (2010). Successful hydraulic stimulation techniques for electric power production in the Upper Rhine Graben, Central Europe. *Proceedings World Geothermal Congres*, 7.

Schmittbuhl, J., Lambotte, S., Lengliné, O., Grunberg, M., Jund, H., Vergne, J., Cornet, F., Doubre, C., & Masson, F. (2022). Induced and triggered seismicity below the city of Strasbourg, France from November 2019 to January 2021. *Comptes Rendus. Géoscience*, *353*(S1), 561–584. https://doi.org/10.5802/crgeos.71

Schoenball, M., Baujard, C., Kohl, T., & Dorbath, L. (2012). The role of triggering by static stress transfer during geothermal reservoir stimulation: Stress transfer during stimulation.

Journal of Geophysical Research: Solid Earth, *117*(B9). https://doi.org/10.1029/2012JB009304

Scholz, C. H. (1998). Earthquakes and friction laws. *Nature*, *391*(6662), 37–42. https://doi.org/10.1038/34097

Scholz, C. H. (2002). *Earthquakes and faulting* (Cambridge University Press).

Schultz, R., Skoumal, R. J., Brudzinski, M. R., Eaton, D., Baptie, B., & Ellsworth, W. (2020). Hydraulic Fracturing-Induced Seismicity. *Reviews of Geophysics*, *58*(3). https://doi.org/10.1029/2019RG000695

Scuderi, M. M., & Collettini, C. (2016). The role of fluid pressure in induced vs. triggered seismicity: Insights from rock deformation experiments on carbonates. *Scientific Reports*, *6*(1), 24852. https://doi.org/10.1038/srep24852

Scuderi, M. M., Collettini, C., & Marone, C. (2017). Frictional stability and earthquake triggering during fluid pressure stimulation of an experimental fault. *Earth and Planetary Science Letters*, *477*, 84–96. https://doi.org/10.1016/j.epsl.2017.08.009

Segall, P. (1989). Earthquakes triggered by fluid extraction. *Geology*, *17*(10), 942. https://doi.org/10.1130/0091-7613(1989)017<0942:ETBFE>2.3.CO;2

Segall, P., & Fitzgerald, S. D. (1998). A note on induced stress changes in hydrocarbon and geothermal reservoirs. *Tectonophysics*, *289*(1–3), 117–128. https://doi.org/10.1016/S0040-1951(97)00311-9

Segall, P., & Lu, S. (2015). Injection-induced seismicity: Poroelastic and earthquake nucleation effects: Injection induced seismicity. *Journal of Geophysical Research: Solid Earth*, *120*(7), 5082–5103. https://doi.org/10.1002/2015JB012060

Shapiro, S. A. (2015). Fluid-induced seismicity. *Cambridge University Press*.

Shapiro, S. A., Dinske, C., & Kummerow, J. (2007). Probability of a given-magnitude earthquake induced by a fluid injection. *Geophysical Research Letters*, *34*(22), L22314. https://doi.org/10.1029/2007GL031615

Shapiro, S. A., Dinske, C., Langenbruch, C., & Wenzel, F. (2010). Seismogenic index and magnitude probability of earthquakes induced during reservoir fluid stimulations. *The Leading Edge*, *29*(3), 304–309. https://doi.org/10.1190/1.3353727

Sibson, R. H. (1973). Interactions between Temperature and Pore-Fluid Pressure during Earthquake Faulting and a Mechanism for Partial or Total Stress Relief. *Nature Physical Science*, *243*(126), 66–68. https://doi.org/10.1038/physci243066a0

Smith, J. D., Heimisson, E. R., Bourne, S. J., & Avouac, J.-P. (2022). Stress-based forecasting of induced seismicity with instantaneous earthquake failure functions: Applications to the Groningen gas reservoir. *Earth and Planetary Science Letters*, *594*, 117697. https://doi.org/10.1016/j.epsl.2022.117697

Stefanou, I., & Tzortzopoulos, G. (2022). Preventing Instabilities and Inducing Controlled, Slow-Slip in Frictionally Unstable Systems. *Journal of Geophysical Research: Solid Earth*, *127*(7), e2021JB023410. https://doi.org/10.1029/2021JB023410

Stein, R. S. (1999). The role of stress transfer in earthquake occurrence. *Nature*, *402*(6762), 605–609. https://doi.org/10.1038/45144

Stein, R. S. (2005). Earthquake Conversations. *Scientific American Sp*, *15*(2), 82–89. https://doi.org/10.1038/scientificamerican0705-82sp

Steketee, J. A. (1958). Some geophysical applications of the elasticity theory of dislocations. *Canadian Journal of Physics*, *36*(9), 1168–1198. https://doi.org/10.1139/p58-123

Tal, Y., Goebel, T., & Avouac, J.-P. (2020). Experimental and modeling study of the effect of fault roughness on dynamic frictional sliding. *Earth and Planetary Science Letters*, *536*, 116133. https://doi.org/10.1016/j.epsl.2020.116133

Taron, J., & Elsworth, D. (2009). Thermal–hydrologic–mechanical–chemical processes in the evolution of engineered geothermal reservoirs. *International Journal of Rock Mechanics and Mining Sciences*, *46*(5), 855–864. https://doi.org/10.1016/j.ijrmms.2009.01.007

Terakawa, T. (2014). Evolution of pore fluid pressures in a stimulated geothermal reservoir inferred from earthquake focal mechanisms. *Geophysical Research Letters*, *41*(21), 7468–7476. https://doi.org/10.1002/2014GL061908

Terakawa, T., Miller, S. A., & Deichmann, N. (2012). High fluid pressure and triggered earthquakes in the enhanced geothermal system in Basel, Switzerland: High fluid pressure in Basel. *Journal of Geophysical Research: Solid Earth*, *117*(B7). https://doi.org/10.1029/2011JB008980

Tester, J. W., Anderson, B. J., Batchelor, A. S., Blackwell, D. D., DiPippo, R., Drake, E. M., Garnish, J., Livesay, B., Moore, M. C., Nichols, K., Petty, S., Nafi Toksoz, M., Veatch, R. W., Baria, R., Augustine, C., Murphy, E., Negraru, P., & Richards, M. (2007). Impact of enhanced geothermal systems on US energy supply in the twenty-first century. *Philosophical Transactions of the Royal Society A: Mathematical, Physical and Engineering Sciences*, *365*(1853), 1057–1094. https://doi.org/10.1098/rsta.2006.1964

Tischner, T., Schindler, M., Jung, R., & Nami, P. (2007). HDR project Soultz: Hydraulic and seismic observations during stimulation of the 3 deep wells by massive water injections. *32nd Workshop on Geothermal Engineering*, 7.

Toda, S., Lin, J., & Stein, R. S. (2011). Using the 2011 M w 9.0 off the Pacific coast of Tohoku Earthquake to test the Coulomb stress triggering hypothesis and to calculate faults brought closer to failure. *Earth, Planets and Space*, *63*(7), 725–730. https://doi.org/10.5047/eps.2011.05.010

Toda, S., Stein, R. S., Richards-Dinger, K., & Bozkurt, S. (2005). Forecasting the evolution of seismicity in southern California: Animations built on earthquake stress transfer. *Journal of Geophysical Research*, *110*(B5), B05S16. https://doi.org/10.1029/2004JB003415

Townend, J., & Zoback, M. D. (2000). How faulting keeps the crust strong. *Geology*, *28*(5), 399. https://doi.org/10.1130/0091-7613(2000)28<399:HFKTCS>2.0.CO;2

Ucar, E., Berre, I., & Keilegavlen, E. (2017). Postinjection Normal Closure of Fractures as a Mechanism for Induced Seismicity. *Geophysical Research Letters*, *44*(19), 9598–9606. https://doi.org/10.1002/2017GL074282

Utsu, T. (1961). A statistical study on the occurrence of aftershocks. *Geophys. Mag.*, *30*, 521–605.

Vilarrasa, V., Bolster, D., Olivella, S., & Carrera, J. (2010). Coupled hydromechanical modeling of CO2 sequestration in deep saline aquifers. *International Journal of Greenhouse Gas Control*, *4*(6), 910–919. https://doi.org/10.1016/j.ijggc.2010.06.006

Vilarrasa, V., De Simone, S., Carrera, J., & Villaseñor, A. (2021). Unraveling the Causes of the Seismicity Induced by Underground Gas Storage at Castor, Spain. *Geophysical Research Letters*, *48*(7). https://doi.org/10.1029/2020GL092038

Vilarrasa, V., De Simone, S., Carrera, J., & Villaseñor, A. (2022). Multiple induced seismicity mechanisms at Castor underground gas storage illustrate the need for thorough monitoring. *Nature Communications*, *13*(1), 3447. https://doi.org/10.1038/s41467-022-30903-6

Wang, H. (2000). *Theory of linear poroelasticity with applications to geomechanics and hydrogeology*. (Princeton University Press).

Wang, T. A., & Dunham, E. M. (2022). Hindcasting injection-induced aseismic slip and microseismicity at the Cooper Basin Enhanced Geothermal Systems Project. *Scientific Reports*, *12*(1), 19481. https://doi.org/10.1038/s41598-022-23812-7

Wei, S., Avouac, J.-P., Hudnut, K. W., Donnellan, A., Parker, J. W., Graves, R. W., Helmberger, D., Fielding, E., Liu, Z., Cappa, F., & Eneva, M. (2015). The 2012 Brawley swarm triggered by injection-induced aseismic slip. *Earth and Planetary Science Letters*, *422*, 115–125. https://doi.org/10.1016/j.epsl.2015.03.054

Wibberley, C. A. J., & Shimamoto, T. (2005). Earthquake slip weakening and asperities explained by thermal pressurization. *Nature*, *436*(7051), 689–692. https://doi.org/10.1038/nature03901

Wiemer, S., & Wyss, M. (2002). Mapping spatial variability of the frequency-magnitude distribution of earthquakes. In *Advances in Geophysics* (Vol. 45, pp. 259–V). Elsevier. https://doi.org/10.1016/S0065-2687(02)80007-3

Wozniakowska, P., & Eaton, D. W. (2020). Machine Learning-Based Analysis of Geological Susceptibility to Induced Seismicity in the Montney Formation, Canada. *Geophysical Research Letters*, *47*(22), e2020GL089651. https://doi.org/10.1029/2020GL089651

Wu, H., Fu, P., Frone, Z., White, M. D., Ajo-Franklin, J. B., Morris, J. P., Knox, H. A., Schwering, P. C., Strickland, C. E., Roberts, B. Q., Vermeul, V. R., Mattson, E. D., Ingraham, M. D., Kneafsey, T. J., & Blankenship, D. A. (2021). Modeling heat transport processes in enhanced geothermal systems: A validation study from EGS Collab Experiment 1. *Geothermics*, *97*, 102254. https://doi.org/10.1016/j.geothermics.2021.102254

Wu, H., Vilarrasa, V., De Simone, S., Saaltink, M., & Parisio, F. (2021). Analytical Solution to Assess the Induced Seismicity Potential of Faults in Pressurized and Depleted Reservoirs. *Journal of Geophysical Research: Solid Earth*, *126*(1). https://doi.org/10.1029/2020JB020436

Wynants-Morel, N., Cappa, F., De Barros, L., & Ampuero, J. (2020). Stress Perturbation From Aseismic Slip Drives the Seismic Front During Fluid Injection in a Permeable Fault. *Journal of Geophysical Research: Solid Earth*, *125*(7). https://doi.org/10.1029/2019JB019179

Yang, Y., & Dunham, E. M. (2021). Effect of Porosity and Permeability Evolution on Injection-Induced Aseismic Slip. *Journal of Geophysical Research: Solid Earth*, *126*(7). https://doi.org/10.1029/2020JB021258

Yeo, I. W., Brown, M. R. M., Ge, S., & Lee, K. K. (2020). Causal mechanism of injection-induced earthquakes through the Mw 5.5 Pohang earthquake case study. *Nature Communications*, *11*(1), 2614. https://doi.org/10.1038/s41467-020-16408-0

Yoo, H., Park, S., Xie, L., Kim, K.-I., Min, K.-B., Rutqvist, J., & Rinaldi, A. P. (2021). Hydro-mechanical modeling of the first and second hydraulic stimulations in a fractured geothermal reservoir in Pohang, South Korea. *Geothermics*, *89*, 101982. https://doi.org/10.1016/j.geothermics.2020.101982

Yoon, J. S., Zang, A., & Stephansson, O. (2014). Numerical investigation on optimized stimulation of intact and naturally fractured deep geothermal reservoirs using hydro-mechanical coupled discrete particles joints model. *Geothermics*, *52*, 165–184. https://doi.org/10.1016/j.geothermics.2014.01.009

Yoon, J. S., Zimmermann, G., & Zang, A. (2015). Discrete element modeling of cyclic rate fluid injection at multiple locations in naturally fractured reservoirs. *International Journal of Rock Mechanics and Mining Sciences*, *74*, 15–23. https://doi.org/10.1016/j.ijrmms.2014.12.003

Zang, A., Niemz, P., Von Specht, S., Zimmermann, G., Milkereit, C., Plenkers, K., & Klee, G. (2023). *Comprehensive data set of in-situ hydraulic stimulation experiments for*

geothermal purposes at the Äspö Hard Rock Laboratory (Sweden) [Preprint]. ESSD – Land/Geophysics and geodesy. https://doi.org/10.5194/essd-2023-170

Zang, A., Oye, V., Jousset, P., Deichmann, N., Gritto, R., McGarr, A., Majer, E., & Bruhn, D. (2014). Analysis of induced seismicity in geothermal reservoirs – An overview. *Geothermics*, *52*, 6–21. https://doi.org/10.1016/j.geothermics.2014.06.005

Zang, A., Zimmermann, G., Hofmann, H., Stephansson, O., Min, K.-B., & Kim, K. Y. (2019). How to Reduce Fluid-Injection-Induced Seismicity. *Rock Mechanics and Rock Engineering*, *52*(2), 475–493. https://doi.org/10.1007/s00603-018-1467-4

Zareidarmiyan, A., Parisio, F., Makhnenko, R. Y., Salarirad, H., & Vilarrasa, V. (2021). How Equivalent Are Equivalent Porous Media? *Geophysical Research Letters*, *48*(9). https://doi.org/10.1029/2020GL089163

Zareidarmiyan, A., Salarirad, H., Vilarrasa, V., De Simone, S., & Olivella, S. (2018). Geomechanical Response of Fractured Reservoirs. *Fluids*, *3*(4), 70. https://doi.org/10.3390/fluids3040070

Zareidarmiyan, A., Salarirad, H., Vilarrasa, V., Kim, K.-I., Lee, J., & Min, K.-B. (2020). Comparison of numerical codes for coupled thermo-hydro-mechanical simulations of fractured media. *Journal of Rock Mechanics and Geotechnical Engineering*, *12*(4), 850–865. https://doi.org/10.1016/j.jrmge.2019.12.016

Zhang, Y., Person, M., Rupp, J., Ellett, K., Celia, M. A., Gable, C. W., Bowen, B., Evans, J., Bandilla, K., Mozley, P., Dewers, T., & Elliot, T. (2013). Hydrogeologic Controls on Induced Seismicity in Crystalline Basement Rocks Due to Fluid Injection into Basal Reservoirs: Y. Zhang et al. Ground Water xx, no. xx: xx-xx. *Groundwater*, *51*(4), 525–538. https://doi.org/10.1111/gwat.12071

Zhu, C., Fan, Z., & Eichhubl, P. (2017). *The Effect of Variable Fluid Injection Rate on the Stability of Seismogenic Faults*. c.

Zhu, J. B., Kang, J. Q., Elsworth, D., Xie, H. P., Ju, Y., & Zhao, J. (2021). Controlling Induced Earthquake Magnitude by Cycled Fluid Injection. *Geophysical Research Letters*, *48*(19). https://doi.org/10.1029/2021GL092885

Zimmerman, R. W. (2000). Coupling in poroelasticity and thermoelasticity. *International Journal of Rock Mechanics and Mining Sciences*, *37*(1–2), 79–87. https://doi.org/10.1016/S1365-1609(99)00094-5